

AD-A265 591



2

Final Report
ONR Grant No. N00014-92-J-1505

PROPERTIES OF INTERFACIAL TRIBO-FILMS

Submitted to:

Scientific Officer Code: 1131N
Peter P. Schmidt
Office of Naval Research
800 North Quincy Street
Arlington, VA 22217-5000

Submitted by:

David D. Makel
Senior Scientist

Doris Kuhlmann-Wilsdorf
University Professor of Applied Science

DTIC
ELECTE
JUN 09 1993
S E D

SEAS Report No. UVA/525755/MSE93/101
June 1993

DEPARTMENT OF MATERIALS SCIENCE AND ENGINEERING

STRIPED STATEMENT

Approved for public release
Distribution Unlimited

SCHOOL OF
ENGINEERING 
& APPLIED SCIENCE

University of Virginia
Thornton Hall
Charlottesville, VA 22903

93-12854



23902

93 6 08 04 2

UNIVERSITY OF VIRGINIA
School of Engineering and Applied Science

The University of Virginia's School of Engineering and Applied Science has an undergraduate enrollment of approximately 1,500 students with a graduate enrollment of approximately 600. There are 160 faculty members, a majority of whom conduct research in addition to teaching.

Research is a vital part of the educational program and interests parallel academic specialties. These range from the classical engineering disciplines of Chemical, Civil, Electrical, and Mechanical and Aerospace to newer, more specialized fields of Applied Mechanics, Biomedical Engineering, Systems Engineering, Materials Science, Nuclear Engineering and Engineering Physics, Applied Mathematics and Computer Science. Within these disciplines there are well equipped laboratories for conducting highly specialized research. All departments offer the doctorate; Biomedical and Materials Science grant only graduate degrees. In addition, courses in the humanities are offered within the School.

The University of Virginia (which includes approximately 2,000 faculty and a total of full-time student enrollment of about 17,000), also offers professional degrees under the schools of Architecture, Law, Medicine, Nursing, Commerce, Business Administration, and Education. In addition, the College of Arts and Sciences houses departments of Mathematics, Physics, Chemistry and others relevant to the engineering research program. The School of Engineering and Applied Science is an integral part of this University community which provides opportunities for interdisciplinary work in pursuit of the basic goals of education, research, and public service.

Final Report
ONR Grant No. N00014-92-J-1505

PROPERTIES OF INTERFACIAL TRIBO-FILMS

Submitted to:

Scientific Officer Code: 1131N
Peter P. Schmidt
Office of Naval Research
800 North Quincy Street
Arlington, VA 22217-5000

Submitted by:

David D. Makel
Senior Scientist

Doris Kuhlmann-Wilsdorf
University Professor of Applied Science

| | |
|--------------------|--|
| Accession For | |
| NTIS CRA&I | <input checked="checked" type="checkbox"/> |
| DTIC TAB | <input type="checkbox"/> |
| Unannounced | <input type="checkbox"/> |
| Justification | |
| By | |
| Distribution / | |
| Availability Codes | |
| Dist | Avail and/or Special |
| A-1 | |

Department of Materials Science and Engineering
School of Engineering and Applied Science
University of Virginia
Thornton Hall
Charlottesville, VA 22903-2442

DTIC QUALITY INSPECTED 2

SEAS Report No. UVA/525755/MSE93/101
June 1993

Copy No. _____

| REPORT DOCUMENTATION PAGE | | | Form Approved OMB No. 0704-0188 | |
|---|---|---|------------------------------------|--|
| <small>Public reporting burden for this collection of information is estimated to average 1 hour per response, including the time for reviewing instructions, searching existing data sources, gathering and maintaining the data needed, and completing and reviewing the collection of information. Send comments regarding this burden estimate or any other aspect of this collection of information, including suggestions for reducing this burden, to Washington Headquarters Services, Directorate for Information Operations and Reports, 1215 Jefferson Davis Highway, Suite 1204, Arlington, VA 22202-4302, and to the Office of Management and Budget, Paperwork Reduction Project (0704-0188), Washington, DC 20503.</small> | | | | |
| 1. AGENCY USE ONLY (Leave blank) | 2. REPORT DATE June 1993 | 3. REPORT TYPE AND DATES COVERED Final Report 3/15/92 - 2/28/93 | | |
| 4. TITLE AND SUBTITLE Properties of Interfacial Tribo-Films | | 5. FUNDING NUMBERS N00014-92-J-1505 | | |
| 6. AUTHOR(S) D. D. Makel D. Kuhlmann-Wilsdorf | | | | |
| 7. PERFORMING ORGANIZATION NAME(S) AND ADDRESS(ES) Department of Materials Science and Engineering University of Virginia Charlottesville, VA 22903-2442 | | 8. PERFORMING ORGANIZATION REPORT NUMBER UVA/525755/MSE93/101 | | |
| 9. SPONSORING/MONITORING AGENCY NAME(S) AND ADDRESS(ES) Office of the Chief of Naval Research Department of the Navy Arlington, VA 22217-5000 | | 10. SPONSORING/MONITORING AGENCY REPORT NUMBER | | |
| 11. SUPPLEMENTARY NOTES | | | | |
| 12a. DISTRIBUTION/AVAILABILITY STATEMENT Approved for public release; distribution unlimited | | 12b. DISTRIBUTION CODE | | |
| 13. ABSTRACT (Maximum 200 words) Research has been conducted on the properties of interfacial films of the kind formed in the course of sliding wear, named "tribo-films." Using specialized instrumentation, in particular the so-called Hoop Apparatus and a Bridgman-Anvil Device, we have found many new insights into the fundamental mechanisms responsible for the phenomena observed during sliding. In particular, advances have been made in, 1) the understanding of lubrication through adsorbed films, 2) the fundamental understanding of stick-slip, 3) the deformation mechanisms at high strains, pertinent to tribo-films and sub-surface regions, 4) micromechanisms of MoS ₂ lubrication, 5) understanding the implications of various materials properties for possible solid lubricants, and 6) the formation of amorphous tribo-material by high strains. The results from this contract have been documented in 14 refereed publications. | | | | |
| 14. SUBJECT TERMS friction and wear, solid lubricants, amorphous metals, adsorbed lubricants, high strain deformation, molybdenum disulfide, tribo-material, Hoop Apparatus, Bridgman-Anvil Device | | 15. NUMBER OF PAGES 3 | | |
| | | 16. PRICE CODE | | |
| 17. SECURITY CLASSIFICATION OF REPORT Unclassified | 18. SECURITY CLASSIFICATION OF THIS PAGE Unclassified | 19. SECURITY CLASSIFICATION OF ABSTRACT Unclassified | 20. LIMITATION OF ABSTRACT UL | |

DEPARTMENT OF MATERIALS SCIENCE AND ENGINEERING
SCHOOL OF ENGINEERING AND APPLIED SCIENCE
UNIVERSITY OF VIRGINIA
CHARLOTTESVILLE, VA 22901

Final Report to Contract N00014-92-J-1505

Properties of Interfacial Tribo-Films

3/15/1992 to 2/28/1993

by

D. D. Makel and Doris Kuhlmann-Wilsdorf

Research has been conducted on the properties of interfacial films of the kind formed in the course of sliding wear, named "tribo-films". Typically, they are composed of elements of both sides plus, not infrequently, that of the ambient atmosphere in particular oxygen; and their crystal structures may be different from those on either side or they may be amorphous. Thus they are fundamental for the understanding, and eventually the beneficial influencing, of friction and wear. We have made use of specialized instrumentation, in particular the Hoop apparatus and the Bridgman Anvil apparatus, and of our considerable know-how in their connection. For these reasons, and because ONR sponsorship was terminated and much research was already "in the pipe-line", much was "closed out", and for a period of several months we continued working without a contract that had been delayed through a clerical error, the results in terms of publications and new insights have been considerably more than normally expected for the sum of about \$100,000 that had been available.

Lubrication Through Adsorbed Moisture

Previous research with specialized apparatus designed and constructed in our own laboratory had provided us with a great deal of background knowledge on adsorbed moisture at sliding interfaces. Specifically, we had become aware of the considerable role which adsorbed moisture plays in reducing friction and wear and of the possibility of deliberately using moisture for lubrication. This has led to a very successful practical method for reducing wear in high-performance sliding contacts published in

"Improved Sliding Electrical Brush Performance Through the Use of Water Lubrication", D.D. Makel and D. Kuhlmann-Wilsdorf, ICEC-IEEE Holm 92 (38th. Holm Conference on Electrical Contacts, IEEE, Philadelphia, PA, Oct. 19-21, 1992), pp.149-155; also IEEE Trans. Components, Hybrids and Manuf. Techn., in the press.

Theory of Stick-Slip

Another very important result of our work on the behavior of adsorbed moisture layers has been a significant advance in the understanding of stiction, e.g. as affecting magnetic recording media:

"Moisture Effects Including Stiction Resulting from Adsorbed Water Films", Chao Gao, Doris Kuhlmann-Wilsdorf and David D. Makel, Trans. ASME J. of Tribology, 114 (1992) pp. 174-180.

The culmination of this research has been the formulation of a general theory of stick-slip:

"Fundamentals of Stick-Slip", Chao Gao, Doris Kuhlmann-Wilsdorf and David D. Makel, Wear, 162-164 (1993) pp.1139-1149. See also "Wear of Materials 1993 Proceedings", (Ed. K. C. Ludema, R. G. Bayer and D. Dowson Elsevier, U.K.), Part B, 1993, pp.1139-1149.

"Dynamic Analysis of Stick-Slip Motion", Chao Gao, Doris Kuhlmann-Wilsdorf and David D. Makel, Wear, submitted Dec. 23, 1992.

Deformation Mechanisms at High Strains, Pertinent to Tribo-Films and Sub-Surface Regions

Another prominent area of interest concerned mechanisms of plastic deformation, e.g. as accommodating the very large shear strains in tribo-films and adjoining subsurface layers. These control the mechanical properties of solid lubricants as well as of the wearing surfaces themselves. The following papers have been published in this area:

"Microstructural Evolution in Rolled Aluminum", B. Bay, N. Hansen and D. Kuhlmann-Wilsdorf, Mater. Sci. Engg., A158 (1992) pp.139-146.

"Evolution of FCC Deformation Structures in Polyslip", B. Bay, N. Hansen, D.A. Hughes and D. Kuhlmann-Wilsdorf, Acta Met. et Mater., 40 (1992) pp. 205-219.

"Theory of Worksoftening in High-Performance Alloys", D. Kuhlmann-Wilsdorf and H.G.F. Wilsdorf, phys. stat. sol., (P. Haasen 65th birthday celebration issue), (b) 172 (1992) pp.235-248.

"Fundamentals of Cell and Subgrain Structures in Historical Perspective", D. Kuhlmann-Wilsdorf, Scripta Met. et Mater., 27 (1992) pp.951-956.

"LEDS Theory of Worksoftening and Hall-Petch Hardening in Extruded MA Alloys", H.G.F. Wilsdorf and D. Kuhlmann-Wilsdorf, Mater. Sci. Eng., in the press.

"Tammann's Grain Boundary Substance Revisited", Doris Kuhlmann-Wilsdorf and Heinz G. F. Wilsdorf, Zeits. f. Metallkunde, in the press.

"Grain Boundary Hardening, Worksoftening and LEDS in MA Alloys", H.G.F. Wilsdorf and D. Kuhlmann-Wilsdorf, in "Modelling of Plastic Deformation and Its Engineering Applications", (Eds. S. I. Andersen, J. B. Bilde-Sorensen, N. Hansen, D. Juul Jensen, T. Leffers, H. Lilholt, T. Lorentzen, O. B. Pedersen and B. Ralph, Risø National Laboratory, Roskilde, Denmark: 13th. Risø Intl. Symp. on Materials Science, Sept. 7-11, 1992) pp.511-517.

Fundamental Studies on the Suitability of Different Metals for Use as Solid Lubricants

A number of predictive parameters are known for the selection of materials for use as solid lubricants. We have endeavored to relate these to underlying physical properties and mechanisms through severely shearing several pure metals under high normal pressures and examining the correlated stress-strain curves as well as structures. This work has given a number of new insights and is being published as

"Pressure and Structure Dependence of Solid Lubrication", M.S. Bednar, B.C. Cai and D. Kuhlmann-Wilsdorf, Lubrication Engineering, in the press.

Study of Solid Lubrication Through MoS₂

By the use of our specialized equipment we have studied sliding between a polished gold substrate and burnished MoS₂. The results have shown that the MoS₂ layers shear within themselves while being thinned out between, and pushed ahead and around contact spots. The considerable known deleterious effect of moisture on MoS₂ lubrication was shown to be due to mechanical softening of the MoS₂. This parallels the previously studied effect of moisture on graphite lubrication where it is, however, beneficial. This work has been published as:

"Micromechanics of MoS₂ Lubrication", Chao Gao, Louis Bredell, Doris Kuhlmann-Wilsdorf and David D. Makel, Wear, 162-164 (1993) pp.480-491; see also "Wear of Materials 1993 Proceedings", (Ed. K. C. Ludema, R. G. Bayer and D. Dowson Elsevier, U.K.), Part A, 1993, pp.480-491.

Amorphization of Tribo-Films

Last but not least, we have studied amorphization of tribo-films through simulations in the Bridgman anvil apparatus. Very large shears were applied under various levels of superimposed normal pressure. It was found that the magnitude of the shear, but not the pressure, is the decisive influence to cause amorphization. A general theory of crystal amorphization through plastic deformation has been proposed on the basis of our observations:

"Mechanism of Metal Amorphization Through Plastic Deformation", D. Kuhlmann-Wilsdorf and M. S. Bednar, Scripta Met. et Mater., 28 (1993) pp.371-376.

IMPROVED SLIDING ELECTRICAL BRUSH PERFORMANCE
THROUGH THE USE OF WATER LUBRICATION

by

David D. Makel and Doris Kuhlmann-Wilsdorf

University of Virginia
Charlottesville, VAABSTRACT

Electrical and wear performance of sliding electrical contacts is critically dependent on the local contact spot temperature resulting from Joule and frictional heating. Continuous operation under significant heat input rates can raise the temperature to the point of severe performance degradation or catastrophic failure. Using a novel method of water application for both lubricating and cooling, greatly decreased wear rates and increases of the useable current densities in continuous operation have been achieved with metal fiber brushes. The method is expected to be similarly effective with other current collecting systems.

KEY WORDS: metal fiber brushes, water lubrication, high current density collectors

BACKGROUNDIncentive for the Present Work

Although the potentially superior properties of metal fiber brushes, in particular low resistance, low noise, and high speed and current density capabilities, have been demonstrated in numerous investigations (1-5), the development of practical metal fiber brushes has proved difficult. Experience in our laboratory has established three particular problems: i) fiber brushes tend to change shape during long term tests, ii) long term wear rates tend to be prohibitively high, and iii) the brushes have little ability to recover from minor perturbations such as temporary overloading or excessive current.

The present investigations have been focussed on producing metal fiber brushes which avoid these problems without sacrificing their beneficial properties. Specifically, our goal has been to produce a current collection system with properties which will be described later, but the technological advances which have resulted from this work are believed to be of great importance to the field of sliding current collectors in general.

Reasons for Developing Metal Fiber Brushes

Metal fiber brushes, which predate the now nearly ubiquitous monolithic graphite based brushes, are, in their simplest form, a bundle of metal fibers held together at one end, with the loose distal fiber ends contacting the moving substrate. Their primary advantages are direct consequences of the large number of contact spots (on the order of 1 to 3 per fiber) which result from the local compliance of the individual fibers. In fact, an approximately 1 cm² metal fiber brush can have many thousands of contact spots, as compared to between approximately 1 to 40 contact spots for a comparably sized monolithic graphite based brush (6-12).

In a typical metal fiber brush the increase in the number of contact spots reduces the constriction resistance (R_c) to the point of being negligible (1), and because the brushes consist of continuous metal fibers the resistance of the brush itself, i.e. the body resistance (R_b), is also typically negligible.

This simplifies the well known relationship for total brush resistance (R_t)

$$R_b = R_o + R_f + R_c \quad \text{eq.1}$$

to

$$R_b = R_f \quad \text{eq.2}$$

where R_o is the resistance due to film resistivity. By definition, then, the measured resistance is described by

$$R = A\sigma_f \quad \text{eq.3}$$

where σ_f is the film resistivity and A is the true area of contact. Correspondingly, the power loss due to Joule heating (Q_j) is defined by

$$\begin{aligned} Q_j &= I^2 R_f \\ &= I^2 \frac{\sigma_f}{A} \end{aligned} \quad \text{eq.4}$$

with I the current.

The true area of contact (A) for fully plastic contact spots is generally described using the Meyer hardness of the softer of the two contacting materials (H) and the normal load (P) (13)

$$A = \frac{P}{H} \quad \text{eq.5}$$

In the case of metal fiber brushes, however, where the loads are typically an order of magnitude smaller than for monolithic brushes, the local contact spot pressure can fall below the material hardness resulting in elastic contact spots, with which the area per load is greater than with plastic spots (1,13). When the effects of electron tunneling at the edges of the contact spots, thermal softening, asperity curvature and contact spot ellipticity are also considered area calculations can be quite tedious. In response to this problem a computer program has been developed in this laboratory which quickly performs the requisite calculations (6,14).

Friction is another critical electrical brush property and the power loss due to friction heating (Q_f) increases with increasing load (P), friction (μ) and sliding speed (v), as

$$Q_f = \mu PV \quad \text{eq.6}$$

The sum of the evolved friction and Joule heat represents the total power loss due to the brushes (Q_t), as described by the familiar equation

$$Q_t = I^2 R_c + \mu PV \quad \text{eq.7}$$

Lowering this power is critical both for increasing the efficiency of the system and also for decreasing the local "flash" temperatures of the contact spots, which typically limit the useable current density (1,2,15).

Wear rate is of obvious interest for any applications which involve significant sliding distances. There are many measures of wear rate but without assuming any particular mechanism the practical wear rate (W) of any brush can best be described as the linear decrease of brush length (Δl) per distance travelled (L).

$$W = \frac{\Delta l}{L} = \frac{\Delta l}{vt} \quad \text{eq.8}$$

with v the sliding velocity and t the sliding time. This dimensionless wear rate will be used in the present paper.

EXPERIMENTAL SETUP

Design of the Brushes

Although increasing the number of fibers in a brush by reducing the fiber diameter should result in improved performance, finer fibers also make for a macroscopically softer brush with a reduced load bearing capacity, the more so with increasing length. A number of schemes to overcome this limit of fiber diameter reduction have been proposed in (16) and others are currently being evaluated in our laboratory. The particular brushes used in this set of experiments are described in Table I.

| | | |
|----------------------------|-------------|---------------|
| Fiber Type: | Ag- | Cu |
| Fiber diameter: | 18 | |
| Fiber Length: | ≈ 1 | 1 |
| Volume Fraction of Fibers: | | |
| Cross-Sectional Area: | | mm^2 |

Table I. Brush specifications

Automated Brush Tester

Due to the currents involved (typically 100 to 500 Amps) and the occasionally catastrophic manner in which the brushes fail, the existing brush testing devices in this laboratory (17,18) have recently been modified for computer-controlled testing (19). The new device automatically adjusts the brush forces, performs data reduction, records data, checks for user specified dangerous or damaging conditions, and shuts down the test when appropriate. This has made it possible to run tests lasting hundreds of hours, such as the one to be described in this paper.

Protective Atmosphere

The importance of excluding oxygen from the operating environment of metal fiber brushes made of readily oxidizable metals has long been recognized (1-4,20) and although the use of noble metals eliminates the need for protective atmospheres (1,2,21), in the present case the practicalities of using copper were dominant. Typical gases used as protective atmospheres are argon, nitrogen and carbon dioxide, and in many cases these gases can be used interchangeably. Preliminary tests conducted with all three gases, however, showed that the use of CO_2 resulted in a moderately low ($\approx 10^{-12} \Omega\text{m}^2$) film resistivity and a friction coefficient on the order of 0.3, while switching to either argon or nitrogen caused a slow increase in the friction and a reduction in the film resistivity, typically to the end of destroying the brushes from excessive frictional forces. For this reason CO_2 was chosen as a protective cover gas.

Water Lubrication

Previous work with metal fiber brushes (1-4,20) has shown that improved wear life and decreased friction can be achieved by using a high degree of moisture in the protective environment, and our initial experiments were conducted using a gas washing bottle to humidify the protective CO_2 . While this often resulted in short periods (sometimes as long as a few hours) of apparently excellent results these intervals were followed by increases in friction and often destruction of the brushes.

In an attempt to increase the reliability of the brushes a number of systems for supplying more humidity were constructed and tested. The first consisted of pieces of moistened felt mounted against the rotor at the leading edges of the brushes. This provided adequate moisture for operation at very high current densities (over 5 MA/ m^2) but the rotor space needed for the wipers decreased the ultimate brush population. For this reason pairs of gas jet atomizers were built, one for each brush, again concentrating the water delivery at the leading edges. This system also worked well, but to avoid using excessive gas the diameters of the jet orifices were very small (around 75 μm), and

this made them prone to clogging.

To solve these problems a new, moderate pressure (approximately 3×10^5 Pa) gas atomizer was designed and built in this laboratory. Using only about $7 \times 10^{-3} \text{ m}^3/\text{hr}$ (≈ 2.5 SCFH) of CO_2 this single atomizer produces a dense, fine fog that can be effectively "piped" into all three of the brush testing stations currently in use. Similar results have subsequently been achieved using standard gas atomizers, although the requisite gas flow rates are many times higher.

Test Parameters

The sliding speed and current magnitude used in the present tests were chosen as typical for the needs of high performance fiber brushes and the brush force and atmosphere were determined to be appropriate in preliminary tests. A summary of the testing parameters is given in Table II.

| | |
|----------------|-------------------------------|
| Sliding Speed: | 15 m/s |
| Current: | 100 Amps |
| Brush Force: | 0.5 N |
| Atmosphere: | Water Saturated CO_2 |

Table II. Brush testing parameters.

EXPERIMENTAL RESULTS

Film Resistivity

One of the most critical questions regarding the feasibility of using a high degree of moisture with the relatively fine ($\approx 18 \mu\text{m}$ diameter) fibers was whether the film resistivity would be prohibitively high (above approximately $3.5 \times 10^{-12} \Omega\text{m}^2$) at the requisite sliding speed of 15 m/s. At the speeds tested (approximately 15 to 25 m/s) the brush resistances remained in the desired low range as shown in Fig. 1. Using the aforementioned computer program the contact spots were determined to be elastic, and the real area of contact (including tunneling) was calculated to be about $2.3 \times 10^{-9} \text{ m}^2$. This corresponds to film resistivity values of about $1.3 \times 10^{-12} \Omega\text{m}^2$ for the negative brush and $6.9 \times 10^{-13} \Omega\text{m}^2$ for the positive brush, in full agreement with earlier analyses (1,2,22).

Although the resistance values in Fig. 1 show considerable scatter there is a consistent polarity effect in which the voltage drop across the positive brush/negative rotor couple (open symbols) is lower than the negative brush/positive rotor couple (solid symbol), except for a transition period just after the current reversal. This type of polarity effect has been long observed in graphite and metal graphite systems (6-8,23-26), stationary tests of metal fiber brushes (1,2), and sliding tests of Cu metal fiber brushes (3,5), although the latter are contradictory.

| | |
|-------------------------|---------------------------------|
| Sliding Vel. (v): | 15 m/s |
| Coef. Frict. (μ): | 0.30 |
| Brush Load (p): | 0.5 N |
| Current (I): | 100 Amps |
| Resist. (R): | 0.4 m Ω |
| Hardness of Cu: | $5.5 \times 10^8 \text{ N/m}^2$ |

Table III. Values used for energy loss and film resistivity calculations.

Friction

Presently the only frictional information on the brushes is a measure of the total power consumed by the rotor drive motor. Unfortunately this has proven to be problematic because of non-brush loads on the drive system which appear to be dependent on ambient temperature and other factors not yet isolated. Also, this measuring method has the shortcoming of only giving data on the combined friction of both brushes, without indication as to the individual contribution of each. Proxy brake calibrations of the brush tester indicated that the average friction is typically in the often observed (15) range of about .20 to .40, but more accurate values and values for each brush are not presently available.

Wear Rates

Because of the long times needed to wear-in and reliably measure low (below $\approx 10^{-10}$) wear rates, a brush pair must perform consistently for an extended test to yield useable data. This situation is complicated by the nature of the fiber brushes with which, because of their comparatively high compliance, increases in the coefficient of friction tend to pull the fiber ends further in the direction of the rotor surface movement. With the geometry of our testing device this appears as brush wear, although it is not related to the removal of material. Similarly, when the friction decreases the fiber ends move in the direction opposite to that of the rotor surface movement, resulting in an apparent "negative" wear. Variations in the friction coefficient during testing, therefore, are the cause of the numerous fluctuations in wear rate.

Wear rate data from the present tests are shown in Fig. 2. Over the course of the test the wear rate of the left brush (squares) was approximately 5.4×10^{-11} and that of the right brush (circles) was about 2.6×10^{-11} . These wear rates are quite respectable, especially for moderately long term tests at the currents carried, as shown in Table IV.

Probably the most dramatic and unexpected result of this test is that the polarity of the brushes has a marked effect on the wear rate. As shown in Figure 2, the wear rate of negative brush/positive rotor couples (solid symbols), which is about 9.7×10^{-12} , is approximately seven times less than that of the positive brush/negative rotor couple (open symbols), at about 5.9×10^{-11} .

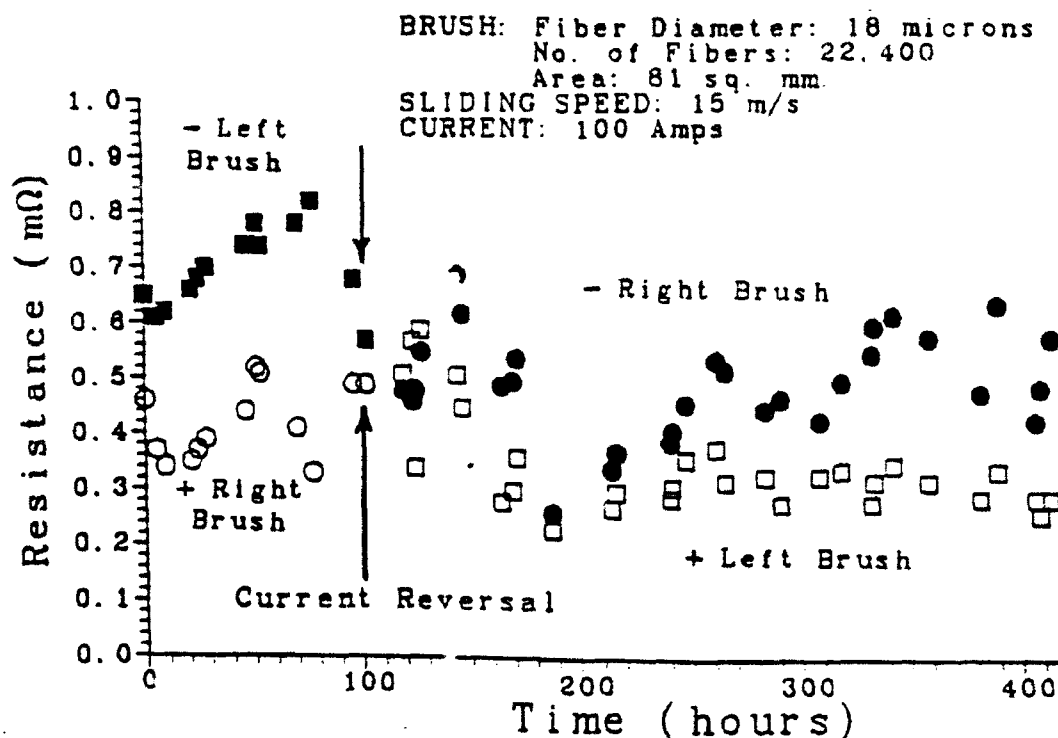


Fig. 1 Electrical resistances for left (squares) and right (circles) brushes during long-term test. Except for a few readings immediately after the current reversal at 100 hours the positive brush (open symbols) had a lower electrical resistance than the negative brush (solid symbols).

| Data Source | Sliding Speed | Applied Current | Wear Rate $\Delta l/L$ |
|---------------|---------------|-----------------|-----------------------------|
| ref.27 | 7-17 m/s | 25 A | $1.8 - 5.4 \times 10^{-10}$ |
| ref.3 | 15.6 m/s | 26.4 A | 4.1×10^{-11} |
| ref.5 | 20-100 m/s | 50 A | $0.9 - 7 \times 10^{-11}$ * |
| Present Study | 15 m/s | 100 A | $0.9 - 5.9 \times 10^{-11}$ |

Table IV. Representative wear data for metal fiber brushes of similar size.

* These contact voltages were about 3 to 20 times higher than for the other brushes in this table.

DISCUSSION

Total Brush Losses

Previous analyses of sliding couples have shown that electrical brush loss is minimized when the electrical and friction losses are approximately equal (22). Using the representative values shown in Table III the friction losses are about 2.25 W and the Joule losses are about 4.0 W for each brush. Although these are not exactly equal they are relatively close, and a total loss of 12.5 W per 100 Amp (.125 W/Amp) per brush pair is comparable to superior results achieved in previous high performance fiber and foil brush tests (1,2,21).

The Role of Water

The present tests have shown that generous amounts of adsorbed water can be used in high-speed, high-current electrical systems for surface protection and for cooling, without degradation of superior brush characteristics. In retrospect this should come as no surprise but the present results are quite gratifying.

The technique employed has been very effective primarily due to the protective properties of the thin, approximately double monomolecular layer of water, which has been found to be quite prevalent under a wide range of sliding conditions with electrical brushes (1,2,7-9,21). This layer, however, can be lost when there is insufficient humidity, when access to the substrate is restricted by high brush populations, or when the substrate becomes too warm due to high heat loads (15). This is where the critical role of water as an evaporative coolant becomes important.

The combined heat capacity and heat of vaporization required to raise room temperature water to 100°C and vaporize it is about 2575 J/ml, and in the case of the present tests (in which the total losses were around 12.5 W) if water were the sole means of heat dissipation only approximately 4.8×10^{-6} l/s of water would be needed for steady state operation. Scaling up this type of cooling for higher power applications poses no problems, and water cooling of this type has recently been shown to be effective even up to extremely high heat dissipation rates (28).

In our atomizer humidified tests, water coverage of the rotor surface is a result of the competition between adsorption, evaporation and mechanical wear. Since the adsorption rate is dependent on the statistical collision of water droplets with the rotor or brush surfaces, better coverage can be achieved by increasing the droplet density. In the present test the heat input rates required a denser "fog" for continuous operation than could

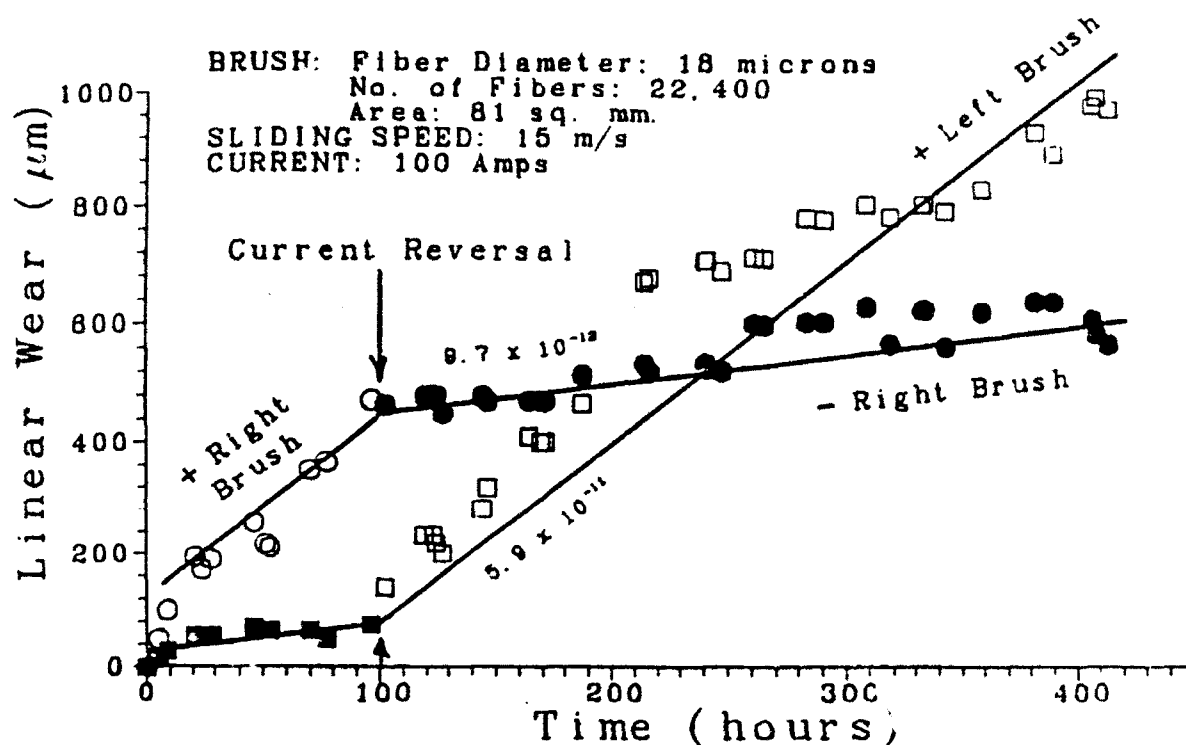


Fig.2 Linear wear of left (squares) and right (circles) brushes during long-term test. The positive brush (open symbols) consistently displayed a higher wear rate of about 5.9×10^{-11} than the negative brush (solid symbols), which was about 9.7×10^{-12} .

be produced using a gas washing bottle, hence the success of our new gas atomizer. Even higher heat input rates and higher brush populations might well demand alternate forms of water application, as are currently being evaluated.

Polarity Effects

The differences in wear rate and contact drop exhibited by the metal-fiber brushes of different polarity raise obvious questions as to the responsible mechanisms. Candidates include electromigration (29-31), electrochemical migration (32,33) and differences in oxidation behavior. Although this may currently represent an achievable lower limit to the brush wear rate at the positive brush/negative substrate interface, proper selection of materials and conditions may mediate or eliminate this effect altogether. At this point, however, the causes of the polarity effects remain undetermined and further studies are being conducted.

CONCLUSIONS

Using atomized water and a CO_2 protective atmosphere Ag-clad Cu metal fiber brushes were run at a current density of 1.25 MA/m^2 with average wear rates in the low to mid 10^{-11} range, minimum wear rates of less than 1×10^{-11} and total (Joule and friction) losses around 0.125 Watt/Amp per brush pair over the course of a 420 hour test.

The substitution of Argon or Nitrogen for CO_2 resulted in increased friction and wear rates, and typically destroyed the brushes within a matter of minutes.

When adequate moisture was provided, in this case from a gas atomizer designed in this laboratory, our metal fiber brushes performed consistently well. Inadequate moisture typically resulted in periods of apparently excellent brush performance followed by high wear rates and often destruction of the brushes.

Brush polarity had a distinct effect on the brush characteristics, with the negative brush-positive rotor couple displaying much lower wear rates (by a factor of about 7) and slightly higher average voltage drops. Additional work is being conducted to determine the mechanisms responsible for these observed polarity effects.

REFERENCES

1. C.M. Adkins III and D. Kuhlmann-Wilsdorf, "Development of High-Performance Metal Fiber Brushes II - Testing and Properties", Electrical Contacts - 1979, III. Inst. Techn., Chicago, IL, 1979, pp.161-174.
2. C.M. Adkins III and D. Kuhlmann-Wilsdorf, "Development of High-Performance Metal Fiber Brushes III - Further Tests and Theoretical Evaluation", Electrical Contacts - 1980, III. Inst. Techn., Chicago, IL, 1980, pp.67-72.
3. P. Reichner, "Metallic Brushes for Extreme High Current Applications", Electrical Contacts - 1979, III. Inst. Techn., Chicago, IL, 1979, pp.191-197.
4. P. Reichner, "High Current Tests of Metal Fiber Brushes", Electrical Contacts - 1980, III. Inst. Techn., Chicago, IL, 1980, pp.73-76.
5. L. Boyer, J.P. Chabreire and J. Saint-Michel, "Low Wear Metallic Fiber Brushes", Wear, Vol. 78, pp.59-68, 1982.
6. D. Kuhlmann-Wilsdorf, D.D. Makel, and N.A. Sondergaard, "Refinement of Flash Temperature Calculations", Engineered Materials for Advanced Friction and Wear Applications (eds. F.P. Schmidt and P.J. Blau), ASM, Metals Park, OH, 1988, pp. 1-32.
7. S. Dillich and D. Kuhlmann-Wilsdorf, "Effects of Surface Films on the Performance of Silver-Graphite (75w% Ag, 25w% C) Electrical Brushes", Electrical Contacts - 1979, III. Inst. Techn., Chicago, IL, 1979, pp.185-190.
8. S. Dillich and D. Kuhlmann-Wilsdorf, "Two Regimes of Current Conduction in Metal-Graphite Electrical Brushes and Resulting Instabilities", Electrical Contacts - 1982, III. Inst. Techn., Chicago, IL, 1982, pp.201-212.
9. S. Dillich and D. Kuhlmann-Wilsdorf, "Extended Performance Limits of Metal-Graphite Brushes at Very High Current Densities", Mater. Sci. Eng., Vol. 57, pp.L13-L16., 1983.
10. D. Kuhlmann-Wilsdorf, D.D. Makel, N.A. Sondergaard and D.W. Maribo, "Interfacial Temperatures and Transition of Surface Films on Monolithic Silver-Graphite Brushes Sliding on Copper", Electrical Contacts, (Proc. 14th Intern. Conf. on Electrical Contacts, Paris, France, SEE) 1988, pp.47-53.
11. J. Schreurs, J.L. Johnson and I.R. McNab, "Characterization of Thick Films Formed on Slip Rings During High Current Density Operation", Electrical Contacts - 1980, III. Inst. Techn., Chicago, IL, 1980, pp.59-65.
12. J.L. Johnson and J. Schreurs, "High Current Brushes VIII: Effect of Electrical Load", Wear, Vol. 78, pp.219-232, 1982.
13. Ragnar Holm, Electric Contacts, 4th. ed., Springer-Verlag, 1967, p.30.
14. D. Kuhlmann-Wilsdorf, "Temperatures at Interfacial Contact Spots: Dependence on Velocity and on Role Reversal of Two Materials in Sliding Contact", Trans. ASME J. of Tribology, 109, pp.321-329, 1987.
15. D. Kuhlmann-Wilsdorf, "Uses of Theory in the Design of Sliding Electrical Contacts", Electrical Contacts - 1991, III. Inst. Techn., Chicago, IL, 1991, pp.1-24.
16. D. Kuhlmann-Wilsdorf, "A Versatile Electric Fiber Brush and Method of Making", U.S. Patent #4,200,000, Nov. 9, 1982.
17. V. Srikrishnan, S. Dillich and D. Kuhlmann-Wilsdorf, "New Apparatus for the Testing of Electrical Brushes in the Laboratory", Electrical Contacts - 1978, III. Inst. Techn., Chicago, IL, 1978, pp.635-640.
18. C.M. Adkins III and D. Kuhlmann-Wilsdorf, "Device for the Control and Measurement of Brush Forces to an Accuracy of a Few Grams-Force While Monitoring Brush Resistance and Brush Wear at Currents Up to 500 Amperes or More", Wear, Vol. 71, pp.119-125, 1981.
19. D.M. Alley, L.J. Hagen, D. Kuhlmann-Wilsdorf, D.D. Makel and C.G. Moore, "Automated Apparatus for Long-Term Testing of Electrical Brushes", ICEC - IEEE Holm 1990, (1990 Holm Conf. on Electrical Contacts, IEEE, Piscataway, NJ), 1990, pp.278-284.
20. I.R. McNab and P. Reichner, "Environment and Brushes for High-Current Rotating Electrical Machinery", U.S. Patent #4,277,708, July 1981.
21. D. Kuhlmann-Wilsdorf, "Gold fibre Brushes: Their Promise for Future High-Technology Applications", Gold Bull., Vol. 16, pp.12-20, 1983.
22. P.B. Haney, D. Kuhlmann-Wilsdorf and H.G.F. Wilsdorf, "Production and Performance of Metal Foil Brushes", Wear, Vol. 73, pp.261-282, 1981.
23. Ragnar Holm, Electric Contacts, 4th. ed., Springer-Verlag, 1967, pp.150-152, 245-248.
24. E. Holm, "Contribution to the Theory of the Brush-Collector Contact", Trans. AIEE, 78, pt.IIIA, pp.431-438, Aug. 1959.
25. E. Holm, "Dependence of the Contact Mechanism on Polarity in Stationary and Sliding Contacts When High-Resistivity Film is Present in the Contact", IEEE Trans., PAS-84, pp.404-411, May 1965.
26. G.D. Joglekar, "Rotating Electrical Contacts and Brush Operation: Part III - Voltage", Electrical Contacts, Vol. 15, no.23, pp.19-20, Dec. 1975.
27. D. Kuhlmann-Wilsdorf and D. Alley, "Oscillation with Metal Fiber Brushes", Electrical Contacts - 1988, III. Inst. Techn., Chicago, IL, 1988, pp.239-246.

28. A. Chalilila, B.K. Ahrens and D.P. Bauer, "Description and Test Results of a Current Collection System for Continuous Duty HPG", Electrical Contacts - 1991, III, Inst. Techn., Chicago, IL, 1991, pp.141-148.
29. H.B. Huntington and A.R. Grone, "Current-Induced Marker Motion in Gold Wires", J. Phys. Chem. Solids, Vol. 20, nos.1/2, pp.75-87, 1961.
30. P.S. Ho and H.B. Huntington, "Electromigration and Void Observation in Silver", J. Phys. Chem. Solids, Vol. 27, pp.1391-1329, 1966.
31. H.R. Patil and H.B. Huntington, "Electromigration and Associated Void Formation in Silver", J. Phys. Chem. Solids, Vol. 31, pp.463-474, 1970.
32. J.J. Steppan, J.A. Roth, L.C. Hall, D.A. Jeanonotte and S.P. Carbone, "A Review of Corrosion Failure Mechanisms during Accelerated Tests", J. Electrochem. Soc., Vol. 134, no.1, pp.175-190, Jan. 1987.
33. S.L. Meiling, M. Samanzadeh, G.W. Warren and P. Wynblatt, "Modeling the Failure of Electronic Devices by Dendrite Growth in Bulk and Thin Layer Electrolytes", Corrosion Sci., Vol. 44, no.9, pp.644-651, 1988.

Moisture Effects Including Stiction Resulting From Adsorbed Water Films

Chao Gao

D. Kuhlmann-Wilsdorf

D. D. Makel

Department of Materials Science,
University of Virginia,
Charlottesville, VA 22901

Stiction resulting from moisture effects at small elastic contact spots has been identified and studied using bundles of fine, gold-plated copper fibers sliding on a gold-plated copper surface. The relevant measurements were made in the hoop apparatus which permits simultaneous monitoring of the momentary coefficient of friction and electrical contact resistance. Previous studies made with the hoop apparatus have shown that under the action of high local pressure, adsorbed moisture is expelled from between the contact spots leaving only one monomolecular layer of adsorbed water on each of the contacting surfaces. Additional details of the observations are varied and permit a refined analysis. Stiction results during periods of very slow motion or rest through local energy reduction at the spots as excess water is slowly drained in the course of molecular ordering of the two adsorbed layers. Complex variations of kinetic friction with humidity and sliding speed are explained through the interplay of excess molecules between the contact spot surfaces, meniscus formation, fluid drag about the spots, and shear thinning in that flow.

Introduction

The tribological and electrical behavior of surface films have recently received a great deal of attention in three areas; 1) the prevention of damage to magnetic head/disk systems caused by stiction (Bhushan and Dugger, 1990; Li et al., 1989; Liu and Mee, 1983), 2) the determination of the effects of surface films on scanning tunneling (STM)/atomic force (AFM) (McClelland and Mate, 1988; Schneir et al., 1988; Mamin et al., 1986) and surface force microscopy (Alsten and Granick, 1988; Homola et al., 1989; Chan and Horn, 1985), and 3) the optimization of sliding conditions for high current density collectors (Johnson, 1986; Adkins and Kuhlmann-Wilsdorf, 1979; 1980).

Both in the laboratory and in daily life, adsorption films on solid surfaces are unavoidable except when the surfaces are carefully cleaned and degassed in ultra high vacuum (Bowden and Throssell, 1951); and on nonreactive surfaces in the normal atmosphere water is the most prevalent adsorbate. For gold-plated surfaces, previous studies (Gao and Kuhlmann-Wilsdorf, 1990a, 1990b, 1991) conducted using the hoop apparatus have revealed that for friction and interfacial electrical resistance the most sensitive experimental variables are humidity and sliding speed, with secondary effects caused by applied load. It was also found that for gold-plated samples and substrates, atmospheres of clean air, argon, nitrogen, carbon dioxide, oxygen and vacuum down to about 0.01 Torr all yield essentially the same results.

The advantage of the present geometry, which employs bundles of gold-plated fibers, is that it renders the constriction resistance negligible due to the large number of the contact

spots (Gao and Kuhlmann-Wilsdorf, 1990a; Holm, 1967). In this condition the contact resistance (R) under normal force P becomes

$$R = \frac{\sigma_F H}{P} \quad (1)$$

with H the impression hardness of the softer side and P/H equal to the area for stationary plastic contact, which is about the same as for the kinetic contact case provided μ is small (say less than 0.5) (McFarlane and Tabor, 1950). Also, the large number of contact spots which results from the use of our metal fiber brushes makes the changes in both number and size of the contact spots statistically insignificant in regard to the interfacial resistance. Furthermore, since the local contact pressures at the constant spots approach or equal the pressure necessary for plastic flow, this results in a somewhat uniform pressure distribution between the contact spots, except in the peripheral regions where the contribution to the contact resistance is *not* dominant.

Throughout these and previous investigations the film resistivity σ_F between contact spots of gold-plated surfaces has been experimentally determined to be near $10^{-12} \Omega \text{m}^2$ within a factor of 2 or so, regardless of the experimental conditions (Adkins and Kuhlmann-Wilsdorf, 1979; 1980; Simmons, 1963). This value of film resistivity is indicative of an electron tunneling film with a thickness of $0.5 \pm 0.1 \text{ nm}$ between the contact spots (Adkins and Kuhlmann-Wilsdorf, 1979; Gao and Kuhlmann-Wilsdorf, 1990a; Holm, 1967), corresponding to a two monomolecular layer thick water film since, in our tests, water is obviously the most prevalent adsorbate on the clean gold surfaces. Because the film resistivity is extremely sensitive to the separation distance, as clearly described in reference [20], the average number of monomolecular layers at the con-

Contributed by the Tribology Division for publication in the JOURNAL OF TRIBOLOGY. Manuscript received by the Tribology Division March 19 1991; revised manuscript received August 1991. Associate Editor: S. Jahanmir.

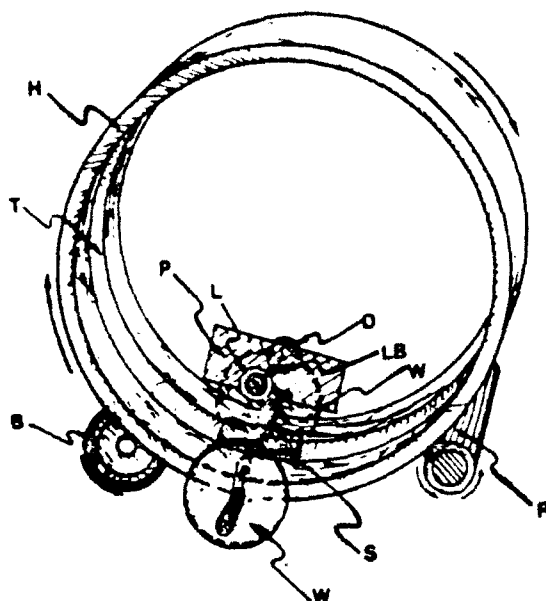


Fig. 1 In the hoop apparatus the sample (S) slides within the metal hoop (H) which is rotated at constant speed via the driving rod (R). The momentary angular position of the slider is monitored by means of a polarized light (LB) from a fixed light source (L) which passes through a polarizer (P) atop the sample and onto a photodiode (d). The four thin wires and contacts which are used to measure the contact resistance (four probe method) are not shown here.

tact spots is limited to a value of 2, plus or minus a small fraction, since in the range of 0.5 nm a 0.1 nm reduction in film thickness causes an order of magnitude decrease in the film resistivity due to the tunneling nature of the contact resistance (Holm, 1967; Simmons, 1963).

The reason for this remarkable persistence of the double monomolecular layer, also found on other metals (Alsten and Granick, 1988; Chan and Horn, 1985), has been recognized to be the high local pressures at the contact spots, namely, as already stated in connection with Eq. (1), comparable to the hardness of the substrate. The reason for such a consistent film thickness has been clarified by recent experiments which have shown that when a liquid interfacial film is very thin (≈ 10 molecular layers) the continuum theory for fluid drainage breaks down and increasing pressure causes the remaining layers to be expelled stepwise, with each ensuing layer taking an increasing amount of pressure (Chan and Horn, 1985). In this regard the result that between the load-bearing areas all but about two monomolecular layers of water are squeezed out due to a contact pressure close to that of plastic flow agrees well with the results by other researchers (Homola et al., 1989; Chan and Horn, 1985).

By contrast, about the periphery of the contact spots the outflow of water expelled from between the contact spots and/or the attraction of water into the re-entrant peripheral gap through surface tension causes the water film to increase towards the periphery and form menisci around the contact spots (Bowden and Throssell, 1951; Christensen, 1985).

The situation of an adsorbed double layer confined between contact spots and a thicker annular layer around the circumference of the spots is believed to be a general phenomenon of adsorption film in tribological situations, not one confined to the case of water and not to specific sliding materials. Several of the processes occurring under such conditions have already been variously considered including the ordering and drainage of the confined adsorbates (Alsten and Granick, 1988; Chan and Horn, 1985) capillary action and the effects of surface tension around contacts (Heyes, 1986; Cross and Picknet, 1963; Gao and Kuhlmann-Wilsdorf, 1990c), and for moving spots, the high strain rate shear thinning of the fluid about the contact

spots (Bair and Winer, 1990; Heyes, 1986), and shear deformation of the meniscus (Israelachvili, 1986; Gao and Kuhlmann-Wilsdorf, 1990d).

Evidence in the present experiments concerns two distinctly different cases depending on ambient humidity; 1) At low humidities meniscus effects are negligible and the friction phenomena are controlled by the specific characteristics of the double monomolecular layer between the contact spots, 2) At high humidities stick-slip occurs accompanied by drainage of extra buried molecules from and subsequent ordering of the remaining molecules between the contact spots, as well as meniscus formation and the attendant negative Laplace force.

At all humidities and sliding speeds viscous drag forces of fluid flowing about the contact spots contribute to the friction. This rises with velocity as well as increasing humidity (on account of increased thickness of the adsorbed moisture film outside of the contact spots) and thereby causes a marked difference between the static and the kinetic cases at high humidities.

While the kinetic friction changes in response to phenomena caused by the movement of the contact spots through the fluid layer, important static friction effects arise while the contact spots are essentially at rest. These lead to "stiction," comprising by definition any phenomenon which causes an increase in the adhesive (normal) or tangential (friction) force as a result of time dependent processes, typically involving a thin liquid layer (Li et al., 1989). In a broader sense, as a matter of physical principle, stiction is a result of the minimization of the local free energy of contact spots at a particular position.

Experimental Procedure

The hoop apparatus, with which the experiments were conducted (Gao and Kuhlmann-Wilsdorf, 1990d), is dynamically similar to the pin on disk device except for different oscillating frequencies and without system damping. A schematic diagram of this device is shown in Fig. 1. It employs a sample sliding in a rotating vertical hoop, in the present case made of gold-plated copper. In effect the hoop provides an infinite inclined plane with a controllable surface speed. The apparatus is housed in a bell jar connected to a vacuum system so that the ambient atmosphere about the contacting surfaces can be carefully controlled. Relative humidity in the bell jar is controlled by bubbling the desired gas, in the present case nitrogen, through temperature controlled distilled water, and the level of relative humidity is measured using a hygrometer.

The momentary position of the sample on the hoop, and therefore the apparent momentary friction coefficient, is monitored by a polarized light beam whose intensity is modulated when it passes through a polarizing sheet mounted on the top of the moving sample holder, which rotates as it moves up and down the inner radius of the hoop. Also fastened to the sample holder are rods for applying different loads. The position of these rods is such as to have the center of gravity of the whole sample as close as possible to the center of the sliding interface in order to minimize off-axis oscillations. To measure the interfacial resistance, a carefully controlled current of 100 mA is maintained across the sample/hoop interface and the voltage between the brushes and the hoop is measured.

In this and some previous studies (Gao and Kuhlmann-Wilsdorf, 1990a, 1990b, 1991) the sample was composed of three rigidly mounted parallel bundles of copper fibers in a triangular arrangement, with a single bundle in the leading position and the other two bundles forming the trailing triangle base. Each of the bundles contained 2700, 50 μ m diameter copper fibers. As already stated, this insures (i) that there are enough contact spots so that deformation of the individual contact spots is essentially elastic and (ii) that the constriction resistance makes only a negligible contribution to the contact resistance as required by Eq. (1). This large number of contact spots also

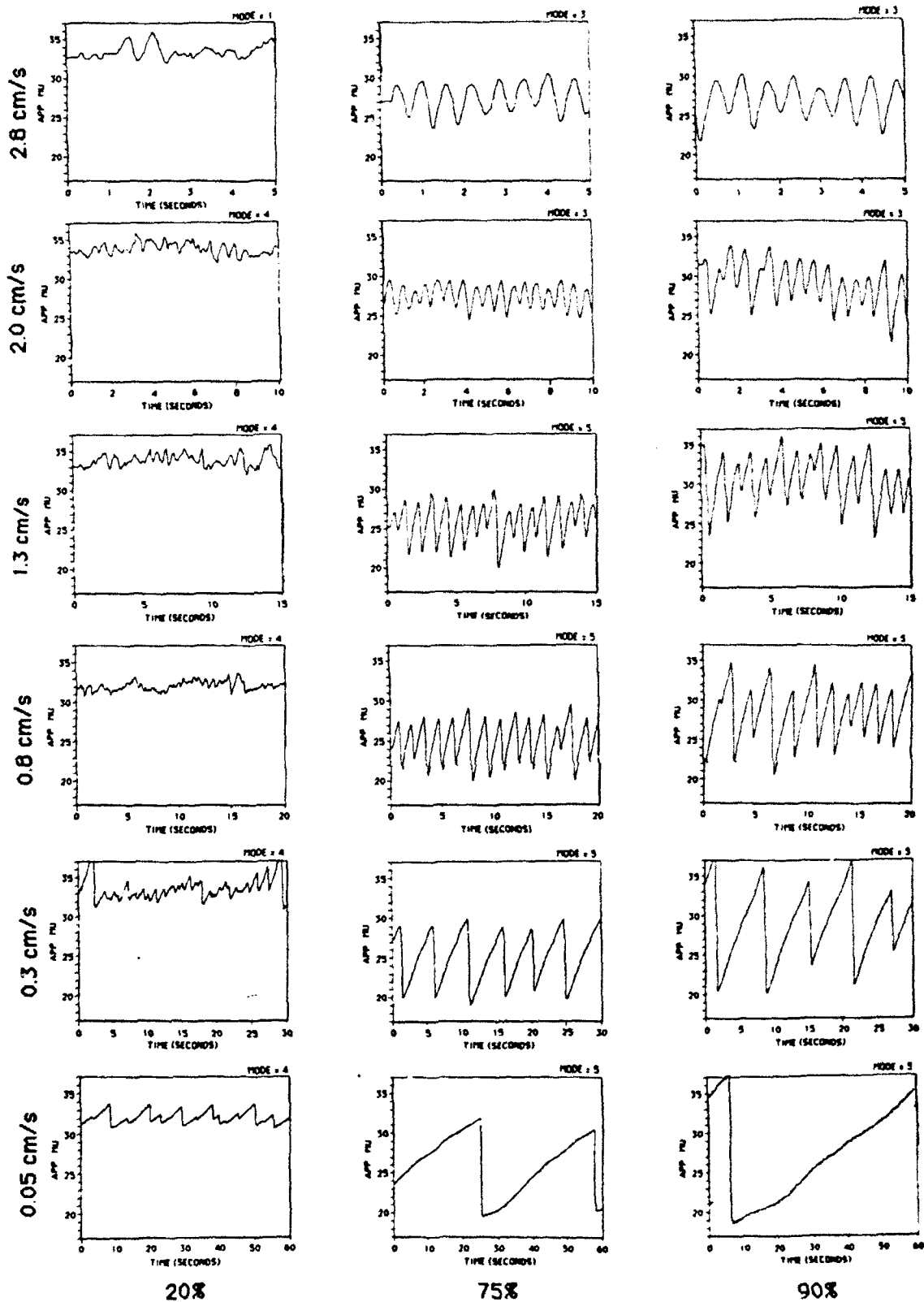


Fig. 2 Representative graphs of the apparent coefficient of friction (momentary slider position) versus time for three different humidities (columns) and five different hoop speeds (rows). The sample used in all tests consists of three bundles of 2700, 50 μ m diameter gold-plated copper fibers, slid in an atmosphere of nitrogen.

minimizes effects which result from statistical fluctuations in the number and size of the contact spots. In the present experiments all of the contacting surfaces were gold-plated in order to avoid complications due to oxidation.

The measurements of friction coefficient and contact resistance have in earlier studies revealed distinct sliding modes and have been shown to contain intriguing information regarding the nature of the speed dependence of friction (Gao and Kuhlmann-Wilsdorf, 1990a; 1990b; 1991). On the most simple level, when the friction coefficient is independent of the sliding velocity, i.e., if $d\mu/dV = 0$, the sample executes a regular pendulum motion with period T_0 about its time averaged equilibrium position, (Gao and Kuhlmann-Wilsdorf, 1990d):

$$\bar{\theta} = \frac{1}{T_0} \int_0^{T_0} \theta(t) dt = \tan^{-1} \mu \quad (2)$$

For significantly large values of μ the oscillating frequency, f_0 , is modified to

$$f_0 = \frac{2\pi}{T_0} = \sqrt{\frac{g}{r} (1 + \mu^2)^{1/2}} = \sqrt{\frac{g}{r} \left(1 + \frac{1}{4} \mu^2\right)} \quad (3)$$

where g and r are the gravitational constant and the radius of the hoop, respectively. In our apparatus, $r = 7.3$ cm and typically $\mu \approx 0.3$, giving $T_0 \approx 0.53$ s.

When μ increases with increasing speed at a sufficiently large rate, the result is smooth sliding, because any momentary increase in the velocity, as when the sample slides downwards, is accompanied by an increase in the friction force tending to move it upwards. In that condition the position of the sample is ideally independent of time and the surface speed is equal to the tangential velocity of the inner radius of the hoop, although in fact surface roughness causes some irregularities.

When μ significantly decreases with increasing speed, $d\mu/dV < 0$, the friction force drops at the initiation of downward motion and the sample initially accelerates. After dynamically overshooting the equilibrium position the sample decelerates and stops and is then carried back up while at relative rest with the inner hoop surface, thereby executing the typical stick-slip motion. Between these cases the slider motion shows a transition stage between of stick-slip and smooth sliding for slightly negative $d\mu/dV$, and between pendulum motion and smooth sliding for slightly positive $d\mu/dV$.

Experimental Results

Data were taken for 30 different conditions which included 6 hoop speeds: 0.05, 0.3, 0.8, 1.3, 2.0, and 2.8 cm/s, and 5 relative humidities: 20, 35, 55, 75, and 90 percent, all with a normal load of 55 grams force (≈ 0.53 N). Figure 2 is a set of representative graphs of time versus the momentary apparent friction coefficient for the whole range of hoop speeds at relative humidities of 20 percent (left column), 75 percent (middle column), and 90 percent (right column). It should be noted that the apparent friction coefficient differs from the true friction coefficient because of inertial effects. In these graphs the coefficient of friction scale is kept constant throughout, while the time scales are increased from top to bottom because of the decreasing hoop speed.

Without detailed consideration four qualitative features are obvious from the graphs in Fig. 2 and numerous similar measurements: (1) the mode of slider motion tends to be smooth, somewhat irregular sliding or oscillating for low humidities and high hoop speeds; (2) the mode of motion tends to be stick-slip for high humidities and low speeds; (3) with increasing speed there is a transition from stick-slip motion to oscillation, and the transition speed increases with increasing humidity; (4) there is an initial decrease in the average friction coefficient with increasing humidity followed by an increase

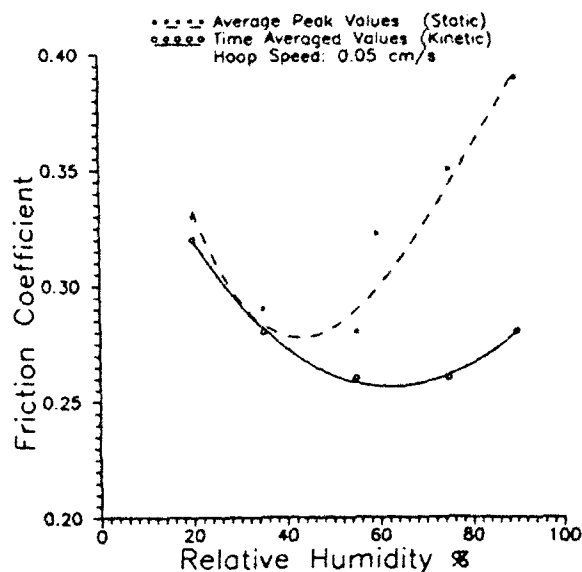


Fig. 3 Graph of the average peak friction coefficients and the time-averaged friction coefficients as a function of relative humidity, at a hoop speed of 0.05 cm/s and the same conditions described in Fig. 2. Because the mode of sliding is stick-slip, the peak values are equal to the static friction and time-averaged values approximately equal the kinetic friction.

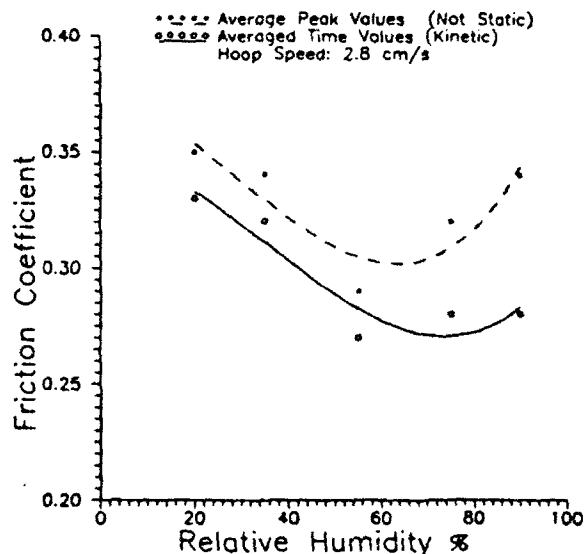


Fig. 4 Graph similar to Fig. 3 except for a hoop speed of 2.8 cm/s. Because there is no stick-slip mode of sliding represented in this graph the peak values are not equal to the static coefficient of friction.

at high relative humidity values, with this increase being less dramatic at the higher hoop speeds.

The last point is documented in Figs. 3 and 4, which are graphs of the average peak (i.e., "static") values and the time-averaged moving (i.e., "kinetic") values of the friction coefficient as a function of relative humidity. Figure 3 pertains to the lowest hoop speed used (0.05 cm/s), and in Fig. 4 to the highest of 2.8 cm/s. For stick-slip motion (as represented in Fig. 3 in accordance with Fig. 2) the peak values are indeed the static friction coefficient, and in both stick-slip and oscillatory motion (as in Fig. 4), neglecting the speed dependence of μ , the time averaged values roughly equal the kinetic friction coefficient. The curves in these figures have been fitted to the data points using a third degree polynomial. Figures 3 and 4 clearly demonstrate the decrease and then increase of the friction coefficient with increasing relative humidity. The peak

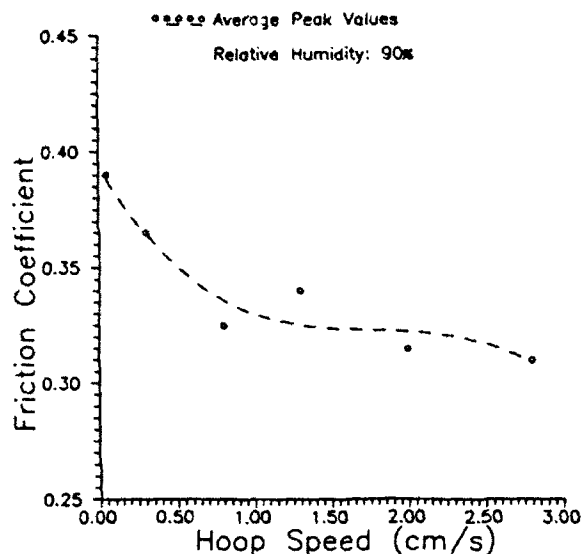


Fig. 5 Graph of the average peak friction values as a function of hoop speed for 90 percent relative humidity. At speeds up to 1.3 cm/s, the sliding mode is stick-slip and the peak values are equal to the static friction values.

friction has a minimum at a relative humidity level around 50 to 65 percent.

Figure 5 shows the average peak friction coefficients versus hoop speed for the highest humidity case (90 percent), again with a best fit curve using a third degree polynomial. This figure shows that the average static friction coefficient (as given by the average peak friction coefficient) decreases with increasing hoop speed up to about 2 cm/s. At higher hoop speeds stick-slip motion ceases. Figure 6 similarly shows the time-averaged (kinetic) friction coefficient values for 20 and 55 percent relative humidity. Average peak values are not shown because these values are close to the time-averaged values for conditions when the surface speed is close to the hoop speed, such as the low-amplitude oscillatory and stick-slip motion which occurs at these lower humidities. As seen in Fig. 6, the friction initially increases with increasing hoop speed and then apparently drops slightly at the highest speeds investigated.

Discussion

A. Free Energy Reduction During Periods of Rest. Previous studies (Gao and Kuhlmann-Wilsdorf, 1990a, 1990b, 1991) on the effects of moisture on friction have resulted in two particularly important experimental observations that are documented also herein: (1) Stick-slip occurs at slow speeds, provided that sufficient moisture is present, and the maximum speed which retains stick-slip motion increases with increasing load. (2) The kinetic friction first increases and then decreases with increasing speed. These results have been explained by a model which includes meniscus effects, a double monomolecular layer between the load bearing areas of contact spots, and the flow of fluid about the moving contact spots (Gao et al., 1991). In this discussion we expand our model to explain the characteristics of the data in greater detail, especially the valley in the friction versus relative humidity data shown in Figs. 3 and 4.

The first experimental result which will be addressed is the tendency of our samples to change from slightly irregular smooth sliding and oscillation to a stick-slip mode with increasing relative humidity and decreasing hoop speed, as evident in Fig. 2. To begin with, stick-slip motion arises when the static coefficient of friction at the onset of a "stick" episode is sufficiently larger than the kinetic coefficient that the initiation of motion results in a net acceleration and a subsequent

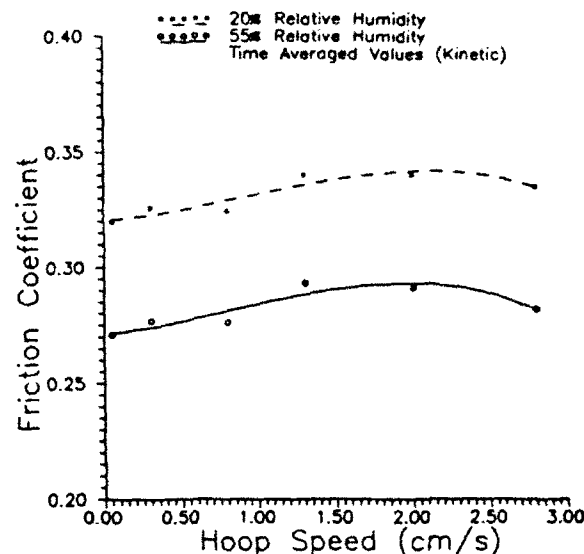


Fig. 6 Graph of time-averaged kinetic friction coefficient values as a function of hoop speed for 20 and 55 percent relative humidities

"slip" episode. This difference between static and kinetic friction arises from the formation of a local energy well while the spots are at rest. The extra force needed to pull the contact spots out of their temporary local energy wells translates into an increase in the friction force during stick episodes, which is followed by a decrease in friction during slip.

As observed, the transition hoop speed between stick-slip and smooth sliding or oscillation increases with increasing relative humidity. This, then, indicates that the relative rate of free energy reduction during stick periods increases with increasing thickness of adsorbed water layers, so that the resting time required to attain the critical energy reduction needed for stick-slip decreases.

B. Effect of Nonequilibrium Excess Water Molecules Between Contact Spot Surfaces. At very low humidities, the adsorption film on the free surfaces is too thin to lead to any, or significant, meniscus formation about the periphery of the contact spots. Regardless of the thickness of the water adsorbed on the free surfaces, however, at the contact spots the local pressure is typically so high that only a double monomolecular layer can exist in equilibrium. Yet, contact spot motion in conjunction with finite drainage speeds prevents ideal equilibration. Instead, moving contact spots form a kind of "bow wave" of displaced water ahead of them, slightly ride up on that bow wave and thereby "bury" a small amount of excess water between the contact spot surfaces. With increasing humidity, movement of the contact spots through correspondingly thicker water layers will cause the number of such "buried" water molecules in excess of the two monomolecular layers to increase. The observed increased lubrication, i.e., decrease of μ_k with increasing humidity at low humidities, is ascribed to that increased density of buried molecules.

This velocity dependent trapping of an excess partial monomolecular layer beyond the two monolayers expected in equilibrium may be considered to be the earliest stage of hydroplaning. Still, the average density of buried molecules must be very limited. We know this because the film resistivity is extremely sensitive to the separation distance at the contact spots, due to the tunnelling nature of the current conduction, and although the film resistivity does increase slightly with increasing speed, the observed small increases indicate the addition of less than one tenth of an extra molecular layer of water.

Drainage of these extra "buried" molecules takes consid-

erably more time than the viscous drainage of thick moisture layers. It is this sluggishness of energy reduction through drainage and ordering which results in the low value of the stick-slip transition velocity at low moisture levels. This also explains why stick-slip motion does not occur at higher speeds.

C. Interplay of Excess Molecules, Meniscus Effects and Viscous Drag. At high relative humidity levels both peak and time-averaged friction values increase with increasing humidity, as shown in Figs. 3 and 4. The most dramatic increase in friction with increasing humidity is seen in μ_{static} at a hoop speed of 0.05 cm/s, as shown in Fig. 3. In our current experiments this represents the situation in which the contact spots have the greatest time at rest during the "stick" events.

With thicker adsorbed moisture layers energy reduction during rest periods arises from: (i) the drainage of water molecules from between the contact spots and the concurrent ordering of the remaining molecules in the two monolayers, and (ii) molecular flow driven by surface tension resulting in meniscus formation. Meniscus effects, which tend to increase the static coefficient of friction, include the negative Laplace force exerted by the menisci around the contact spots through capillary action which adds to the applied normal force, and the fact that the initiation of motion requires extra force to plow through the liquid "hump" presented by the meniscus.

Figure 5 shows that at high relative humidity (here 90 percent), the *peak* friction, which in this case is the static friction up to about 2.0 cm/s, initially decreases rapidly with increasing hoop speed. This is a clear demonstration of the time required for local energy reduction at the contact spots which is responsible for the increased static friction. The aforementioned time dependent mechanisms which reduce the local free energy on a microscopic scale at higher humidities are the sources of the observed stiction.

Variations of the time-averaged (kinetic) friction values with humidity shown in Figs. 3 and 4 have slightly different characteristics. As already indicated, the initial decrease of friction with humidity can be ascribed to lubrication through the "burying" of excess molecules beyond the two monolayers in equilibrium between the contact spots. They tend to reduce μ_k and their density increases with rising humidity as the contact spots move through thicker adsorbed water layers, thereby causing the initial drop of μ_k with humidity. The subsequent increase of kinetic friction with increasing relative humidity is explained by fluid viscosity: As the contact spots must plow through increasingly thick layers of water the viscous drag forces equal and then surpass the decrease of friction resulting from the buried molecules. The observed minimum and then increase in kinetic friction as a function of humidity results from this interplay.

D. Shear Thinning About the Contact Spots. The variation of time-averaged (kinetic) friction with hoop speed, as shown in Fig. 6, is distinctly different from the static case. As a function of increasing hoop speed, kinetic friction (μ_k), at 20, 50 percent and in fact all humidities first increases, peaks, and then apparently decreases slightly. Although the initial increase can be explained by the discussed viscous drag effect, an additional mechanism must be invoked to explain the decrease of μ_k at the highest hoop speed. Additional information regarding this effect is obtained from the electrical resistance values. These increase only slightly with speed, in agreement with the slowly increasing density of buried molecules, but not enough to suggest any dramatic increase at the highest rates, as would be needed to explain the discussed drop of friction at the highest speeds. It is, therefore, proposed to be "shear thinning" in the fluid flowing *about* the contact spots which is responsible for that effect. Shear thinning i.e., the reduction of fluid viscosity at high velocities has been documented for a wide range of liquids (Bair and Winer, 1990; Heyes, 1986)

and there is reasonable expectation that is also occurs in the adsorbed water films. Indeed, it may be related to the pencil glide dislocation model of liquids (Kotze and Kuhlmann-Wilsdorf, 1971) via the Barker "tunnel model" (Barker, 1960, 1961, 1962a, 1962b, 1963).

Conclusions

1 In equilibrium, the interfacial film between contact spots in the system investigated consists of two monolayers of adsorbed water.

2 A minor excess of "buried" molecules arises through contact spot motion. Their density increases with sliding speed and humidity, i.e., the thickness of the adsorbed water films on the free surfaces.

3 That excess has a lubricating effect which correspondingly increases with increasing humidity.

4 During periods of relative rest (i.e., stick episodes in stick-slip), various processes occur at the contact spots which reduce the local free energy and result in stiction. These include formation of menisci around the contact spots if there is sufficient moisture, drainage of the excess water molecules and the attendant ordering of the molecules which remain in the equilibrium double monomolecular layer.

5 Kinetic friction somewhat increases and then apparently slightly decreases with increasing sliding speed. The initial increase can be explained by an increase in the viscous drag of the fluid layers about the contact spots, while the decrease at higher rates can be explained by "shear thinning" of the liquid flow around the spots.

6 An observed friction minimum at about 50 percent humidity is explained by a competition with increasing film thickness between increased lubrication due to the excess "buried" molecules and an increased viscous drag of the fluid flow around the contact spots.

7 It is expected that the model proposed herein is widely applicable and may be employed to optimize sliding conditions in many systems which are deliberately or incidentally lubricated by thin fluid films.

Acknowledgment

The financial support of this research through the Materials Division (P. P. Schmidt and M. E. Peterson, Tribology) of the Office of Naval Research, Arlington, VA, as well as through the Defense Advanced Research Projects Agency (P. Kemmeyer, TTO, Arlington, VA, monitored by T. Gora, Piccatinny Arsenal) is gratefully acknowledged.

References

- Adkins, C. M., and Kuhlmann-Wilsdorf, D., 1979, "Development of High Performance Metal Fiber Brushes II—Testing and Properties," *Electrical Contacts—1979, Proc. Twenty-Fifth Holm Conference on Electrical Contacts*, III, Inst. Techn., Chicago, IL, Sept. 10-12, pp. 171-184.
- Adkins, C. M., and Kuhlmann-Wilsdorf, D., 1980, "Development of High Performance Metal Fiber Brushes III—Further Tests and Theoretical Evaluation," *Electrical Contacts—1980, Proc. Twenty-Sixth Holm Conference on Electrical Contacts*, III, Inst. Techn., Chicago, IL, Sept. 29-Oct. 1, pp. 67-72.
- Alsten, J. V., and Granick, S., 1988, "Molecular Tribometry of Ultrathin Liquid Films," *Phys. Rev. Lett.*, Vol. 61, pp. 2570-2573.
- Bair, S., and Winer, W. O., 1990, "The High Shear Stress Rheology of Liquid Lubricants at Pressure of 2 to 200 MPa," *ASME JOURNAL OF TRIBOLOGY*, Vol. 112, pp. 246-253.
- Barker, J. A., 1960, "A New Theory of Fluids—The Tunnel Model," *Aust. J. Chem.*, Vol. 13, pp. 187-193.
- Barker, J. A., 1961, "Tunnel Theory of Fluids—12-6 Fluids," *Proc. R. Soc. A*, Vol. 259, pp. 442-457.
- Barker, J. A., 1962a, "Statistical Mechanics of Almost 1-Dimensional Systems," *Aust. J. Phys.*, Vol. 15, p. 127.
- Barker, J. A., 1962b, "Structure of Simple Fluids—Tunnel Model," *J. Chem.*, Vol. 37, pp. 1061-1066.

- Barker, J. A., 1963, *Lattice Theories of the Liquid State*, Pergamon Press, Oxford, pp. 42-104.
- Bhushan, B., and Dugger, M. T., 1990, "Liquid-Mediated Adhesion at the Thin-Film Magnetic Disk/Slider Interface," *ASME JOURNAL OF TRIBOLOGY*, Vol. 112, pp. 217-223.
- Bowden, F. P., and Throssell, W. R., 1951, "Adsorption of Water Vapour On Solids Surfaces," *Proc. Roy. Soc. of London, Series A209*, pp. 297-308.
- Chan, D. Y., and Horn, R. G. J., 1985, "The Drainage of Thin Liquid Films between Solid Surfaces," *Chem. Phys.*, Vol. 83, pp. 5311-5324.
- Christensen, H. K., 1985, "Capillary Condensation in Systems of Immiscible Liquids," *J. Colloid Interface Sci.*, Vol. 104, pp. 170-178.
- Cross, N. L., and Picknett, R. G., 1963, "The Liquid Layer between a Sphere and a Plane Surface," *Trans. Faraday Soc.*, Vol. 59, pp. 846-855.
- Fisher, L. R., and Israelachvili, 1981, "Experimental Studies on the Applicability of the Kelvin Equation to Highly Curved Concave Menisci," *J. of Colloid and Interface Science*, Vol. 80, pp. 528-535.
- Gao, C., and Kuhlmann-Wilsdorf, D., 1990a, "Adsorption Films, Humidity, Stick-Slip and Resistance of Sliding Contacts," *ICEC-IEEE, 1990 Holm Conf. on Electrical Contacts*, IEEE, Montreal, Aug. 20-24, IEEE, Piscataway, NJ 08855-1331, pp. 292-300. Also in *IEEE Trans. Components Hybrids and Manufacturing Technology*, Vol. 14, 1991, pp. 37-44.
- Gao, C., and Kuhlmann-Wilsdorf, D., 1990b, "Observations on the Effect of Surface Morphology on Friction and Sliding Modes," *Tribology of Composite Materials*, P. J. Blau and P. Rohatgi, Eds., ASM Int., Metals Park, OH, pp. 195-201.
- Gao, C., and Kuhlmann-Wilsdorf, D., 1990c, "Experiments on, and a Two-Component Model for, the Behavior of Water Nano-Films on Metals," *MRS Symposium Proc.*, Vol. 188, M. F. Doerner, W. C. Oliver, G. M. Pharr and F. R. Brotzen, Eds., Mater. Res. Soc., Pittsburgh, PA, pp. 237-242.
- Gao, C., and Kuhlmann-Wilsdorf, D., 1990d, "On Stick-Slip and the Velocity Dependence of Friction at Low Speeds," *ASME JOURNAL OF TRIBOLOGY*, Vol. 112, pp. 354-360.
- Gao, C., Wilsdorf, D. K., and Bednar, M. S., 1991, "On the Tribological Behavior of Adsorbed Layers, Especially Moisture," *Proceedings of 8th International Conference on Wear of Materials*, pp. 433-441.
- Haney, P. B., Kuhlmann-Wilsdorf, D., and H. G. F. Wilsdorf, 1981, *Wear*, Vol. 73, p. 261.
- Heyes, D. M., 1986, "Some Physical Consequences of Large Shear Rates on Simple Liquids," *J. Chem. Phys.*, Vol. 85, pp. 997-1008.
- Holm, R., 1967, *Electric Contacts*, 4th Ed., Springer-Verlag.
- Homola, A. M., Israelachvili, J. N., Gee, M. L., and McGuiggon, P. M., 1989, "Measurements of and Relation Between the Adhesion and Friction of Two Surfaces Separated by Molecularly Thin Liquid Films," *ASME JOURNAL OF TRIBOLOGY*, Vol. 111, pp. 675-682.
- Israelachvili, J. N., 1986, "Measurement of the Viscosity of Liquids in Very Thin Films," *Journal of Colloid and Interface*, Vol. 110, pp. 263-270.
- Johnson, J. L., 1986, "Sliding Monolithic Brush Systems for Large Currents," *Electrical Contacts—1986*, Ill. Inst. Techn., Chicago, IL, pp. 3-17.
- Kotze, I. A., and Kuhlmann-Wilsdorf, D., 1971, "Radial Correlation-Function of Melts Calculated from Structural Models of Liquid State," *Phil. Mag.*, Vol. 23(185), pp. 1133-1153.
- Li, Z., Rabinowicz, E., and Saka, N., 1989, "The Stiction Between Magnetic Recording Heads and Thin Film Disks," *Tribology and Mechanics of Magnetic Storage Systems*, STLE SP-26, pp. 64-70.
- Liu, C. C., and Mee, P. B., 1983, "Stiction at the Winchester Head-Disk Interface," *IEEE Transactions on Magnetics*, Mag-19, pp. 1659-1661.
- Mamin, J. H., Ganz, E., Abraham, D. W., Thomson, R. E., and Clarke, J., 1986, "Contamination-mediated Deformation of Graphite by the Scanning Tunneling Microscope," *Phys. Rev.*, Vol. B34, pp. 9015-9018.
- McClelland, G. M., and Mate, C., 1988, "Atomic Scale Friction Measured with an Atomic Force Microscope," *Engineered Materials for Advanced Friction and Wear Applications*, P. J. Blau and F. Smidt, eds., ASM Intl., Metals Park, OH, pp. 13-22.
- McFarlane, J. S., and Tabor, D., 1950, "Relation between Friction and Adhesion," *Proc. Roy. Soc., Series A* 202, pp. 244-253.
- Rabinowicz, E., 1965, *Friction and Wear of Materials*, Wiley Pub., 1965, p. 95.
- Schneir, J., Marti, O., Remmers, D., Glaser, D., Ronnenfeld, R., Drake, B., and Hansma, P. K., 1988, "Scanning Tunneling Microscopy and Atomic Force Microscopy of the Liquid-Solid Interface," *J. Vac. Sci. Technol.*, Vol. A 6(2), Mar./Apr., pp. 283-286.
- Simmons, J. G., 1963, "Generalized Formula for the Electric Effect between Similar Electrodes Separated by a Thin Insulating Film," *Journal of Applied Physics*, Vol. 34, pp. 1793-1803.

Fundamentals of stick-slip

Chao Gao, Doris Kuhlmann-Wilsdorf and David D. Makel

Department of Materials Science and Engineering, University of Virginia, Charlottesville, VA 22901 (USA)

Abstract

Simultaneous measurements of momentary friction and electrical resistance using the hoop apparatus have resulted in new insights into the behavior of the ubiquitous thin interfacial films at contact spots. The experimental focus of the present paper is the amplitude of the stick-slip motion of a multifiber slider as a function of the humidity, speed and applied load. The stick-slip amplitude is found to increase with increasing relative humidity and contact spot size, respectively, and to decrease with increasing substrate speed. Furthermore, the interfacial electrical resistance spikes at the beginnings of slip episodes and shows an unexpected hysteresis during stick-slip cycling. The data suggest a two-component model, including (i) an approximate double molecular layer of adsorbed water between the contact spots and (ii) menisci at the periphery of the contact spots at high humidities. Together with the general analysis presented in appendix A, this model presents a framework for the understanding and control of stick-slip in sliding systems.

1. Introduction

Stick-slip, in which two sliding surfaces cycle between relative rest and motion, is a widely observed phenomenon, ranging from the atomic to macroscopic scale, and from delicate instrumentation to daily life [1-4]. Such intermittent motion has a number of very important consequences, *i.e.* stick or slip boundary conditions in fluid dynamics, acoustic effects in stringed musical instruments, static friction (stiction) in magnetic information storage systems, severe wear or 'seizing' of different materials of electric contacts, and jerking of brakes [4-8]. Phenomenologically, the most widely accepted cause for stick-slip is that static friction exceeds kinetic friction or, more rigorously, that the friction coefficient drops rapidly at small speeds [9].

To explain why the static friction coefficient μ_s is higher than the kinetic coefficient μ_k , a number of proposed mechanisms and experimental results have been adduced over the past decades. Bowden and Tabor [7] suggested that μ_s is larger than μ_k owing to molecular bonding 'adhesion' between the surfaces. Based on gradually increasing interactions between opposing asperities, Derjagin *et al.* [10] derived a dependence of μ_s on the stick time t_s in the form of $t_s/(t_0 + t_s)$, where t_0 is a constant. Using viscoelastic and plastic deformation theory, Kosterin and Kraghelsky [11] derived the same dependence on the stick time as that of Derjagin *et al.*, while Howe *et al.* [12] derived an exponential dependence of μ_s on time t_s , using the Van

der Waal's electrostatic interaction resulting from electric dipole fluctuations between the contact surfaces. Kato *et al.* [13] proposed an empirical formula similar to that of Howe *et al.*, except that t_s is replaced with t_s^n , where n is less than unity. A more frequently used relationship for the time dependence of the static friction coefficient, which may be derived from a process similar to viscous creep, is that the difference between the static and the kinetic friction coefficients increases with the stick time as $t_s^{n'}$, where n' is also less than unity [14, 15]. Since this relationship indicates an infinite growth rate of the static friction at the beginning of stick episodes, it is physically unreasonable for very short times (see Appendix A).

2. Various physical processes affecting static friction

It has long been recognized that interfacial films, whether intentional or unintentional, play a critical role in tribological systems, and their effects on adhesion, *i.e.* the attractive forces between two surfaces in close proximity, have been extensively studied [2, 15-23].

In their classic work, Bowden and Tabor [2] describe two mechanisms by which adhesion is enhanced by thin liquid films. Firstly, menisci form around contact spots and pull the two sides together through capillary action and the negative Laplace pressure (for wetting angles less than 90°). The second mechanism - 'viscous impulse' - arises when two surfaces are pulled apart

locally, forcing liquid to flow into the space between them. If the viscosity of the liquid is appreciable, the force required to separate the surfaces briefly can be quite large.

Recently, knowledge regarding liquid surface films has greatly expanded thanks to new techniques, including the use of surface force apparatus (SFA), molecular tribometry and atomic force microscopy [17, 19, 24–32]. Specifically, the contributions of ordering and drainage of interfacial fluid molecules to static friction have been explored and, in this regard, adsorbed water has been found to have an especially strong effect on increasing the friction force [6, 17, 22, 23, 30].

Molecular ordering occurs when liquid molecules confined between two surfaces, spaced several nanometers to fractions of nanometers apart, order into a solid-like phase of an integer number of discrete layers, approximately parallel to the surfaces [27–29]. Upon shearing, such layered interfacial films undergo a phase transition from solid-like to liquid-like states.

Molecular drainage [24, 30] refers to the squeezing-out under pressure of interfacial liquid films confined between surfaces. Films which are more than about 10 molecular layers thick roughly obey Reynolds' continuum theory, but for thinner films the discussed layer ordering and strong surface interactions take place and the continuum theory breaks down. With increasing pressure, such films are squeezed out stepwise by single layers until only two or three layers remain [24, 27, 29]. Both of these processes lower the free energy of the system, thereby contributing to the static friction.

This paper describes an indirect study of meniscus formation, molecular ordering and fluid drainage for the case of adsorbed water films. Simultaneous measurements of the electric contact resistance and the shear force required to initiate and sustain motion were made experimentally. These were then compared with the predictions of a mathematical theory of stick-slip which is described briefly in Appendix A.

3. Double molecular water layer at contact spots

In the present study, the coefficient of friction and the electrical resistance were measured simultaneously in the hoop apparatus [20, 21, 30, 33–35], using gold-plated copper solid and fiber sliders on a gold-plated copper substrate. The sliding surfaces were gold plated to minimize complications from oxidization, and a metal fiber slider was used to reduce to negligible the effect of electric constriction resistance as well as fluctuations in the number and size of the contact spots [33, 36]. In this case, the measured contact resistance is proportional to the resistance of the adsorbed film at the contact spots.

As in previous studies [21, 30, 33], the fiber slider consisted of three bundles of fibers 3 mm in diameter (each consisting of 2700 copper wires gold plated to 50 μm) mounted in a holder so as to run end-on on the inner hoop surface. The bundles were arranged in a triangle, such that a single bundle was in the leading position and the other two were side by side in the trailing position. For loading, weights were hung on shafts connected to the sliding sample. In order to minimize oscillations, the center of gravity of the sample assembly was made to be as close as possible to the center of the sample-hoop interface. The electrical resistance was monitored continuously, using a four-probe circuit, and the resistance and friction data were displayed real-time on a computer screen and simultaneously stored to magnetic disk.

It has been found that, for clean gold-plated surfaces, both the friction coefficient and the interfacial electrical resistance are dependent on the humidity but are essentially independent of environmental gases (O_2 , CO_2 , N_2 and Ar) as well as of ambient pressure down to 0.01 Torr. Most importantly, the measured interfacial film resistivity indicates that the interfacial water film has an average thickness of about 0.5 nm between the contact spots, i.e. a double molecular layer, regardless of a wide range of the experimental variables [33, 36]. With such an ultrathin film, the current is transmitted by tunneling and a 0.1 nm increase in the film thickness would increase the film resistance by an order of magnitude. Thus, only the load-bearing area between the contact spots, plus a narrow annular region about each, contribute significantly to the electric conduction across the interface. In addition, the chemical nature of the insulating interfacial films has no effect. Also, the roughness of the surface has little effect on the average film thickness, since at the typical plastically deformed contact spot there exists a more or less uniform pressure (that of the Meyer hardness of the softer of the contacting material). This is the case except for the peripheral region where the gap width increases, though this does not contribute significantly to the current conduction.

Water is the most prevalent adsorbate on clean gold surfaces [37] and the conclusion mentioned already, that the film at the contact spots is (nearly) a double molecular film of water, was established in a number of previous investigations [30, 33, 36]. However, depending on the humidity, the film thickness outside of the load-bearing areas of the contact spots can be much larger, as shown schematically in Fig. 1, which illustrates a moving contact spot in plan and cross-sectional views [33]. Recently, the double interfacial layer of thin films under high local pressure also has been confirmed by other researchers [24–27].

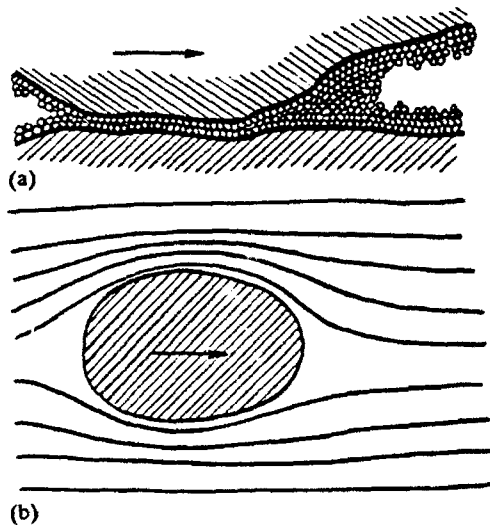


Fig. 1. Schematic diagram of the proposed two-component model: (a) each side of a contact spot carries an approximate monomolecular layer at the load-bearing area with a thicker adsorption film outside of it; (b) flow of adsorbed molecules about the contact spot.

4. Evidence for meniscus formation about contact spots

Figures 2(a)–2(c) show examples of correlated measurements of the interfacial resistance (upper part of the graphs) and the apparent coefficient of friction, *i.e.* the tangent of the instantaneous inclination angle of the hoop at the sample position to the horizon (lower part of the graphs). The static friction coefficient μ_s was identified as the apparent friction coefficient value at which the sample starts to slip, while the kinetic friction coefficient μ_k is calculated as the time-average of the apparent friction coefficient in the slip phase.

Figure 2(a) is for a fiber sample at moderately high humidity ($H=60\%$) and shows typical stick-slip motion with a regular cycling period. Figure 2(b) results from the same experimental conditions as for Fig. 2(a), except for a much lower humidity ($H=25\%$), resulting in smooth sliding. This implies that at low humidity the kinetic friction coefficient increases with speed and approaches static friction at small speed. Figure 2(c) is for much the same experimental conditions as Fig. 2(a) but using a solid slider, and this displays irregular stick-slip. The irregularities in Fig. 2(c) probably are due to statistical fluctuations in the low number of contact spots for the solid sample and/or the local variations of the friction coefficient, as discussed by Rabinowicz [15].

A striking result shown in Figs. 2(a) and 2(c) is that the film resistance spikes whenever the stick phase breaks to a slip episode. Plotting the resistance and the sliding speed on the same graph, as shown in Fig. 3(a), reveals that the resistance peaks at the beginning

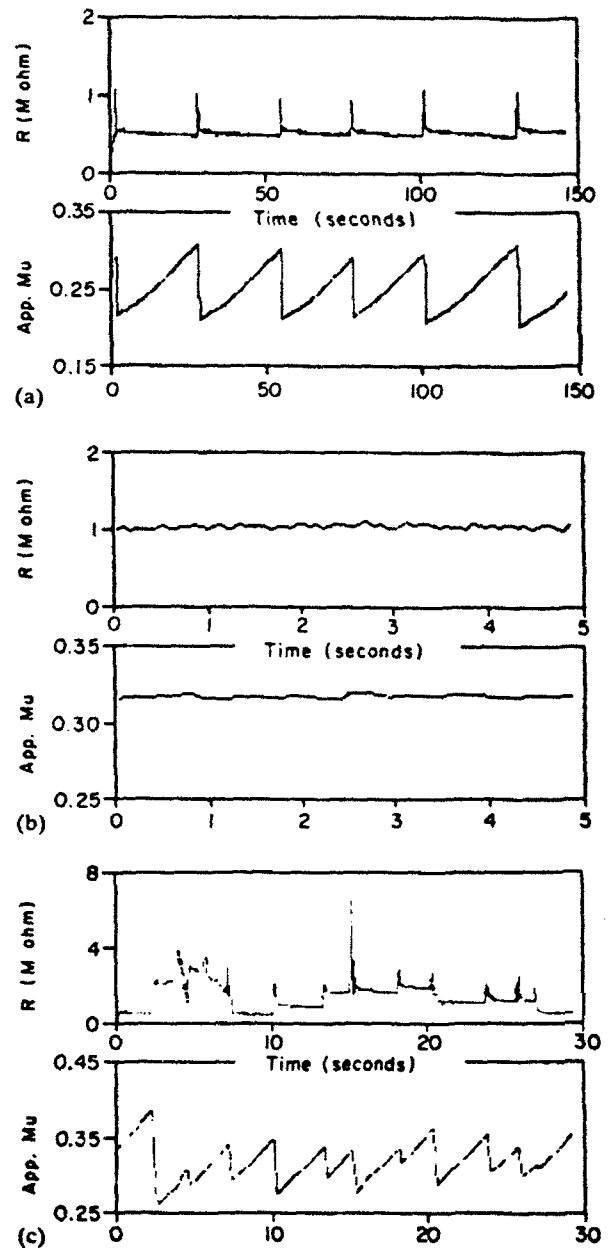


Fig. 2. Effect of humidity on sliding modes for gold-plated surfaces at $P=0.5$ N, showing correlated traces of electric contact resistance (top) and momentary position, *i.e.* apparent friction coefficient (bottom): (a) stick-slip motion of fiber slider at medium high humidity (62%); (b) smooth sliding of fiber slider at low humidity (25%); (c) irregular stick-slip of solid slider at medium high humidity (68%).

of the slip episode, not at the maximum slip speed as one might think, and that the higher resistance persists as long as the sample slides. The symmetric shape of the speed peak demonstrates that the slider motion in the slip episode is nearly that of a harmonic oscillator, indicating that the speed dependence of kinetic friction is very weak (see Appendix A).

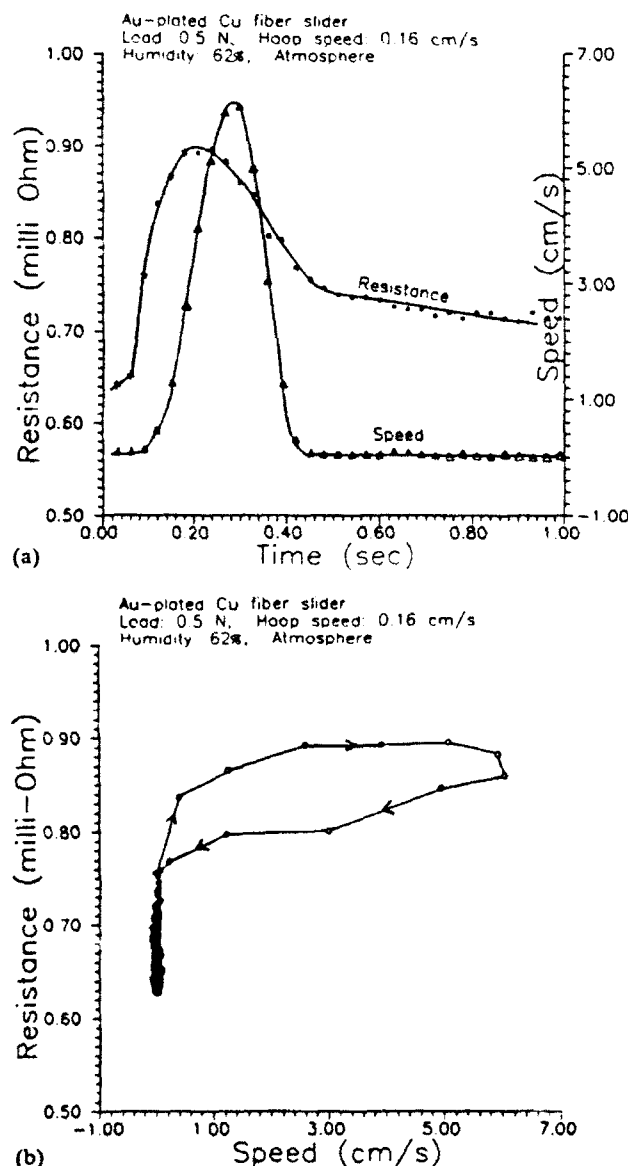


Fig. 3. (a) Interfacial electrical resistance and surface speed of a fiber slider as a function of time. The load, hoop speed and relative humidity were 0.5 N, 0.16 cm s⁻¹ and 62% respectively. Note that the speed curve has a symmetrical shape about the peak, indicating a weak speed dependence of μ_k (see Appendix A). (b) The same interfacial resistance as in (a) but as a function of surface speed. The arrows show the time progression and the dark root is due to the resistance reduction in the stick phase.

Furthermore, a plot of the film resistance as a function of the surface speed (Fig. 3(b)) shows that the resistance has a hysteresis effect. The arrows in the figure indicate the time progression and the dark vertical root at zero speed is due to the resistance decreasing with stick time. This is interpreted as evidence that menisci form around the contact spots during stick episodes, thereby increasing the local pressure through surface tension and Laplace pressure. This in turn causes (i) the drainage of molecules in excess of the two monolayers trapped

during the previous slip episodes and (ii) increased ordering of the two layers. At the breaking point, the sample slips 'over' the meniscus and thus temporarily more molecules than amount to the double layer film are 'buried' under the contact spots. This results in the resistance spikes and the symmetry of the meniscus breaks down, as shown in Fig. 1(a).

The hysteresis of Fig. 3 and the shape of the resistance curve during the slip phase indicate that shortly after sliding begins the conditions responsible for the initial transient voltage spike are modified by equilibration to the particular sliding speed, possibly involving the meniscus shape and drainage of some excess molecules. The time-dependent establishment of the equilibrium layer thickness and flow pattern about the spots (Fig. 1(a)) is responsible for the hysteresis shown in Fig. 3(b).

A simple calculation based on the Wentzel-Kramers-Brillouin semiclassical approximation of quantum mechanics [38], or simply a comparison with Fig. 26.11 of Holm's book [39], shows that the resistance spike at its maximum corresponds to about a 10% increase in the film thickness. This will be partly due to disordering of the double layer by dislocation-like defects and partly through excess buried molecules. However, at low humidity levels, menisci cannot form owing to an insufficient adsorption film thickness, resulting in smooth sliding, as shown in Fig. 2(b). In fact, according to the dynamic analysis (see Appendix A), smooth sliding as shown in Fig. 2(b) indicates that the static friction is essentially the same as the kinetic friction at low sliding speeds.

The two-component model for a moving contact spot shown in Fig. 1, namely a double-layer film between the contact spot and a liquid hump in front of it, is thus consistent with the experimental results presented so far. This model will be further tested as we proceed.

5. Static friction and film resistance as a function of stick time and humidity

In the following analysis, only fiber samples are considered, since for solid samples the film resistance is complicated by the constriction resistance and irregularities already pointed out in connection with Fig. 2(c).

Measurements were made of the dependence of μ_s on the 'stick time', *i.e.* the time at rest, by measuring the critical inclination angle at which the sample starts to slide after different periods of rest. As it turns out, μ_s is mildly time dependent in a modest vacuum or in any of the inert atmospheres tested, if the relative humidity is below about 50%. This agrees with the previous deduction that changes in μ_s with time are

due to adsorbed moisture, and this idea is further supported in Figs. 4(a)–4(c).

Figure 4(a) shows the increase in static over kinetic friction ($\mu_s - \mu_k$), averaged over more than 10 cycles of stick-slip, as a function of the stick time at relative humidities of 75% and 90%. It should be noted that, with a continuously rotating hoop, the stick time equals the stick-slip amplitude divided by the hoop speed. The overall trend of the curves shown in Fig. 4(a) agrees with those found by other researchers using different experimental conditions [13, 14, 20, 40], i.e. ($\mu_s - \mu_k$) grows very quickly with time at short stick times and then the increase more or less levels off.

Figure 4(b) shows the same data as Fig. 4(a) but using a logarithmic time scale; and Fig. 4(c) shows the film resistance as a function of stick time with the insert, also using a logarithmic scale. As may be seen in Figs. 4(b) and 4(c), ($\mu_s - \mu_k$) as well as the film resistance vary roughly exponentially with time. It should be noted that (1) the difference between static and kinetic friction increases faster at the higher humidity levels and (2) for short stick times (less than about 2 s), it also increases faster at the heaviest load (8 N) than at lighter loads. This can be explained qualitatively in terms of our model: for short stick times, the formation of the menisci around the contact spots and the drainage of excess molecules make comparable contributions to μ_s . For longer times, the meniscus about the average spot is completed but the drainage continues, leading to ordering within the double layer. These effects dominate the long-time drop of the tunnelling resistance.

This conclusion also is in line with the experiments on those processes as investigated using atomically smooth mica surfaces in surface force apparatus and molecular tribometry [24–29]. It is further strongly supported by additional observations as follows.

Although μ_s is apparently independent of the stick time at humidities below about 50% as well as in a moderate vacuum (down to 0.01 Torr) [33, 34], the film resistance always decreases with contact time. However, the film resistance data indicate no more than a 10% variation of the film thickness between the contact spots throughout the humidity range. This shows (i) that a meniscus is formed only at humidities above about 50%, and (ii) that a meniscus contributes to both the friction and the resistance through negative Laplace pressure, which has the same effect as adding an external load to the slider. At low humidities or *in vacuo*, no menisci form and only the discussed drainage of excess molecules and ordering in the double layer are responsible for the changes in friction and film resistance.

If the moisture films were not swept aside by moving contact spots, as indicated in Fig. 1, and squeezed out under the high local pressures between the contact spots except for the double layer, the film resistance

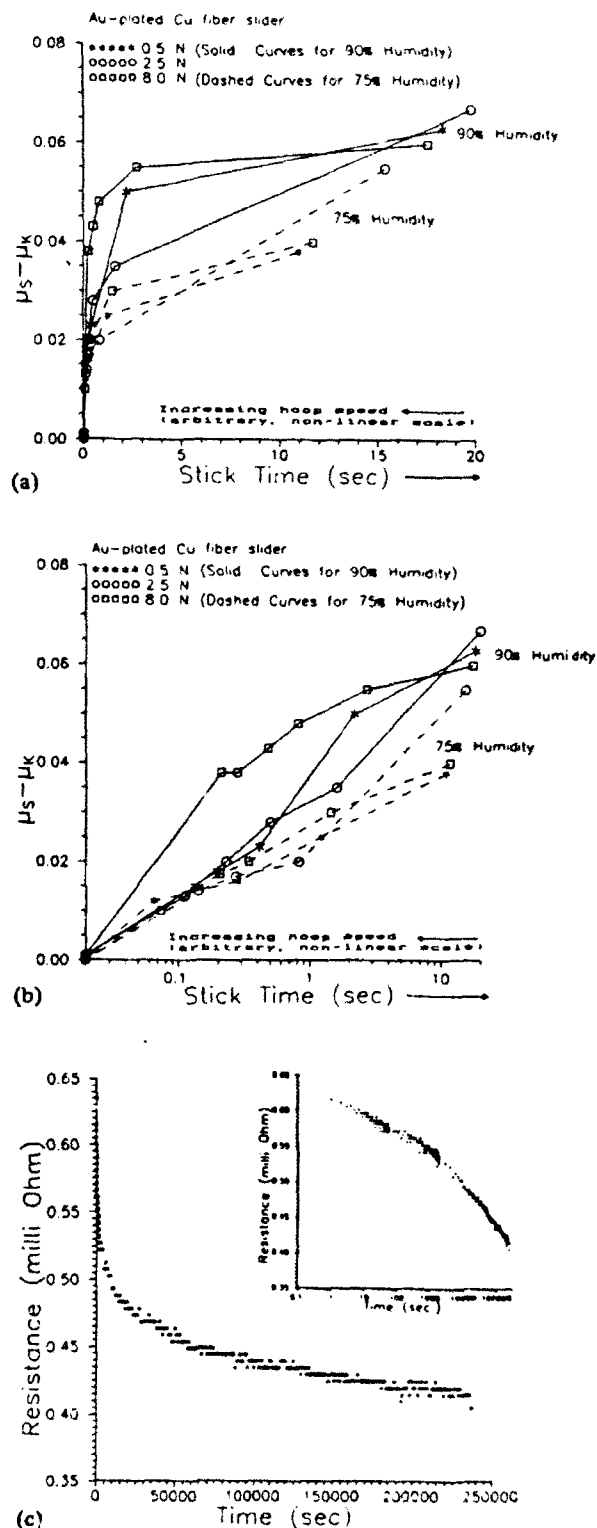


Fig. 4. (a) Difference between static and kinetic friction coefficient ($\mu_s - \mu_k$) for a gold-plated copper fiber slider as a function of stick time. (b) The same data as in (a) but with a logarithmic time scale. (c) Interfacial electrical resistance of the fiber slider as a function of time at rest for a load of 1 N at 75% humidity. The insert shows the same data but with a logarithmic time scale.

would rise drastically with humidity owing to the thicker adsorption films. In fact, the resistance decreases with increasing humidity in spite of an expected larger fraction of buried molecules, which is in line with a dominant meniscus effect which increases with humidity (up to the point of flooding [6]). The double layer, however, is of vital importance, because if it were to be removed, say, by degassing in ultrahigh vacuum, cold welding would occur and hence seizing with $\mu_s > 1$ [7].

6. Stick-slip amplitude as a function of substrate speed and humidity

6.1. The evidence

It is well known that not only the static friction but also the kinetic friction depend on experimental conditions [20, 21, 30, 33, 40, 41]. Specifically, μ_k decreases with increasing humidity up to about 50%, which can be attributed to the lubricating effect of an increasing excess of 'buried' water molecules above the double layer between the contact spots with thicker adsorbed films. In contrast, at relative humidity levels above about 50%, μ_k increases with increasing humidity, as the contact spots must plow through the thicker adsorbed films, in addition to the effect from the menisci which form only at high humidities [21, 30].

Figures 5(a)–5(c) show the stick-slip amplitude of a fiber slider at five humidity levels and six hoop speeds, at loads of 0.5 N (Fig. 5(a)), 2.5 N (Fig. 5(b)), and 8 N (Fig. 5(c)). A zero stick-slip amplitude simply means that no stick-slip occurred and the motion was either smooth sliding with essentially zero amplitude or an oscillating (not necessarily harmonic) motion. Similar plots for the solid sample are not shown here on account of data scatter, as demonstrated in Fig. 2(c).

In Fig. 5, the following three features are clearly seen.

(1) The stick-slip amplitude in radians, being closely equal to $2(\mu_s - \mu_k)$, decreases with increasing substrate speed and, depending on the humidity, stick-slip ceases above some critical substrate speed. This behavior is explained fully by the dynamic analysis described in Appendix A. Physically, the reason is that, with increasing substrate speed, the sample experiences shorter stick times. As a result, at the end of stick, μ_s falls increasingly short of its saturation level, which results in the observed decrease in the stick-slip amplitude with speed.

(2) For all loads, the stick-slip amplitude increases with increasing humidity. According to our two-component model, the effect of the menisci, and drainage and ordering processes, is to raise μ_s with increasing humidity (i.e. thicker adsorbed moisture films), since these effects progress faster for thicker films. Hence, according to the dynamic analysis in Appendix A, faster increases of μ_s at the beginning of stick episodes cause larger stick-slip amplitudes.

(3) Stick-slip is more persistent for heavier loads than for lighter loads. This is explained by the increasing size of the contact spots with rising load, somewhat depending on whether they are elastic or plastic. A subsidiary contributing effect is the corresponding rise in local contact spot pressure, which increases the rate with which excess moisture drains out.

As an illustration the calculated average contact spot radius for hertzian contact (ball-on-plane geometry) is shown in Fig. 6 as a function of the number of the contact spots and the applied load [42], assuming no functional coupling of the two variables. Here, the heavy horizontal line indicates the transition between elastic and plastic contact spots, i.e. the condition for which

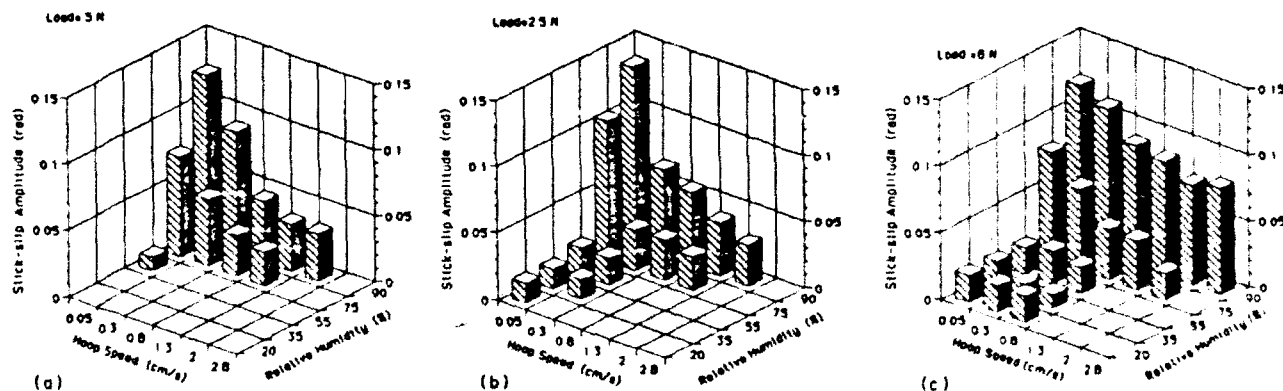


Fig. 5. (a) Stick-slip amplitude as a function of substrate speed and relative humidity for the fiber slider at a load of 0.5 N, and thus with elastic contact spots. (b) The same as (a) but for a load of 2.5 N. (c) The same as (a) but for a load of 8 N, and thus plastic deformation at contact spots, as shown in Fig. 6.

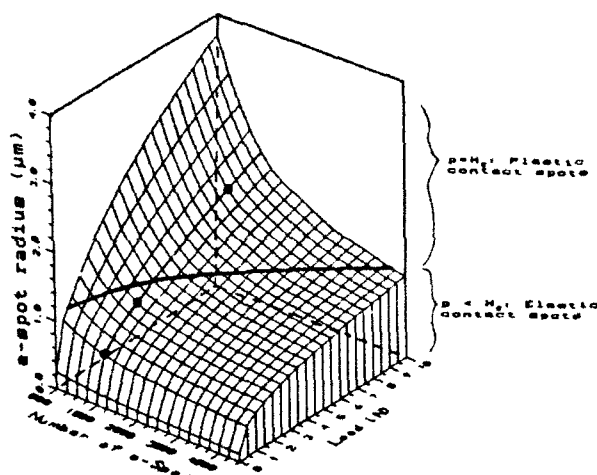


Fig. 6. Calculated average contact spot radius [42] as a function of load and number of contact spots respectively. The three heavy dark points are for the experimental loads of 0.5, 2.5 and 8 N. The heavy line divides the figure into regions of elastically deformed contact spots (lower) and plastically deformed contact spots (upper).

the average elastic hertzian pressure equals the Meyer impression hardness (H_s) of the softer of the two materials, which in this case is gold plate with $H_s = 4.5 \times 10^8 \text{ N m}^{-2}$. Above the line, the local pressure (p) is essentially constant at H_s but below this p decreases with decreasing applied load (P).

The number of contact spots for the fiber sample used is estimated at only about 1500, based on the fact that after testing only about 20% of the fibers appear to be polished when examined in a scanning electron microscope. Using this number the effects of the contact spot size, pressure and the type of deformation can be compared with the experimental results. Specifically, in Fig. 5 it is seen that stick-slip extends to lower humidities at higher loads. According to Fig. 6, for 1500 contact spots, the two lower loads (0.5 and 2.5 N) are in the elastic deformation region and the highest load (8.0 N) lies in the plastic region. Also, the average contact spot radius increases with increasing load, as indicated by the heavy solid line through the dots marking the three loads used. Contact spot area vs. load calculations also show that the local pressure increases with increasing load. This rules out any possible effects of the deformation type, since for the two lighter loads the deformation is elastic.

We are left with the question of whether the increasing persistence of stick-slip with increasing load is due to an increase in the contact spot size or pressure. In this connection, it is highly relevant that stick-slip is much more persistent at low humidities and high substrate speeds for a solid sample at 0.5 N [33, 35] than for the fiber sample at 8 N. Although the load for the solid sample is smaller than that for the fiber sample,

the average contact spot radius for the solid sample is much larger, because of the much smaller number of contact spots (of the order of 10) [33, 35]. Since in both cases the contact spots are plastic, the contact pressures are essentially the same, i.e. near H_s , but there is a large difference in the contact spot radii. Therefore, we may conclude that the size of the contact spots at least contributes to and may well be dominant for the persistence of the stick-slip motion at lower humidities, regardless of the deformation nature.

6.2. The model

The data in Figs. 4 and 5 are accounted for by the following model: in agreement with Fig. 1, the amount of moisture required to form a meniscus is proportional to

$$L = 2\pi a$$

where L is the circumference of a contact spot and the rate of meniscus formation rises with the amount of available excess molecules around the contact spot. In the case of an initial static contact, that amount is nearly equal to the liquid volume of the free surface film displaced by the contact spot. In the case of moving contact spots, the sweeping effect of surface film material, as indicated in Fig. 1, extends to some distance ahead of the spot and builds up to some thickness, with dimensions approximately proportional to the spot diameter. Therefore, the growth rate of μ_s owing to meniscus formation will be roughly proportional to the swept up volume (V) divided by the meniscus circumference, i.e.

$$V/L \approx (dA)/L = 0.5ad$$

where $A = \pi a^2$ is the contact area and d the thickness on the free surface film. Accordingly, μ_s increases with stick time faster for higher loads (larger a) and for higher humidities (larger d), as demonstrated by Figs. 4(a) and 4(b). From the dynamical analysis outlined in Appendix A, it then follows that the stick-slip motion should be more persistent at higher loads. Indeed, this result is in accordance with Fig. 5, because a faster increasing μ_s at small stick times leads to a higher critical speed up to which stick-slip motion persists.

7. Conclusions

The dynamic analysis, as outlined in Appendix A, demonstrates that $\mu_s > \mu_k$ is a necessary condition for stick-slip and that $(d\mu_s/dt)_{t=0}$, i.e. the rate with which μ_s increases at very small stick times, is a critical parameter. Based on the proposed two-component model, together with the dynamic analysis, the experimental results on stick-slip motion and interfacial

resistance are explained semi-quantitatively through the interplay of meniscus formation, moisture drainage and ordering processes at contact spots. Specifically, the experimental results are as follows.

(1) The static friction increases and the electric contact resistance decreases with increasing time at rest.

(2) The electric contact resistance spikes at the onset of slip after a stick episode and shows hysteresis during the slip.

(3) The stick-slip amplitude decreases with increasing substrate speed and there exists a critical speed beyond which no stick-slip motion occurs.

(4) This critical speed increases with increasing humidity and with increasing load, leading to increasing prevalence of stick-slip motion at higher loads and at higher humidities.

(5) Stick-slip motion is more persistent at higher loads and larger contact spot sizes, regardless of whether contact spots are elastic or plastic.

Acknowledgment

The financial support of this research through Materials Division (P. Schmidt and M. B. Peterson, Tribology) of the Office of Naval Research, Arlington, VA is gratefully acknowledged.

References

- 1 G. M. McClelland and C. Mate, Atomic scale friction measured with an atomic force microscope in P. J. Blau and F. Smid (eds.), *Engineered Materials for Advanced Friction and Wear Applications*, ASM International, Metals Park, OH, 1988, pp. 13-22.
- 2 F. P. Bowden and D. T. Tabor, *The Friction and Lubrication of Solids*, Clarendon, Oxford, 1986.
- 3 C. Gao and D. Kuhlmann-Wilsdorf, On stick-slip and the velocity dependence of friction at low speeds, *Trans. ASME, J. Tribol.*, **112** (1990) 354-360.
- 4 K. Khurana, *Phys. Today*, **41**(5) (1988) 17.
- 5 B. Skalmierski, The construction of old Italian violins: tentative explanation, *Bull. Acad. Polon. Sci. (Techniq.)*, **29** (1981) 175-181.
- 6 Z. Li, E. Rabinowicz and N. Saka, The Stiction Between Magnetic Recording Heads and Thin Film Disks, *Tribol. Mech. Magn. Stor. Syst., STLE, SP-26* (1989) 64-70.
- 7 F. P. Bowden and D. Tabor, *Friction - An Introduction to Tribology*, Anchor Press/Doubleday, New York, 1973.
- 8 G. Galton, The action of brakes. On the effect of brakes upon railway trains, *Engineering*, **25** (1878) 469-472.
- 9 A. A. Andronow and C. E. Chaikin, *Theory of Oscillations*, Princeton University Press, Princeton, NJ, 1949, p. 161.
- 10 B. V. Derjagin, V. E. Push and D. M. Tolstoi, A theory of stick-slip sliding of solids, *Proc. Conf. on Lubrication and Wear, London, October 1957*, p. 265.
- 11 J. I. Kosterin and I. V. Kraghelsky, Relaxation oscillation in elastic friction system, *Frict. Wear Mach.*, **12** (1958) 111.
- 12 P. H. Howe, D. P. Benton and I. E. Puddington, London-Van der Waals attractive forces between glass surfaces, *Can. J. Chem.*, **6** (1955) 1375.
- 13 S. Kato, N. Sato and T. Matsubayashi, Some considerations on characteristics of static friction of machine tool: dewey, *Trans. ASME J. Lubric. Technol.*, **94** (July 1972) 237-247.
- 14 C. A. Brockley and H. R. Davis, The time-dependence of static friction, *Trans. ASME J. Lubric. Technol.*, **90** (January 1968) 35-41.
- 15 E. Rabinowicz, *Friction and Wear of Materials*, Wiley, New York, 1965.
- 16 J. L. Streater, B. Bhushan and D. B. Bogy, Lubricant performance in magnetic thin film disks with carbon overcoat - Part I: dynamic and static friction, *Trans. ASME J. Tribol.*, **113** (1991) 22-31.
- 17 A. M. Homola, J. N. Israelachvili and P. M. McGuiggon, Measurements of a relation between the adhesion and friction of two surfaces separated by molecularly thin liquid films, *Trans. ASME J. Tribol.*, **111** (1989) 675-682.
- 18 N. L. Cross and R. G. Picknett, The liquid layer between a sphere and a plane surface, *Trans. Faraday Soc.*, **59** (1963) 846-855.
- 19 J. N. Israelachvili, Measurement of the viscosity of liquids in very thin films, *J. Coll. Inter. Sci.*, **110** (1986) 263-270.
- 20 C. Gao and D. Kuhlmann-Wilsdorf, Experiments on, and a two-component model for, the behavior of water nano-films on metals, *Mater. Res. Soc. Symp. Proc.*, **188** (1990) 234-242.
- 21 C. Gao, D. Kuhlmann-Wilsdorf and M. S. Bednar, On the tribological behavior of adsorbed layers, especially moisture, *Proc. 8th Int. Conf. on Wear of Materials*, 1991, pp. 433-441.
- 22 C. C. Liu and P. B. Mee, Stiction at the Winchester head-disk interface, *IEEE Trans. on Magn., Mag-19* (1983) 1659-1661.
- 23 B. Bhushan and M. T. Dugger, Liquid-mediated adhesion at the thin-film magnetic disk/slider interface, *Trans. ASME J. Tribol.*, **112** (1990) 217-223.
- 24 D. Y. Chan and R. G. J. Horn, The drainage of thin liquid films between solid surfaces, *Chem. Phys.*, **83** (1985) 5311-5324.
- 25 J. Van Alsten and S. Granick, Molecular tribometry of ultrathin liquid films, *Phys. Rev. Lett.*, **61** (1988) 2570-2573.
- 26 J. Van Alsten and S. Granick, Tribology studied using atomically smooth surfaces, *Tribol. Trans.*, **33** (1990) 436-445.
- 27 J. Van Alsten and S. Granick, Origin of static friction in ultrathin liquid films, *Langmuir*, **6** (1990) 876-880.
- 28 R. M. Pashley and J. N. Israelachvili, Molecular layering of water in thin films between mica surfaces and its relation to hydration forces, *J. Coll. Inter. Sci.*, **101** (1984) 511-523.
- 29 M. L. Gee, P. M. McGuiggon and J. N. Israelachvili, Liquid to solidlike transitions of molecularly thin films under shear, *J. Chem. Phys.*, **93**(3) (1990) 1895-1906.
- 30 C. Gao, D. Kuhlmann-Wilsdorf and D. D. Makel, Moisture effects including stiction resulting from adsorbed water films, *Trans. ASME J. Tribol.*, **114** (1992) 174-180.
- 31 C. M. Mate and V. J. Novotny, Molecular conformation and disjoining of polymeric liquid films, *J. Chem. Phys.*, **94** (1991) 8420-8427.
- 32 C. M. Mate, M. R. Lorenz and V. J. Novotny, Atomic force microscopy of polymeric liquid films, *J. Chem. Phys.*, **90** (1989) 8420-8427.
- 33 C. Gao and D. Kuhlmann-Wilsdorf, Adsorption films, humidity, stick-slip and resistance of sliding contacts, *IEEC-IEEE, 1990 Holm Conf. on Electrical Contacts, IEEE, Montreal, August 20-24, IEEE, Piscataway, NJ, 1990*, pp. 292-300. Also in *IEEE Trans. Compon. Hybr. Manufact. Technol.*, **14** (1991) 37-44.

- 34 C. Gao, D. Kuhlmann-Wilsdorf and D. D. Makel, Stick-slip/smooth slip as a function of ambient gases and pressures, disproving previous models of adhesive wear, in L. E. Pope, L. Fehrenbacher and W. O. Winer (eds.), *New Materials Approaches to Tribology*, Materials Research Society, Pittsburgh, PA, 1989, pp. 397-404.
- 35 C. Gao and D. Kuhlmann-Wilsdorf, Observations on the effect of surface morphology on friction and sliding modes, in P. J. Blau and P. Rohatgi (eds.), *Tribology of Composite Materials*, ASM International, Materials Park, OH, 1990, pp. 195-201.
- 36 C. M. Adkins, III and D. Kuhlmann-Wilsdorf, Development of high-performance metal fiber brushes. II - testing and properties, *Electrical Contact-1979, Proc. 25th Holm Conf. on Electrical Contacts, Chicago, IL, 1979*, pp. 171-184.
- 37 F. P. Bowden and W. R. Throssell, Adsorption of water vapour on solid surfaces, *Proc. R. Soc. London, Ser. A*, 209 (1951) 297-308.
- 38 J. G. Simmons, Generalized formula for the electric effect between similar electrodes separated by a thin insulating film, *J. Appl. Phys.*, 34 (1963) 1793-1803.
- 39 R. Holm, *Electric Contacts*, Springer, Berlin, 1967, 4th edn.
- 40 E. Rabinowicz, The nature of static and kinetic coefficient of friction, *J. Appl. Phys.*, 222 (1951) 1373-1379.
- 41 I. L. Maksimov, Thermal instability of sliding and oscillations due to frictional heating effects, *Trans. ASME J. Tribol.*, 110 (1988) 69-72.
- 42 D. Kuhlmann-Wilsdorf, D. D. Makel and N. A. Sondergaard, Refinement of flash temperature calculations, in F. A. Smidt and P. J. Blau (eds.), *Engineered Materials for Advanced Friction and Wear Applications*, ASM International, Metals Park, OH, 1988, pp. 23-32.

Appendix A

Nomenclature

| | |
|------------|---|
| g | earth's gravitational constant |
| K | spring constant of measuring systems |
| m | sample mass |
| P | normal force between sample and substrate |
| r | hoop radius |
| t | time |
| t' | time in a slip episode |
| t_s | time in a stick episode |
| V | absolute sample velocity |
| V_0 | substrate velocity |
| V_c | critical substrate speed above which stick-slip motion ceases |
| V_h | hoop velocity (equals V_0) |
| V_m | maximum speed in a slip episode |
| V_r | relative velocity (velocity between sample and substrate) |
| α | coefficient for the linear term of μ - V curve |
| β | effective damping coefficient of measuring systems |
| θ | momentary angular position of sample on hoop |
| θ_0 | time-average angular position on the hoop |

| | |
|-----------------|--|
| θ_r | difference between momentary and time-average angular position ($\theta - \theta_0$) |
| ω | oscillation frequency in harmonic motion |
| Ω | oscillation frequency in damped or pumped harmonic motion |
| λ_{\pm} | two roots for second order auxiliary equation |
| μ_k | kinetic friction coefficient |
| μ_s | static friction coefficient |

Dynamics of stick-slip for the hoop apparatus

A detailed account of the present dynamic analysis of stick-slip motion for general systems is to be published in the near future [A1]. In summary, for the particular case of the hoop apparatus, the equation of motion is

$$r \frac{d^2\theta}{dt^2} = -g \sin \theta + g \cos \theta \mu_k(V_r) \quad (A1)$$

where r is the hoop radius, V_0 the hoop (substrate) velocity, $V_r = V_0 - r d\theta/dt$ the sliding surface speed and $g = 980 \text{ cm s}^{-2}$, i.e. the earth's gravitational constant.

In general, $\mu_k(V_r)$ can be a complicated function of the surface speed, and an analytic solution of eqn. (A1) is impossible to achieve. To solve eqn. (A1) analytically, we assume μ_k to be a linear function of the surface speed, i.e.

$$\mu_k = \mu_0 + \alpha V_r = \mu_0 + \alpha \left(V_0 - r \frac{d\theta_r}{dt} \right) \quad (A2)$$

with μ_0 and α arbitrary constants. Then, denoting $\theta_r = \theta - \theta_0$, with θ_0 the time-average position of the slider, and neglecting higher orders of θ_r which are quite small, eqn. (A1) can be rewritten as

$$\frac{d^2\theta_r}{dt^2} + \frac{\alpha g}{(1 + \tan^2 \theta_0)^{1/2}} \frac{d\theta_r}{dt} + \omega^2 \theta_r + \cos \theta_0 [\tan \theta_0 - (\mu_0 + \alpha V_0)] = 0 \quad (A3)$$

Here, $\theta_0 = \tan^{-1}(\mu_0 + \alpha V_0)$ is, by definition, the time-average position. The oscillation frequency is

$$\omega = \left(\frac{g}{r} \cos \theta_0 \{1 + (\mu_0 + \alpha V_0) \tan \theta_0\} \right)^{1/2} = \left(\frac{g}{r} \right)^{1/2} \{1 + (\mu_0 + \alpha V_0)^2\}^{1/4} \quad (A4)$$

where we have made use of the facts that $d\theta/dt = d\theta_r/dt$ and that $gr \gg V_0^2$, since $V_0 < 5 \text{ cm s}^{-1}$ and $r = 7.3 \text{ cm}$ in this case. For a typical value of $\mu_k = 0.3$, one obtains $\omega \approx 11.85 \text{ Hz}$. As can be seen from eqn. (A3), the hoop apparatus is dynamically similar to, say, a pin-on-disk device with an effective spring constant of $K = m\omega$.

Denoting $\beta = \alpha g / 2 \{1 + (\mu_0 + \alpha V_0)^2\}^{1/2}$, the general solution of eqn. (A3) is

$$\begin{aligned}\theta_r &\equiv \theta - \theta_0 = A \exp(\lambda_+ t) + B \exp(\lambda_- t) & \text{if } |\beta| \neq \omega \\ \theta_r &\equiv \theta - \theta_0 = A \exp(\beta t) + B t \exp(\beta t) & \text{if } |\beta| = \omega\end{aligned}\quad (\text{A5})$$

with A and B to be determined from the initial conditions, while $\lambda_{\pm} = -\beta \pm i(\omega^2 - \beta^2)^{1/2}$.

The above equations can only be applied to the slip phase of stick-slip motion. Stick-slip motion as a whole, however, can be considered as follows: during a stick episode, the slider velocity equals that of the substrate. When relative motion begins (at the beginning of a slip episode), we define $t=0$ and the displacement is $\theta_{+s} > \theta_0$ (the time-averaged position). After the slider reaches its lowest point θ_{-s} (if no backward sliding, there will be no further stick), the direction of its velocity changes to the direction of the substrate's, and the slider start to accelerate. If the slider velocity reaches the substrate velocity, V_r vanishes and the sample sticks to the substrate once again, at $t=t'$ and with a displacement of $\theta_{-s} < \theta_0$. Therefore, the observed stick-slip amplitude is $x_s = r(\theta_{+s} - \theta_{-s})$. The boundary conditions at the separation point ($t=0$) for the displacement and the velocity are

$$\theta(A, B, t=0) = \theta_{+s}$$

$$r \left. \frac{d\theta}{dt} \right|_{t=0} = V_0 \quad (\text{A6a})$$

Similarly, the boundary conditions at the stick point ($t=t'$) are

$$\theta(A, B, t=t') = \theta_{-s}$$

$$r \left. \frac{d\theta}{dt} \right|_{t=t'} = V_0 \quad (\text{A6b})$$

From eqn. (A6), it can be seen that the total stick time is $t_s = r(\theta_{+s} - \theta_{-s})/V_0$.

Evidently the four equations in eqn. (A6) are insufficient to determine the stick-slip amplitude, since there are five unknown constants, namely A , B , θ_{+s} , θ_{-s} , and t' . The requisite fifth equation is that θ_{+s} also has to satisfy the force-balance equation at the separation point, i.e.

$$\tan \theta_{+s} = \mu_s(t_s) \text{ or } \theta_{+s} - \theta_0 \approx \mu_s(t_s) - \mu_k(V_0) \quad (\text{A7})$$

Thus, the stick-slip amplitude $x_s = r(\theta_{+s} - \theta_{-s}) = V_0 t_s$ can be determined from eqns. (A6) and (A7), and no stick-slip will occur if the solution gives unrealistic relation: $(\theta_{+s} - \theta_{-s}) \leq 0$.

To illustrate how to derive the stick-slip amplitude for a general form of $\mu_s(t)$, assume that $|\alpha| < 2\omega/g$ in eqn. (A2), i.e. the kinetic friction is a linear slowly varying function of sliding speed, so that $|\beta| < \omega$. According to eqn. (A5), the motion in this case is either a damped harmonic oscillation (if $0 < \beta < \omega$) or a driven

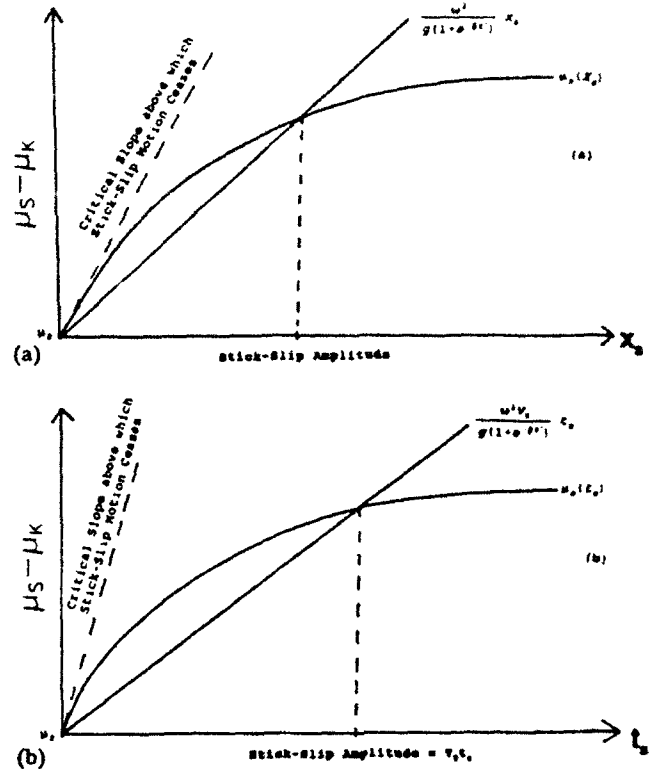


Fig. A1. Graphical method for finding the stick-slip amplitude X_s if the time dependence of static friction is known and is of the type in Fig. 4, according to eqn. (A11) of Appendix A. (a) The value of X_s at the intercept gives the stick-slip amplitude. (b) The value of t_s at the intercept gives the stick-slip amplitude via $X_s = V_0 t_s$.

harmonic oscillation (if $0 > \beta > -\omega$), while for a stronger speed dependence the motion is smooth sliding for $\beta \geq \omega$ or is unstable for $\beta \leq -\omega$. More explicitly, the motion in the slip phase is derived from eqn. (A5) as

$$\begin{aligned}\theta(A, B, t) - \theta_0 &= \exp(-\beta t) (A \cos \Omega t + B \sin \Omega t) \\ \frac{d\theta}{dt} &= -\exp(-\beta t) \{ (\beta A - \Omega B) \cos \Omega t \\ &\quad + (\Omega A + \beta B) \sin \Omega t \}\end{aligned}\quad (\text{A8})$$

where $\Omega = (\omega^2 - \beta^2)^{1/2}$. Equation (A8), of course, represents harmonic motion if $\beta=0$ or near-harmonic motion if $|\beta| \ll \omega$.

Applying eqn. (A6) to eqn. (A8) and after some algebra, one arrives at

$$\begin{aligned}\theta_{-s} - \theta_0 &= -(\theta_{+s} - \theta_0) \\ \text{if } |\beta| &\ll \omega \text{ (for any } V_0) \\ \theta_{-s} - \theta_0 &= -(\theta_{+s} - \theta_0) \exp(-\beta\pi/\Omega) \\ \text{if } V_0 &\rightarrow 0 \text{ (full stick-slip)} \\ \theta_{-s} - \theta_0 &= -(\theta_{+s} - \theta_0) \exp(-2\beta\pi/\Omega) \\ \text{if } V_0 &\rightarrow V_m \text{ (nearly no stick-slip)}\end{aligned}\quad (\text{A9})$$

We can draw quantitative conclusions regarding the stick-slip amplitude by making use of eqn. (A9) to obtain

$$x_s \equiv r(\theta_{+s} - \theta_{-s}) = r(\theta_{+s} - \theta_0)\{1 + \exp(-\beta t')\}$$

$$\text{or} \quad \theta_{+s} = \theta_0 + \frac{\theta_s}{1 + \exp(-\beta t')} \quad (\text{A10})$$

and with the aid of eqn. (A7) to arrive at

$$\frac{\omega^2}{g\{1 + \exp(-\beta t')\}} x_s \approx \mu_s(X_s) - \mu_k(V_0)$$

$$\text{or} \quad \frac{\omega^2 V_0}{g\{1 + \exp(-\beta t')\}} t_s \approx \mu_s(t_s) - \mu_k(V_0) \quad (\text{A11})$$

recalling again that $\omega^2 \approx g/r$ for small μ_0 , $\Omega' \rightarrow \pi$ for $V_0 \ll V_m$ (full stick-slip) and $\Omega' \rightarrow 2\pi$ for $V_0 \rightarrow V_m$ (near extinction of stick-slip).

For a given dependence of μ_s on stick time, in a general functional form, the stick-slip amplitude now can be obtained graphically from eqn. (A11) by plotting the left-hand side of the equation as a function of x_s (or t_s), which is a straight line with a constant slope, and by plotting the right-hand side of the equation on

the same figure, as shown in Fig. A1. The point of interception, if any, gives x_s (or t_s) and, hence, one finds the stick-slip amplitude $x_s = V_0 t_s$.

As can be seen from Fig. A1(a), increasing ω , i.e. increasing the stiffness of the spring, at a given substrate speed increases the slope of the straight line. Consequently, the point of interception moves toward the origin of the coordinate system, resulting in decreasing stick-slip amplitudes. At a critical value of ω , the two curves only meet at the origin, leading to a zero stick-slip amplitude and thus the cessation of stick-slip for larger values of ω .

Similarly, increasing the substrate speed reduces the stick-slip amplitude. Physically, this occurs because the stick times shorten progressively and there is increasingly less time for μ_s to increase. Mathematically, a larger substrate speed increases the slope of the straight line when using t_s as the variable instead of x_s , as shown in Fig. A1(b). At a critical value of V_0 and above, the two curves only meet at the origin, indicating a zero stick-slip amplitude and thus the cessation of stick-slip motion.

Reference for Appendix A

A1 C. Gao, D. Kuhlmann-Wilsdorf and D. D. Makel, The dynamic analysis of stick-slip motion, to be submitted.

Microstructural evolution in rolled aluminium

Bent Bay

The Engineering Academy of Denmark, Department of Mechanical Engineering, Lyngby (Denmark)

Niels Hansen

Materials Department, Risø National Laboratory, Roskilde (Denmark)

D. Kuhlmann-Wilsdorf

University of Virginia, Department of Materials Science, Charlottesville, VA 22901 (USA)

(Received March 16, 1992)

Abstract

The evolution of the microstructure of cold-rolled pure aluminium (99.996%) was studied by transmission electron microscopy (TEM), extending a previous study that was limited to 30% strain ($\epsilon = 0.36$). The present work concentrates on rolling strains from 50% ($\epsilon = 0.69$) to 90% ($\epsilon = 2.3$). The observations are explained through the governing principle that, in the course of polyslip, grains break up into volume elements within each of which fewer slip systems operate simultaneously than required by the Taylor model. The boundaries between the volume elements accommodate the lattice misorientations arising from the correspondingly different glide. They are therefore geometrically necessary boundaries and in TEM they appear variously as dense dislocation walls, different types of microbands and subgrain boundaries. The morphology and the spatial arrangement of the geometrically necessary boundaries were characterized and it is discussed how these boundaries form with increasing strain as an integral part of the microstructural evolution.

1. Introduction

In a recent paper [1] the microstructural evolution during the plastic deformation of polycrystals was analysed in terms of two governing principles: (i) a continuous subdivision of grains into volume elements deforming through different combinations of slip systems and (ii) mutual trapping of dislocations into low energy configurations (LEDs). Good agreement was found between these principles and transmission electron microscopy (TEM) observations for a number of medium or high stacking fault energy materials deformed by different modes to low and medium strains [1–7]. The governing principles should also apply to materials deformed to high strains but experimental observations in the strain range from 0.7 to 2.3 are scarce. This range was covered in the present experiments where the microstructural evolution was analysed in cold-rolled pure aluminium (99.996%) deformed 50%–90% by cold-rolling.

2. Governing principles

In refs. 1 and 3 it was suggested that a governing principle of plastic deformation is that the number and

selection of simultaneously acting slip systems differ between neighbouring volume elements and that in every element the number of slip systems is in general smaller than that required by the Taylor model [8] for microscopic strain accommodation.

Fewer slip systems lead to a reduction of dislocation intersections and thus fewer jogs and lower flow stress at the expense of less perfect approximation to homogenous deformation. However, the constraints between the differently oriented grains will, with locally fewer simultaneously operating systems, lead to the corresponding subdivision into volume elements with increasingly different lattice orientations but which collectively closely approximate homogenous strain. The subdivision appears to take place on a smaller and smaller scale beginning with relatively few domains per grain at small strains to many cell blocks and finally to a large number of subgrains as the predominant arrangement at large strains. Each volume element is characterized by its own combination of slip systems, therefore by different lattice rotations with strain, and the dislocation boundaries between the elements arise out of geometrical necessity. It is therefore suggested [9] that such boundaries should be termed geometrically necessary boundaries (GNB) in order to distinguish them from ordinary cell boundaries which are

due to mutual trapping of glide and forest dislocations and have been dubbed incidental dislocation boundaries [9]. In previous work different types of GNBs have been analysed, among others dense dislocation walls which are long and have relatively large lattice rotations across. The spacing between the dense dislocation walls decreases with strain as an integral part of the grain subdivision. Other types of GNBs are microbands and a combination of dense dislocation walls and microbands. Although the GNBs differ in morphology they have similar function. A list of definitions for the various dislocation arrangements has been suggested in ref. 1. The definitions of cell blocks, dense dislocation walls and microbands are given below.

Cell blocks (CBs). These are domains of contiguous dislocation cells which share the same selection of operating glide systems.

Dense dislocation walls (DDWs). These are undissociated dislocation rotation boundaries with a high dislocation density separating adjoining cell blocks, i.e. separating regions with different combinations of simultaneously operating glide systems.

Microbands (MBs). Well formed plate-like zones of material bounded by dislocation rotation boundaries whose morphology and crystallography indicate that the combination of operating glide systems in them differs from that of the adjoining material and which accordingly are bounded by rotation boundaries. MBs are therefore CBs. MBs are commonly subdivided into dislocation cells which are smaller on average than the dislocation cells in the adjoining material.

First generation microbands (MB1s). Microbands which are developing through the splitting of dense dislocation walls over part or all of their length.

Second generation microbands (MB2s). Microbands which are narrow plate-like zones passing through one or more pre-existing dislocation cells along one of the crystallographic slip planes.

3. Microstructural evolution in rolled aluminium

The starting material was aluminium of 99.996% purity having an average grain size of $130\text{ }\mu\text{m}$. The thickness of the material before the final cold-rolling was 2.6 mm. Specimens were produced from rolling plane sections and from longitudinal sections. It was possible to produce thin foils from longitudinal sections after 90% cold-rolling, the specimen thickness in that case being only 0.26 mm. The material and the experimental methods are further described in ref. 3.

The microstructural evolution was studied with increasing degree of cold-rolling from 50% to 90% ($\epsilon=0.69$ –2.3, where ϵ is the true strain), to extend earlier observations in the range 10%–30%



Fig. 1. Thin foil from a longitudinal section of 50% cold-rolled aluminium. The directions of the DDW-MB1s are marked by thick arrows. The rolling direction is marked rd.



Fig. 2. Thin foil from a longitudinal section of 50% cold-rolled aluminium. The DDW-MB1s are mainly lying in one direction, which is marked by thick arrows. In a few places DDW-MB1s are observed lying almost parallel to the rolling direction. A thin arrow is placed to the right of the band of cells.

($\epsilon=0.11$ –0.36). The characteristics and the frequency of a number of typical microstructural features led to a classification into three strain ranges which will be used in the description of the experimental observations which follows.

Typical microstructures are shown in Figs. 1–6, and characteristic features are illustrated schematically in Figs. 7(a)–7(d).



Fig. 3. Thin foil from a longitudinal section of 70% cold-rolled aluminium. The structure is dominated by large areas with only one set of DDW-MB1s, the direction of which is marked by thick arrows. These areas are separated by narrow areas of a laminar structure consisting of bands of elongated cells (subgrains), which make angles of approximately -15° to $+15^\circ$ with the rolling direction. The directions of these bands are marked by thin arrows. Note the pronounced S-shape of the DDW-MB1s at A and the sharp intersection between bands at B (see the text and Fig. 7(c)).

3.1. Low to moderate strains (10%–50%)

The major microstructural features are cells, cell blocks (CBs), dense dislocation walls (DDWs), first generation microbands (MBs) and mixtures of walls and bands (DDW-MB1s), see Figs. 1 and 2. The majority of DDW-MB1s form an angle of approximately 40° with the rolling direction, as seen in the longitudinal plane. A second set of DDW-MB1s forms an angle of 15° or less with the rolling direction, again as seen in the longitudinal plane. The two sets of DDW-MB1s have been described previously [10].



Fig. 4. Thin foil from a longitudinal section of 80% cold-rolled aluminium. To the right the structure mainly consists of a laminar structure of elongated subgrains making angles of 0° – 10° with the rolling direction. Some areas to the left with DDW-MB1s are marked by thick arrows.



Fig. 5. Thin foil from a longitudinal section of 90% cold-rolled aluminium. The majority of the structure is composed of a laminar structure containing subgrain boundaries lying within a few degrees of the rolling direction. Several recovered subgrains are seen, some of which are marked by r. To the left of the three arrows a band of elongated subgrains is seen making an angle of 47° with the rolling direction.



Fig. 6. Thin foil from a longitudinal section of 90% cold-rolled aluminium. An area of limited size is seen consisting of narrow DDW-MB1s, the direction of which is marked by thick arrows. To the left and to the right laminar structures are seen lying almost in the rolling direction.

The microstructure evolves from (i) predominantly ordinary dislocation cells after 10% deformation to (ii) predominantly DDWs, CBs, MB1s and DDW-MB1s after 20%–50% deformation. Thus, the number of DDW-MB1s increases with deformation and the width of the CBs decreases (see Table 1 and Figs. 7(a) and 7(b)). Also, the cell size in the CBs and the width of the cells in the MB1s decrease with strain. The width of the MB1s and the number of cells across the MB1s reaches its maximum in 30% deformed material and is smaller in 50% deformed material.

The angle between the DDW-MB1s and the rolling plane remains approximately constant independent of the degree of deformation. The lattice rotations across the DDW-MB1s increase with increasing deformation from 10% to 30% and remain practically constant when the deformation is increased from 30% to 50%. The lattice rotations can be as large as 10° – 15° . Finally,

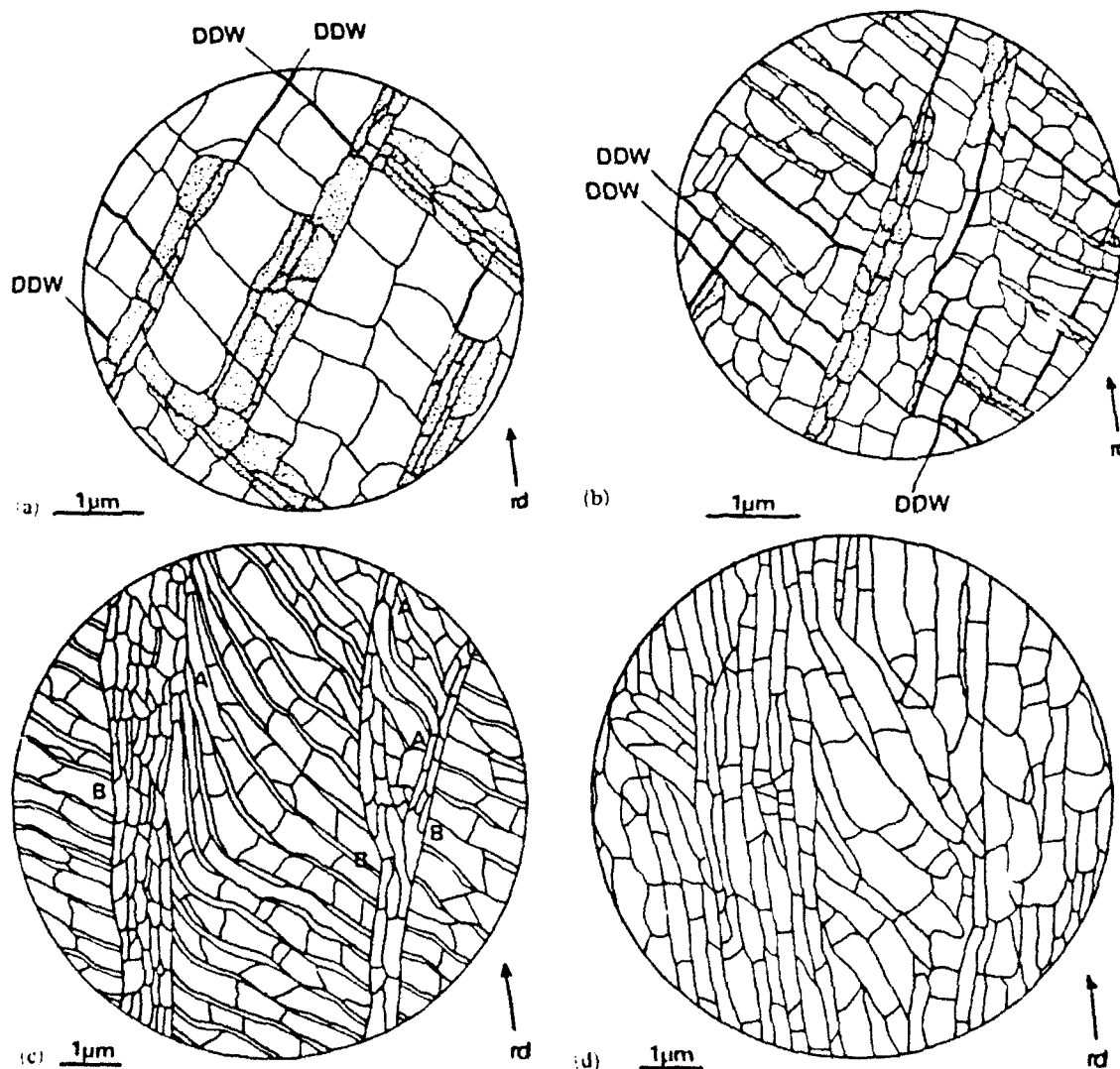


Fig. 7. Sketches illustrated in longitudinal sections, which show the most characteristic changes in microstructure which take place, when the degree of cold-rolling is increased from 30% to 90%. In (a) and (b) the DDWs are drawn as thick lines, and subgrains in MB1s are dotted.

TABLE 1. Width of microbands and cell blocks (longitudinal section)

| Deformation (%) | Width of MB1s ^a (μm) | Width of CBs between MB1s (μm) | Width of CBs in lamellar structure (μm) |
|-----------------|--|---|--|
| 30 | 0.5 (0.2-1.0) | 1.4 (0.5-2.5) | — |
| 50 | 0.15 (0.07-0.4) | 0.8 (0.4-2.5) | — |
| 70 | 0.1 (0.05-0.3) | 0.55 (0.25-1.2) | 0.3 (0.1-0.7) |
| 80 | — ^b (0.02-0.15) | 0.4 (0.2-0.7) | 0.3 (0.1-0.7) |
| 90 | — ^b (0.02-0.08) | 0.45 (0.15-1.0) | 0.4 (0.1-2.0) |

^aOnly microbands forming an angle of approximately 40° with the rolling direction were analysed.

^bThe mean was not calculated as the number of microbands was small.

the frequency of grains subdivided by DDW-MB1s increases with strain to about 80% at a strain of 30%; the rest of the grains are dominated by an ordinary cell structure, *i.e.* incidental dislocation boundaries. Figures 1 and 2 show typical microstructures of 50% deformed material.

3.2. Intermediate strain (70%)

After 70% cold-rolling a new microstructural feature has developed in all grains which contain DDW-MB1s (see Fig. 3 and Table 1). The new feature is layers of elongated cells or subgrains forming a lamellar structure. The lamellae are grouped in bands which have a width of 0.5–3 μm . The lamellae make angles between 15° and zero with the rolling direction. The lamellar structure can be described as an elongated cell block structure mostly containing only one cell or subgrain across the cell block. The structure is different from the first generation microband structure observed at low strains, as no small dislocation cells are found in the walls between the cell blocks. The width of the cell blocks is in the range 0.1–0.7 μm (see Table 1).

The lamellar structure makes up about 25% of the structure in grains containing DDW-MB1s. This percentage varies somewhat from grain to grain. In many cases the lamellae meet forming a Y shape (see Figs. 3 and 7(c)); in other cases the lamellae form an undisturbed band as shown to the left in Fig. 7(c). The density of bands of lamellae can be estimated from the spacing between the bands measured from centreline to centreline. The spacing was measured as 6.4 $\mu\text{m} \pm 1.3 \mu\text{m}$ with a minimum spacing of 4.5 μm .

A DDW-MB1 structure making an angle of 40° with the rolling direction is present between the lamellar

bands and frequently the two types of structure are clearly separated from each other (see the markings B in Figs. 3 and Fig. 7(c)). However, in a number of cases the DDW-MB1 structures are curved towards the direction of the lamellae in the area where the two meet. This characteristic S-shaped structure is seen near the markings A in Figs. 3 and 7(c).

The crystallographic orientation of the planes of the lamellae was calculated from the direction of the traces of the lamellae and the orientation of the longitudinal plane, assuming that the plane of the lamellae lies approximately perpendicular to the longitudinal plane. This assumption is based on the observation in transverse sections that the subgrains are elongated with boundaries approximately parallel to the transverse direction. The results from two grains show that the lamellae lie on planes which form angles of 12°–31° with the nearest {111} plane (see Table 2). For the same two grains it was examined whether there is an angular correlation between the lamellae, where the S-shaped features are observed and either the {111} planes or the rolling plane, but no such correlations were found. However, further work is needed.

By increasing the degree of deformation from 50% to 70% the spacing between the DDW-MB1s decreases. The width of the MB1s as well as the width of the cells in the MB1s decrease, and many walls are observed which contain no cells. These observations are shown in Table 1 and can be observed by comparing Fig. 1 with Fig. 3 and Fig. 7(b) with Fig. 7(c).

3.3. Large strain (80%–90%)

In 80% and 90% cold-rolled aluminium the lamellae dominate the microstructure. The angle between the lamellae and the rolling direction decreases with increasing degree of deformation, being between –10° and +10° after 80% cold-rolling and only a few degrees after 90% cold-rolling (see Figs. 4 and 6). The lamellar structure consists of elongated cell blocks, the large majority of which show only one cell across. Misorientations across individual cell block walls up to 10°–15° are observed in the lamellar structure, largest in the 90% deformed material. Still the lattice rotation from one end of a grain to the other is small owing to more or less alternating rotations. The S-shaped structure seen in 70% cold-rolled material is less frequently observed in the highly deformed aluminium.

Approximately 20% of the grains in 30%–90% deformed aluminium are dominated by an ordinary cell-subgrain structure. At large strain these grains show elongated pancake-shaped subgrains lying within a few degrees of the rolling plane, forming cell blocks with only one cell (subgrain) across. This microstructure shows subboundaries, which are more wavy (less straight) than the boundaries in the lamellar structure

TABLE 2. Relation between planes of the lamellae, {111}-planes and the rolling plane; the lamellae are grouped in bands and numbers 2-5 are the four groups of lamellae seen in Fig. 3 from left to right in the micrograph (longitudinal section)

| Grain number | Band number | Longitudinal plane | Rolling direction | Trace of band in plane of thin foil | Plane of band | Angle between trace of band and rolling direction (deg) | Angle between plane of band and nearest {111}-plane (deg) | Angle between trace of band and trace of {111} (deg) |
|--------------|-------------|--------------------|-------------------|-------------------------------------|----------------|---|---|--|
| 1 | 1 | | | [12, 7, 14] | (147, 140, 56) | -2 | 20 | 16 |
| | 2 | | | [18, 21, 31] | (182, 125, 21) | -13 | 31 | 29 |
| | 3 | (477) | [12, 7, 14] | [5, 1, 4] | (35, 51, 31) | +12 | 12 | 0 |
| | 4 | | | [9, 7, 12] | (133, 111, 35) | -4 | 24 | 21 |
| | 5 | | | [5, 1, 4] | (35, 51, 31) | +14 | 12 | 0 |
| 2 | 1 | (123) | [121] | (12, 16, 7) | (62, 29, 40) | 11 | 17 | 17 |

described above. Otherwise the two structures resemble each other, also as to the misorientations across the subboundaries. No correlation between the crystallographic orientation of the grains and the characteristic microstructures was found.

After 90% cold-rolling a very small number of bands is observed, approximately 2 μm in width and 5-20 μm in length (see Fig. 5). These bands make approximately the same angles with the rolling direction as MB1s, *i.e.* about 40°, but they are separated from the neighbouring structure by high-angle boundaries. These bands have the characteristics of shear bands and on average only one is found in each grain. Shear bands of similar appearance have been observed both in single crystals [11] and in polycrystals of aluminium [12, 13].

90% cold-rolling results in some recovery of the microstructure. Three subgrains which have undergone recovery are shown in Fig. 5.

4. Discussion

4.1. Strain accommodation and subdivision of grains

The microstructural evolution of pure aluminium specimens, deformed up to 90% in cold-rolling (*i.e.* to a true strain of 2.3), follows a general pattern for polycrystalline deformation of cell-forming metals (see Section 1), namely that grains break up into volume elements in order to accommodate the macroscopic plastic strain by simultaneous operation of fewer slip systems than required by the Taylor model [1, 3, 5, 6, 8, 14, 15]. This break up with abruptly changing slip system combinations, will take place on a smaller and smaller scale, say from relatively few domains per grain at the start of plastic deformation to many cell blocks

until finally slip system combinations change for each subgrain at large strain [1].

The abrupt lattice orientation changes due to the operation of the different slip system combinations in neighbouring volume elements are accommodated by dislocation boundaries, for which the average spacing correspondingly shrinks with strain. The average misorientation across those geometrically necessary boundaries (GNBs) must increase with strain until the final orientation due to the respective slip system combination, all operating at the same resolved shear stress, is attained. It is expected that the lattice rotations across GNBs decrease with the number of simultaneously active slip systems since this permits a closer approach to the condition of homogeneous deformation. The material between GNBs is subdivided by ordinary cell walls having a relatively small misorientation across. These walls are formed by dislocation trapping and they are the incidental dislocation boundaries as described in ref. 9.

The various types of GNBs have the same function but they differ in morphology. Dislocation boundaries between domains have not been studied in detail. While it is still unclear whether DDWs are in fact domain boundaries, their development into MB1s has been discussed previously [1] in great detail. The present observations show that at large strains the typical DDW-MB1 structure develops into a structure dominated by GNBs almost parallel to the rolling plane. This lamellar structure has frequently been observed both in single crystals and in polycrystals deformed at large strains [13, 16-21].

The relative frequency of the different types of GNBs shows some variation both with grains and between grains. Such differences may be the result of different factors such as grain size, initial crystallogra-

phic orientation, and interaction among neighbouring grains. In spite of such differences, the observed microstructural evolution is quite uniform and in good agreement with the suggested pattern for polycrystalline deformation.

4.2. Spatial arrangement of geometrically necessary boundaries

The GNBs may have different spatial arrangements and orientations with respect to the sample axes. This has been observed in cold-rolled samples [1, 3, 5, 10] where different characteristic types have been identified:

(i) DDW-MB1s forming angles of approximately 40° and 15° or less respectively with the rolling direction (in the longitudinal plane);

(ii) a lamellar structure built up of straight dislocation boundaries forming angles between 15° and zero with the rolling direction;

(iii) extended subgrain boundaries lying within a few degrees of the rolling plane.

Both at low and medium strains the DDW-MB1s dominate the microstructure whereas the lamellar structure dominates at large strain. A comparison of the 40° DDW-MB1s and the lamellar structure shows that not only the frequency of the two types of structures changes differently with increasing strain, but also their spatial arrangement. The orientation of the DDW-MB1s remains almost constant at 40° with respect to the rolling direction throughout rolling, i.e. a constant rearrangement of these GNBs takes place. By contrast, the lamellar structure becomes more and more aligned with the rolling plane. This alignment may reorient to a certain extent the DDW-MB1s, being curved in an S-shape.

The spatial arrangement of the DDW-MB1s is discussed in ref. 1. While at present there is no specific explanation as to why and how the macroscopic strain is translated into the discussed orientation of the DDW-MB1s, it is taken for granted that the arrangement is that of low energy dislocation structures or LEDS [22] which best approximates the lowest free energy per unit length of dislocation line, i.e. follows the LEDS principle [14, 22, 23]. This type of arrangement corresponds with the very common observation of alternating lattice rotation across neighbouring cell blocks [3, 5].

5. Summary

For pure aluminium specimens deformed up to 90% in rolling, the experimental observations are in good agreement with the governing principle that grains break up on a smaller and smaller scale into volume

elements within each of which fewer slip systems operate simultaneously than required by the Taylor model.

The volume elements subdividing the grains are characterized by individual combinations of operating slip systems and the boundaries between them accommodate the lattice misorientations arising from the correspondingly different glide. These boundaries are therefore geometrically necessary boundaries (GNBs).

Two dominating types of GNBs are recognized, one more or less parallel to the sheet, the other remaining inclined about 40° against it, which implies a good mobility. At large strain the GNBs inclined against the sheet plane are gradually eliminated.

The formation of GNBs and their spatial arrangement has a significant effect on the microstructural evolution and may also have a pronounced effect on the texture development which is being investigated.

Acknowledgments

The authors thank J. Lindbo for very skilful preparation of thin foils and Palle Nielsen for assistance with the experimental work. Dr. D. Juul Jensen and Dr. D. A. Hughes are thanked for helpful discussions.

References

- 1 B. Bay, N. Hansen, D. A. Hughes and D. Kuhlmann-Wilsdorf, *Acta Metall. Mater.*, **40** (1992) 205.
- 2 C. Y. Barlow, B. Bay and N. Hansen, *Philos. Mag. A*, **51** (1985) 253.
- 3 B. Bay, N. Hansen and D. Kuhlmann-Wilsdorf, *Mater. Sci. Eng., A113* (1989) 385.
- 4 D. A. Hughes and W. D. Nix, *Mater. Sci. Eng., A122* (1989) 153.
- 5 D. A. Hughes and N. Hansen, *Mater. Sci. Technol.*, **7** (1991) 544.
- 6 N. Hansen, *Mater. Sci. Technol.*, **6** (1990) 1039.
- 7 V. S. Ananthan, T. Leffers and N. Hansen, *Mater. Sci. Technol.*, **7** (1991) 1069.
- 8 G. I. Taylor, *J. Inst. Mater.*, **62** (1938) 307.
- 9 D. Kuhlmann-Wilsdorf and N. Hansen, *Scripta Metall. Mater.*, **25** (1991) 1557.
- 10 D. Juul Jensen and N. Hansen, *Acta Metall. Mater.*, **38** (1990) 1369.
- 11 T. Kamijo, A. Fujiwara and H. Inagaki, *Scripta Metall. Mater.*, **25** (1991) 949.
- 12 D. J. Lloyd, in A. K. Sachdev and J. D. Embury (eds.), *Formability and Metallurgical Structure*, The Metallurgical Society, Warrendale, PA, 1987, p. 193.
- 13 Y.-L. Liu, L. Delaey, E. Aernoud and D. Arkens, *Mater. Sci. Eng.*, **96** (1987) 125.
- 14 D. Kuhlmann-Wilsdorf, *Mater. Sci. Eng., A113* (1989) 1.
- 15 N. Hansen, in T. C. Lowe et al. (eds.), *Modelling the Deformation of Crystalline Solids*, The Metallurgical Society, Warrendale, PA, 1991, p. 37.
- 16 H. G. Grewe and E. Kappler, *Phys. Status Solidi*, **6** (1964) 699.

- 17 A. S. Malin and M. Hatherly, *Met. Sci.*, 13 (1979) 463.
- 18 J. Gil-Sellano, P. Van Houtte and E. Aernoudt, *Progr. Mater. Sci.*, 25 (1980) 69.
- 19 H. Chandra Holm and J. Embury, in T. N. Baker (ed.), *Yield, Flow and Fracture of Polycrystals*, Elsevier, London, 1983, p. 275.
- 20 W. H. Zimmer, S. S. Hecker, D. L. Rohr and L. E. Murr, *Met. Sci.*, 17 (1983) 198.
- 21 S. S. Hecker and M. Stout, in G. Krauss (ed.), *Deformation, Processing and Structure*, American Society for Metals, OH, 1984, p. 1.
- 22 M. N. Bassim, W. A. Jesser, D. Kuhlmann-Wilsdorf and H. G. F. Wilsdorf (eds.), *Low Energy Dislocation Structures, 1986*, in *Mater. Sci. Eng.*, 81 (1986).
- 23 N. Hansen and D. Kuhlmann-Wilsdorf, *Mater. Sci. Eng.*, 81 (1986) 141.

Submitted to Wear
12/22/92

DYNAMIC ANALYSIS OF STICK-SLIP MOTION

by

Chao Gao, Doris Kuhlmann-Wilsdorf and David D. Makel
Department of Materials Science and Engineering
University of Virginia, Charlottesville, VA 22901

ABSTRACT

The most widely accepted cause of stick-slip motion is that the static (μ_s) exceeds the kinetic friction coefficient (μ_k), or that μ_k drops rapidly at small speeds. Using a dynamic analysis it is shown that the rate of increase of $\mu_s(t)$ with time during stick episodes is a crucial parameter in addition to the condition of $\mu_s > \mu_k$, and that, in contrast to the normal requirement of a rapidly decreasing μ_k , stick-slip may occur even if μ_k increases with speed (V). A general equation is derived which describes the stick-slip amplitude (X_s) in terms of substrate speed (V_0), spring stiffness (K), and damping (γ), for an arbitrary $\mu_s(t)$ and a linearized $\mu_k(V)$, in contrast to a set of previous equations derived by Brockley et. al. for an exponential $\mu_s(t)$ and a linearized $\mu_k(V)$ [1]. Additional equations are developed for the "saturation" speed (V_{ss}), below which X_s is independent of V_0 , and also for a critical substrate speed above which the stick-slip amplitude vanishes. In between V_{ss} and V_c , depending on the detailed $\mu_s(t)$ curve, the stick-slip amplitude decreases with increasing V_0 , K and γ . Depending on the detailed sliding conditions, different sliding modes including smooth sliding, near-harmonic oscillations, or stick-slip can result. Equations developed in this paper suggest practical methods of reducing or eliminating stick-slip for a general system.

NOMENCLATURE

| | |
|------------------|---|
| A | integral constant |
| B | integral constant |
| g | acceleration due to gravity |
| K | spring constant of measuring system |
| m | sample mass |
| P | normal force between sample and substrate |
| r | hoop radius |
| t | time |
| t' | time in a slip episode |
| t _s | time in a stick episode |
| t _∞ | time beyond which static friction ceases to grow |
| t _∞ | infinite time |
| V | absolute sample velocity |
| V ₀ | substrate velocity |
| V _c | critical substrate speed above which stick-slip motion ceases |
| V _h | hoop velocity |
| V _r | relative velocity (V-V ₀) |
| V _∞ | saturation substrate speed below which stick-slip amplitude is independent of the substrate speed |
| X | momentary sample displacement |
| X ₀ | time-averaged sample displacement |
| X _{max} | maximum sample displacement |
| X _{min} | minimum sample displacement |
| X _s | stick-slip amplitude |
| X _s | displacement at beginning of a stick episode |
| X ₊ | displacement at end of a stick episode |
| dx/dt=V | absolute sample velocity (V) |
| α | coefficient of the linear term for the μ-V curve |
| β | effective damping coefficient of measuring system |
| γ | damping coefficient of measuring system |
| θ | momentary angular position of sample on hoop |
| θ ₀ | time-averaged angular position of sample on the hoop |
| θ _r | difference between momentary and time-averaged angular position (θ-θ ₀) |
| ω | oscillation frequency in harmonic motion |
| Ω | oscillation frequency in damped or pumped harmonic motion |
| λ _± | two roots for second order auxiliary equation |
| μ _k | kinetic friction coefficient |
| μ _s | static friction coefficient |

*All displacements measured relative to the free spring position

I. INTRODUCTION

Stick-slip motion, in which two sliding surfaces cycle between relative rest and motion, is a widely observed phenomenon in friction-measuring systems such as pin-on-disk tribometers, the so-called hoop apparatus, atomic force microscopes, surface force devices, and others [2-9]. Its effects range from atomic to macroscopic scale, as well as from delicate instrumentation to daily life. Phenomenologically, the most widely accepted cause for stick-slip is that the static friction coefficient (μ_s) exceeds the kinetic friction coefficient (μ_k), or more rigorously, that μ_k drops rapidly at small speeds [4,10].

Generally speaking, μ_s and μ_k can be complicated functions of sticking time and surface speed, respectively. Furthermore, static friction is a constraining force during stick, while kinetic friction is an applied force during slip. Owing to these complications, stick-slip motion is ordinarily studied by graphical methods [10,11] which give only semi-quantitative results.

Bowden and Tabor [4] treated stick-slip motion analytically for an undamped system for constant μ_k and constant μ_s ($>\mu_k$). They showed that for such systems the stick-slip amplitude is exactly proportional to the difference between μ_s and μ_k , regardless of experimental parameters. As they pointed out, however, the assumption of constant μ_s and μ_k is certainly an oversimplification.

To deduce the speed dependence of μ_k from stick-slip motion while assuming constant μ_s , Sampson etc. al. [12] dealt with the

stick-slip problem semi-analytically for both damped and non-damped systems. They concluded that for most sliding surfaces μ_s depends weakly on, and can be linearized with, speed, and that μ_k depends on sticking time.

By assuming a linear dependence of the kinetic friction on speed and an exponential dependence of the static friction on stick time, Brockley et. al. [1] obtained three coupled equations for the critical substrate speed V_c above which stick-slip motion ceases as follows. For substrate speeds tending to zero, they derived an approximate equation for stick-slip amplitude as a function of substrate speed, and then deduced the critical substrate speed by letting the amplitude approach zero. However, their equations are flawed by the assumption of very low substrate speeds (V_0) compared to the critical speed (V_c), which holds true only for stick-slip amplitudes near saturation but breaks down as the stick-slip amplitude approaches zero.

Based on experimental results for different surface geometries and lubricants, Eguchi and Yamamoto [13] proposed an empirical relationship in which the growth rate of the static friction force is proportional to the product of critical substrate speed and the spring constant of the system. Their empirical equation is close to the theoretical equation derived herein, except that the present analysis also takes into consideration system damping and the speed dependence of kinetic friction.

In this paper, starting with a general dynamic analysis, it will be shown that $\mu_s > \mu_k$ is a necessary but not sufficient

condition for stick-slip motion, that $d\mu_s/dt$ is a crucial parameter, and that in contrast to the requirement of a rapidly decreasing μ_k , stick-slip may occur even if μ_k increases with speed (V). Explicit equations for determining the slip mode, the stick-slip amplitude (X_s), the critical substrate speed (V_c) above which stick-slip ceases, and the saturation substrate speed ($V_{s\infty}$) below which the stick-slip amplitude is constant, are developed in terms of V_0 , K , γ , μ_s , μ_k , $d\mu_s/dt$ and $d\mu_k/dV$. These equations are based on the model of a general $\mu_s(t)$ and a linearized $\mu_k(V)$. Comparisons are also made between the theoretical predictions of these equations and a wide range of experimental observations.

II. BASIC MATHEMATICAL THEORY OF SLIDING WITH VELOCITY DEPENDENT FRICTION

A. Equation of Motion for a General System

Although the present mathematical description was stimulated by experiments conducted with the so-called hoop apparatus whose essential geometry is shown in Fig. 1 (a) [2,14-16], it is equally applicable to other friction measuring systems such as a pin-on-disk tribometer (Fig.1b) or a surface-force-apparatus (Fig.1c). In the last two friction measuring systems, the slider (assumed to be a point-mass) is acted on by a spring force, Kx , and a friction force $P\mu_k(V)$. The corresponding equation of motion for the slider then is

$$m \frac{d^2x}{dt^2} + \gamma \frac{dx}{dt} + kx = P \mu_k(V_r) \quad (1)$$

Here the surface velocity between the slider and the substrate is $V_r = V_0 - dx/dt$, while γ designates the system damping other than the inter-surface friction, $k = m\omega^2$ the spring constant with ω the system frequency, and P the normal force. It should be noted, however, that eq. (1) can only be applied to slip phases since during sticking the static friction is a constraining force.

B. Equation of Motion for the Hoop Apparatus

In the hoop apparatus a sample with mass m slides in a rotating hoop under the actions of gravity ($-mg \sin\theta$) and friction ($\mu mg \cos\theta$) where, as seen in Fig. 1(a), θ is the angle between the hoop tangent at the momentary position of the sample mass and the horizon. In effect, the hoop provides an infinite plane with variable inclination angle θ and a controllable substrate speed. The apparent momentary friction coefficient, $\mu_{app} = \tan\theta(t)$, is monitored using a polarized beam of light whose intensity is modulated when it passes through a polaroid sheet mounted on the top of the moving sample holder. The polarizing angle, and hence the light intensity, changes as the sample moves on an arc up and down on the inner surface of the hoop, and the resulting light intensity is measured using a photo diode.

Thus for the hoop apparatus, as shown in Fig. 1 (a), the assumed point-mass slider moves on the inner hoop surface in response to the friction force, $mg \cos\theta \mu_k(V)$, and the gravitational

force, $-mg \sin\theta$, resulting in the following equation of motion

$$r \frac{d^2\theta}{dt^2} = g \cos\theta \mu_k(V_r) - g \sin\theta \quad (2)$$

with r the hoop radius, V_0 the hoop speed, and $V_r = V_0 - r d\theta/dt$ the sliding surface speed.

In order to solve eq. (2) it is desirable to define the angular position of the slider in terms of the time-averaged position (θ_0) and the displacement away from the time averaged position (θ_r), as shown in Fig. 1a. In substituting $\theta_r + \theta_0$ for θ , higher orders of θ_r can be neglected because $\theta_r \ll 1$ and $\theta_r \ll \theta_0$, thereby permitting eq. (2) to be rewritten as

$$\frac{r}{g} \frac{d^2\theta_r}{dt^2} + [\cos\theta_0 + \mu_k(V_r) \sin\theta_0] \theta_r + [\sin\theta_0 - \mu_k(V_r) \cos\theta_0] = 0 \quad (3)$$

This is an important approximation for achieving a tractable equation for slider motion in the hoop apparatus. Again eq. (3) can only be applied to slip phases.

C. Solution to Equation of Motion for Linearized Kinetic Friction

In general, $\mu_k(V)$ can be a complicated function of surface speed due to viscous flow, shear thinning, or friction heating [4,14,17], for example. A complicated $\mu_k(V)$ would make it impossible to achieve analytical solutions for either a general system (eq.1) or the hoop apparatus (eq.3). In such cases, one must turn to graphical or numerical methods. Nevertheless, in the context of stick-slip motion, possible effects of chaotic behavior

on the motion trajectories can be neglected [11] because of the short time scale of each slip phase.

Both eqs. (1) and (3) are readily solved analytically, and are indeed equivalently the same, if μ_k is assumed to be a linear function of speed, an assumption which was found to be quite satisfactory in an earlier analysis of stick-slip [12]. Namely in that case

$$\left[\begin{array}{l} \mu_k = \mu_0 + \alpha V_r = \mu_0 + \alpha V_0 - \alpha \frac{dx}{dt} \\ \quad = \mu_0 + \alpha V_0 - \alpha r \frac{d\theta}{dt} \quad \text{for the hoop apparatus} \end{array} \right] \quad (4)$$

with μ_0 and α arbitrary constants. Such a speed dependence of μ_k is shown in Fig. 2(a) in which the vertical dark line at $V_r=0$ denotes the increasing static friction coefficient μ , as a function of stick time.

Using the linearized form of $\mu_k(V_r)$, equation (1) becomes

$$\frac{d^2x}{dt^2} + \frac{\gamma + \alpha P}{m} \frac{dx}{dt} + \omega^2(x - x_0) = 0 \quad (5)$$

where $X_0 = (\mu_0 + \alpha V_0)P/K$ defines the time-averaged position.

With this same $\mu_k(V_r)$ and again neglecting higher orders of $\theta, d\theta_r/dt = d\theta_r^2/2dt$, eq.(4) for the hoop apparatus becomes

$$\frac{d^2\theta_r}{dt^2} + \frac{\alpha g}{\sqrt{1 + \tan^2\theta_0}} \frac{d\theta_r}{dt} + \omega^2\theta_r + \cos\theta_0 [\tan\theta_0 - (\mu_0 + \alpha V_0)] = 0 \quad (6)$$

where $\tan\theta_0 = \mu_0 + \alpha V_0$ defines the time-averaged slider position θ_0 .

While the oscillation frequency for mass-spring systems is defined

by $\omega = (K/m)^{1/2}$, in the case of the hoop apparatus the frequency is found as

$$\omega = \sqrt{\frac{g}{r} \cos \theta_0 [1 + (\mu_0 + \alpha V_0) \tan \theta_0]} = \sqrt{\frac{g}{r}} [1 + \mu_k^2]^{\frac{1}{4}} \quad (7)$$

where we have made use of the facts that $d\theta_0/dt = d\theta/dt$, and that $gr \gg V_0^2$ since $r = 7.3$ cm and $V_0 < 5$ cm/s.

From eq. (7), we can see that the hoop apparatus furnishes a 'spring' without system damping. In the particular experiments cited in this paper the hoop radius was 7.3 cm as already indicated, and for a typical value of $\mu_k \approx 0.3$ the angular frequency was $\omega \approx 11.85$ Hz. That sliding in the hoop is indeed a type of pendulum motion, can be recognized by considering the frictionless case, in which according to eq. 7 for $\mu_k = 0$ the motion is harmonic at small angles with frequency $\omega = (g/r)^{1/2}$.

Comparing eqs. (5) and (6) shows that the hoop apparatus is dynamically similar to the systems described by eq. (5) but with the following notable differences: (i) the frequency, as given by eq. (7), is independent of the slider mass, and (ii) the system is undamped ($\gamma = 0$).

Denoting

$$\left[\begin{array}{ll} \beta = \frac{\gamma + \alpha P}{2m} & \text{for general systems} \\ \beta = \frac{\alpha g}{2\sqrt{1 + (\mu_0 + \alpha V_0)^2}} & \text{for the hoop apparatus} \end{array} \right] \quad (8)$$

the general solution of eq. (5) as well as eq. (6) has the form of

$$\left[\begin{array}{ll} x(t) - x_0 = Ae^{\lambda_+ t} + Be^{\lambda_- t} & \text{if } |\beta| \neq \omega \\ x(t) - x_0 = Ae^{\beta t} + Bte^{\beta t} & \text{if } |\beta| = \omega \end{array} \right] \quad (9)$$

where A and B are determined from the initial conditions and x_0 is the time-averaged slider position, and further

$$\left[\begin{array}{l} \lambda_+ = -\beta + i\sqrt{\omega^2 - \beta^2} \\ \lambda_- = -\beta - i\sqrt{\omega^2 - \beta^2} \end{array} \right] \quad (10)$$

As can be seen from both eqs. (9) and (10), the motion of the slider depends on the relative magnitudes of the parameters. Several typical modes of motion can be identified according to relative magnitudes of the friction parameter (α) and the measuring system characteristic (ω, γ, V_0), as discussed in the next section.

III. APPLICATION OF THE EQUATIONS TO DIFFERENT MODES OF SLIDING

As an introduction to a discussion of the sliding modes described by eqs. (9) and (10), Fig. 2(b) summarizes them according to ranges of the effective damping parameter $\beta \equiv (\gamma + \alpha P) / 2m$ (eq. 8). In this analysis, corresponding to different values of λ_+ and λ_- in equation (10) (such as positive or negative, real or imaginary), $\beta \leq -\omega$ leads to stick-slip motion, $-\omega < \beta < 0$ to driven oscillation mixed with stick-slip motion, $\beta = 0$ to harmonic oscillation, $0 < \beta < \omega$ to damped oscillation, and $\beta \geq \omega$ to smooth sliding.

Fig. 3 shows some experimental examples of these modes observed in the hoop apparatus, namely (a) smooth sliding at 0.5 cm/s hoop speed and 25% humidity corresponding to the case of $\beta \geq$

ω , (b) near-harmonic motion at 2.8 cm/s hoop speed and 62% humidity i.e. approximating $\beta = 0$ for large sliding speeds, (c) stick-slip at 0.05 cm/s hoop speed and 62% humidity for $\beta < -\omega$ at small sliding speeds, (d) negative stick-slip at 0.15 cm/s in air after prolonged testing in a vacuum of 0.04 Torr, indicating $\beta > \omega$ at small sliding speeds but < 0 at large sliding speeds , and (e) irregular stick-slip. A fiber slider was used for (a) to (d) and a solid slider for (e).

The above sliding modes are in turn (through eqs. 4 and 8) related to the speed dependence of μ_k as follows:

Case 1. When μ_k is constant in cases of no system damping ($\alpha=0$ in eq.(6)), or when μ_k decreases with speed such as to counterbalance the system damping, i.e. $\alpha=-\gamma/P$ in eq.(5), parameter β vanishes. In these cases $\lambda_+=i\omega$ and $\lambda_-=-i\omega$, and the slider executes harmonic oscillations (see Fig. 3b). Thus, the only effect of a constant or slowly decreasing friction force at low system damping is to place the time-averaged position of the oscillation at $\mu_0 P/K$ from $x=0$ in the direction of substrate motion.

Case 2. When the kinetic friction coefficient μ_k increases slowly with surface speed such that $0 < \alpha < (2m\omega/P - \gamma/P)$, β is positive and $\beta^2 < \omega^2$. Then $\lambda_+ = -\beta + i(\omega^2 - \beta^2)^{1/2}$ and $\lambda_- = -\beta - i(\omega^2 - \beta^2)^{1/2}$ and the motion is that of a damped harmonic oscillator.

Case 3. If μ_k increases with speed fast enough so that $\alpha \geq (2m\omega/P - \gamma/P)$, then $\beta \geq \omega$. In this case $\lambda_+ = -\beta + (\beta^2 - \omega^2)^{1/2} < 0$ and $\lambda_- = -\beta - (\beta^2 - \omega^2)^{1/2} < 0$ (both λ_+ and λ_- are real and negative). In this case the motion is exponentially damped resulting in smooth sliding

after any excitation (see Fig. 3a) and neither the position of the slider nor the sliding speed varies with time. This mode can be understood physically since any momentary increase in surface speed is accompanied by an increase in friction force tending to decrease surface speed, and conversely any momentary decrease in surface speed causes a decrease in friction force which increases the surface speed. Thus the slider moves smoothly with a more or less constant surface speed equal to the substrate speed V_0 .

Case 4. For μ_k slowly decreasing with speed, i.e. $0 > \alpha > -(2m\omega/P - \gamma/P)$, then $0 > \beta > -\omega$. $\lambda_+ = |\beta| + i(\omega^2 - \beta^2)^{1/2}$ and $\lambda_- = |\beta| - i(\omega^2 - \beta^2)^{1/2}$. In this case the motion is that of a driven harmonic oscillator.

Case 5. For a still more rapid decrease of friction with speed, i.e. $\alpha \leq -(2m\omega/P - \gamma/P)$, then $\beta \leq -\omega$. In this case $\lambda_+ = |\beta| + (\beta^2 - \omega^2)^{1/2} > 0$ and $\lambda_- = |\beta| - (\beta^2 - \omega^2)^{1/2} > 0$, and any excitation leads to an exponential increase of both displacement and velocity.

It should be noted here that the above solutions of cases 4 and 5 are formal only, since for negative values of β the motion is unstable. Negative β values either lead to stick-slip motion (Fig. 3c) for $\beta \leq -\omega$ or to a mixture of both stick-slip and oscillation for $-\omega < \beta < 0$ [10]. This complication arises from a physical constraint, in that using the assumption of a linear decrease of μ_k , a cut-off speed is required to prevent the friction force from becoming negative. If this cut-off speed is very small the situation closely resembles the situation of $\mu_s > \mu_k(0)$, since the slider spends only a very short time interval in the low speed

region. Experimentally it is very difficult, if not impossible, to differentiate between these two situations as both are dynamically unstable [10,18].

Case 6. The final sliding mode is an unusual type of motion called "negative stick-slip" [14] in which the sample slides smoothly at a fixed position, suddenly slips to a smaller displacement, and then immediately returns to smooth sliding, an example of which is shown in Fig. 3d. This behavior is the result of a μ_k which is schematically displayed in Fig. 2c. Here friction increases with surface speed at low speeds (smooth sliding) but decreases at slightly higher and statistically achievable sliding speeds. This case of "negative stick-slip" [14] is rare but certainly not unusual. The reason is that the described type of speed dependence of μ_k as shown in an idealized form in Fig. 2c, can be caused by flow of adsorbed fluid films, most prominently moisture, about contact spots which at low speeds is viscous but transitions to shear-thinning at high speeds [14,16,19]. Similarly the condition of Fig. 2c can be caused by a speed induced transition from dry to full lubrication [17], as on occasion probably by softening of surface layers through friction heating.

IV. GENERAL CONSIDERATIONS ON STICK-SLIP MOTION

To this point the analysis has only involved the slip phase. Stick-slip motion as a whole can be treated in terms of Fig. 4 depicting a general motion trajectory $X(t)$ in which during stick episodes the slider velocity equals that of the substrate. In the

diagram of Fig. 4, the relative motion of a slip episode after a stick phase begins at $t=0$ at a displacement of X_+ , which is larger than X_0 , the time-averaged position. Inertia continues to carry the slider further upwards for a short interval to X_{\max} , where its absolute velocity vanishes, then to become increasingly negative. The maximum relative velocity is reached at the average position X_0 and then diminishes. After turning at the lowest point of the displacement curve at X_{\min} , the sample speeds up to catch up with the substrate. The velocity of the sample reaches the substrate velocity, i.e. V_r vanishes at $t=t'$, when the sample sticks to the substrate once again at a displacement of $X_s < X_0$. The observed stick-slip amplitude is thus $X_s = X_+ - X_s$.

Obviously, the slider velocity equals that of the substrate, i.e. $V_r=0$, for the duration of each stick event. Interestingly, the velocity of the slider can become larger than the substrate velocity and thus the slider can overshoot the previous sticking point where $V_r=0$, but only in the rare case of $\mu_s > 3 \mu_k$, as will be shown in the Appendix.

As long as $\mu_s(t, \infty) < 3\mu_k(V_r=0)$ so that overshooting does not occur, the slider velocity and displacement are subject to the following boundary conditions: at the stick point ($t=t'$)

$$\left[\begin{array}{l} x(A, B, t=t') = x_s \\ \frac{dx}{dt}|_{t=t'} = V_0 \end{array} \right] \quad (11a)$$

and at the separation point ($t=0$)

$$\left[\begin{array}{l} x(A, B, t=0) = x_{s.} \\ \frac{dx}{dt}|_{t=0} = V_0 \end{array} \right] \quad (11b)$$

From this analysis the total stick time is $t_s = (X_{+} - X_{-})/V_0$ and the stick-slip amplitude $X_s = V_0 t_s$.

The four equations in eq. (11) are insufficient to determine the stick-slip amplitude since there are five unknown constants: A, B, X_{+} , X_{-} , and t' . The requisite fifth equation is that X_{+} must also satisfy the force-balance equation at the separation point

$$K X_{s.} = P \mu_s(t_s) \quad (12)$$

Equation (12), in fact, describes the static friction force on the slider in the stick phase, during which $V_s = 0$. In this way the stick-slip amplitude, $X_s = (X_{+} - X_{-}) = V_0 t_s$, can be determined from eqs. (11) and (12) for a general motion trajectory, and no stick-slip will occur if the solution yields X_s equal to or larger than X_{+} .

V. STICK-SLIP AMPLITUDES AND CESSATION OF STICK-SLIP

A. Solving Equations for Linearized Kinetic Friction

To illustrate how to derive the stick-slip amplitude for a general form of $\mu_s(t_s)$, we shall consider the example of $\mu_k(V_s)$ described by eq. (4) (see also Fig. 2a) with $|\alpha| < (2m\omega/P - \gamma/P)$. This is case 2 or 4 in which the kinetic friction is a linear slowly varying function of sliding speed, so that $|\beta| < \omega$ and an analytic trajectory can be found from the equation of motion.

Accordingly, the motion is either a damped harmonic oscillation if $0 < \beta < \omega$ (case 2), or a driven oscillation if $0 > \beta > -\omega$ (case 4), while as we saw for a strong speed dependence the motion is smooth sliding for $\beta \geq \omega$ (case 3), or is unstable for $\beta \leq -\omega$ (5). With the assumption of μ_k slowly varying with velocity, the motion in the slip phase is readily solved from equation (5) or (6) as

$$\left[\begin{array}{l} x(A, B, t) - x_0 = e^{-\beta t} (A \cos \Omega t + B \sin \Omega t) \\ \frac{dx}{dt} = -e^{-\beta t} [(\beta A - \Omega B) \cos \Omega t + (\Omega A + \beta B) \sin \Omega t] \\ \text{with } \Omega = \sqrt{\omega^2 - \beta^2} \\ x_0 = \frac{P}{K} (\mu_0 + \alpha V_0) = \frac{P}{K} \mu_k(V_0) \end{array} \right] \quad (13)$$

Eq. (13) represents, of course, harmonic motion if $\beta=0$, or near-harmonic motion if $|\beta| \ll \omega$.

Applying eq. (11b) at $t=0$ (the beginning of the slip episode) to equation (13), we find

$$\left[\begin{array}{l} A = x_{s,s} - x_0 \equiv x_{s,s} - \frac{P}{K} (\mu_0 + \alpha V_0) \\ B = \frac{\beta}{\Omega} + x_{s,s} - x_0 \equiv \frac{\beta}{\Omega} + x_{s,s} - \frac{P}{K} (\mu_0 + \alpha V_0) \\ x(t) - x_0 = e^{-\beta t} [(x_{s,s} - x_0) \cos \Omega t + \frac{V_0}{\Omega} \sin \Omega t + \frac{\beta}{\Omega} (x_{s,s} - x_0) \sin \Omega t] \\ v(t) = e^{-\beta t} [V_0 \cos \Omega t - \frac{\beta}{\Omega} V_0 \sin \Omega t - (1 + \frac{\beta^2}{\Omega^2}) \Omega (x_{s,s} - x_0) \sin \Omega t] \end{array} \right] \quad (14)$$

Since $dx/dt=0$ at the first turning point, i.e. at $t=t_{\max}$, the maximum displacement $x_{\max}=x(t_{\max})$ and maximum speed $v_{\max}=v(t_{\max}+\pi/2\Omega)$ are described by

$$\left[\begin{aligned}
x_{\max} - x_0 &= \frac{e^{-\beta t_{\max}} \left[\frac{V_0^2}{\Omega} + 2 \frac{\beta^2}{\Omega^2} V_0 (x_{+s} - x_0) + \Omega \left(1 + \frac{\beta^2}{\Omega^2} \right) (x_{+s} - x_0)^2 \right]}{\sqrt{V_0^2 + \left[\frac{\beta}{\Omega} V_0 + \Omega \left(1 + \frac{\beta^2}{\Omega^2} \right) (x_{+s} - x_0) \right]^2}} \\
\text{with } ctan\Omega t_{\max} &= \frac{\beta}{\Omega} + \frac{\Omega}{V_0} \left(1 + \frac{\beta^2}{\Omega^2} \right) (x_{+s} - x_0) \\
V_{\max} &= \frac{e^{-\beta (t_{\max} + \frac{\pi}{2\Omega})} \left(1 + \frac{\beta^2}{\Omega^2} \right)}{\sqrt{V_0^2 + \left[\frac{\beta}{\Omega} V_0 + \Omega \left(1 + \frac{\beta^2}{\Omega^2} \right) (x_{+s} - x_0) \right]^2}} [V_0^2 + V_0 \beta (x_{+s} - x_0) + \Omega^2 (x_{+s} - x_0)^2]
\end{aligned} \right] \quad (15)$$

noting that x_{+s} is to be determined from eq. (12).

Similarly applying eq. (11a) at $t=t'$ (the end of the slip episode and the beginning of the stick phase) to eq. (14), we obtain

$$\left[\begin{aligned}
x_{-s} - x_0 &= - \frac{e^{-\beta t'}}{\sqrt{1 + ctan^2 \Omega t'}} \left[(x_{+s} - x_0) \left(ctan\Omega t' + \frac{\beta}{\Omega} \right) + \frac{V_0}{\Omega} \right] \\
ctan\Omega t' &= - \frac{\frac{\beta}{\Omega} (x_{+s} - x_0) + \frac{\beta}{\Omega} (x_{-s} - x_0) + \frac{\Omega}{V_0} \left(1 + \frac{\beta^2}{\Omega^2} \right) (x_{+s} - x_0) (x_{-s} - x_0) + \frac{V_0}{\Omega}}{x_{+s} - x_{-s}}
\end{aligned} \right] \quad (16)$$

Here $\pi \leq \Omega t' \leq 2\pi$ because sticking can occur only after turning at the point when $t=t_{\min}$.

Ideally, x_{+s} in eq. (16) and shown in Fig. 4 should be expressed in terms of x_{+s} , which in turn can be determined from eq. (12). But as one can see from eq. (16), it is very difficult, if not impossible, to obtain an explicit expression for x_{+s} , except in the following cases.

1. In harmonic oscillation, $\beta=0$ (see Fig. 2), $x_{-s} - x_0 = -(x_{+s} - x_0)$ by symmetry, and the same solution will approximately hold for near harmonic oscillation when $|\beta| \ll \omega$.

2. For any value of β , we can see from eq.(15) that when $V_0 \rightarrow 0$ or $V_0 \ll V_{\max}$, it is $X_{+} \rightarrow X_{\max}$, meaning $\Omega t' \rightarrow \pi$ ($t_{\max} \rightarrow 0$) and there is all stick-slip.

3. Similarly, when $V_0 \rightarrow V_{\max}$, $X_{+} \rightarrow X_0$ meaning $\Omega t' \rightarrow 2\pi$, lead to near extinction of stick-slip.

Thus, from eq.(16), we obtain

$$\left[\begin{array}{ll} x_{-s} - x_0 = - (x_{+s} - x_0) & \text{if } |\beta| < \omega \text{ (for any } V_0) \\ x_{-s} - x_0 = - (x_{+s} - x_0) e^{-\frac{\beta\pi}{\omega}} & \text{if } V_0 \rightarrow 0 \text{ (full stick-slip)} \\ x_{-s} - x_0 = - (x_{+s} - x_0) e^{-\frac{2\beta\pi}{\omega}} & \text{if } V_0 \rightarrow V_m \text{ (near no stick-slip)} \end{array} \right] \quad (17)$$

B. Graphical Determination of the Stick-Slip Amplitude

Calculating the stick-slip amplitude ($X_s = X_{+s} - X_{-s}$) is still not trivial, since a specific form of static friction as a function of stick time, $\mu_s(t_s)$, has to be supplied. Appropriate forms of $\mu_s(t_s)$ can be quite diverse, depending on the assumptions and the specific experimental conditions [2,12,13,20-27]. As an example, Fig. 5 shows experimental curves of μ_s as a function of stick time for a gold-plated copper fiber sample sliding in a gold-plated copper hoop in an atmosphere of humid nitrogen. The interesting feature here is that the initial rate of increase of μ_s apparently rises with increasing applied load. This is in accord with a theoretically developed model which takes the size of contact spots into consideration [2].

At any rate, both theories and experimental observations

[2,12,13,20-27] indicate that the static friction coefficient initially increases rapidly with stick time and then levels off asymptotically at long periods of stick, as depicted in Fig. 6. On this basis, we can draw quantitative conclusions regarding the stick-slip amplitude by making use of eq. (17) to obtain

$$\left[\begin{array}{l} x_s \equiv x_{.s} - x_{-s} = (x_{.s} - x_0) (1 + e^{-\beta t'}) \\ \text{namely } x_{.s} = x_0 + \frac{x_s}{1 + e^{-\beta t'}} \end{array} \right] \quad (18)$$

and with the aid of eq. (12) to arrive at

$$\left[\begin{array}{l} \frac{K}{P(1 + e^{-\beta t'})} x_s = \mu_s(x_s) - \mu_k(V_0) \\ \text{Namely } \frac{K V_0}{P(1 + e^{-\beta t'})} t_s = \mu_s(t_s) - \mu_k(V_0) \end{array} \right] \quad (19)$$

recalling again that $KX_0 = P\mu_k(V_0)$, $\Omega t' \rightarrow \pi$ for $V_0 \ll V_{\max}$ (full stick-slip), and $\Omega t' \rightarrow 2\pi$ for $V_0 \rightarrow V_m$ (near extinction of stick-slip).

For a given dependence of μ_s on stick time in a general functional form, the stick-slip amplitude can now be obtained graphically from eq. (19) by plotting the left side of the equation as a function of X_s (or t_s) which is a straight line with a constant slope, and by plotting the right side of the equation on the same figure, as shown in Figure 6. The point of intersection, if any, gives X_s (or t_s), and hence the stick-slip amplitude, $X_s = V_0 t_s$.

C. Cessation of Stick-Slip

As can be seen from Fig. 6(a), at a given substrate speed, increasing K (the stiffness of the spring) rotates the straight

line counter-clockwise. Consequently, the point of intersection, if present, moves toward the origin of the coordinate system, indicating a decreasing stick-slip amplitude. At a critical value of K the two curves meet only at the origin, leading to a zero stick-slip amplitude and indicating cessation of stick-slip for larger values of K .

Similarly, increasing the substrate speed reduces the stick-slip amplitude. Physically, this is because stick times shorten progressively and there is less time for μ_s to increase. Mathematically, a larger substrate speed increases the slope of the straight line when using t_s as the variable instead of x_s , as shown in Fig. 6(b). Since μ_s saturates more or less after, say t_{ss} , we find $\mu_s(t_{ss}) \approx \mu_s(t_{\infty})$. Therefore, from eq. (19), the maximum stick-slip amplitude $x_{ss} = V_0 t_{ss} = (P/K) (1 + e^{-\frac{\pi \beta}{\sqrt{\omega^2 - \beta^2}}}) [\mu_s(t_{\infty}) - \mu_k]$, will be affected very little by substrate speed if $V_0 < V_{ss}$. This, therefore is named the saturation speed, and is defined by

$$V_{ss} = \frac{x_s}{t_{ss}} \approx \frac{P}{K t_{ss}} \left(1 + e^{-\frac{\pi \beta}{\sqrt{\omega^2 - \beta^2}}} \right) [\mu_s(t_{\infty}) - \mu_k] \quad (20)$$

because the stick time t_s for a substrate speed less than V_{ss} is larger than t_{ss} . For $V_0 > V_{ss}$, however, the stick-slip amplitude decreases with rising substrate speed until a critical substrate speed, V_c . Above V_c stick-slip motion ceases.

This critical substrate speed can be determined as follows: As can be seen from Figs. 5 and 6, the slope of the μ_s curve has it's maximum for $t_s \rightarrow 0$, while the straight line has a constant slope.

Therefore the two curves will intercept only if

$$\left[\begin{array}{l} \text{Namely} \quad \frac{K}{P(1+e^{-\beta t'})} \leq \frac{\partial \mu_s}{\partial x_s} \Big|_{x_s=0} \\ \frac{KV_0}{P(1+e^{-\beta t'})} \leq \frac{\partial \mu_s}{\partial t_s} \Big|_{t_s=0} \end{array} \right] \quad (21)$$

Here, equality of the two terms of each equation represents a trivial solution of $x_s=0$ (zero stick-slip amplitude). Physically, this defines a critical substrate velocity above which no stick-slip occurs. As shown previously, $t'=2\pi/\Omega$ when stick-slip is near extinction. Thus, the critical speed is obtained as

$$V_c = \frac{P}{K} (1+e^{-\frac{2\pi\beta}{\sqrt{\omega^2-\beta^2}}}) \frac{\partial \mu_s}{\partial t_s} \Big|_{t_s=0} \quad (22)$$

As may be deduced from Fig. 3, this critical speed is on the order of 1 cm/s in the case of the hoop apparatus tests, and depends on humidity, load, and type of slider.

VI. COMPARISON WITH EXPERIMENTS

Based on eqs. (19), (20) and (22), and the above discussion the stick-slip amplitude stays essentially constant as the substrate speed increases from zero to V_{∞} and then decreases until the extinction of the stick-slip motion as the substrate speed approaches V_c . Experimentally, the occurrences of both V_{∞} and V_c have been reported in the literatures [2,13-17,26,28]. In particular, experiments using the hoop apparatus at different loads and humidities (Fig. 7a), experiments reported in ref. 17 with a

pin-on-disk type system for different spring constants (Fig. 7b), and experiments of ref. 13 using a block-on-flat for different lubricants (Fig. 7c) show the same features as our theoretical deductions. Further, eq. (22) has been empirically determined and experimentally verified by Eguchi and Yamamoto [13] under lubricated conditions for different surface geometries. Clearly from eqs. (19), (20) and (22), the stick-slip amplitude, critical speed and saturation speed all depend on the details of the experimental parameters and the static and kinetic friction properties.

Also, the effects of the damping ($\beta > 0$) or pumping ($\beta < 0$) on the stick-slip amplitude can be understood, specifically via eq. (19). In the case of $\beta > 0$ (damping) in which μ_k increases with speed slowly or decreases with speed too slowly to cancel the damping term, the effects are two-fold. First, the slope of the straight line in Fig. 6 is increased, resulting in a smaller stick-slip amplitude. Second, the difference between μ_s and $\mu_k(V_0)$ is smaller, also resulting in a diminished stick-slip amplitude. In the case of $\beta < 0$ (pumping), by contrast, the effects are the opposite, namely resulting in a larger stick-slip amplitude. Thus, from the relation of $\beta = (\gamma + \alpha mg)/2m$, we can see that $d\mu_k/dV = \alpha < 0$ is only one of the cases which will induce stick-slip motion. Indeed, even $d\mu_k/dV \geq 0$ may cause stick-slip motion as long as eq. (21) is satisfied.

In this manner eqs. (19) to (22) explain why, in practice, increasing the spring stiffness, substrate speed, and/or system

damping, not only reduces the stick-slip amplitude but also can completely eliminate stick-slip motion, as in the observation related by Rabinowicz [17].

Finally, two limiting cases are worth noting. (1) If there is no difference between static and kinetic friction, as would be represented by a horizontal line coinciding with the stick time axis in fig. 6b, regular stick-slip motion cannot occur since equation (21) cannot be satisfied. (2) If μ_s is constant but higher than μ_k , meaning a discontinuity of μ , or a positive infinitely large slope at $t_s=0$, equation (21) is always satisfied, but stick-slip cannot occur unless the slip speed becomes equal to the substrate velocity. In that case, the motion may be smooth or oscillatory sliding without any sticking while $V_r \neq 0$, and the motion is independent of the properties of μ_s .

VII. CONCLUSIONS

By means of a dynamic analysis, a complete set of five equations has been derived which describe the stick-slip motion for an arbitrary slip trajectory. Different slip behaviors including commonly observed stick-slip motion result, depending on speed dependence of the kinetic friction and time dependence of the static friction.

Assuming a linear speed dependence of the kinetic friction, equations describing slider trajectory in slip phases for a spring-mass system and for the hoop apparatus have been obtained analytically from the equation of motion. The sliding modes are

controlled by the effective damping coefficient β (eq. 8). Smooth sliding occurs for large positive β values, damped harmonic motions for small positive β values, harmonic oscillations for vanishing β , driven harmonic oscillations for small negative β values, and unstable sliding (leading to stick-slip) for large negative β values.

For modes other than smooth sliding and for a general static friction function $\mu_s(t_s)$, an equation has been derived for calculating the stick-slip amplitude in terms of substrate speed, system frequency and damping, and kinetic and static friction. Based on that equation, the critical speed V_c above which no stick-slip occurs, and the saturation speed V_{s_0} below which the stick-slip amplitude is almost independent of the substrate speed have also been determined. Starting at V_{s_0} , depending on the details of $\mu(t_s)$, the stick-slip amplitude decreases with increasing substrate speed until the extinction of stick-slip motion at V_c .

Further, a condition (eq. A3) for which the slider may slip over the previous stick point has been determined as given in the appendix. Visually, such a slippage may occur only when the stick episode traverses at least the free spring equilibrium position.

This paper has also shown that stick-slip motion does not necessarily occur even if static friction is larger than kinetic friction. Rather it depends on detailed experimental parameters such as sliding speed, spring stiffness, and system damping. Above all, stick-slip depends on $d\mu_s/dt$, i.e. the rate at which μ_s increases with stick time above its' initial value of μ_k . This

growth rate, in turn, depends on specific sliding conditions such as sliding materials, lubrication, contamination, environment, surface roughness, etc. In addition to the case of a rapidly decreasing μ_k with speed V , stick-slip also may occur even if μ_k increases with speed. In this regard, the system damping γ acts as a positive component of $d\mu_k/dV$ which can be, in effect, added to the linear term of $\mu_k(V)$ as shown in eq. (8).

The predictions of this analysis are fully consistent with a wide range of observations on stick-slip amplitude, sliding modes, critical and saturation speeds, not only of this research group but also others, conducted over a wide range of experimental conditions. Correspondingly, the equations presented in this analysis are confidently expected to be widely useful for understanding and controlling the different aspects of stick-slip motion in terms of both friction and system properties.

ACKNOWLEDGMENT

The financial support of this research through the Materials Division (P. Schmidt and M. B. Peterson, Tribology) of the Office of Naval Research, Arlington, VA is gratefully acknowledged.

APPENDIX

It has been stated in the text that the velocity of the slider can become larger than the substrate velocity and thus the slider can overshoot the previous sticking point where $V_r=0$, but only in the rare case of $\mu_s > 3 \mu_k$. This is so because static friction provides a constraining force which is equal and opposite to the spring force during stick but does not come into action until V_r vanishes. Normally, at the onset of stick no net force acts on the slider resulting in no acceleration or deceleration, and sticking occurs when the velocity of the slider increases to the substrate velocity, i.e. when $V_r=0$.

However, in cases of $\mu_s > 3 \mu_k$, the sample can overshoot the stick point where $V_r=0$. As a simple example of this concept consider the case of harmonic oscillation, when $\beta=0$ or when μ_k is constant in the absence of system damping (case 1 of the previous section): By symmetry the difference in displacement between the separation (slip) point and the time-averaged position is the same as that between the stick point and the time-averaged position, i.e. $X_{+,-} - X_0 = -(X_s - X_0)$. Noting that $KX_0 = P\mu_k$ from eq.(5) and $KX_{+,-} = P\mu_s(t_s)$ at the separation point, we have

$$\mu_s(t_s) + \frac{KX_{-s}}{P} = 2\mu_k \quad (A1)$$

In regard to the position of the stick point, two cases need to be distinguished. (i) The case of sticking at a negative displacement, i.e. $X_s < 0$, if the restoring force of the spring is larger than the static friction at the instant of stick, i.e. if

$$-KX_s > P\mu_s(t_s=0) \quad (A2)$$

the slider is accelerated toward the spring equilibrium with a velocity larger than the substrate velocity. (ii) For a positive stick point position, i.e. for $X_s \geq 0$, slippage at the stick point requires that $KX_s > P\mu_s(t_s=0)$. This, however, is not possible because it is equivalent to requiring at least $\mu_k > \mu_s(0)$, since $KX_s < KX_0 = P\mu_k$, leading to no stick-slip. Combining eqs. (A1) and (A2) the condition for the slider velocity exceeding the substrate velocity at the "stick" point becomes

$$\mu_s(t_s) - \mu_s(0) > 2\mu_k \quad (A3)$$

This can occur only when the motion during the stick episode at least includes the free spring equilibrium position. Assuming $\mu_s(0) = \mu_k$ Eq. (A3) may be simply expressed as $\mu_s > 3\mu_k$ [12], which is highly unlikely.

REFERENCES

1. Brockley, C. A., Cameron, R., and Potter, A. F., "Friction Induced Vibration", Journal of Lubrication Technology, April, 1967, pp.101-108.
2. Gao, C., Kuhlmann-Wilsdorf, D., and Makel, D. D., "Fundamentals of Stick-Slip", WEAR, in the press.
3. McClelland, G. M., and Mate, C., "Atomic Scale Friction Measured with an Atomic Force Microscope", Engineered Materials for Advanced Friction and Wear Applications, P. J. Blau and F. Smidt, Eds., ASM Intl., Metals Park, OH, 1988, pp.13-22.
4. Bowden, F. P. and D. T. Tabor, "The Friction and Lubrication of Solids", Clarendon Press, Oxford, 1986.
5. Khurana, K., Physics Today 41 (5), 1988, p. 17.
6. Skalmierski, B., "The Construction of Old Italian Violins: Tentative Explanation", Bull. Acad. Polonaise Sci. (techniques) 29, 1981, pp.175-181.
7. Li, Z., E. Rabinowicz and N. Saka, "The Stiction Between Magnetic Recording Heads and Thin Film Disks", Tribology and Mechanics of Magnetic Storage Systems, STLE SP-26, 1989, pp.64-70.
8. Bowden, F. P. and Tabor, D., "Friction-An Introduction to Tribology", Anchor Press/Doubleday, New York, 1973, pp.68-71.
9. Galton, G., "The Action of Brakes: On the Effect of Brakes upon Railway Trains", Engng 25, 1878, pp.469-472.
10. Andronow, A.A. and Chaikin, C.E., "Theory of Oscillations",

Princeton University Press, 1949, p.161.

11. Popp, K. and Stelter, P., "Stick-Slip Vibrations and Chaos", Phil. Trans. R. Soc. Lond. A332, 1990, pp.89-105.
12. Sampson, J.B., Morgan, F., Reed, D.W., and Muskat, M., "Studies in Lubrication; XII. Friction Behavior During the Slip Portion of the Stick-Slip Process", J. of Applied Physics, 14, 1943, pp.689-700.
13. Eguchi, M. and Yamamoto, T., "Effect of Surface Geometry on Relationship Between Static Friction and Stationary Contact Time in Stick-Slip Oscillation.", Proceeding of the Japanese Society of Lubrication Engineering, July, 1985, Tokyo, Japan, pp.1053-1058.
14. Gao, C., and Kuhlmann-Wilsdorf, D., "On Stick-Slip and the Velocity Dependence of Friction at Low Speeds", Trans. ASME, J. of Tribology, 112, 1990, pp.354-360.
15. Gao, C. and Kuhlmann-Wilsdorf, D., "Adsorption Films, Humidity, Stick-Slip and Resistance of Sliding Contacts", ICEC-IEEE (1990 Holm Conf. on Electrical Contacts, IEEE, Montreal, Aug. 20-24, 1990, IEEE, Piscataway, NJ 08855-1331), pp.292-300. Also in IEEE Trans. Components Hybrids and Manufacturing Technology, 14, 1991, pp. 37-44.
16. Gao, C., Kuhlmann-Wilsdorf, D., and Makel, D. D., "Moisture Effects Including Stiction Resulting from Adsorbed Water Films" ASME J. of Tribology, 114, 1992, pp.174-180.
17. Rabinowicz, E., "Friction and Wear of Materials", Wiley & Sons, Inc., 1965.

18. Karnopp, D., "Computer Simulation of Stick-Slip Friction in Mechanical Dynamic Systems", Transactions of ASME, 107, 1985, pp.100-103.
19. Heyes, D. M., "Some Physical Consequences of Large Shear Rates on Simple Liquids", J. Chem. Phys. 85, 1986, pp.997-1008.
20. Derjagin, B. V., Push, V. E., and Tolstoi, D. M., "A Thoery of Stick-Slip Sliding of Solids", Proc. Conf. Lubrication and Wear, Oct. 1957. p.265.
21. Howe, P. H., Benton, D. P., and Puddington, I. E., "London-Van der Waals Attractive Forces Between Glass Surfaces", Canadian J. of Chemistry, 6, 1955, p.1375.
22. Kosterin, J. I. and Kraghelsky, I. V., "Relaxation Oscillation in Elastic Friction Systems", Friction and Wear in Machinery, 12, 1962, p.111.
23. Bowden, F. P. and Tabor, D., "The Friction and Lubrication of Solids", Part II, Oxford, 1965, pp. 338-340.
24. Brockley, C. A. and Davis H. R., "The Time-Dependence of Static Friction", Journal of Lubrication Technology, Jan. 1968, pp.35-41.
25. Gao, C. and Kuhlmann-Wilsdorf, D., "Experiments on, and a Two-Component Model for, the Behavior of Water Nano-Films on Metals", MRS Symposium Proc., 188, M. F. Doerner, W. C. Oliver, G. M. Pharr and F. R. Brotzen, Eds., Mater. Res. Soc., Pittsburgh, PA, 1990.
26. Burwell, J. T. and Rabinowicz, E., "The Nature of the Coefficient of Friction", J. Applied Physics, 24(2), 1953,

pp.136-139.

27. Kato, S., Sato, N., and Matsubayashi, T., "Some Considerations on Characteristics of Static Friction of Machine Tool Slideway ", ASME, J. of Lubrication Technology, July, 1972, pp.234-247.
28. Gee, M. L., McGuiggan, P. M., and Israelachvili, "Liquid to Solidlike Transitions of Molecularly Thin Films under Shear", J. Chem. Phys., 93(3), 1990, pp.1895-1906.

FIGURE CAPTIONS

Figure 1. Schematic diagrams for the dynamics of (a) the hoop apparatus; (b) the pin on disc device [adapted from ref. 17, Fig. 4.38]; (c) the surface force apparatus [adapted from ref. 28, Fig. 2]. K , γ , and V_0 (or V) are the spring constant, the damping coefficient, and the substrate velocity, respectively.

Figure 2 (a) Schematic graph indicating the range of the static friction coefficient, and a linear dependence of the kinetic friction coefficient (μ_k) on the relative velocity (V_r) between sample (V) and substrate velocity V_0 . Note that the static friction coefficient $\mu_s(V_r=0)$ rises with stick time t , and that a positive sample velocity ($V=dx/dt$) decreases V_r by $-dx/dt$.

Figure 2 (b) Parameter diagram. Under the assumption of the linear speed dependence shown in (a), the five indicated sliding modes will be observed depending on the parameter $\beta \equiv (\gamma + \alpha P)/2m$ in all friction measuring systems shown in Figure 1.

Figure 2 (c) As Fig. 2(a) but showing a bilinear dependence of the kinetic friction coefficient (μ_k) on the relative velocity (V_r).

Figure 3. Experimental traces of $\mu(t)$ under different conditions, all for a gold-plated copper fiber slider on gold-plated copper in the hoop apparatus, except for 3(e) which refers to a solid slider. (a) Smooth sliding at 0.5 cm/s hoop speed and at 25% humidity, corresponding to the case of $\beta \geq \omega$. (b) Nearly harmonic oscillation at 2.8 cm/s hoop speed and 62% humidity, i.e. approximating $\beta = 0$ for large speeds. (c) Stick-slip motion at

0.05 cm/s hoop speed and 62% humidity, meaning $\beta < 0$ for small speeds. (d) Negative stick-slip at 0.15 cm/s hoop speed and in air immediately after a prolonged testing in a vacuum of 0.04 Torr, indicating $\beta > \omega$ at small sliding speeds but < 0 at large sliding speeds. (e) Irregular stick-slip motion of a solid slider at 0.15 cm/s hoop speed and 68% humidity. The load was 0.5 N in all cases.

Figure 4. Schematic illustration of the displacement and velocity in stick-slip motion.

Figure 5. Experimental data for $\mu_s, -\mu_k$ as a function of stick time for three different applied loads as indicated.

Figure 6. Graphical method for finding the stick-slip amplitude, x_s , if the time dependence is known (shown here of the type in Fig. 5, also see Fig. 4.42 in ref. 9), according to equation (19). Fig. 6(a) The value of x_s at the intercept gives the stick-slip amplitude. Fig. 6(b) The value of t_s at the intercept gives the stick-slip amplitude via $x_s = V_0 t_s$.

Figure 7. Experimental stick-slip amplitude as a function of substrate speed, (a) in the hoop apparatus at different humidities and loads, (b) in a pin-on-disk type device for different spring constants according to ref. 17 (Fig. 4.44), and (c) in a block-on-flat type system for different lubricants according to ref. 13 (Fig. 6). Note the saturation speed V_{s0} (eq. 20) below which the stick-slip amplitude is nearly constant, and the critical speed V_c (eq. 22) above which the stick-slip amplitude is practically zero, all of course, depending on the detailed experimental conditions.

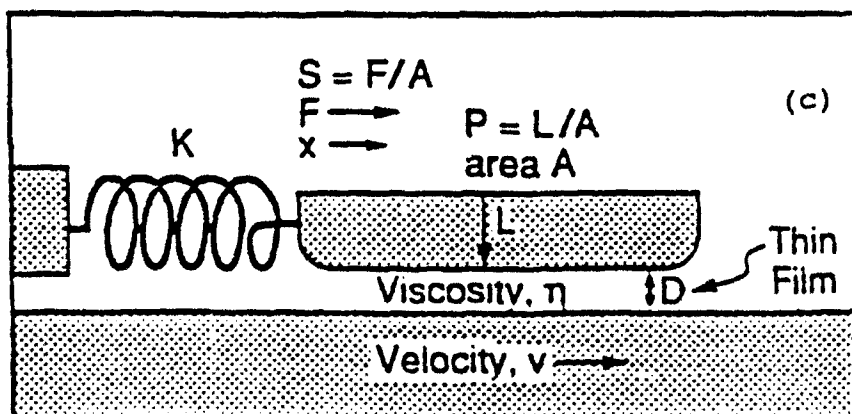
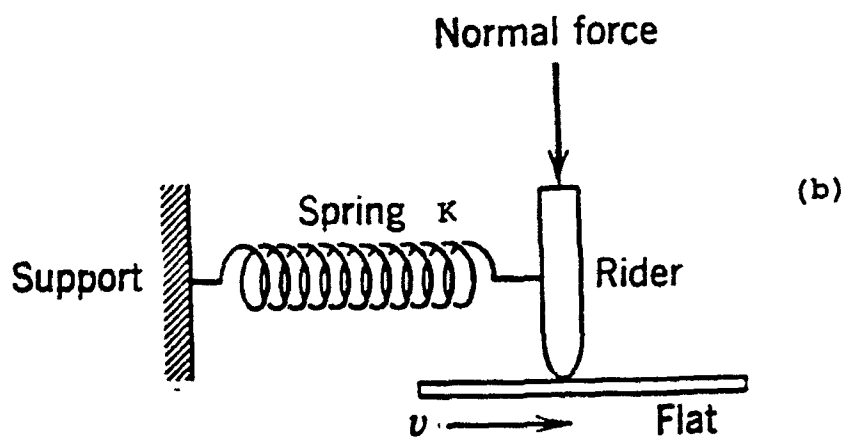
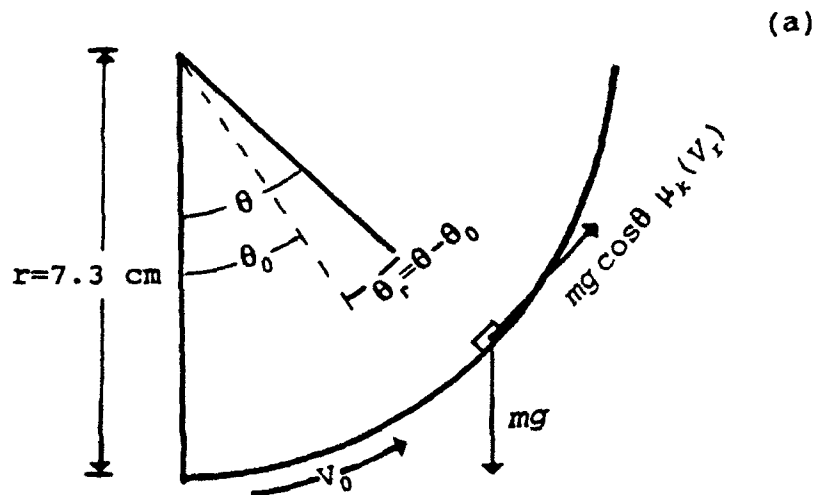


Figure 1

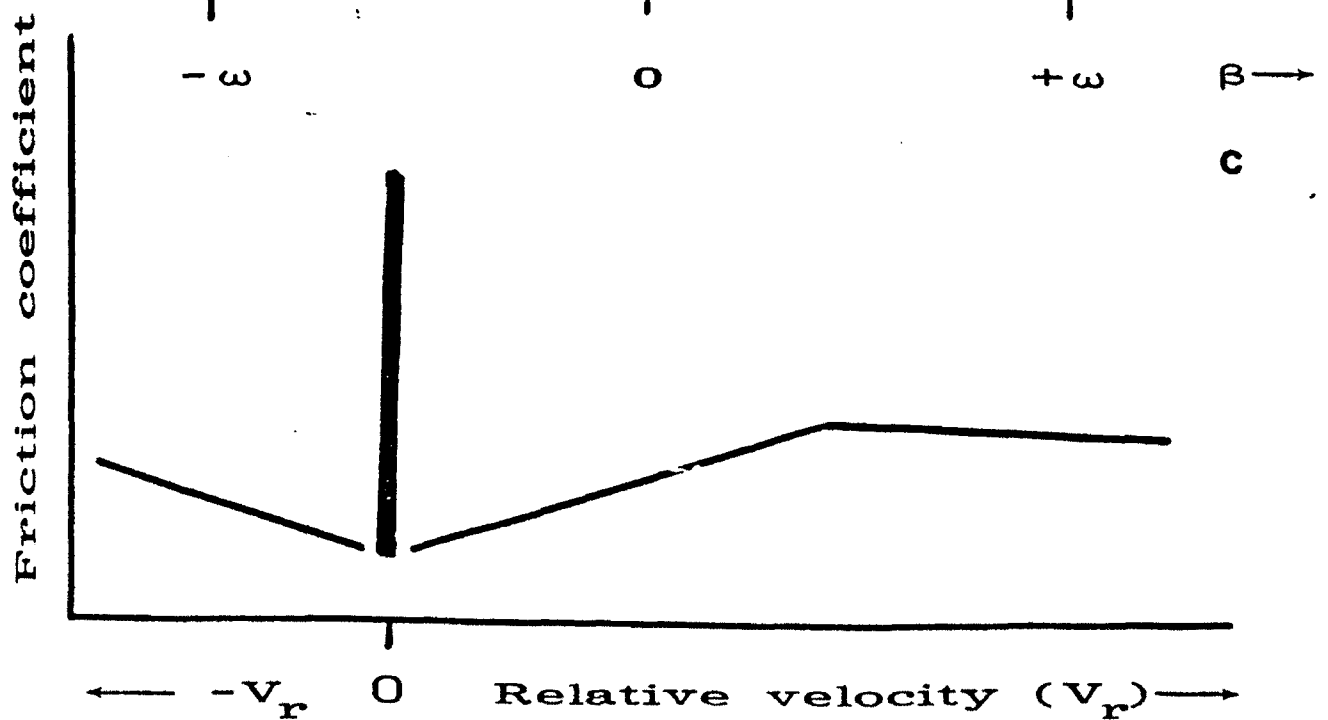
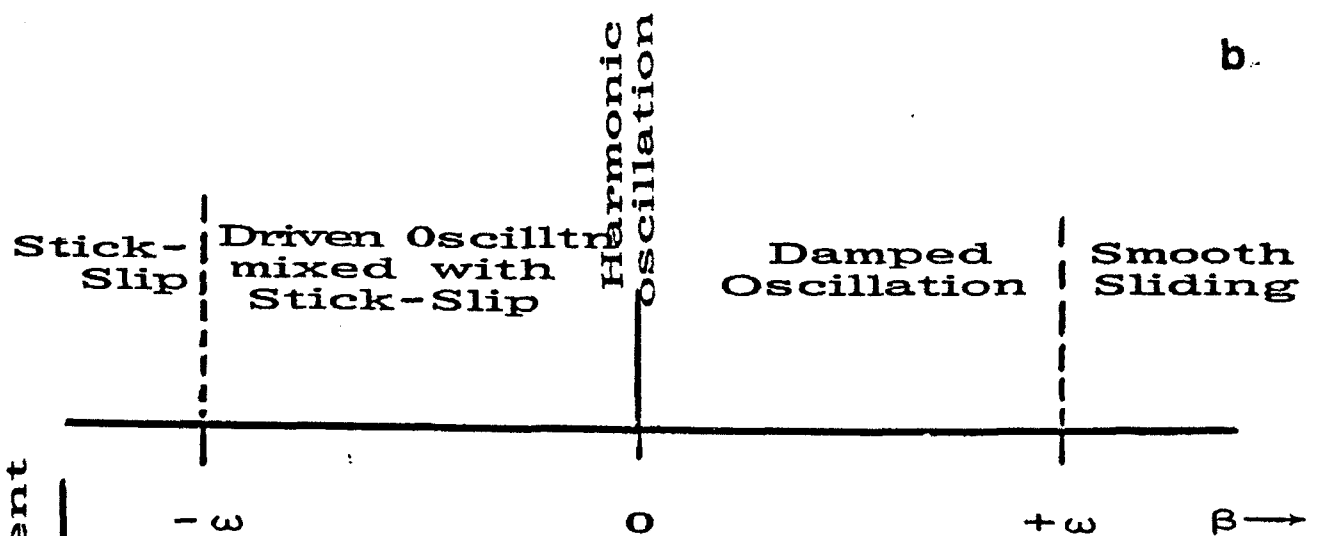
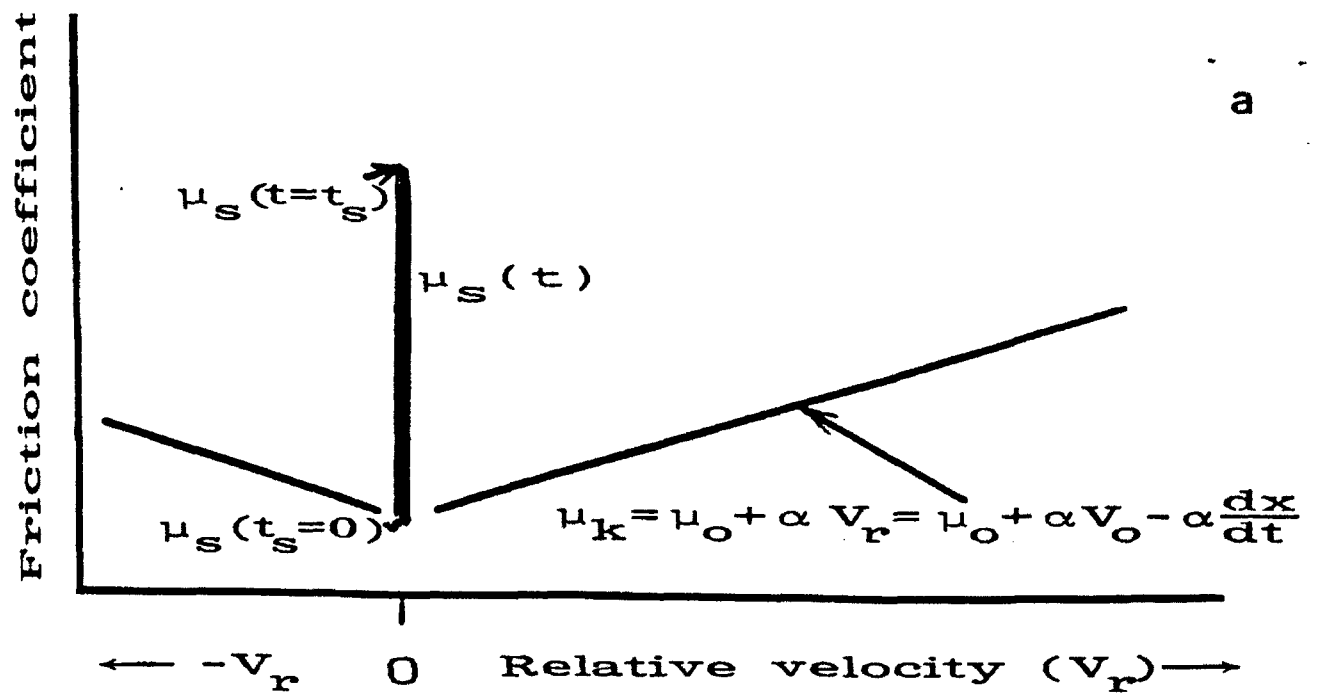
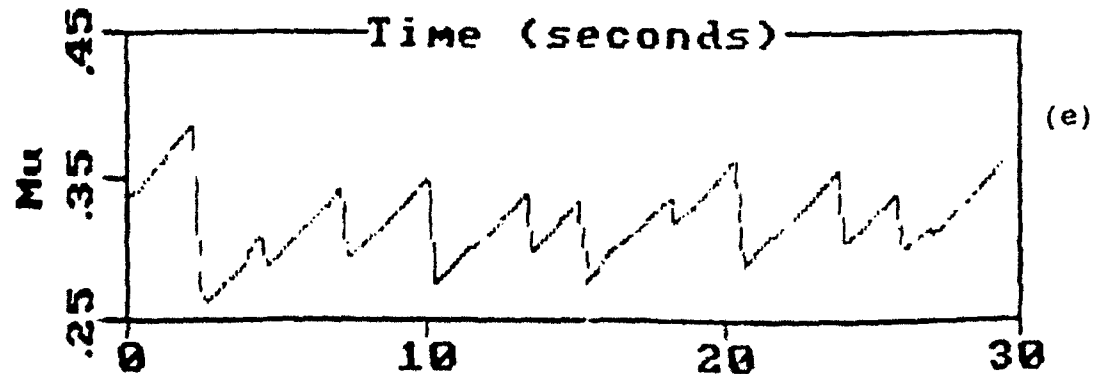
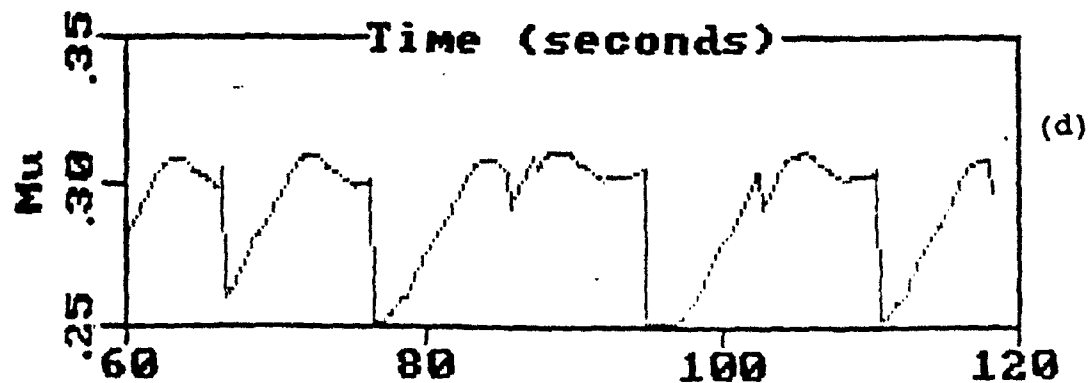
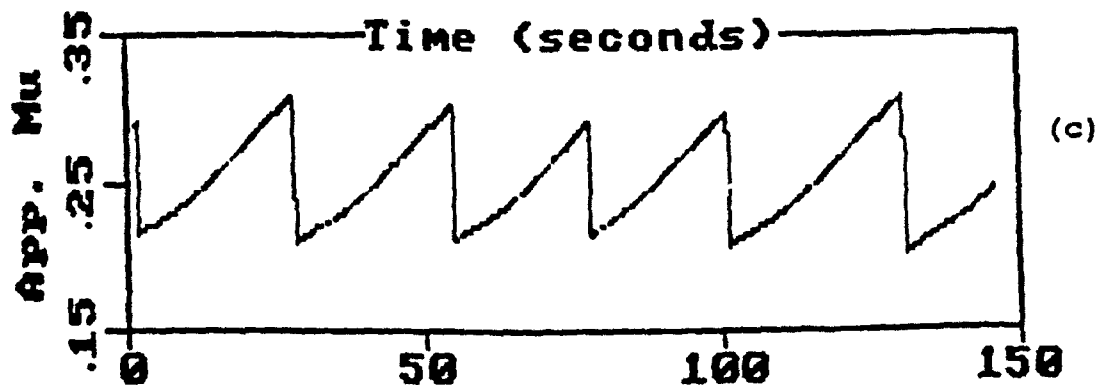
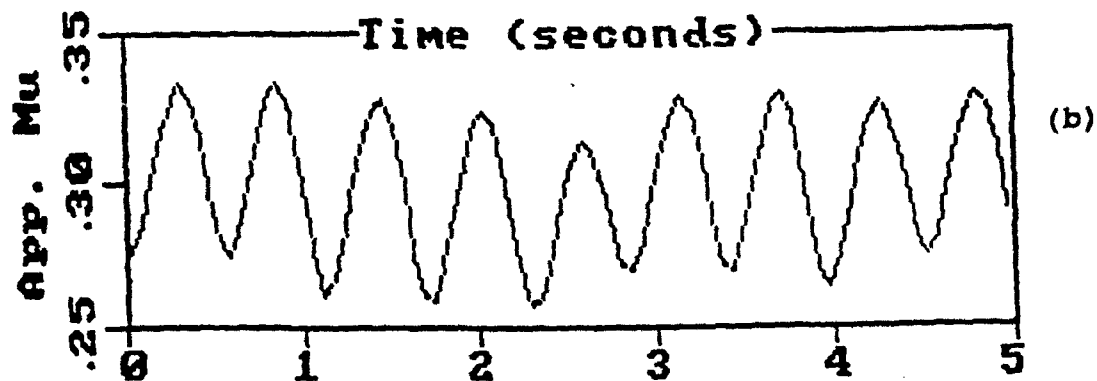
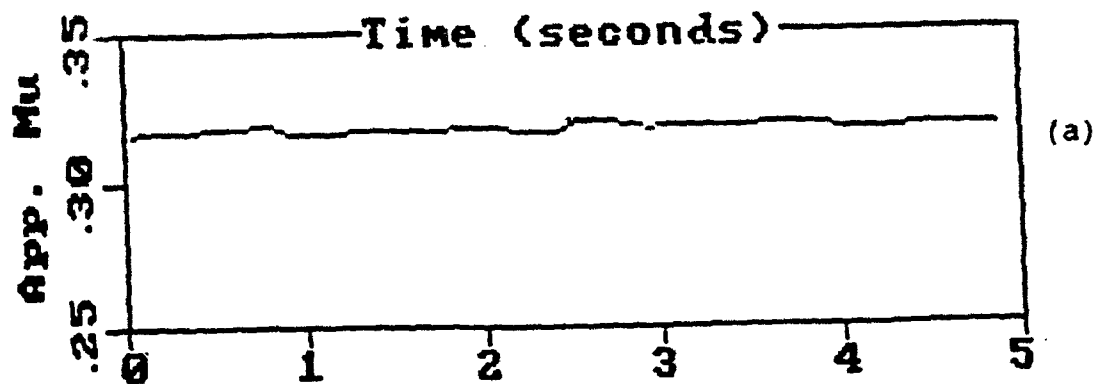


FIG. 2



Figure

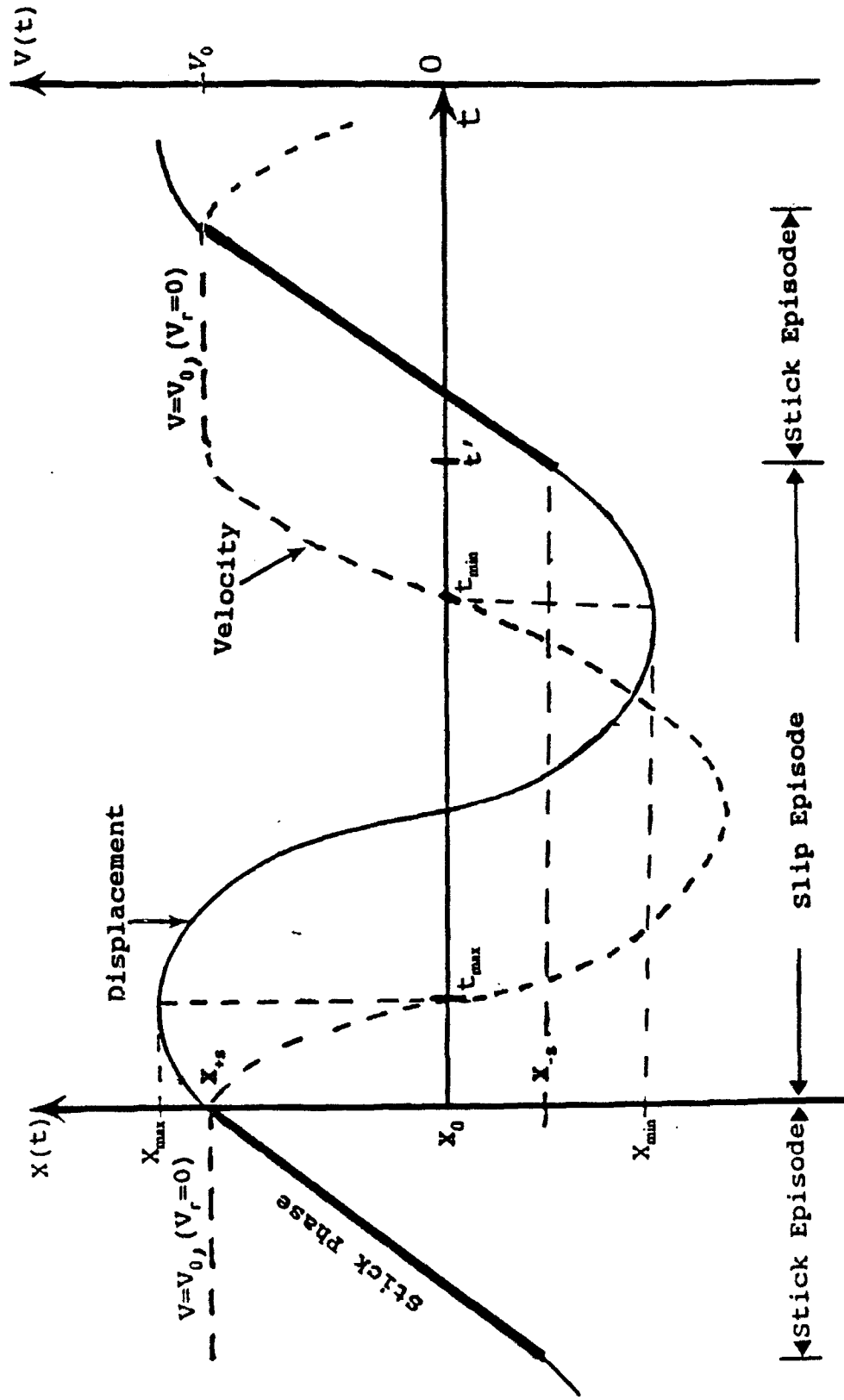


Figure 4

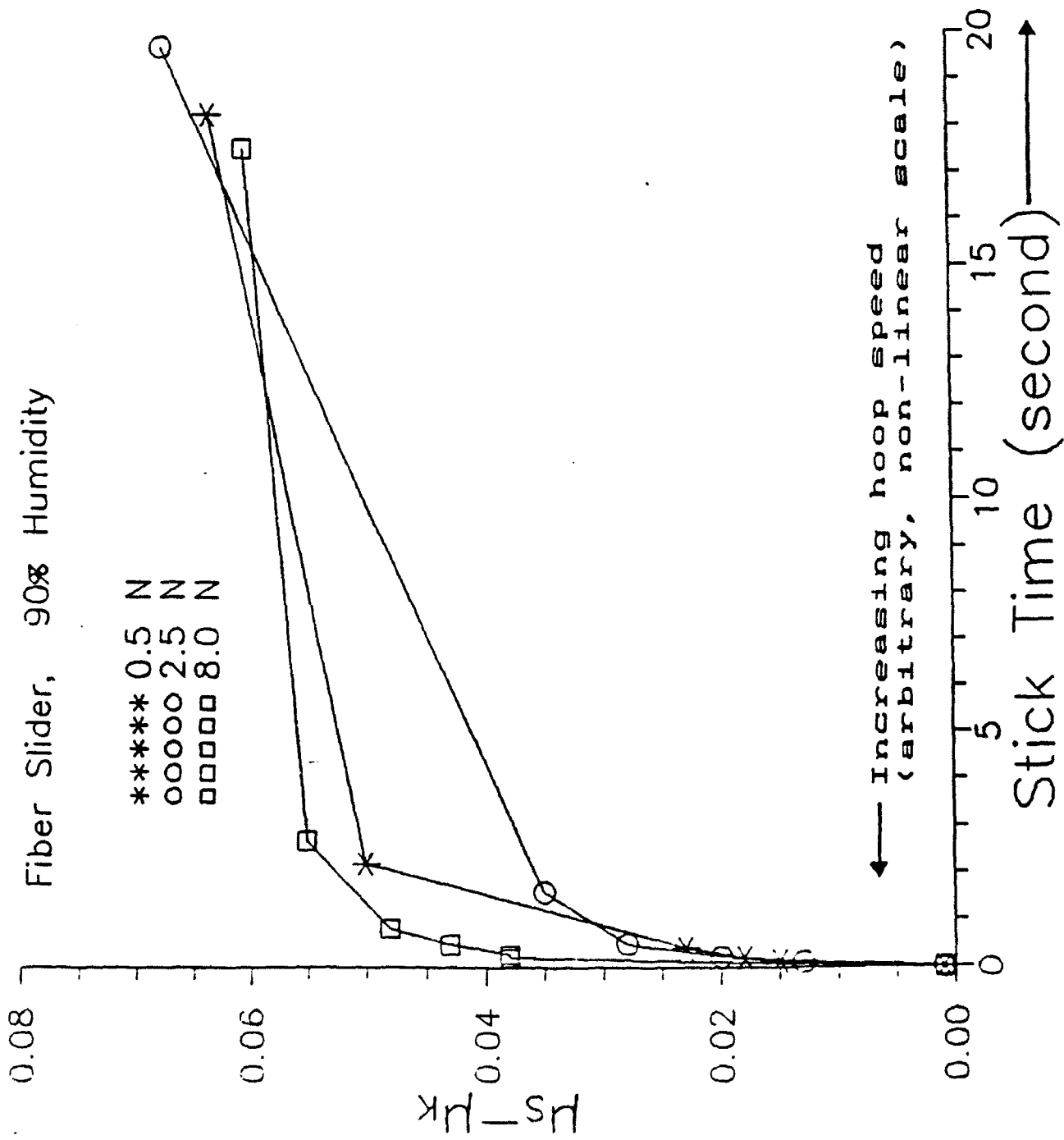
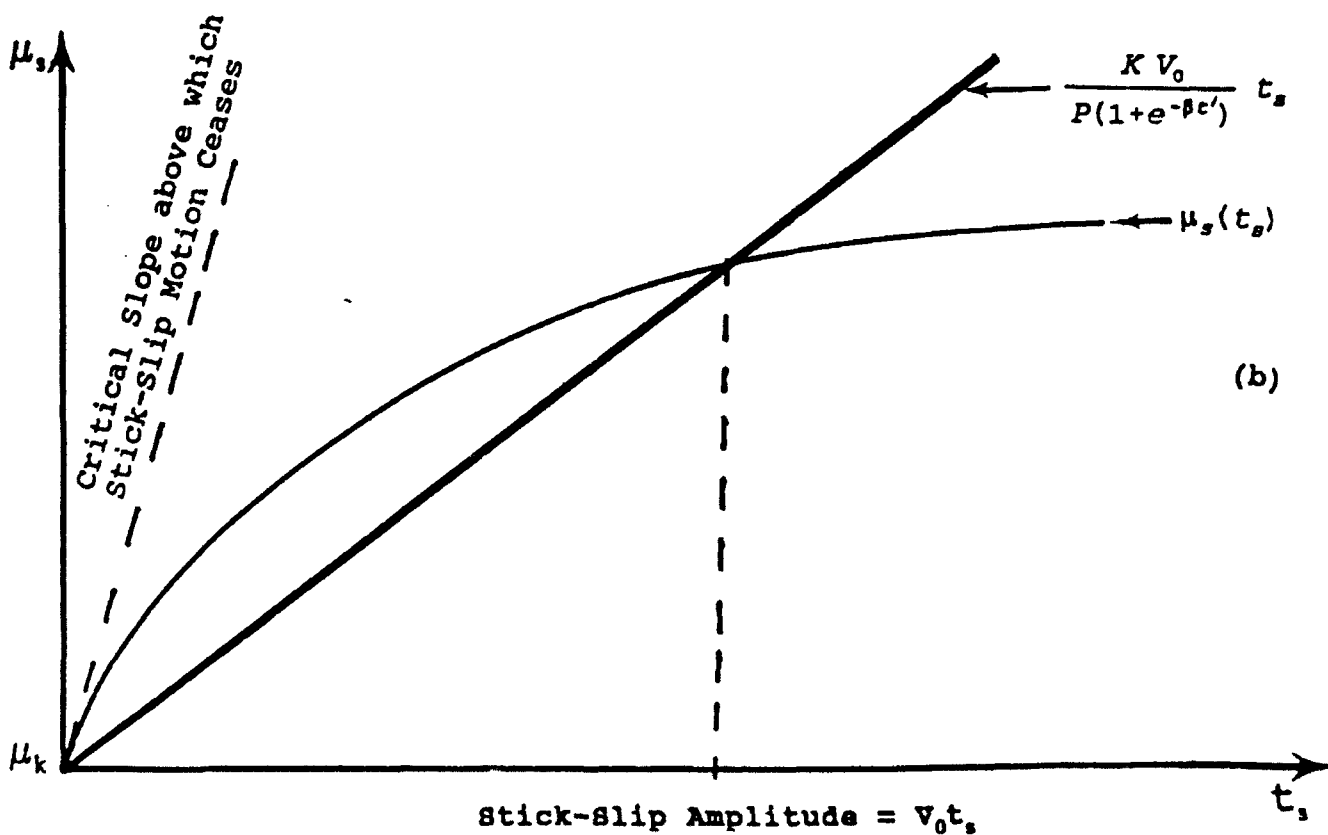
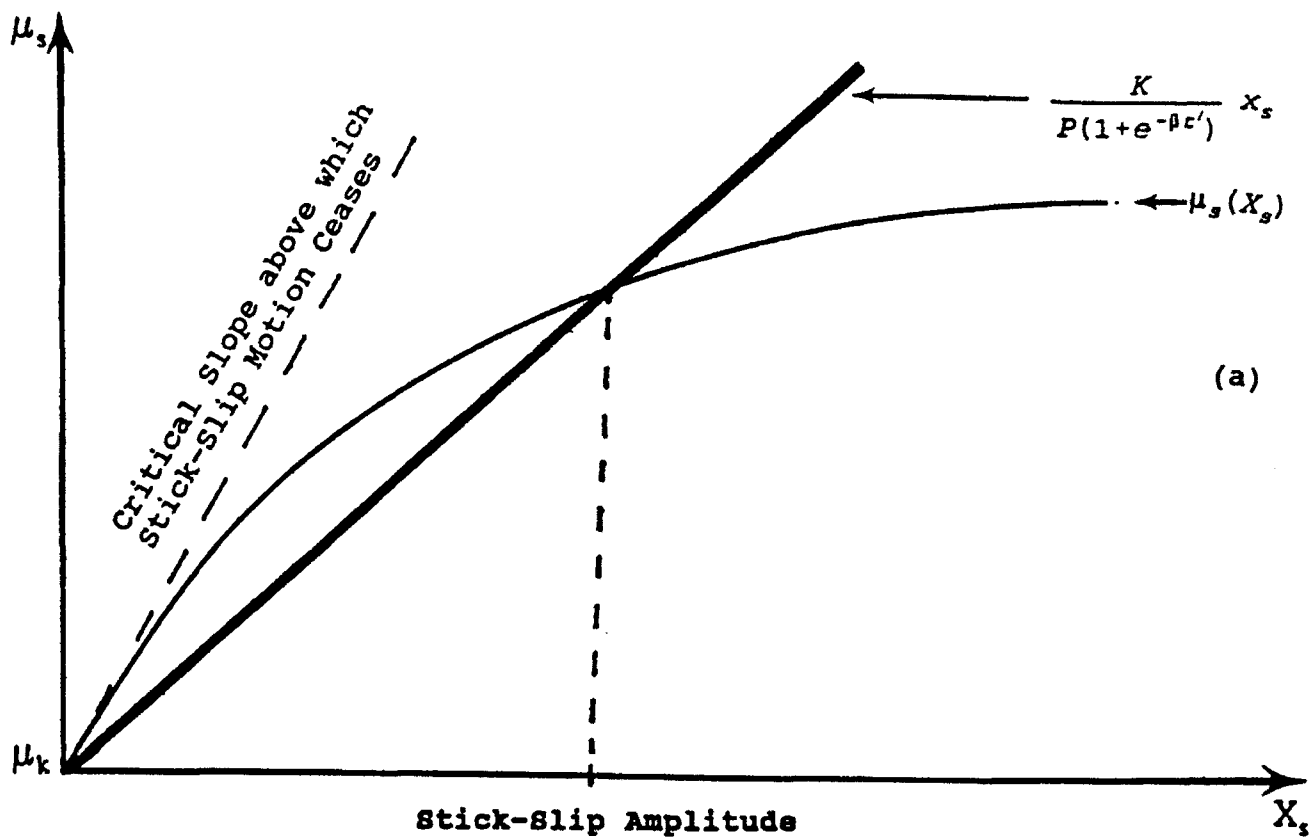
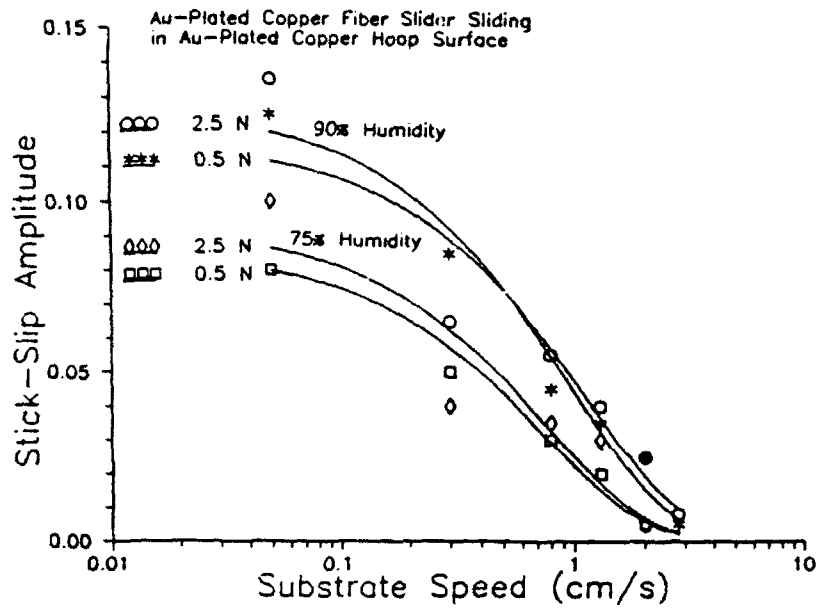


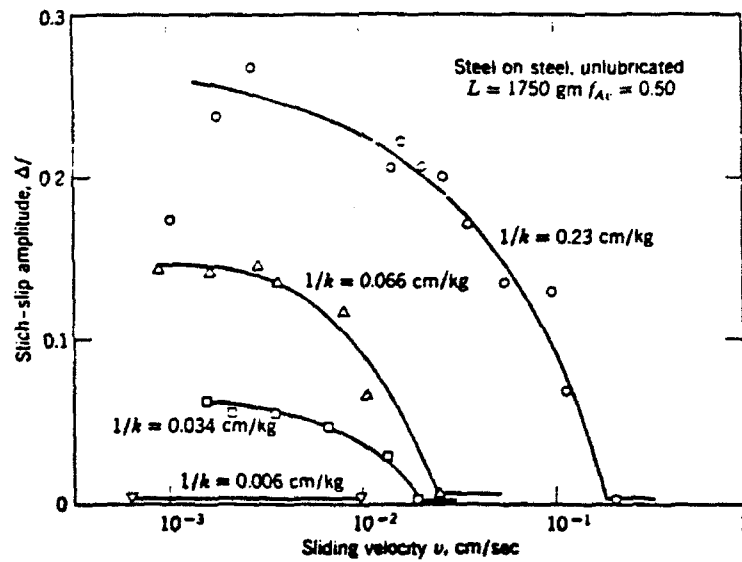
Figure 5



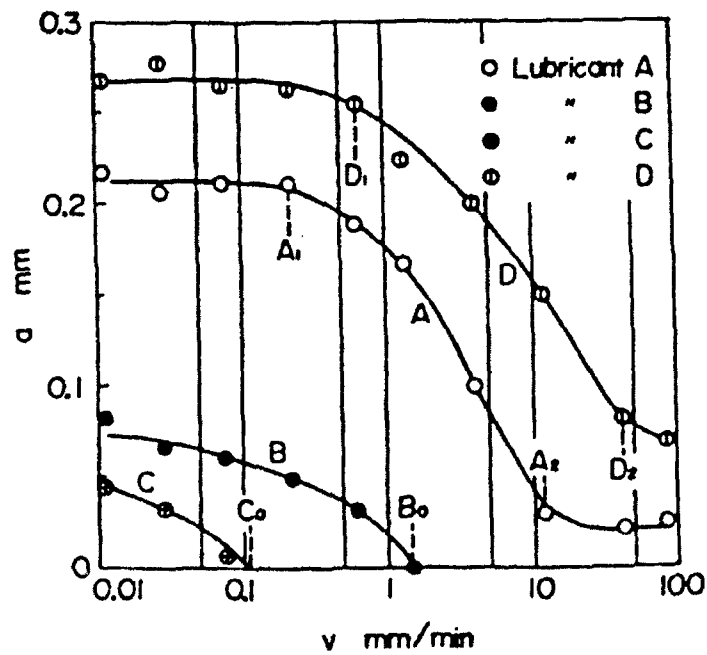
Figure



(a)



(b)



(c)

Amplitude-driving velocity curves for various lubricant

Reprinted from

ACTA METALLURGICA ET MATERIALIA

Vol. 40, No. 2, pp. 205-219

OVERVIEW NO. 96
EVOLUTION OF F.C.C. DEFORMATION
STRUCTURES IN POLYSLIP

B. BAY¹, N. HANSEN², D. A. HUGHES³ and D. KUHLMANN-WILSDORF⁴

¹The Engineering Academy of Denmark, Department of Mechanical Engineering, Lyngby, Denmark,

²Materials Department, Risø National Laboratory, 4000 Roskilde, Denmark, ³Materials Department,

Sandia National Laboratories, Livermore, CA 94540, U.S.A. and ⁴Department of Materials Science,

University of Virginia, Charlottesville, VA 22901, U.S.A.

PERGAMON PRESS PLC
OXFORD · NEW YORK · SEOUL · TOKYO

OVERVIEW NO. 96

EVOLUTION OF F.C.C. DEFORMATION STRUCTURES IN POLYSLIP

B. BAY¹, N. HANSEN², D. A. HUGHES³ and D. KUHLMANN-WILSDORF⁴

¹The Engineering Academy of Denmark, Department of Mechanical Engineering, Lyngby, Denmark.
²Materials Department, Risø National Laboratory, 4000 Roskilde, Denmark. ³Materials Department,
Sandia National Laboratories, Livermore, CA 94550, U.S.A. and ⁴Department of Materials Science,
University of Virginia, Charlottesville, VA 22901, U.S.A.

(Received 7 September 1990; in revised form 16 May 1991)

Abstract—The microstructural evolution during polyslip in f.c.c. metals is investigated by the examples of Al, Ni, Ni-Co alloys and an Al-Mg alloy, deformed at room temperature either by rolling or by torsion. The principles governing this evolution appears to be the following: (a) There are differences in the number and selection of simultaneously acting slip systems among neighboring volume elements of individual grains. In any one volume element (called a cell block), the number of slip systems falls short of that required for homogeneous (Taylor) deformation, but groups of neighboring cell blocks fulfil the Taylor criterion collectively. (b) The dislocations are trapped into low-energy dislocation structures in which neighbor dislocations mutually screen their stresses. The microstructural evolution at small strains progresses by the subdivision of grains into cell blocks delineated by dislocation boundaries. These boundaries accommodate the lattice misorientations, which result from glide on different slip system combinations in neighbouring cell blocks. The cell blocks are subdivided into ordinary cells and both cell blocks and cells shrink with increasing strain. All observations appear to be in good accord with the theoretical interpretation. However, some problems remain to be solved quantitatively.

Résumé—On étudie l'évolution microstructurale pendant le glissement multiple dans les métaux c.f.c., dans des alliages d'Al, de Ni, de Ni-Co et de Al-Mg, déformés à la température ambiante soit par laminage, soit par torsion. Les principes qui gouvernent cette évolution sont les suivants: (a) Il existe des différences dans le nombre et le choix des systèmes de glissements simultanément actifs parmi les éléments de volume entourant les grains individuels. Dans un élément de volume quelconque (appelé bloc cellulaire) le nombre de systèmes de glissement n'atteint pas celui que requiert la déformation homogène (Taylor), mais des groupes de blocs voisins remplissent collectivement le critère de Taylor. (b) Les dislocations sont piégées dans des structures de dislocations de basses énergies dans lesquelles les dislocations voisines constituent mutuellement des écrans de contraintes. L'évolution microstructurale aux faibles déformations consiste en une subdivision des grains en blocs cellulaires délimités par des parois de dislocations. Ces parois accommodent les désorientations du réseau, qui résultent du glissement sur des combinaisons de différents systèmes de glissement au voisinage des blocs cellulaires. Ces blocs sont subdivisés en cellules ordinaires et tant les cellules que les blocs cellulaires retrécissent lorsque la déformation augmente. Toutes les observations semblent en bon accord avec l'interprétation théorique. Cependant, il reste à résoudre quantitativement quelques problèmes.

Zusammenfassung—Die Entwicklung der Mikrostruktur in k.f.z. Metallen während Vielfachgleitung wird an den Beispielen Al, Ni, Ni-Co-Legierungen und einer Al-Mn-Legierung, verformt bei Raumtemperatur durch Walzen oder in Torsion, untersucht. Das dieser Entwicklung unterliegende Prinzip scheint wie folgt zu sein: (a) Es bestehen Unterschiede in Anzahl und Auswahl der gleichzeitig aktivierten Gleitsysteme in benachbarten Volumelementen der einzelnen Körner. In jedem Volumelement (genannt Zellblock) ist die Zahl der Gleitsysteme geringer als die für homogene (Taylor-) Verformung erforderliche, aber Gruppen benachbarter Zellblöcke erfüllen kollektiv das Taylor-Kriterium. (b) Die Versetzungen werden in Konfigurationen niedriger Energie, in denen benachbarte Versetzungen ihre Spannungsfelder gegenseitig abschirmen, eingefangen.

1. INTRODUCTION

The development of deformation microstructures in f.c.c. metals at low homologous temperatures has been studied extensively in single crystals and polycrystals [e.g. Refs 1-14]. For materials with a medium or high stacking fault energy the earliest microstructures develop with strain from "tangled" dislocations

to a structure consisting of cells or subgrains. The profuse jogging and kinking at low strains, which gives the visual impression of tangling, is due to dislocation point defect interactions and is not significant except at the lowest stresses [8]. Additionally, especially in polyslip, a number of larger inhomogeneities also characterize the deformed state, for example dense dislocation walls, microbands,

transition bands and shear bands [7, 13]. The structural characteristics of these inhomogeneities depend on several metallurgical parameters, including grain size, initial texture, and stacking fault energy (SFE), and on process parameters such as plastic strain, strain, rate and deformation mode.

A unified description of the development and interrelationships of these structural features has been lacking. The present paper provides this unified description for medium to high stacking fault energy (SFE) metals under conditions of stable polyslip. This unified description for cell forming metals is

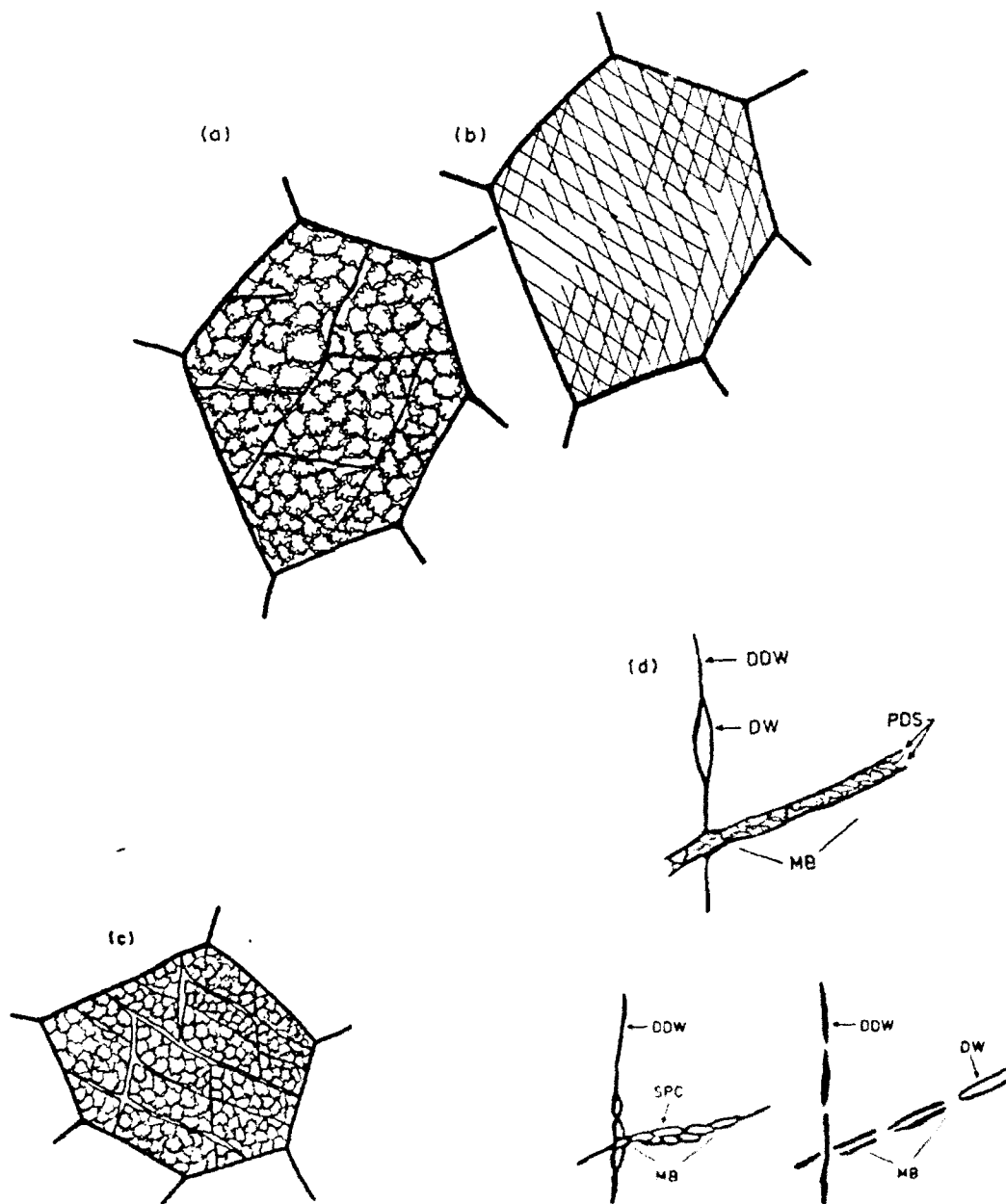


Fig. 1. Idealized microstructures. (a) Dense dislocation walls (DDW's) delineating cell blocks (CB's) consisting of ordinary equiaxed cells. (b) Slip line pattern on the surface of grain having the microstructure shown in (a). (c) Dislocation structure formed at a larger strain than that in (a). The structure is subdivided by long continuous DDW's which form first generation microbands (MB's) shown as double walls. (c) First generation MB's may take the form of paired dislocation sheets (PDS), double walls (DW), or strings of small pancake-shaped cells (SPC) [Note, that in real structures dislocation rotation boundaries cannot simply end as shown in (d). There are groups of disorganized dislocations at the end of the walls and at the gaps in the walls.]



Fig. 2. Microstructure parallel to the rolling plane in pure aluminum following 30% cold rolling. An example of the sharp DDW's which form in aluminum is marked D. Part of this DDW has been replaced by a first generation MB composed of small pancake shaped cells. The three microbands marked M border cell blocks of ordinary dislocation cells.

illustrated by TEM observations on aluminum, nickel and nickel-cobalt, deformed by rolling and torsion. An analogous description for non-cell forming metals is illustrated by TEM observations on Al-5.5% Mg.

The evidence clearly indicates that in high-SFE polycrystalline metals individual grains subdivide into volume elements (named "cell blocks" or CB's) which deform by fewer slip systems than specified by the Taylor criterion for strain accommodation [10]. The CB's in turn are subdivided into ordinary dislocation cells. All of these elements shrink with increasing strain. The above behaviour is the result of general theoretical principles applied to individual dislocations and their group behavior. Their group behavior is important at two levels: (a) the selection and interaction of locally different glide system combinations and (b) the reduction of free dislocation

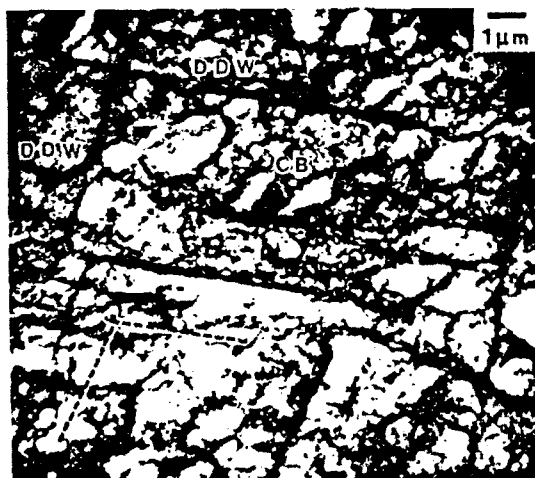


Fig. 3. Microstructure parallel to the longitudinal plane in pure nickel following 20% cold rolling. These continuous DDW, which are parallel to $\{111\}$ planes within 5° , delineate CB's of ordinary cells. Dashed lines indicate the trace of $\{111\}$ plane 90° to the micrograph in this $H = [011]$ condition. The rolling direction is 70° from the horizontal DDW's.

energy, via the formation of low-energy dislocation structures (LEDS) [8, 15-19].

The outlined microstructural evolution, based on [10-12] plus subsequent results, is schematically presented in Fig. 1. It is further illustrated by selected micrographs for the high-SFE materials in Figs 2-12, and for the aluminum-magnesium alloy in Fig. 13. Since the micrographs are partly devoted to the verification of still uncertain points, their detailed discussion is preceded by an outline of the theoretical background. This background includes the general behavior of dislocations and the effects of polyslip on microstructural evolution. A list of definitions is suggested in the Appendix for the various dislocation arrangements observed.

2. DISLOCATION ARRANGEMENTS INDEPENDENT OF POLYSLIP CONDITIONS

2.1. Dislocation interaction (the LEDS concept)

According to the LEDS concept [8, 15-19], the increase in dislocation density during straining is due

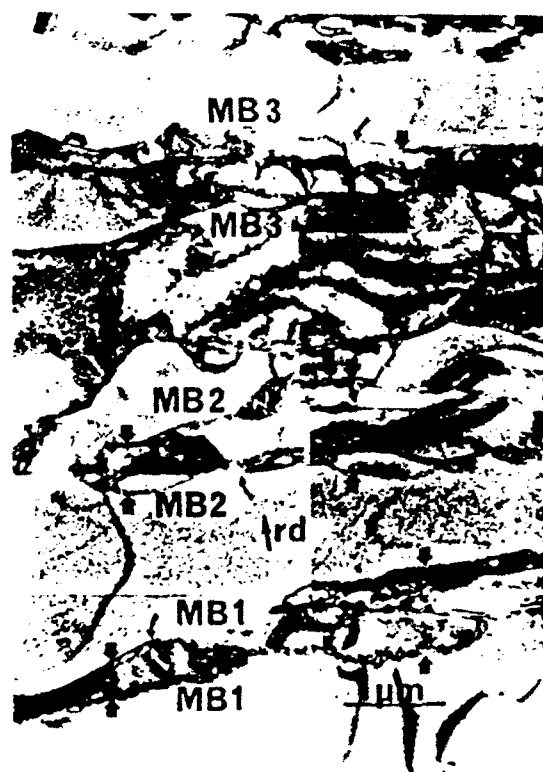


Fig. 4. Microstructure parallel to the rolling plane in pure aluminum following 30% cold-rolling. The width of three well-developed first generation MB's is marked by straight arrows. Viewed in three dimensions MB 1 and MB 3 belong to one set of parallel bands, whereas MB 2 belongs to an intersecting set. The average orientations of the cell blocks between the MB's show alternating misorientations (RP)[RD] = $\{114\}[401]$. Cumulative misorientations across the microbands range from 8° to 14° . The misorientations across cell boundaries within the microbands range from 0.2° to 12° , while those between cells within the same CB range from 0.2° to 2° .

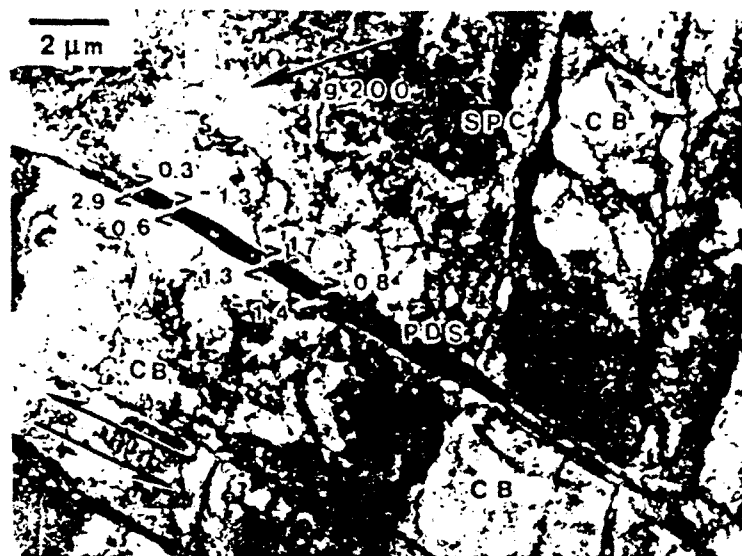


Fig. 5 First generation microbands in nickel formed during torsion deformation to a strain of $\tau_{0.2} = 0.6$ which is equivalent to 35% cold rolling. (The direction of the applied shear stress is marked with double arrows.) Microbands with small pancake-shaped cells like those in pure aluminum are marked SPC. Some of the parallelepipedal CB's delineated by the microbands are marked CB. A sharp narrow microband marked PDS is similar to those observed in rolling (Fig. 6) but is not on (111). The misorientations in degrees from CB to MB and from MB to CB are shown in the figure. The misorientations change along the length of the MB from cumulative to alternating in character ($g = [200]$ near $B = [103]$)

to the mutual trapping of dislocations into low-energy configurations. Dislocation trapping implies mutual stress-screening of the resolved shear stress components to the level of the frictional stress (τ_0) among the near-neighbor dislocations. The resolved shear stress components include the effects of any internal and applied stress as well as the stress by which a curved dislocation act on itself [8].

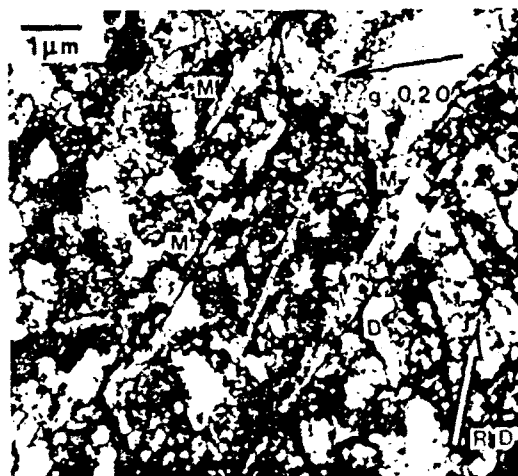


Fig. 6 DDW (marked D) and first generation microband (marked M) in the longitudinal plane of pure nickel following 30% cold-rolling. These long (20 μm) sharp narrow bands marked M are usually observed to form in grains which have a well defined cell structure like Fig. 3. Traces of microband clusters are $\approx 12^\circ$ from the trace of (111) plane marked as dotted line - inclined 69° from the plane of the micrograph. Beam direction near $B = [103]$.

The LEDS principle further asserts that, among the configurations accessible to the dislocations, that particular dislocation microstructure forms which minimizes the energy per unit length of dislocation line [8, 15-19]. Accessibility to a given cell configuration is driven by the applied stress and constrained by available slip systems, dislocation mobility, non-dislocation obstacles and frictional stress. Even with this minimization LEDS structures cannot be free of random long-range stresses [8]. Some random long range stresses are possible because the stress-screening is only effective to the level of τ_0 and for each dislocation only in regard to the resolved shear stress component. (Long range stresses manifest themselves in TEM through continuous changes of shading within individual cells.)

The relative level of stress screening of the other stress components besides the resolved shear stress, causes some LEDS to form in preference to others [8, 15]. This factor complicates the prediction of expected dislocation structures from a known dislocation density and types of participating Burgers vectors. However, it is a general principle that in all dislocation structures the energy decreases with increasing number of participating Burgers vectors since this permits increasingly effective stress-screening [20, 21].

2.2. Dislocation rotation boundaries and dipolar/multipolar walls

The trapping of dislocations into LEDS leads preferential to the formation of two-dimensional dislocation arrays (i.e. walls). These dislocation arrays are

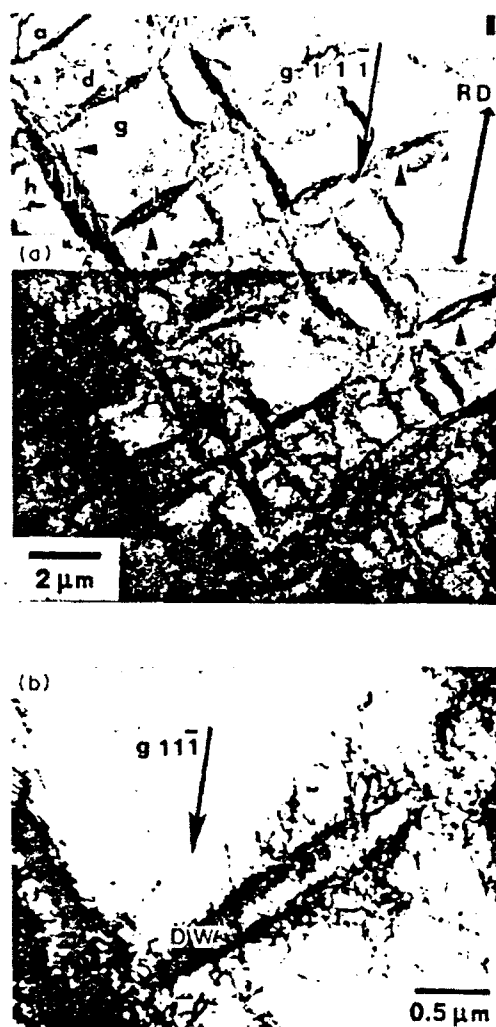


Fig. 7. (a) Microstructure parallel to the longitudinal plane in pure nickel following 10% cold-rolling. Two intersecting sets of walls are observed. They have a patchy discontinuous character compared to those shown in Fig. 3 but form in a long organized line. Many of the walls are subdivided to produce double walls [as sketched at the lower right of Fig. 1(d)] and are marked with arrows. Misorientation measurements were also made across the discontinuous DDW's and MB's. These misorientations have been tabulated in [12] with the location keyed to Fig. 7(a). A complex pattern of small misorientations for this region differs from pure aluminum in which a clear alternating misorientation pattern of large misorientations occurs from CB to CB [10]. (b) An enlarged view of the subdivision of a DDW into a double wall.

generally favored over a quasi-uniform three-dimensional distribution since for a given total dislocation density, the dislocation spacing (and thereby the energy per unit length of dislocation line) is smaller in the arrays. The ubiquitous dislocation cells [22, 23] are thus the very type of structure theoretically expected [24]. Cells are forming the mosaic block structure that was inferred from X-ray diffraction patterns first by Darwin [25] and subsequently confirmed in innumerable experiments. Yet, except in

a few simple cases (e.g. 26) we cannot predict the detailed shape of the cells or the directions of the angular misorientations among them. We can however predict some general features, which will be outlined in Section 2.4.



Fig. 8. Microstructure in pure nickel following torsion deformation to a strain of $\epsilon_{111} = 0.36$ which is comparable to 20% cold rolling. This structure is indistinguishable from that formed during rolling of pure nickel (Fig. 7). The gradual evolution from equiaxed cells and dense dislocation walls to a double walled microband structure and interspersed flattened dislocation cells (i.e. first generation MB's) can be imagined by viewing the progression of structures from the bottom to the top of the figure. Many of the DDW's in the figure have double walls which appear dark under these diffraction conditions. Dashed lines are traces of {111} planes.

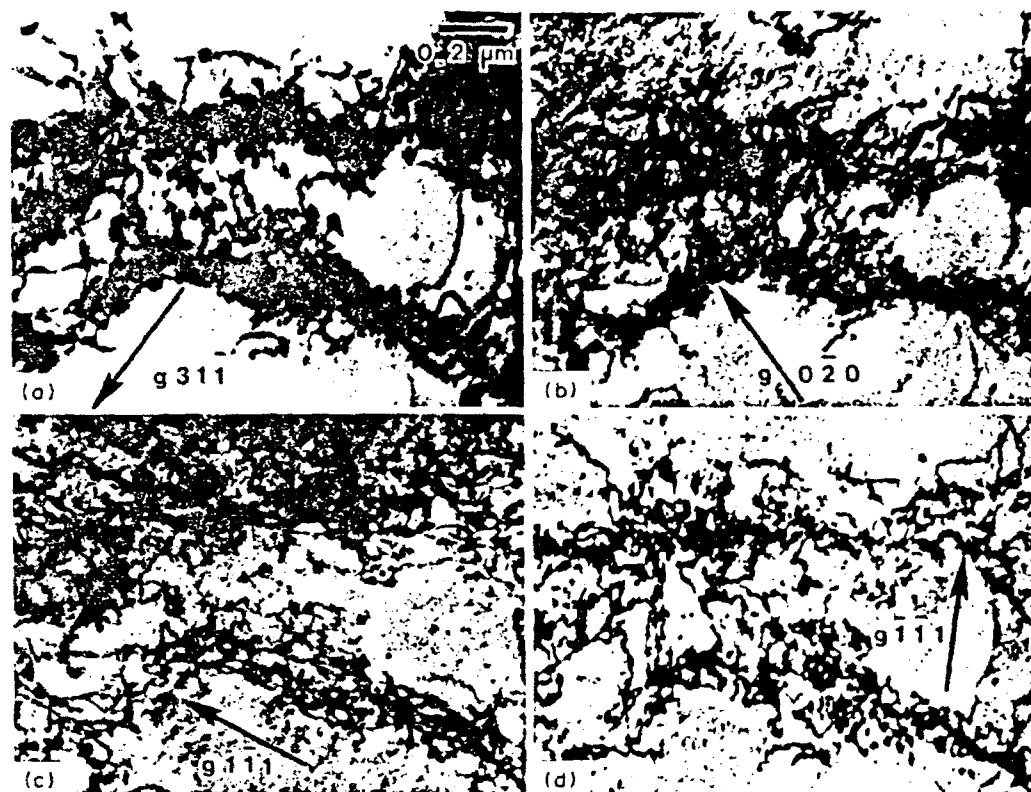


Fig. 9. Examples from a diffraction contrast experiment [11] in pure nickel following torsion deformation showing that the types of participating Burgers vectors of a new double wall MB differ from one wall to the other. They are not dipolar walls since the contrast would remain similar during tilting for dipolar walls. Note that in (a) for $g = [311]$ near $B = [011]$ both walls are similar in thickness but differ in arrangement, while in (b) for $g = [020]$ near $[001]$ more dislocations are in contrast in the top wall than the bottom one. In (c), with $g = [111]$ near $B = [011]$, both walls have many similar dislocations ($b = [101]$) but their density and distribution differs. The bottom wall in (d) ($g = [111]$ near $B = [112]$) has more dislocations in contrast and is thicker than the top wall. This difference is opposite to that shown in (b).

Many planar arrays are geometrically possible but only a small fraction are free of long-range stresses as required for LEDS. Indeed, there are only two types of two-dimensional dislocations arrays which are LEDS. These types are, firstly, dipolar or multipolar walls in which parallel dislocation segments of the same type, but with Burgers vectors of opposite sign, are equally frequent on a small scale and, secondly, dislocation rotation boundaries.

Dislocation rotation boundaries define a boundary across which the lattice orientation changes abruptly. The theoretical tool for identifying such arrays is Frank's formula [27]

$$B = 2 \sin(\theta/2) [u \times v] \quad (1)$$

where θ is the angle of relative rotation between the lattices on either side of the boundary and u is unit vector parallel to the axis of relative misorientation. Next, v is any arbitrary unit vector in the boundary and B is the vectorial sum of all dislocations intersected by v . B is also the size of the closure failure of a Burgers circuit encircling all dislocations intersected by an arbitrary unit vector v in the boundary. The verification of equation (1) for dislocation "walls" as

observed by TEM, is quite difficult in detail, even though it may be somewhat simplified by use of a graphical method [28]. However, such effort is rarely needed. The magnitude and crystallographic direction of the lattice rotation are more simply found from electron diffraction patterns of the areas on either side of the wall. The identification of the LEDS character which includes the freedom from (significant) long-range stresses, is indicated by (fairly) uniform TEM contrast near the Bragg condition, on either side of the boundary. While the contrast is uniform in the lattice the contrast value differs from one side of the boundary to the other. The contrast change occurs abruptly at the wall.

The formation of dislocation walls has been discussed above on the basis of the LEDS concept. Also crucial, is the law of the conservation of Burgers vectors, comparable to the law of the conservation of electrical charge. According to it, Burgers vectors cannot be created nor destroyed. As a result, dislocations can only be created pairwise. However, the formation of a rotation boundary requires an asymmetric influx of dislocations with the requisite Burgers vectors. Similarly the Burgers

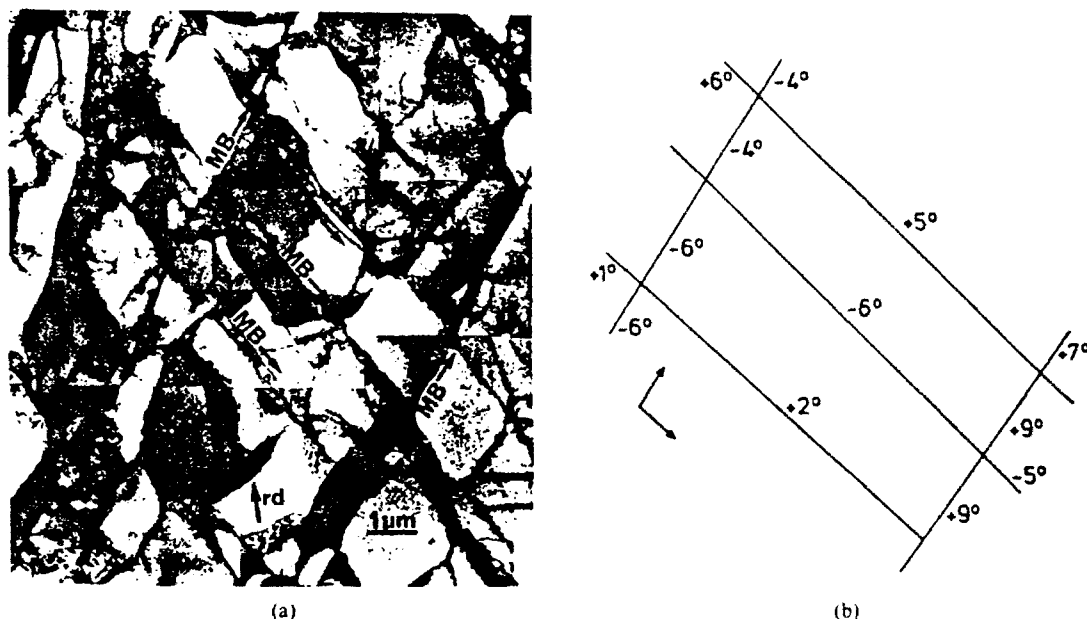


Fig. 10. (a) Microstructure parallel to the longitudinal plane section in pure aluminum following 30% cold-rolling. Two and three DDW MB's belonging to two intersecting sets of first generation MB's are seen. The thin foil is perpendicular to $[128]$ and is tilted to $[001]$. (b) Measured rotation angles about the $[100]$ component of the rotation axis $[\hat{u}$ of equation (1)] for the five DDW MB's seen in (a). In all cases the rotations about the $[001]$ component of \hat{u} are smaller. As seen, the relative rotations alternate in a fairly regular way according to a three-dimensional checkerboard pattern but involving more than one rotation axis. The arrows mark the directions of the measurements.

vector content (in particular B) of any dislocation rotation boundary cannot be destroyed. Consequently, walls may be quite mobile but they are persistent. Therefore, unlike dipolar/multipolar walls for which $B = 0$, without an asymmetrical influx of glide dislocations new cell or CB walls can only be formed pairwise or by the dissociation of preexisting walls.

2.3. Taylor lattices

The formation of dislocation rotation boundaries is greatly facilitated by three-dimensional dislocation mobility since a large fraction of the dislocations involved must leave their respective glide planes. As a consequence, crystals with significantly dissociated dislocations, such as f.c.c. metals with low SFE, do not form dislocation cell structures but Taylor lattices [8]. Crystals in which solute interactions increase the friction stress and promote planar glide may also form Taylor lattices. The Taylor lattices are composed of sets of parallel dislocations of alternating sign in a three-dimensional arrangement of quasi-uniform dislocation density. Relatively much less is known about these than about cell structures [8].

2.4. Refinement and morphology of the deformation structure

Deformation structures have been widely observed to shrink in scale as the applied stress is increased.

This refinement with stress occurs in Taylor lattices and dipolar/multipolar structures formed in fatigue as well as in ordinary cell structures [29]. The refinement of a cell structure requires dissociation of dislocation walls or the generation of new dislocation walls within preexisting cells. The latter can occur via the formation and subsequent splitting of dipolar/multipolar walls into two similar walls but with opposite angle of rotation [8, 28, 30, 31]. The dislocation cell size and in general the arrangement of dislocation walls is significantly affected by wall-end stresses [20, 21, 32, 33]. Numerical computations [20, 21] have shown that in a mosaic block structure, in which the cell walls are connected, the end-stresses are much lower than in the geometrically equivalent distribution of isolated cells in a matrix (analogous to pebbles in concrete) [20, 21]. Additionally the computations have led to the conclusions that for a mosaic block structure composed of dislocations with three co-planar Burgers vectors, the energy per unit length of dislocation line is lowest when the cells are (i) similar, (ii) roughly equiaxed, (iii) of similar size, (iv) relatively rotated about the same axis by equal but alternating angles, and (v) are parallelepipedal rather than of hexagonal shape as would minimize the wall to volume ratio.

Together the above points describe the so-called "checkerboard structure" [20, 30, 34]. In polyslip the same tendencies are preserved even though more



Fig. 11. Grain boundary offsets at DDW/MB grain boundary intersections observed in longitudinal plane sections. (a) Pure aluminum cold-rolled 30%. Four 0.5–1.0 μm deep offsets marked with arrows on the micrograph. (b) Pure nickel cold-rolled 37%. Three 0.7 μm deep offsets are marked with arrows. Dashed lines are traces of $\{111\}$ planes. Hollow cone dark field (about $\{111\}$ diffraction spots).

than three co-planar Burgers vectors participate. Thus a definite tendency to form parallelepipedal cells in a checkerboard pattern has been observed [10, 11, 13, 14] and will be illustrated later in this paper. End-stress reduction can also be a driving force to cause dislocation walls to line up, even when different selections of Burgers vectors participate along the line up. Since the strain energy rises as the square of the stress level and wall-end stresses drop off with distance they must act towards a uniform spacing among parallel dislocation walls of similar type [35].

3. EFFECTS OF POLYSLIP CONDITIONS ON DISLOCATION ARRANGEMENTS

3.1. Strain accommodation and number of slip systems

Polycrystalline deformation has been described by a number of models [36] of which only the Taylor model [37, 38] will be considered. According to this model, slip is uniform within each grain of a polycrystal and strain compatibility is achieved by simultaneous operation of at least five slip systems.

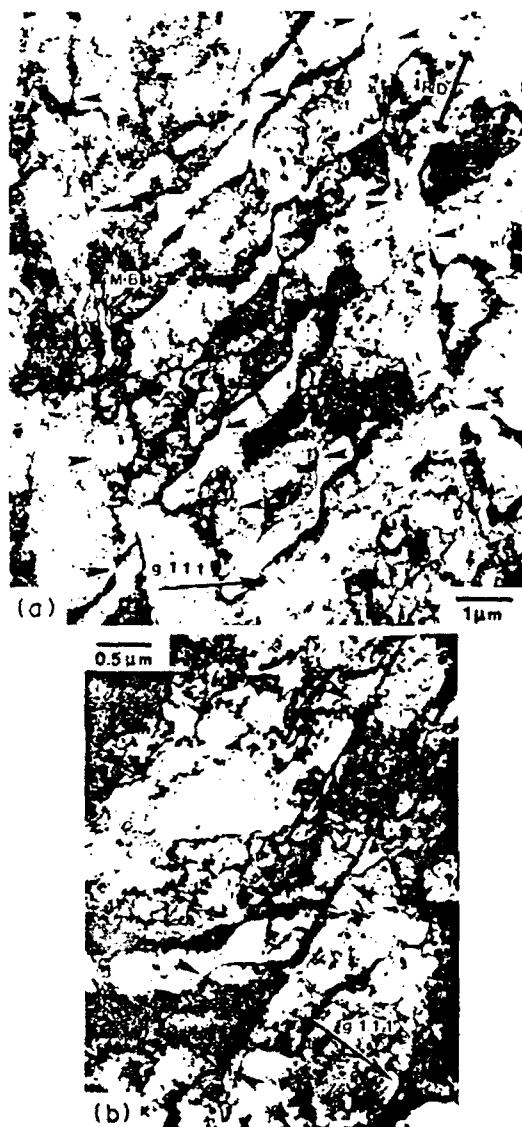


Fig. 12 Second generation MB's in a longitudinal section in pure nickel following 37% cold-rolling. Six second generation microbands along $\{111\}$ are marked with arrows. One of the very narrow zones of slip at the bottom left corner of (a) widens to a second generation microband at MB. An enlarged view of that narrow zone of slip and an adjacent one is shown in (b). The large shear offsets produced by these microbands during their formation can be seen in both (a) and (b).

Geometrically, i.e. independent of a consideration of the stress distribution, five independent glide systems can accommodate any arbitrary strain. In some special cases strain compatibility can be achieved with even fewer slip systems than five, since the number of requisite slip systems depends on the number of constraints on strain. For example, fewer constraints on strain are required when grains are either flat or elongated. Thus in such cases slip can occur with fewer than five slip systems [39].

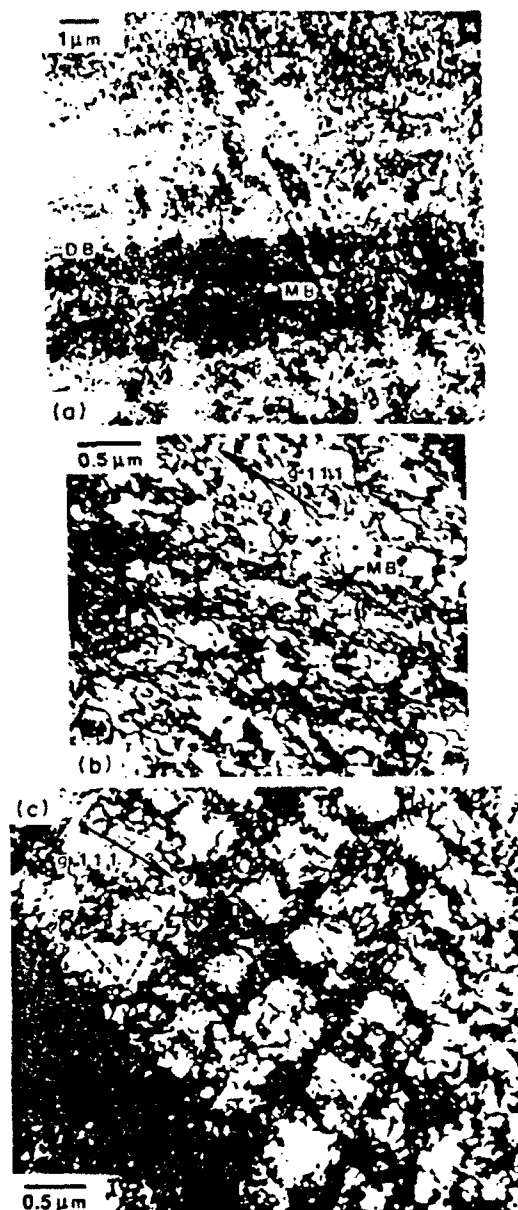


Fig. 13. Microstructure parallel to the longitudinal plane in Al + 5.5 at.% Mg alloy, following 10% cold-rolling. Note the quasi-uniform distribution of dislocations characteristic of the Taylor lattice structure, in lieu of the cells seen in the preceding micrographs. Even so, break-up into CB's occurs much as in those. This is indicated by domain boundaries (marked DB) and microbands (marked MB). (a) The light and dark contrast in this micrograph indicates that the DB's delineate regions of differing orientations and selection of slip systems. Hence the role of DB's in this alloy without cells is essentially the same as that of DDW's in cell forming metals. Single DB's extend horizontally in the figure, while in the diagonal direction double walled microbands have formed from the DB's. Tilt experiments show that the walls are parallel to $\{111\}$. The traces of $\{111\}$ planes are indicated by the dashed and dotted lines in the $B = [112]$ oriented foil. (b) High magnification view of the wall structure of the right diagonal microband in (a). (c) Higher magnification view of the distribution of background dislocations showing their organization about $\{111\}$ planes (marked as dashed lines) as expected in a Taylor lattice.

The number of simultaneously acting glide systems (N) is presumably the result of two competing effects. The flow stress is lower with fewer N because the number of intersecting dislocations and thus the density of dislocation jogs decreases. Conversely, stress screening becomes more effective as the number of different Burgers vectors increases. The number of Burgers vectors increases with increasing N . However, the individual contribution to stress screening from an additional Burgers vector diminishes significantly when the total number of Burgers vectors increases beyond three or four [20, 21]. Consequently N may fall short of the five systems expected on the basis of the Taylor model. The active glide systems, N may be realistically estimated at three to four, even when the imposed stress is entirely uniform. Independent of the number of slip systems operating, strain accommodation is required. Thus deformation of polycrystals with a reduced number of slip systems can take place by volume elements of individual grains (i.e. cell blocks) each characterized by a specific selection of glide systems [10]. While each cell block will conform as best as possible to the Taylor criterion, but with less than five systems cannot fulfil it, neighboring cell blocks will fulfil it collectively. This deformation pattern is schematically illustrated in Fig 1(a-c).

3.2. Break-up of polycrystals into rotated volume elements on two levels

3.2.1. Initial cell block formation. At the start of deformation different slip system combinations are activated in different parts of any one grain through the interaction among grains [40-42]. At the surface this is manifested by change in the slip line pattern (see Fig. 1(b)) subdividing the grains into regions. Frequently, intersecting slip lines are seen in these regions, testifying to the simultaneous action of two or more glide systems in each, i.e. polyslip does take place as expected [43]. This, then, is the break-up of grains into differently oriented regions whose deformation collectively will conform as best as possible to the Taylor condition [10].

For grain sizes above a few microns, the regions deforming with any particular selection of slip systems are initially much larger than the cell size, meaning that each CB contains several to many ordinary dislocation cells as indicated in Fig. 1(a).

Since the deformation within a CB does not fully obey the Taylor criterion, the average orientations of neighboring CB's increasingly deviate. As a result the boundaries between CB's are both longer and associated with larger average rotation angles θ in ordinary cell walls. These boundaries are identified with the previously discovered "dense dislocation walls" (DDW) [9, 10] and drawn as heavy lines in Fig. 1(a). Due to the gradual lattice reorientation, the average resolved shear stresses will change in each CB. Because that reorientation will differ among neigh-

boring CB's, the CB's will begin to interact in the same manner as did the initial grains. As a result, new CB's will be required to accommodate strain. New CB's will be formed through the subdivision of the initial CB's.

3.2.2. 1st generation MB's. The most frequent mechanism for the nucleation of new CB's is the splitting of preexisting DDW's into two or more roughly parallel walls whose cumulative angle of rotation initially equals that of the splitting DDW. The result of this splitting is approximately parallel double or multiple DDW's, which in the TEM, appear as bands of morphologically distinct dislocation cells. These bands are known as "microbands" (MB's). The morphology of these microbands is sketched in Fig. 1(d). In the volume opened up between the edges of any split DDW, a different selection of glide systems operates than on either side. Thus, the zone between the split parts of an earlier DDW is a new CB and is bounded by new DDW's that arose from the pre-existing DDW.

Sometimes DDW's and the microbands formed from them have a crystallographic orientation along a preferred slip plane. While there may be a tendency for this orientation, there is no compelling theoretical reason for this. Rather, the slip plane orientations of DDW's may often be coincidences and much the same holds true for ordinary cell walls.

Since this form of CB nucleation described above tends to be the earliest, the corresponding bands and their underlying dislocation structure have been dubbed "first generation microbands" to distinguish them from the "second generation microbands" to be discussed presently.

3.2.3. Second generation MB's. A less common way to start new CB's is through the intersection of the cell structure by glide on a previously dormant glide plane. The initiation of glide on an intersecting plane requires the joggling of a large fraction of the dislocations threading the plane. Therefore, like the phenomenon of "overshooting" in α -brass, glide initiation under these conditions requires a slight higher stress than further glide on the prior plane. Consequently, after initiation of the intersecting glide, there is local and momentary work-softening [8]. The degree of work softening increases with a higher density of threading dislocations. Fairly uniform narrow glide zones form by this mechanism. These glide zones can become CB's which may operate with one or more Burgers vectors. The resulting dislocation structures have been dubbed "second generation microbands" because they appear as bands in the TEM and they form after first generation microbands. Second generation microbands tend to intersect first generation MB's with noticeable shear offsets.

In f.c.c. metals, second generation MB's are necessarily parallel to {111} planes. Since the slip concentration within second generation microbands is the result of the operation of a new slip system

parallel to $\{111\}$, any second generation microband can develop into a new cell block. Like first generation microbands, the second generation can also be subdivided by small dislocation cells.

3.3. Microstructure at large strains

At small strains the lattice rotation across DDW's increases at a higher rate than at cell walls (Section 3.2). However, at strains above 30%, the rate of lattice rotations decreases. Thus, the averaged rotation angle across DDW's will increase at a much slower rate at large strains than at small strains. By contrast, the increasing dislocation density will continue to cause the rotation angle across ordinary dislocation walls to increase. Thereby the resolved shear stresses in neighboring cells within any one CB will diverge. Ultimately cells within a cell block can no longer operate with the same glide system combination. As rotation angles across cell walls increase, cells will become subgrains. The above reasoning leads to the theoretical expectation that at large strains the size of CB's will decrease to the size of one cell or subgrains. At large strains therefore the structure will consist of individual subgrains, which are the last stage developing from a complex hierarchy [15] of different dislocation rotation boundaries.

4. DEFORMATION STRUCTURES OF POLYCRYSTALS

4.1. Introduction

The theoretical interpretation of the microstructural evolution of polycrystals was partly derived from the detailed analysis of many TEM micrographs. Some of these studies have been documented in two recent papers describing the microstructures observed by TEM in Al deformed by rolling [10] and Ni and Ni-Co deformed in torsion [11]. More recent experiments cover similar microstructural studies in Ni and Al-Mg deformed by rolling [12, 44]. These new experiments allow a comparison, firstly between different metals deformed by the same deformation mode, secondly, between different deformation modes, and, thirdly, between metals (in our case Al and Ni) in which a dislocation cell structure is readily formed and an example of a metal (in this case Al-Mg alloys) which does not form cells but Taylor lattices. Typical microstructures are illus-

trated in Figs 2-13 and the relevant experimental parameters are summarized in Table 1. The experimental techniques and a number of quantitative structural observations of Al, Ni and Ni-Co are described in detail elsewhere [10, 11].

4.2. Cell blocks and dense dislocation walls

For Al, Ni and Ni-Co, the microstructure develops with increasing strain from a tangled dislocation structure to a structure consisting of equiaxed cells. Within this structure, dense dislocation walls (DDW's) are formed as the grains are subdivided into cell blocks (CB's), see Figs 2 and 3. This microstructural development was the same for both rolling and torsion as seen by comparing Figs 7 and 8.

4.3. First generation microbands

At increasing strain, $\geq 5-10\%$, the single DDW's split into two or more walls. The volume elements swept out by the splitting DDW's are first generation MB's (Section 3.2). Initially, MB boundaries and interior cell walls are formed from the dislocation content of the parent DDW's. However, almost immediately within the MBs their own specific combination of glide systems begins to operate and add to the dislocation content of the DDW's. The new glide systems will also cause previously unrealized dislocation annihilation and affect the developing misorientations.

This developing pattern of misorientations across MB's and CB's [10, 12] reveals the function of MB's. Progressing across the MB, the lattice misorientations include a component of rotation which provides a transition from one misoriented cell block to the adjacent CB, but other components which rotate the MB orientation away from that of either CB. The new rotation component is the result of the new selection of glide systems within the MB. Consequently the MB is a new CB.

Although all microbands define plate-like regions, first generation microbands appear in three different morphologies. (a) Strings of "small pancake shaped cells" [SPC's, see bottom left of Fig. 1(d)], (b) long paired dislocation sheets (PDS) formed from the division of long continuous DDW's (e.g. the nearly horizontal trace at the top of Fig. 1(d)), and (c) double walls (DW's) formed from splitting of short DDW's [bottom right of Fig. 1(d)], or small DDW segments.

Table 1

| Material | Deformation mode | Characteristic strain* | Figures |
|--------------|------------------|---|-----------------|
| Al (99.996%) | Rolling | 0 to 30% in thickness | 2, 4, 10, 11 |
| Ni (99.99%) | Torsion | Up to 200% shear strain (ϵ_{90}) | 5, 8, 9 |
| Ni (99.99%) | Rolling | 0 to 37% reduction in thickness | 3, 6, 7, 11, 12 |
| Ni-Co | Torsion | Up to 200% shear strain (ϵ_{90}) | — |
| Al-5.5% Mg | Rolling | 0 to 15% reduction in thickness | 13 |

*All deformation was done at room temperature.

Microbands which are composed of a string of SPC's are mainly observed in Al (Figs 2 and 4) [10] which also has the most sharply defined DDW's. However, on occasion such bands of SPC's are also observed in Ni (Fig. 3). They tend to develop from long continuous DDW's in grains with well-formed cells. This suggests that the parent DDW's formed very early when CB's were large, perhaps already as boundaries between the regions generated in response to interactions among neighboring grains as sketched in Fig. 1(a).

In the above description, first generation microbands evolve gradually from DDW's. Shear offsets, like those observed in deformation twinning, were not observed at either MB-MB intersections or MB-grain boundary intersections for newly formed MB's at small strains [10, 12]. However, at larger strains, localized shear was observed within some preexisting first generation MB's (Fig. 11).

4.4. Alignment of DDW's and first generation microbands

DDW's and MB's tend to form with a geometric orientation to the sample axis. This geometric orientation is along the direction of maximum shear stress (Figs 2, 5-8). These aligned DDW's and MB's may have either a high-index crystallographic orientation or be oriented along a slip plane. In Fig. 5 two families of geometrically aligned DDW's and MB's are shown. These DDW MB's delineate about 20 CB's. The CB's form a parallelepipedal structure (see Section 2.4) with a checkerboard pattern. These parallelepipedal CB's are themselves subdivided into much less regular cells.

An early form of the geometrically aligned DDW's which results in a checkerboard pattern, appears to be seen in Figs 7 and 8. These micrographs show the poorly defined cells and short discontinuous DDW's with a very high dislocation content which are typical for Ni and Ni-Co at lower strains [11]. In Figs 7 and 8 the short DDW's are arranged such that their cross sections form discontinuous lines. The alignment of these shorter DDW's into sets of rather straight and regularly spaced sheets is explained through their end-stresses (see Section 2.4). Individual sections of these single DDW's in Figs 7 and 8 subdivide into double walls (DW's) forming microbands as shown in Fig. 7(b). A similar subdivision into DW's has also occasionally been observed in long continuous DDW's like those shown in Fig. 3 [12]. The interpretation of the DW as a microband is confirmed by determinations of the Burgers vectors in DW's as well as their rotation axis direction and angles of relative misorientation (i.e. u and Θ of equation (1), respectively) using diffraction contrast techniques [11]. An example is given in Fig. 9, in which the parent DDW was not a dipolar or multipolar wall. If the DW had formed from the subdivision of an ordinary cell wall, rather than a DDW, a dipolar or multipolar wall would have been found.

The checkerboard pattern is also identified by determinations of the average lattice orientations of CB's, both in Al and Ni. These determinations show that the rotation axis directions [u of equation (1)] of one parallel set of DDW MB's tend to be similar, while the rotation angles (Θ) are of similar magnitude but alternate in sign. This pattern is most clearly observed in grains with only one set of DDW/MB's obtained from longitudinal sections of rolled Al. In grains which contain two intersecting sets of MB's the alternating misorientations belonging to each of the two sets of MB's show a three-dimensional checkerboard pattern [Fig 10(a, b)]. Thus the checkerboard pattern, which had initially been predicted only for dislocation cell walls [21], is now clearly documented for DDW's and MB's.

4.5. Second generation microbands

A less important microstructural feature, second generation microbands are characterized by their crystallographic orientation and shear offsets where they intersect other walls. These MB's are generally observed as narrow slip zones about $0.2 \mu\text{m}$ wide along (111) slip planes (Fig. 12). Unlike first generation microbands, shear offsets associated with second generation microbands form as the microband is created.

Second generation microbands were not observed in aluminum nor in nickel after torsion deformation, but they were observed in rolled nickel (Fig. 12). They have been frequently reported and emphasized, especially for copper rolled to intermediate and large strains [7, 45-49]. In most studies [45-48], however, no distinction was made between a first generation microband formed from a DDW along (111) and a second generation microband. This distinction is sometimes difficult, since the appearance of first and second generation microbands can be similar at later stages of their development.

4.6. Taylor lattices in Al-Mg alloy

In Al-Mg [44], which does not form cells, the formation of Taylor lattices separated by domain boundaries and microbands parallels the evolution of cell blocks separated by DDW's and MB's in the cell forming metals. The sheet-like dislocation structure of the domain boundaries and microbands is shown in Fig. 13. These domain boundaries and microbands separate regions of apparently random dislocation networks in Figs 13(a) and (b). However, these "random" dislocations are imaged in Fig. 13(c) to reveal their organization into a multi-Burgers vector Taylor lattice. As in Al and Ni, new microbands at small strains in Al-Mg do not produce shear offsets [44]. Shear offsets like those reported previously [45, 46] were confirmed in preexisting first generation MB's at larger strains.

5. DISCUSSION

5.1. Evolution of deformation structures

In general the observations presented in Section 4 are in good agreement with the theoretical predictions outlined in Sections 2 and 3. The formation of DDW's, CB's and MB's has been observed for all the materials and deformation modes examined. This subdivision of the microstructure is very characteristic for microstructural evolution in materials deforming by polyslip. For materials with adequate three-dimensional dislocation mobility, the described mechanisms for subdividing the microstructure with increasing strain is prototypical for microstructural evolution under a wide range of conditions. The described mechanisms follow the basic principles and agree with the wide range of micrographic evidence in the literature (e.g. [50–56]) as well as our own results. At present our detailed examination of microstructural evolution also includes data at large strains in torsion. These results indicate that subgrains are formed as a last stage of the structural evolution and that subgrain walls tend to be aligned with a more or less uniform spacing between the walls. These observations are in good agreement with the theoretical predictions (Section 3.3).

5.2. Morphology of microbands

Characteristic for the structural evolution is the formation of CB's bounded by DDW's and the nucleation of new CB's via the morphologically distinct MB's. In the more common first generation MB's the requisite boundaries are formed by the splitting of parent DDW's. In the second generation MB's the interior walls are mostly formed by an asymmetric influx of new dislocations, but the outer walls are essentially of dipolar type, at least initially.

Although newly formed first and second generation MB's may be quite different, at a later stage their appearance can be very similar. Consequently the MB's are subject to adjustments in morphology and orientation as their dislocation content and the local stress distribution changes. Therefore walls intersected by second generation MB's will not remain in an offset configuration, but will easily realign because of end stresses. This mobility permitting ready recovery from stepped configurations is evident because the plastic deformation which produced the dislocations does not determine the LEDS wall morphology nor cause serrations parallel to local intersecting glide.

Second generation MB's which are formed through concentrated intersecting glide are necessarily (nearly) parallel to a prominent crystallographic glide plane. It is therefore not surprising that in our micrographs they are (roughly) parallel to (111) planes (Fig. 12). However, particularly in Al, and at high strains, other crystallographic planes can also

serve as glide planes and non-crystallographic slip lines have been frequently reported [57, 58]. Thus also second generation MB's may not always appear as straight features parallel to (111) planes.

5.3. Worksoftening in microbands

In the absence of geometrical worksoftening, concentrated shear is always the result of structural worksoftening, which is a decrease of the critical resolved flow stress on planes after glide on them has been initiated. Little or no structural work softening is expected in first generation MB's. Correspondingly the shear in first generation MB's compares to that in the adjoining CB's. By contrast, the formation of second generation MB's implies at least some modest amount of structural worksoftening (see Section 3.2). This structural work softening results from the intersection, and consequent destabilization, of a pre-existing dislocation structure. Plentiful slip line evidence [57, 58] and the worksoftening observed in the phenomenon of "overshooting" in α -brass [59–61] supports this destabilization process. Another potential cause of structural worksoftening is the removal of point defect debris, e.g. as left through prior radiation damage [62]. There is no reason to expect a significant contribution to structural work softening through this last process in our case.

At low strains a third cause for structural worksoftening can be an initial scarcity of long dislocation links with a requisite Burgers vector. Once the first glide dislocations with the initially rare Burgers vector have been formed, they will automatically provide sources for more dislocations and the local flow stress will decrease. At its extreme, the increase of flow stress through the absence of dislocations imparts a very high strength to dislocation-free crystals [63]. In our case this mechanism may be discounted, as the extra flow stress is liable to be compensated at small to moderate strains due to the presence of three or more operating glide systems.

5.4. Comparisons between MB's and macroscopic shear bands

In the overshooting as well as in the debris-clearing types of worksoftening only the friction stress τ_0 is decreased. Therefore the relative magnitude of the corresponding softening cannot be large in all moderately to highly stressed f.c.c. metals. Even so on account of low workhardening the extent of localized glide in the second generation MB's can be sizeable, in the neighborhood of one. However, in view of the narrow width of the MB's and their moderate relative volume this local strain will translate into a relatively small contribution to the macroscopic shear strain.

It follows that if a local decrease of τ_0 through intersecting glide is the major cause of the strain concentration observed in second generation MB's, the connection of these with macroscopic shear bands is only tenuous. Although a decrease of τ_0

may also occur in macroscopic shear bands, strain concentration in those bands is predominantly due to geometrical worksoftening, i.e. an instability of lattice orientation such that at the same applied stress the resolved shear stress increases with further strain [64, 65].

Some geometrical worksoftening may also occur in MB's of both types, but worksoftening is certainly not responsible for the sizeable localized sheer offsets occasionally observed in first generation microbands, e.g. as in Fig. 11. Rather, localized shear in first generation MB's is caused by a shortfall of the number of simultaneously acting glide systems compared to other CB's. This difference in the number of glide systems causes the corresponding differences in local shear deformation and also gives rise to the occasionally large misorientations in first generation MB's relative to the surrounding structure [10], on occasion rivalling that of macroscopic shear bands [64].

6. CONCLUSION

Deformation microstructures of polycrystalline single phase materials with medium to high SFE's show a continuous evolution with strain in conditions in which stable glide dominates. An important characteristic of this evolution is the subdivision of the grains into cell blocks (CB's) which deform by fewer slip systems than specified by the Taylor criterion for strain accommodation. However, groups of neighbouring CB's fulfil the Taylor criterion collectively. With increasing strain the size of the CB's shrinks faster than that of the ordinary dislocation cells. Subgrains are formed as a last step in this evolution. The nucleation of new dislocation walls as required for cell refinement occurs by the formation and subsequent splitting of walls within individual cells. New CB's can be formed principally through the formation of first generation microbands (MB's). The manifold microscopical observations are in fine accordance with the general theoretical principles. Those principles are (i) strain accommodation and (ii) formation of dislocation walls and Taylor lattices through the trapping of dislocations into low-energy dislocation structures (LEDS). Outstanding problem relates to the orientation and the morphology of DDW's MB's and more generally to the effect of the suggested deformation pattern on mechanical properties including anisotropy and the development of deformation textures.

Acknowledgements—D. Hughes gratefully acknowledges the support of the United States Department of Energy (DOE) under contract No. DE-AC04-76DP00789. D. Kuhlmann-Wilsdorf gratefully acknowledges the financial support of this research through the office of Naval Research, Arlington, Va as well as through the Defence Advanced Research Projects Agency (P. Kemmery, TTC), Arlington, Va, monitored by T. Gora, Picatinny Arsenal).

REFERENCES

1. J. W. Steeds, *Proc. R. Soc. A* **292**, 343 (1966).
2. E. Göttler, *Phil. Mag.* **28**, 1057 (1973).
3. Y. Kawasaki, *Japan J. appl. Phys.* **18**, 1429 (1979).
4. Y. Kawasaki and T. Takuchi, *Scripta metall* **14**, 183 (1980).
5. P. R. Swann, *Electron Microscopy and Strength of Crystals* (edited by G. Thomas and J. Washburn), p. 131. Wiley-Interscience, New York (1963).
6. Ch. Schwink and W. Vorbrugg, *Z. Naturforsch* **22a**, 626 (1967).
7. M. Hatherly, *ICSM4* 6 (edited by R. C. Gifkins), p. 1181. Pergamon Press, Oxford (1983).
8. D. Kuhlmann-Wilsdorf, *Mater. Sci. Engng A113*, 1 (1989).
9. C. Y. Barlow, B. Bay and N. Hansen, *Phil. Mag.* **51A**, 253 (1985).
10. B. Bay, N. Hansen, D. Kuhlmann-Wilsdorf, *Mater. Sci. Engng A113*, 585 (1989).
11. D. A. Hughes and W. D. Nix, *Mater. Sci. Engng A122*, 153 (1989).
12. D. A. Hughes and N. Hansen, *Mater. Sci. Technol.* **7**, 544 (1991).
13. N. Hansen, *Mater. Sci. Technol.* **6**, 1039 (1990).
14. V. S. Ananthan, T. Leffers and N. Hansen, in *Mater. Sci. Technol.* (1991). To be published.
15. N. Hansen and D. Kuhlmann-Wilsdorf, *Mater. Sci. Engng 81*, 141 (1986).
16. *Low Energy Dislocation Structures* (edited by M. N. Bassim, W. A. Jesser, D. Kuhlmann-Wilsdorf and H. G. F. Wilsdorf), Elsevier Sequoia, Lausanne (1986); see also *Mater. Sci. Engng*, Vol. 81 (1986).
17. D. Kuhlmann-Wilsdorf, *Mater. Sci. Engng 86*, 53 (1987).
18. D. Kuhlmann-Wilsdorf, *Physica status solidi (a)* **104**, 121 (1987).
19. *Low Energy Dislocation Structures* (edited by M. N. Bassim, W. A. Jesser, D. Kuhlmann-Wilsdorf and G. J. Shiflet), Elsevier Sequoia, Lausanne (1989); see also *Mater. Sci. Engng 113* (1989).
20. M. N. Bassim and D. Kuhlmann-Wilsdorf, *Physica status solidi (a)* **17**, 379 (1973).
21. M. N. Bassim and D. Kuhlmann-Wilsdorf, *Physica status solidi (a)* **19**, 335 (1973).
22. *Direct Observations of Imperfections in Crystals* (edited by J. B. Newkirk and J. H. Wernick), Interscience, New York (1962).
23. *Electron Microscopy and Strength of Crystals* (edited by G. Thomas and J. Washburn), Interscience, New York (1963).
24. D. Kuhlmann-Wilsdorf, in *Workhardening* (edited by J. P. Hirth and J. Weertman), p. 97. Gordon & Breach, New York (1968).
25. C. G. Darwin, *Phil. Mag.* **27**, 325 (1914).
26. D. Kuhlmann-Wilsdorf and N. R. Comins, *Mater. Sci. Engng 60*, 7 (1983).
27. F. C. Frank, *Proc. Symp. on Plastic Deformation of Crystalline Solids*, Mellon Institute, Pittsburgh, Pa, p. 150. U.S. Dept of Commerce, Washington, D.C. (1950).
28. D. Kuhlmann-Wilsdorf, *J. appl. Phys.* **33**, 648 (1962).
29. S. V. Raj and G. M. Pharr, *Low Energy Dislocation Structures* (edited by M. N. Bassim, W. A. Jesser, D. Kuhlmann-Wilsdorf and H. G. F. Wilsdorf), p. 217. Elsevier Sequoia, Lausanne (1986), see also *Mater. Sci. Engng 81*, 217 (1986).
30. D. Kuhlmann-Wilsdorf, *Recent Progress in Understanding of Pure Metal and Alloy Hardening* (edited by A. W. Thompson), p. 1. Am. Inst. Min. Engrs, New York (1977).
31. C. T. Young, T. J. Headley and J. L. Lytton, *Low Energy Dislocation Structures* (edited by M. N. Bassim,

- W. A. Jesser, D. Kuhlmann-Wilsdorf and H. G. F. Wilsdorf), p. 391. Elsevier Sequoia, Lausanne (1986); see also *Mater. Sci. Engng* **81**, 391 (1986).
32. D. Kuhlmann-Wilsdorf and J. H. van der Merwe, *Mater. Sci. Engng* **55**, 79 (1982).
33. P. Charsley and D. Kuhlmann-Wilsdorf, *Phil. Mag.* **A44**, 1351 (1981).
34. W. Scoble and S. Weissmann, *Cryst. Latt. Defects* **4**, 123 (1973).
35. D. Kuhlmann-Wilsdorf and E. Aernoudt, *J. appl. Phys.* **54**, 164 (1983).
36. *Deformation of Polycrystals: Mechanisms and Microstructures* (edited by N. Hansen, A. Horsewell, T. Leffers and H. Lilholt), p. 490. Risø National Laboratory, Roskilde (1981).
37. G. I. Taylor, *J. Inst. Metals* **62**, 307 (1938).
38. J. F. W. Bishop and R. Hill, *Phil. Mag.* **42**, 414 (1951).
39. U. F. Kocks and G. R. Canova, *Deformation of Polycrystals: Mechanisms and Microstructures* (edited by N. Hansen, A. Horsewell, T. Leffers and H. Lilholt), p. 35. Risø National Laboratory, Roskilde (1981).
40. Ch. Barrett and L. H. Levenson, *Trans. Am. Inst. Min. Engrs* **137**, 112 (1940).
41. N. Hansen, *Metall. Trans.* **16A**, 2167 (1985).
42. J. B. Bilde-Sørensen and N. Hansen, in *Conf. Proc. ICSSMA 7*, p. 141. Pergamon Press, Oxford (1985).
43. U. F. Kocks, *Metall. Trans.* **1**, 1105 (1970).
44. D. A. Hughes, unpublished results (1990).
45. A. Korbel, J. D. Embury, M. Hatherly, P. L. Martin and H. W. Erbsloh, *Acta metall.* **34**, 1999 (1986).
46. A. Korbel and P. Martin, *Acta metall.* **34**, 1905 (1986).
47. F. J. Torrealdea and J. Gil Sevillano, *ICSSMA 6* (edited by R. C. Gifkins), p. 547. Pergamon Press, Oxford (1983).
48. A. S. Malin and M. Hatherly, *Metal Sci.* **13**, 463 (1979).
49. V. S. Ananthan, T. Leffers and N. Hansen, *Scripta metall. mater.* **25**, 137 (1991).
50. N. Hansen, *Trans. T.M.S.-A.I.M.E.* **245**, 2061 (1969).
51. J. Gil Sevillano, P. van Houtte and E. Aernoudt, *Prog. Mater. Sci.* **25**, 69 (1980).
52. B. Bay and N. Hansen, *Deformation of Polycrystals: Mechanisms and Microstructures* (edited by N. Hansen, A. Horsewell, T. Leffers and H. Lilholt), p. 137. Risø National Laboratory, Roskilde (1981).
53. J. Gil Sevillano and F. J. Torrealdea, *Deformation of Polycrystals: Mechanisms and Microstructures* (edited by N. Hansen, A. Horsewell, T. Leffers and H. Lilholt), p. 185. Risø National Laboratory, Roskilde (1981).
54. H. Chandra-Holm and J. D. Embury, *Yield, Flow and Fracture of Polycrystals* (edited by T. N. Baker), p. 275. Applied Science, London (1983).
55. S. S. Hecker and G. Stout, *Deformation, Processing and Structure*, p. 1. Am. Soc. Metals, Metals Park, Ohio (1984).
56. N. Hansen and T. Leffers, *Rev. Phys. Appl.* **23**, 519 (1983).
57. D. Kuhlmann-Wilsdorf and H. Wilsdorf, *Acta metall.* **1**, 394 (1953).
58. D. Kuhlmann, *Z. Metallk.* **41**, 129 (1950).
59. E. Schmid and W. Boas, *Plasticity of Crystals*. Hughes, London (1950). Translation of *Kristallplastizität*. Springer, Berlin (1936).
60. Z. S. Basinski and P. J. Jackson, *Physica, status solidi* **9**, 805 (1965).
61. J. Washburn and G. Murry, *Can. J. Phys.* **45**, 523 (1967).
62. I. G. Greenfield and H. G. F. Wilsdorf, *J. appl. Phys.* **32**, 827 (1961).
63. J. J. Gilman, *Mech. Engng* **55**, 55 (1961).
64. S. V. Harren, H. E. Deve and R. J. Asaro, *Acta metall.* **36**, 2435 (1988).
65. S. V. Harren and R. J. Asaro, *J. Mech. Phys. Solids* **37**, 191 (1989).
66. J. T. Fourie, P. J. Jackson, D. Kuhlmann-Wilsdorf, D. A. Rigney, J. H. van der Merwe and H. G. F. Wilsdorf, *Scripta metall.* **16**, 157 (1982).

APPENDIX

Definitions of Dislocation Arrangements

A number of dislocation arrangements were defined in an earlier paper [66]. Additional terms have been used by other authors [16, 17]. The listing below only includes those arrangements which have been clearly observed in the experiments under discussion.

Tangled dislocations. Dislocation structures either without any underlying larger-scale geometry or whose geometry is unrecognizable because of the profuse kinking and direction changes of individual dislocation lines.

Dislocation wall. Any essentially two-dimensional dislocation array.

Low energy dislocation structure (LEDS). Any dislocation structure within which neighbour dislocations mutually screen their respective resolved shear stresses.

Dislocation rotation boundaries. Essentially two-dimensional dislocation arrays which (nearly) obey Frank's formula [equation (1)] and separate crystals which are rotated against each other.

Dislocation cells. Roughly equilaxed volume elements within which the dislocation density is well below the average density and which are rigidly rotated relative to similar adjacent volume elements from which they are separated by more or less well-formed rotational dislocation boundaries.

Subgrains. Dislocation cells where the relative rotation between the lattices on either side of the boundary has become so large that neighbouring cells can no longer operate with the same combination of simultaneously operating glide systems.

Taylor lattice. More or less uniform distribution of dislocations composed of one or more sets of parallel dislocations of alternating sign preferentially in edge orientation.

Cell blocks (CB's). Domains of contiguous dislocation cells which share the same selection of operating glide systems [Fig. 1(a, c)].

Dense dislocation walls (DDW's). Undissociated dislocation rotation boundaries with a high dislocation density separating adjoining cell blocks, i.e. separating regions with different combinations of simultaneously operating glide systems [Fig. 1(a, c)].

Microbands (MB's). Well-formed plate-like zones of material bounded by dislocation rotation boundaries whose morphology and crystallography indicates that the combination of operating glide systems in them differs from that of the adjoining material and which accordingly are bounded by rotation boundaries. MB's are therefore CB's. Very commonly, MB's are subdivided into dislocation cells which are smaller on average than the dislocation cells in the adjoining material.

First generation microbands. MB's, which are developing through the splitting of dense dislocation walls (DDW's) over part or all of their length [see Fig. 1(b)].

Second generation microbands. MB's which are narrow plate-like zones passing through one or more pre-existing dislocation cells along the crystallographic slip planes. Shear offsets are formed where these MB's intersect other walls.

phys. stat. sol. (b) 172, 235 (1992)

Subject classification: 61.70 and 62.20; S1; S4

Department of Materials Science, University of Virginia, Charlottesville¹⁾

Theory of Worksoftening in High-Performance Alloys

By

DORIS KUHLMANN-WILSDORF and H. G. F. WILSDORF

Dedicated to Professor Dr. PETER HAASEN on the occasion of his 65th birthday

In conventional alloys ductility decreases with rising flow stress to negligible values at some maximum yield stress (τ_m), whereas high-performance alloys, e.g. formed through mechanical alloying or nano-powders, can have much higher yield stresses with ductility, but tend to worksoften. A simple theory is presented, based on the LEDS concept, to account for both of these behaviors: The flow stress is $\tau = \tau_0 + \text{const} \sqrt{\rho}$ with ρ the dislocation density, and the workhardening coefficient is $\theta \approx d\tau_0/d\gamma + C\beta$ with β the rate of glide dislocation trapping. β depends on the specific LEDS formed but always decreases with stress and can become negative for $\tau > \tau_m$ at artificially high ρ . Worksoftening results when unconventional manufacturing methods have produced LEDS with metastable ρ and/or τ_0 values that are higher than conform to the LEDS generated through the conventional straining conditions in testing or use.

In konventionellen Legierungen nimmt die Duktilität mit zunehmender Festigkeit ab, um bei einer oberen Spannung (τ_m) zu verschwinden. Dagegen können wesentlich höhere Streckgrenzen mit nennenswerter Verformbarkeit durch mechanisches Legieren oder Verwendung von Feinstpulvern erzielt werden, aber solche Legierungen neigen zur Erweichung durch Verformung. Beide Erscheinungen können aufgrund des LEDS Konzeptes wie folgt erklärt werden: Die Fließspannung ist $\tau = \tau_0 + \text{const} \sqrt{\rho}$ (ρ Versetzungsdichte), und der Verfestigungskoeffizient ist $\theta \approx d\tau_0/d\gamma + C\beta$ (β Rate der Versetzungszunahme). β hängt von der spezifischen LEDS ab, sinkt aber immer mit der Spannung und kann bei überhöhten Versetzungsdichten negativ werden. Erweichung kann deswegen durch metastabile LEDS mit zu hohen τ_0 und/oder ρ -Werten entstehen, wie sie etwa durch unkonventionelle Herstellungsmethoden erzeugt werden.

1. Introduction

The LEDS (low-energy dislocation structure) concept has proven to be a very fruitful guiding principle for understanding plastic deformation and workhardening [1, 2]. According to it, the dislocation content of crystalline materials approaches that among all configurations accessible to them which most nearly minimizes the free energy per unit length of dislocation line. When dislocations are relatively free to leave their glide planes, they minimize their energy by mutual trapping into dislocation rotation walls [3 to 8]. This is the reason for the widely observed formation of cell structures, typically composed of dislocation rotation walls variously distinguished as (i) ordinary dislocation cell walls, and as (ii) dense dislocation walls (DDW's), and (iii) microbands (MB's) of different types which together delineate cell blocks (CB's), wherein the manifold details depend on the type and severity of the preceding plastic deformation [9 to 12].

The very general correlation of high yield strength and low ductility of conventionally produced alloys, which seemingly puts an upper limit on achievable strength combined

¹⁾ Charlottesville, VA 22901, USA.

with ductility as best exemplified through spring steel, must evidently also derive from LEDS behavior. The present paper correspondingly aims to give a broad-based explanation of that phenomenon in line with earlier work [7], and add to this a simple theory of worksoftening in specially produced alloys, e.g. as made through the compaction and/or extrusion of nano-powders, produced via chemical vapor deposition, mechanical alloying, splat cooling, or other.

2. The Dependence of the Flow Stress on Dislocation Density in LEDS

From the broad-based perspective of the LEDS concept, the correlation between the dislocation density (ρ) in crystalline materials and their strength in terms of the critical resolved shear stress on the operative glide systems (τ), is very simple. It is in accord with the very widely observed empirical correlation between ρ and τ first documented by Bailey and Hirsch [13]

$$\tau = \tau_0 + \tau_G \approx \tau_0 + \alpha Gb \sqrt{\rho} \quad (1)$$

with G the shear modulus, τ_G that part of the flow stress which depends on temperature as G [14], b the Burgers vector, α equal to 0.4 within a factor of two or so, and τ_0 the frictional stress acting on the dislocations.

The underlying reason for (1) has been repeatedly explained for the case of the typical dislocation cell structures (e.g. [7] and [9]). In general it is that ever new glide dislocations have to be formed, normally through the supercritical bowing of dislocation links from or through the present dislocation structure. The requisite Frank-Read bowing stress [15, 16] rises with increasing dislocation density, i.e. decreasing average free link length, and this is that part of the flow stress which is proportional to G [14]. In the less common case of Taylor lattices, e.g. as best investigated for α -brass type alloys [4, 7, 8], passage between parallel sequence of dislocations plays the same role as supercritical bowing does in cell structures. Thereby the value of α is changed but otherwise the theory is not significantly affected.

In either case, the reason for the increase of dislocation density through plastic deformation is mutual trapping of glide dislocations into configurations out of which the applied stress cannot release them. The simplest example of such trapping are two similar dislocations on parallel glide planes d apart. When the prevailing resolved shear stress is smaller than $Gb/[(1 - \mu)8\pi d]$, the two edge dislocation will trap into a dipole, which is the potential start of a tilt wall if they are of same sign, and of a dipolar wall if they have opposite sign. The application of a higher resolved shear stress would release the dislocation out of this mutual trap, but smaller stresses and any amount of annealing short of that required for climb will be ineffective. Thus the dislocations are certainly not in equilibrium, but as they react to their mutual shear stresses to form a dipole, they minimize the total of their free energy per unit length of dislocation line among all possible arrangements accessible to them (i.e. in this case being limited to glide on their glide planes).

In the more general case, since ordinary low-temperature plastic deformation is accomplished by the formation and glide of multitudes of dislocations, the application of increasing flow stresses will cause the release of isolated widely spaced dislocation pairs, but that effect will be dwarfed by the profuse generation of increasingly closely spaced dislocation groupings. As in the idealized example of the isolated edge dislocation pair, the physical cause of such trapping is the elimination of long-range dislocation stresses through mutual

stress screening. Strictly speaking, in the absence of climb as is assumed throughout, this is confined to the resolved shear stresses of the interacting dislocations, which for two parallel edge dislocations leaves a great deal of stress. However, the involvement of a variety of slip systems, largely in the form of "forest" dislocation [3 to 9], greatly increases the effectiveness of stress screening [4, 9, 17]. After some modest strain, therefore, the described trapping amounts to an effective elimination of longer-range stresses beyond the near-neighbor dislocation spacing, \bar{l} , i.e. of

$$\bar{l} = m/\sqrt{\rho} \quad (2)$$

with the geometrical constant, m , somewhat dependent on details of the structure but typically not far from unity. In this simple way, then, the configuration and average spacing of mutually trapped dislocations give rise to (1), except that in a more precise treatment the logarithmic term in the Frank-Read stress [16] imparts a moderate stress dependence to α [18].

Somewhat paradoxically, therefore, while the density of the trapped dislocations and the free energy of the dislocations as a whole typically continue to rise in the course of plastic strain, the free energy per unit length of dislocation line decreases with decreasing screening distance \bar{l} . Most notably, and as repeatedly indicated, the free energy per unit length of dislocation line will be near minimum for all configurations accessible to the dislocations. If this is not so, the excess free energy of the momentary configuration will be present in the form of unscreened longer-range dislocation stresses, and as these build up they will trigger the motion and/or formation of dislocations that will screen those stresses.

The application of the above simple principle of free energy minimization per unit length of dislocation line, i.e. the LEDS principle [1, 2], has already been variously used to interpret details of increasingly complex dislocation structures, not only for the case of unidirectional deformation (e.g. [4, 9 to 12, 19 to 23]) to give a somewhat arbitrary selection, but also very effective in fatigue (e.g. [24 to 29]).

In all cases (1) remains eminently useful although the different types of dislocation rotation walls introduced above have somewhat different characteristics: Ordinary cell walls are what has been dubbed "incidental" boundaries while DDW's and MB's are "geometrically necessary" boundaries [8, 11, 12, 30]. For the present purposes this is unimportant except that, typically, geometrically necessary boundaries have so high angles that they are "subboundaries" defining subgrains, with the individual dislocations in them not always still evident. As a result they generally contribute to the flow stress of the material in accordance with the Hall-Petch relationship [7, 8, 31 to 33] and not in accordance with the Frank-Read bowing stress as discussed above.

The continued usefulness of (1) rests on the fact that the necessary correction gives rise to only a modestly modified stress dependence of α . In fact the functional difference between the simplified and the improved expression is difficult to determine experimentally [33]. The salient points, then, are (i) that (1) with a mildly stress dependent value of α represents the data well, and (ii) that α is somewhat but not drastically different for different specific LEDS's, and thus for different deformation conditions.

3. The Workhardening Coefficient

With the dependence of flow stress on dislocation density given through (1), workhardening results principally from the accumulation of dislocations in the course of straining since τ_0 is normally almost independent of strain. The workhardening coefficient can be derived

with various degrees of sophistication. Most basically, and neglecting a number of refinements such as found in [7, 20, 34] and those due to the different types of dislocation rotation walls just discussed, we may simply consider the supercritical bowing of dn dislocation links per unit volume. On average these sweep out an area of $L^2 = (g\bar{l})^2$, i.e. typically the cross-section of a more or less quadratic dislocation cell or subgrain of diameter L , before impinging on dislocation boundaries where they are partly annihilated.

Let us introduce the "dislocation retention parameter", β , as the fraction which the newly trapped dislocation line length represents of $4L$, i.e. the line length which had been generated. With it, the incremental dislocation density increase caused by the supercritical bowing of the dn links is

$$d\rho = 4L\beta \, dn = 4g\bar{l}\beta \, dn, \quad (3)$$

while the incremental shear deformation is

$$d\gamma = L^2 b \, dn = g^2 \bar{l}^2 b \, dn. \quad (4)$$

Combining (3) and (4) with (1) and (2) yields

$$d\tau_G \approx \frac{2\alpha\beta G}{mg} d\gamma \quad (5)$$

and the workhardening coefficient

$$\frac{d\tau}{d\gamma} = \theta \approx \frac{d\tau_0}{d\gamma} + \frac{2\alpha\beta G}{mg} \quad (6a)$$

with which the typically small strain dependence of τ_0 often reduces to

$$\theta \approx \frac{d\tau_G}{d\gamma} \approx \frac{2\alpha\beta G}{mg}. \quad (6b)$$

4. Stress Dependence of the Dislocation Retention Parameter at High Stresses

For a number of years it had been tentatively assumed that the decrease of θ in stage III, after substantially constant workhardening in stage II, was caused by the establishment of a constant minimum value of L , so that the parameter g increased while β remained constant. The discovery and investigation of stage IV [35 to 39] proved this assumption to be incorrect. Instead it seems now clear that both α and g decrease moderately with increasing flow stress [9] and m cannot vary greatly as long as a dislocation cell structure persists. As a result the stress dependence of the workhardening coefficient substantially mirrors the stress dependence of the dislocation retention parameter β [7, 40].

The end of stage II appears indeed to mark the point at which β begins to decrease through the onset of cross slip, much as had since long been argued by Seeger [14] and Haasen [41, 42]. Albeit, it seems that full-blown cross slip develops only gradually in the course of stage III, causing the observed gradual decrease of the stress-strain curve, until in stage IV, β stabilizes at a low value due to the full operation of cross slip on a multitude of atomistic slip planes. In other words, it has been suggested [40] that cross slip becomes increasingly prevalent as the flow stress rises in stage III, until pencil glide has been established in stage IV.

A theoretical derivation of β has not yet been possible. In fact, the stress dependence of β can presumably be quite complex, and it is not intended to pursue that subject in the present paper, devoted to worksoftening in high-performance alloys, i.e. stresses so high that stage IV will normally be attained. What we shall examine, instead, is a further possible reduction of β , and in fact the decline of β to negative values. That possibility derives from the often observed upper limiting dislocation density through plastic deformation, of about $\approx 4 \times 10^{11} \text{ cm}^{-2}$, for which Rigney has offered a theoretical explanation [43] which is in fine accord with the present paper. At any rate, there certainly is a stress level so high that most crystallographic lattice planes containing the Burgers vector can become active, and at which glide dislocation loops are formed spontaneously.

Naming this critical upper limiting stress τ_m , the parameter β must depend on stress such that it vanishes at $\tau_G = \tau_m$. Assuming as a first simplified model that mutual dislocation annihilation occurs principally between parallel dislocations, there will then be a limiting distance of approach which leads to certain destruction, i.e. in first approximation,

$$\beta^* = \beta_0 \left(1 - \frac{\tau_G}{\tau_m} \right), \quad (7a)$$

yielding

$$\theta^* \approx \theta_0 \left(1 - \frac{\tau_G}{\tau_m} \right). \quad (7b)$$

where the subscript 0 denotes the behavior when dislocations are far apart.

Alternatively, one may consider that dislocation destruction occurs whenever anywhere dislocation lines approach more closely than the critical distance, i.e. that there is an excluded volume proportional to g . In that second model one obtains, again in first approximation,

$$\beta^* = \beta_0 \left[1 - \left(\frac{\tau_G}{\tau_m} \right)^2 \right] \quad (8a)$$

yielding

$$\theta^* \approx \theta_0 \left[1 - \left(\frac{\tau_G}{\tau_m} \right)^2 \right]. \quad (8b)$$

5. Negative Values of β and θ through Extreme Deformation Conditions

At least formally, (7) and (8) suggest the possibility of negative β -values and thus negative workhardening rates if by some or the other means a higher than critical dislocation density has been generated. This cannot happen through progressive deformation in any one mode. Therefore, in the course of continuing deformation β will decrease (in accordance with (7a) or (8a) or similar, as the case may be) until θ vanishes, unless fracture has occurred before then. No doubt τ_m , β_0 , and θ_0 can, indeed must, somewhat depend on deformation conditions and the specific LEDS formed. As long as these remain essentially unchanged with $\tau_0 \ll \tau_m$, the stress-strain curves in continuing deformation, i.e. without change in the type of LEDS generated, is found from (7a) and (8a) as

$$\tau^* = \tau_m \left[1 - \exp \left(\frac{-\beta \theta_0}{\tau_m} \right) \right] \quad (9)$$

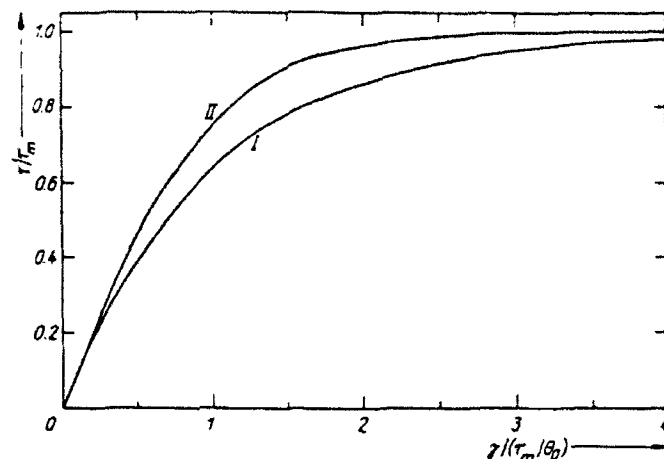


Fig. 1. Theoretical stress-strain curves for uniform deformation and negligible friction stress, assuming that the dislocation trapping parameter β decreases linearly (mode I) and quadratically (mode II) with stress in accordance with (7) to (10)

in mode 1 and

$$\tau^+ = \tau_m \tanh\left(\frac{\gamma\theta_0}{\tau_m}\right) \quad (10)$$

in mode 2.

Fig. 1 presents these two curve types and shows them to be rather similar. In either case, necking and fracture will ordinarily have caused failure well before τ_m is attained. In any event workhardening ceases asymptotically as the critical dislocation density

$$\varrho_m \approx \frac{\tau_m}{(\alpha G b)^2} \quad (11)$$

is approached, and thus τ_m cannot be exceeded through continuing deformation at same or slowly changing α .

However, considering the methods of making some of the modern alloys already mentioned, e.g. mechanical alloying, splat cooling, and compacting of nano-powders through extrusion, leaves little doubt that these will cause extraordinarily high dislocation densities and will cause different LED's than can be attained by simply continuing some form of conventional workhardening, be it through forging, twisting, rolling, etc. At least one crucial feature here is the deliberate or incidental application of high hydrostatic pressures superimposed on the deforming tractions. In first approximation this causes a reversible increase of flow stress due to the pressure dependence of the shear modulus [44, 45], but also generally changes τ_0 . Presumably there are additional aspects of the manufacturing conditions of the most advanced alloys which have much the same effect of inducing super-high dislocation densities and/or τ_0 values, as specifically the establishment of nonequilibrium degrees of solid solution and/or partial amorphization.

The dislocation densities $\varrho > \varrho_m$ in such alloys are metastable. They do not simply vanish once the inducing conditions have ceased. In fact, relative stability of the alloy structures

is an indispensable feature of successful unconventional manufacturing processes. A major reason for the metastability of the ultrahigh dislocation densities is doubtlessly the geometrical arrangement, namely overwhelmingly in the form of subgrain boundaries delineating a very fine subgrain size. At any rate, on the basis of the preceding arguments, without pre-existing flaws which would cause brittle failure, a material with a dislocation density in excess of that ρ_m which would be established in use conditions, will exhibit negative values of β . Thus it will worksoften on the basis of (7) and (8) provided that τ_0 is small or at the least does not significantly change with strain.

6. Flow Stress-Flow Strain Curves

6.1 Effect of decreasing β at negligible or constant τ_0

Even at negligible or constant τ_0 as assumed so far, actual stress-strain curves are not only affected by the discussed dependence of β on flow stress but also by correlated changes in the values of α , m , and g . Such changes are bound to occur, especially in the case of worksoftening which will be accompanied by a gradual change from the initial metastable LEDS to the LEDS appropriate to the testing or use conditions. That same behavior is known already from fatigue experiments in which cyclic softening is accompanied by the establishment of new, lower-energy LEDS.

In the present case of worksoftening high-performance alloys, the new LEDS may not always be obviously different from the old one. Typically both will contain fine subgrains, perhaps of different shapes and mutual misorientations, and in the new LEDS the grain size will presumably be somewhat larger, but certainly the dislocation networks in the subgrain boundaries will be at least subtly different. A detailed theoretical prediction of those changes is still well beyond our capabilities. In terms of semi-quantitative theory we can at this point do no better than present stress-strain curves which are expected on the basis of (7) and (8) with all parameters except β remaining constant.

For the case of pre-straining to different levels of workhardening, without change between the conditions of pre-strain and testing or use, (9) and (10) simply predict substitution of elastic deformation to the level of the previously highest flow stress. This conventional behavior, indicated for mode I in Fig. 2, generates the expected curves for ordinary metals

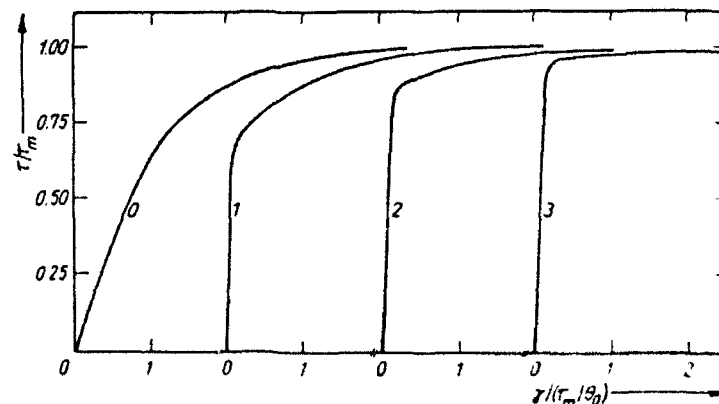


Fig. 2. Theoretical stress-strain curves for mode I, derived from that in Fig. 1, for different pre-strains (in units of τ_m/τ_0) as indicated at the curves

and alloys pre-strained to different levels of hardness through one and the same type of deformation. By contrast, if unconventional manufacturing conditions have established a flow stress

$$\tau = \tau_m + \delta\tau_m, \quad (12)$$

worksoftening results as

$$d\tau = -\theta_0 \left(\frac{\tau}{\tau_m} - 1 \right) d\gamma \quad (13)$$

in mode I, and

$$d\tau = -\theta_0 \left[\left(\frac{\tau}{\tau_m} \right)^2 - 1 \right] d\gamma \quad (14)$$

in mode II in accordance with (7) and (8).

Integrating (13) and (14) yields, for the virgin material,

$$\tau = \tau_m + \delta\tau_m \exp \left(-\frac{\gamma\theta_0}{\tau_m} \right) \quad (15)$$

for mode I and

$$\tau = \tau_m \coth \left[(\gamma + \gamma_x) \frac{\theta_0}{\tau_m} \right] \quad (16)$$

for mode II, with γ_x that negative strain for which τ would become infinite.

Fig. 3 presents worksoftening curves, without pre-strain after manufacturing, resulting from (15) and (16) for $\delta\tau_m/\tau_m = 2/3$, which requires $\gamma_x = 0.694\tau_m/\theta_0$.

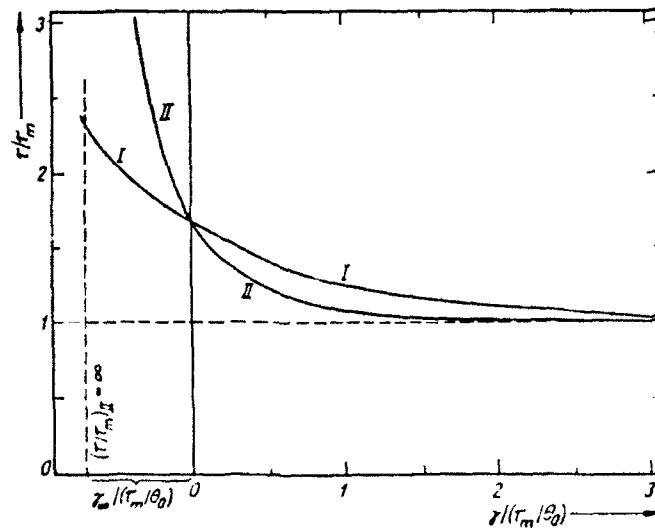


Fig. 3. Theoretical worksoftening curves due to negative values of the trapping parameter θ on account of excess dislocation density for mode I and mode II in accordance with (15) and (16)

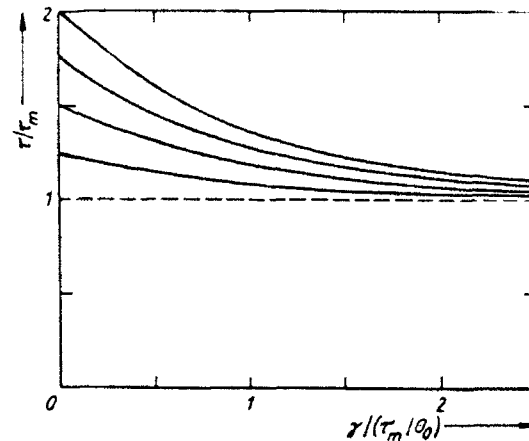


Fig. 4. Worksoftening curves due to negative β -values for mode I, as in Fig. 3, but for different initial flow stresses caused by either pre-strain or annealing

At such rather high excess hardening through the manufacturing process, the difference between the two modes is evidently more pronounced than for the conventional cases shown in Fig. 2. That difference will, of course, decrease with decreasing $\delta\tau_m/\tau_m$. Dependence on this parameter is shown for mode I in Fig. 4, which at the same time presents the evolution of the worksoftening curve when $\delta\tau_m$ is progressively reduced through either straining or annealing after manufacturing but prior to testing or use.

6.2 Effect of decreasing τ_0

Changes in τ_0 have two independent effects. On the one hand, τ_0 is simply additive in accordance with (1), on the other hand, increasing τ_0 shortens the closest distance of approach of the dislocations before they can annihilate, which has the effect of increasing β as well as ϱ_m .

Matters are further complicated because part of the increase of τ_0 through hydrostatic pressure concerns the Peierls-Nabarro stress and is simply reversible, but another part is due to the increased stress required for dislocation cross slip and dislocation intersections [46, 47]. The latter can in fact cause a reduction in β through decreasing the number of dislocation nodes. It is therefore possible that this latter effect, plus perhaps other more subtle changes in the LEDS including possible redistribution of precipitates and inclusions, can in cases more than counterbalance the first effect. In that case there will be a net reduction of β when τ_0 is increased through hydrostatic pressure.

There is no known intrinsic maximum value of τ_0 , and the most likely cause of reductions in τ_0 on straining unconventionally formed alloys is the reorganization of the dislocations into a LEDS pattern with fewer nodes. Therefore, the most simple assumption would be that each newly released loop decreases τ_0 by a like amount, while β is nearly zero so that the dislocation density remains essentially constant at ϱ_m . In that case, since the strain increment per loop would remain constant until the excess frictional stress ($\delta\tau_n$) has been removed at some final strain γ_n , it would be

$$\delta\tau_n = \delta\tau_{n1} \left[1 - \frac{\gamma}{\gamma_n} \right]. \quad (17)$$

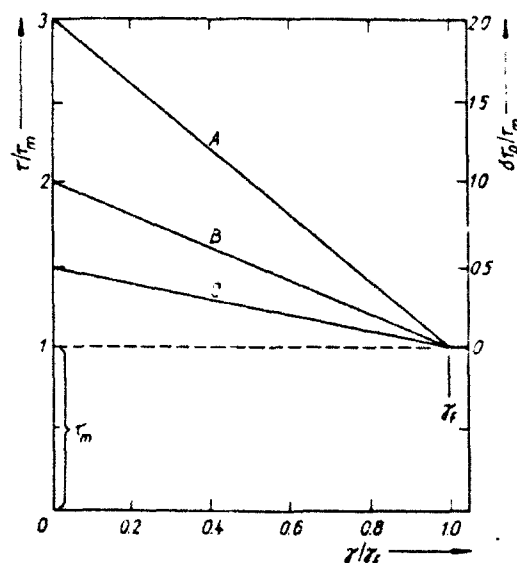


Fig. 5. Worksoftening due to decrease of excess friction stress in accordance with (17) with constant γ_f for different initial flow stress values, either due to pre-strain or annealing

We may estimate the value of γ_f from considering that transformation from the old to the new LEDS will be completed, and thereby $\delta\tau_0$ will have been eliminated, when the newly generated loop length equals some moderate fraction, C , of the dislocation density ϱ_m . Thus in accordance with (2) to (4), with n_f the number of links that have been activated between $\gamma = 0$ and γ_f ,

$$n_f 4g\bar{l} = C\varrho_m \quad (18)$$

and

$$\gamma_f = n_f g^2 \bar{l}^2 h = C g m b \sqrt{\varrho_m} / 4. \quad (19)$$

This type of worksoftening curve is represented in Fig. 5 with γ_f independent of $\delta\tau_0$, the initial value of the friction stress. Such constancy of C is, however, not a foregone conclusion as follows.

In order to estimate a probable range of values for γ_f one must first estimate C . Clearly, C must lie well below unity but cannot be a very small number. This is for the reason that the new dislocations are replacing an equal length of pre-existing dislocation length that had been subject to the excess frictional stress, and will have triggered additional spontaneous reorganization among the pre-existing dislocations. Thus for somewhat similar initial and final LEDS's $0.1 < C < 0.5$ may be a reasonable range. With those values and with $b = 3 \times 10^{-10}$ m, $\varrho = 4 \times 10^{15}$ m $^{-2}$, $m \approx 1$, and $g \approx 25$ typical for highly strained metals [7] one finds γ_f to range between about 1% and 10%. That result appears to be in line with observed worksoftening curves.

However, one will expect C to be larger when initial and final LEDS configurations and energies are similar, i.e. when the driving forces are small, than when those differences and the driving forces are large, such as presumably tend to accompany large drops in the friction stress. This reasonable argument suggests that C decreases with rising $\delta\tau_0$. Also the value of ϱ_m , while probably not deviating much from 4×10^{15} cm $^{-2}$ as previously

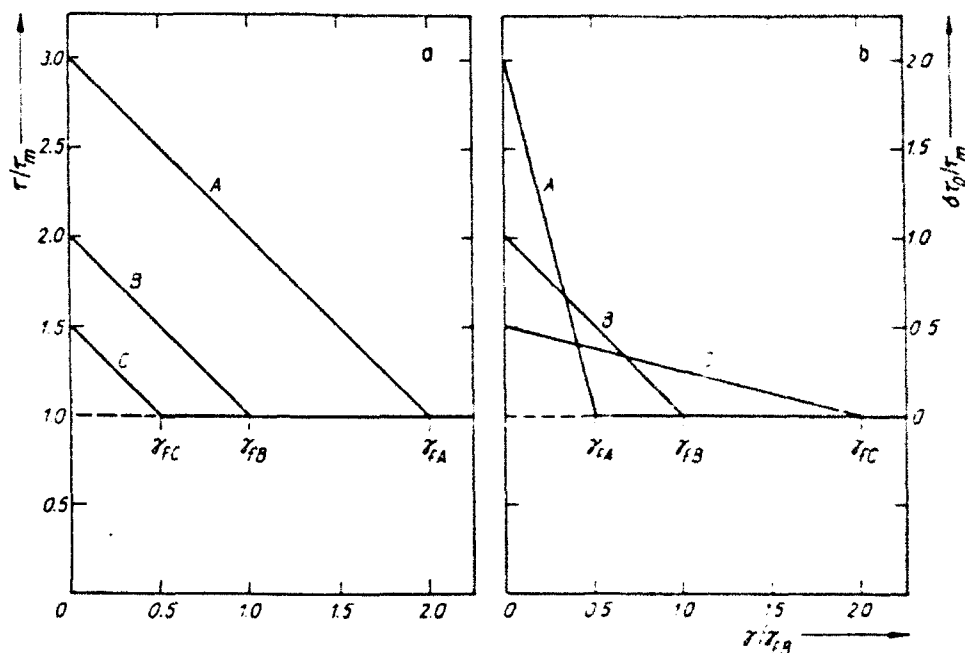


Fig. 6. Worksoftening curves based on (17), as in Fig. 5, but assuming that a) γ_f is proportional to $\delta\tau_0$, and b) γ_f is inversely proportional to $\delta\tau_0$.

introduced, will in fact not be the same in all cases and indeed the LEDS reorganization will generally not take place at accurately constant dislocation density.

In order to assess the overall effect of these complications, somewhat arbitrarily one may assume that, for relatively large LEDS energy differences, the value of γ_f could be inversely proportional to $\delta\tau_0$. On the other extreme, every loop might simply decrease $\delta\tau_0$ by the same amount independent of LEDS energy differences, which would amount to γ_f being proportional to $\delta\tau_0$. These extreme behaviors are depicted in Fig. 6.

7. First Comparison with Experimental Data

The theory evidently provides a broad framework for the classification of different types of worksoftening, and thence hopefully an entrance to their deeper understanding. An independent paper [48] shall begin this task. Here only one first example as shown in Fig. 7, namely Fig. 6 of [48], obtained from two very similar mechanically alloyed aluminum-niobium samples of same grain size and composition except for the addition of 1 wt% of Y_2O_3 to the B2 alloy. As seen, this addition caused a strong increase of yield strength, followed by a much steeper worksoftening curve on straining than without it.

A detailed metallographic examination and perhaps still other studies will doubtlessly be needed in order to determine the distribution of the yttrium oxide and its effect on the friction stress and, presumably, on the LEDS formed. However, independent of such studies, the curves clearly are not of the type in Fig. 3 and 4 but they do conform to Fig. 6b. The present theory therefore leads to the following conclusions.

(i) The worksoftening in both alloys is due, at least principally, to a reduction of the friction stress during straining.

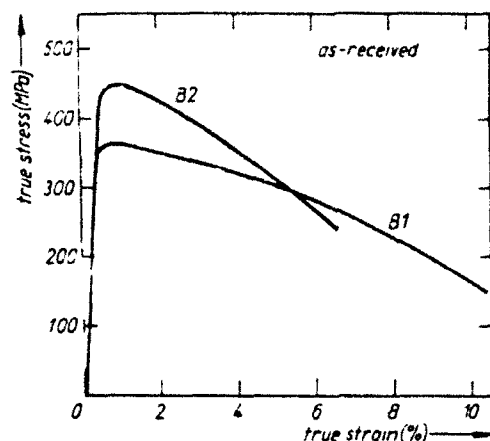


Fig. 7. True stress-true strain curves of mechanically alloyed aluminium-niobium with identical grain sizes but with (B2) and without (B1) an addition of 1 wt% of Y_2O_3 , according to Fig. 6 of [48].

(ii) The effect of the yttrium oxide is to strongly raise the friction stress beyond the already high level present without it.

(iii) The yttrium oxide caused a significant increase in the energy stored in the LEDS in the as-received state, while the energy and presumably geometry of the LEDS established through straining is not much affected by it.

(iv) Therefore the transformation into the new LEDS required the movement of fewer dislocations in the alloy with the yttrium oxide than needed without it.

(v) On the basis of (19) applied to Fig. 7, the percentage of newly generated compared to pre-existing dislocation density required for transformation of the LEDS, was about 50% without and 25% with the yttrium oxide.

(vi) Since the activation of one link increases the dislocation length from \bar{l} to $4g\bar{l}$, more or less, with g believed to be near 25, this means, therefore, that the activation of only 0.5% and 0.25%, respectively, of the pre-existing dislocations was sufficient to transform the LEDS.

(vii) That fine scale of the dislocation reorganization is the reason why the drastic worksoftening observed is not yet accompanied by Luders band formation.

The above conclusions must, of course, be checked against all available evidence, first and foremost the micrography, and depending on the results obtained the theory may have to be modified and/or expanded. That task will be begun in the follow-up paper [48].

8. Summarizing Discussion

To the simplified first approximations discussed herein, worksoftening due to negative values of β is characterized by concave workhardening curves. This result is independent of specific assumptions as to the functional dependence of β on ρ , provided that β decreases, and the flow stress increases, monotonically with the excess population of dislocations, and that β vanishes asymptotically at the equilibrium flow stress τ_m .

By contrast, there is no known a-priori argument to relate the magnitude of excess friction stress to the dislocation density and therefore none to relate its decrease to the shear strain. The most simple assumptions lead to a linear decline of stress with strain, whereby the slope of the decline is proportional to $\delta\tau_m$, the initial excess frictional stress. In that most simple case, therefore, worksoftening ceases at some strain γ_f independent of $\delta\tau_m$. However, since large drops in $\delta\tau_m$ are presumably correlated with relatively large dislocation energy

differences and thus driving forces to establish the new LEDS, probabilities are that τ_0 decreases with increasing $\delta\tau_{0i}$ values. The specific experimental example of Fig. 7 appears to bear this out.

At the other extreme, driving forces may have no effect at all and every loop could cause the same reduction of $\delta\tau_0$ no matter what the conditions. In that case the slope of the workhardening curve is independent of $\delta\tau_{0i}$.

Doubtlessly different assumptions or, better, different actual conditions in the alloys, can give rise to a still much wider variety of stress-strain curves in worksoftening due to decreasing τ_0 . At any rate, the theory will have opened a new way for further research into worksoftening, of which an example, including a number of tentative conclusions, is presented in connection with Fig. 7. A subsequent paper [48] will expand on these.

Acknowledgements

The financial support of this research through the Materials Division (P. Schmidt and M. B. Peterson, Tribology) of the Office of Naval Research, Arlington, VA, as well as through the Defense Advanced Research Projects Agency (P. Kemmey, TTO, Arlington, VA, monitored by T. Gora, Piccatinny Arsenal) is gratefully acknowledged. The experimental work was supported by US Air-Force contract F 33615-86-C-5074.

References

- [1] M. N. BASSIM, W. A. JESSER, D. KUHLMANN-WILSDORF, and H. G. F. WILSDORF, *Low-Energy Dislocation Structures I*, Elsevier Sequoia, Lausanne 1986; see also *Mater. Sci. Engng.* **81**, 1 to 574 (1986).
- [2] M. N. BASSIM, W. A. JESSER, D. KUHLMANN-WILSDORF, and G. J. STUELT (Ed.), *Low-Energy Dislocation Structures II*, Elsevier Sequoia, Lausanne 1989; see also *Mater. Sci. Engng. A* **113**, 1 to 458 (1989).
- [3] D. KUHLMANN-WILSDORF, *Proc. Internat. Symp. Solid State Physics, Calcutta 1977* (p. 10); see also *Indian J. Phys.* (special issue) (1980).
- [4] D. KUHLMANN-WILSDORF and N. COMINS, *Mater. Sci. Engng.* **60**, 7 (1983).
- [5] D. KUHLMANN-WILSDORF, *Mater. Sci. Engng.* **86**, 53 (1987).
- [6] D. KUHLMANN-WILSDORF, *phys. stat. sol. (a)* **104**, 121 (1987).
- [7] D. KUHLMANN-WILSDORF, see [2] (p. 1); see also *Mater. Sci. Engng. A* **113**, 1 (1989).
- [8] D. KUHLMANN-WILSDORF, in: *Modeling the Deformation of Crystalline Solids*, Ed. T. C. LOWE, T. ROLLETT, P. S. FOLLANSBEE, and G. S. DAHIN, TMS, Warrendale (PA) 1991 (p. 105).
- [9] N. HANSEN and D. KUHLMANN-WILSDORF, *Mater. Sci. Engng.* **81**, 141 (1986).
- [10] B. BAY, N. HANSEN, and D. KUHLMANN-WILSDORF, see [2] (p. 385).
- [11] B. BAY, N. HANSEN, D. A. HUGHES, and D. KUHLMANN-WILSDORF, *Acta Metall. et Mater.* **40**, 205 (1992).
- [12] B. BAY, N. HANSEN, and D. KUHLMANN-WILSDORF, *Acta Metall. et Mater.*, in the press.
- [13] J. E. BAILEY and P. B. HIRSCH, *Phil. Mag.* **5**, 485 (1960).
- [14] A. SEIGER, in: *Hdb. Physik*, Vol. VII/2, Ed. S. FLUGGE, Springer-Verlag, Berlin 1958.
- [15] E. C. FRANK and W. T. READ, *Phys. Rev.* **79**, 722 (1950).
- [16] T. E. MITCHELL and R. L. SMALICK, in: *Workhardening*, Ed. J. P. HIRTH and J. WEHRMANN, Gordon & Breach, New York/London 1968 (p. 365).
- [17] M. N. BASSIM and D. KUHLMANN-WILSDORF, *phys. stat. sol. (a)* **17**, 281 (1973), **19**, 335 (1973).
- [18] D. KUHLMANN-WILSDORF, see [16] (p. 97).
- [19] K. HIGASHIDA, J. TAKAMURA, and M. NARITA, see [1] (p. 239).
- [20] K. JAGANNADHAM and H. G. F. WILSDORF, see [1] (p. 273).
- [21] C. T. YOUNG, T. J. HEADLY, and J. L. LYTTON, see [1] (p. 391).
- [22] A. FOITZIK, W. SKROTZKI, and P. HAASEN, see [2] (p. 399).
- [23] M. LUTER-KNIPPMER and T. LINK, see [2] (p. 191).

- [24] T. K. LEPISTÖ, V. T. KUOKKALA, and P. O. KETTUNEN, see [1] (p. 457).
- [25] P. NEUMANN, see [1] (p. 465).
- [26] J. I. DICKSON, L. HANDFIELD, and G. L'ESPERANCE, see [1] (p. 477).
- [27] C. LAIRD, Z. WANG, B.-T. MA, and H.-F. CHAI, see [2] (p. 245).
- [28] Z. G. WANG, Z. M. SUN, and S. H. AI, see [2] (p. 259).
- [29] R. KELLER, W. ZIELINSKI, and W. W. GERBERICH, see [2] (p. 267).
- [30] D. KUHLMANN-WILSDORF and N. HANSEN, *Scripta Metall. et Mater.* **25**, 1557 (1991).
- [31] E. O. HALL, *Proc. Roy. Soc. B* **64**, 474 (1951).
- [32] N. J. PETCH, *J. Iron Steel Inst.* **174**, 25 (1953).
- [33] N. HANSEN and D. JUUL JENSEN, in: *Proc. Internat. Conf. Strength of Metals and Alloys*, Ed. D. G. BRANDON, R. CHAIMAND, and A. ROSEN, Freund Publ. House, London 1991 (p. 953).
- [34] D. KUHLMANN-WILSDORF, *Metallurg. Trans.* **1**, 3173 (1970).
- [35] J. GIL SEVILLANO, P. VAN HOUTTE, and E. AERNOUDT, *Progr. Mater. Sci.* **25**, 69 (1980).
- [36] A. D. ROLLET, U. F. KOCKS, and R. D. DOHERTY, in: *Formability and Metallurgical Structure*, Ed. A. K. SACHDEV and J. D. EMBURY, TMS, Warrendale (PA) 1987 (p. 211).
- [37] J. GIL SEVILLANO and E. AERNOUDT, *Mater. Sci. Engng.* **86**, 35 (1987).
- [38] H. MECKING and Y. ESTRIN, in: *8th Internat. Symp. Metallurgy and Materials Science, Riso 1987*, Ed. S. I. ANDERSEN, J. B. BILDE SORESEN, N. HANSEN, T. LEFFERS, H. LILHOLT, O. B. PEDERSEN, and B. RALPH, Nat. Lab., Roskilde (Denmark) 1987 (p. 123).
- [39] N. HANSEN and D. JUUL JENSEN, *ibid.* (p. 332).
- [40] D. KUHLMANN-WILSDORF and N. HANSEN, *Metallurg. Trans.* **20A**, 393 (1989).
- [41] P. HAASEN, *Phil. Mag.* **3**, 384 (1958).
- [42] P. HAASEN, *Physikalische Metallkunde*, Springer-Verlag, Berlin 1974 (pp. 276 to 280).
- [43] D. A. RIGNEY, *Scripta metall.* **13**, 353 (1979).
- [44] P. HAASEN and A. W. LAWSON, *Z. Metallk.* **49**, 280 (1958).
- [45] D. KUHLMANN-WILSDORF, B. C. CAI, and R. B. NELSON, *J. Mater. Res.* **6**, 2547 (1991).
- [46] W. A. JESSER and D. KUHLMANN-WILSDORF, *Mater. Sci. Engng.* **9**, 111 (1972).
- [47] D. KUHLMANN-WILSDORF, *phys. stat. sol. (b)* **47**, 639 (1978).
- [48] H. G. F. WILSDORF and D. KUHLMANN-WILSDORF, *Z. Metallk.*, in the press.

(Received February 12, 1992)

FUNDAMENTALS OF CELL AND SUBGRAIN STRUCTURES IN HISTORICAL PERSPECTIVE

Doris Kuhlmann-Wilsdorf
Department of Materials Science
University of Virginia, Charlottesville, VA 22901

(Received July 27, 1992)

The Mosaic Block Structure

Since 1914 crystallographers have known that real crystals are overwhelmingly composed of a 'mosaic block structure' (1) which in P. Ewald's words of 1933 (2) consists "of many by themselves ideal 'coherent' blocks . . . which are fitted together with mutual small rotations . . ." Correspondingly, as soon as dislocations were recognized as the carriers of plastic deformation (3,4), materials scientists have accepted that the mean free path of dislocations starts and ends at mosaic block boundaries (3,5,6). Further, already in his epoch-making papers proposing the first dislocation based theory of workhardening, G. I. Taylor introduced the edge dislocation tilt wall as the prototypical mosaic block boundary (3).

That all mosaic block boundaries are composed of dislocations, being what we now call dislocation cell walls or subgrain boundaries, as the case may be, was not known for decades to come. Namely, when finally dislocations could be directly observed in the electron microscope, the ubiquitous presence of the mosaic block structure had faded from active consideration and no connection was made between mosaic block boundaries and the pervasive dislocation "tangles" and "cottonwool structure" seen in lightly deformed single crystals. This is quite understandable since tangles and cottonwool structures did not at all conform to the expected appearance of mosaic block boundaries. When accumulating evidence showed that with continuing strain those woolly structures gradually developed into dislocation cell walls and these into subgrain boundaries, their initial explanation as obstacles against glide due to random dislocation collisions was not abandoned. The identification of dislocation walls with mosaic block boundaries was first established only in 1968 (7), and for the outlined and other historical reasons discussed in greater detail elsewhere (8), it did not find ready acceptance.

Nowadays there can be no doubt left that all dislocation cell and subgrain structures are mosaic block structures: The typically abrupt change of electron diffraction contrast across the boundaries and its typical constancy over individual dislocation cells and subgrains testify that those volume elements are substantially free of lattice misorientations and that the dislocation walls defining them accommodate well-defined lattice rotations. This qualitative evidence is buttressed and transformed into quantitative knowledge by a constantly increasing mass of detailed lattice orientation determinations, e.g. (9,10). Phrased differently, it has been established without reasonable doubt that the boundaries delineating dislocation cells and subgrains are "dislocation rotation boundaries". The task, then, is to understand why and how dislocations so overwhelmingly assemble into mosaic dislocation rotation boundaries and what effect that has on mechanical properties.

Frank's Formula

The concept of "dislocation rotation boundaries" is by far not as widely understood as would be commensurate with its importance. It is based on F.C. Frank's brilliant insight (11) elaborated in W.T. Read's book (12) that, besides the discussed lattice misorientations, every arbitrary two-dimensional dislocation arrangement with finite, uniformly distributed net Burgers vector content is associated with long-range stresses unless it obeys a very stringent requirement. This requirement, known as Frank's formula, is that \vec{B} , the sum of the Burgers vectors of all dislocations intersected by unit vector \vec{v} of arbitrary orientation in the network, be

$$\vec{B} = 2\sin(\Theta/2) [\vec{u} \times \vec{v}] \quad (1)$$

where \vec{u} is the axis vector of relative misorientation between the material on either side of the boundary, and Θ is the magnitude of the misorientation angle. Of course, \vec{B} can vanish for all orientations of \vec{v} simply because the wall has no net Burgers vector content; but if \vec{B} is finite for any orientation of \vec{v} and eq. 1 is not fulfilled, the wall has long-range stresses. Evidently, then, dislocation cell and subgrain boundaries fulfill the stringent requirement of Frank's formula at the least in first approximation. We shall further discuss eq. 1 in the next section for the polygonization structure.

If a given density of dislocations is randomly distributed, their mutual distances will be larger than if arranged in the form of planar arrays. Since further the stresses of the dislocations in dislocation rotation boundaries are screened to the range of their mutual spacing, more or less, in accordance with Frank's formula, theory establishes dislocation rotation boundaries as the form of lowest possible free dislocation energy. Even so, theory cannot yet predict the specific boundary geometry which will minimize free energy and thus be the most stable.

The Polygonization Structure

The simplest type of dislocation boundary structure is the polygonization structure which consists of (nearly) parallel tilt walls. It is most perfectly observed in bent plate-shaped single crystals with the most highly stressed, and only significantly activated, glide plane containing the bending axis and the active Burgers vector parallel to the narrow side face (13), the geometry indicated in Fig. 1. With only one active slip system, \vec{B} must have the direction of the one active Burgers vector, while according to eq. 1 \vec{B} must be normal to both \vec{v} and \vec{u} . Since \vec{v} can have all orientations in the boundary, \vec{B} is thus normal to the boundary, and the rotation axis \vec{u} lies in the boundary. Lastly, with only one set of parallel dislocations present, \vec{B} vanishes only if \vec{v} is parallel to the dislocation lines, and therefore \vec{u} must also be parallel to the dislocations. Thus the only dislocation boundary which fulfills Eq. 1 and is constructible with but one set of dislocations is the edge dislocation tilt wall.

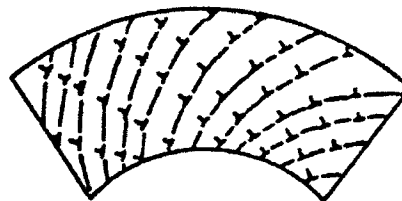


Fig. 1 Idealized polygonization structure of a bent single crystal gliding on just one slip system.

Stresses and Energies of Dislocation Cells: The LEDS Principle

The empirical observation that dislocations very commonly assemble into a mosaic block structure composed of dislocation rotation boundaries suggests the general rule that actual dislocation structures nearly minimize the free energy per unit length of dislocation line, among all configurations accessible to the dislocations under the constraints of applied tractions and dislocation mobility (7,14). This theorem, now known as the LEDS principle, follows from the second law of thermodynamics, to wit that forces act to drive systems down energy gradients. LEDS, from the acronym for Low-Energy Dislocation Structures (15,16), are dislocation structures in which neighbor dislocations mutually screen their stresses.

The specific theoretical reason for the formation of LEDS, and in particular also for the LEDS principle, is that dislocations interact with glide forces in accordance with their elastic stresses, and as they are mobile in glide, populations of dislocations will move until they have mutually screened their resolved shear stresses to the level of the friction stress τ_0 . In other words: glide forces will compel the dislocations to move until nowhere along their length will there be any resolved shear stress in excess of τ_0 , including any stresses with which curved dislocations act on themselves, i.e. those most simply regarded as due to line tension. In the case of just one Burgers vector, i.e. in the polygonization structure, only one stress component will thus be screened, and similarly in the Taylor lattice, a checkerboard pattern of alternating positive and negative dislocations (3,17). It is for this reason that lower energy per unit length of dislocation line is achieved with increasing number of Burgers vectors (18). Hence stress-screening becomes more effective with increasing number of Burgers vector directions available in the LEDS, and any stress component in excess of τ_0 will tend to move and suitably multiply dislocations with Burgers vectors of a kind that can screen those stress components.

As an example of the above, somewhat imperfect Taylor lattices can be formed in fatigue (17) when dislocations of opposite sign are forced to mix intimately, and in uni-directional deformation when dislocations cannot leave their respective slip planes, as is the case when dislocations are extended as in α -brass (21) but not otherwise since unidirectional glide tends to separate dislocations according to sign. In fact, and as already Taylor recognized, his edge dislocation lattice is unstable against lateral spreading and has to be confined between mosaic block or grain boundaries (3). This instability is due to the unscreened alternating compressive and tensile stresses in the parallel slabs of material defined by the rows of like dislocations on the glide planes. We shall return to the specific dislocation motions triggered thereby when we consider the cell formation in fcc metals that marks the onset of stage II.

In order to gain some insight as to which dislocation configurations might have the lowest possible energy when three coplanar equivalent Burgers vectors are available, such as on {111} in fcc metals, a series of computations were performed on the stress distributions about simple dislocation cells constructible from dislocation rotation boundaries with such Burgers vectors (19). The results confirmed that increasing number of participating Burgers vectors decreases the energy per unit length of dislocation line. They also showed that dislocation cells arranged in the form of isolated rotated volume elements, much like pebbles in concrete, have a much higher energy than the mosaic block structure. Next they showed that roughly equiaxed cells would be preferred and, finally, that a three-dimensional checkerboard pattern of simi-

lar rectangled cells, misoriented about the same rotation axis but with alternating sense of rotation has an especially low energy. These, then, are features theoretically predicted from the LEDS principle, and they are indeed very largely observed (see 14, 18, 20 and many examples in refs. 15 and 16).

Mechanisms of Dislocation Cell Formation and "Forest Dislocations"

In single crystal experiments in macroscopic single glide, the onset of stage II is characterized by the profuse generation of non-primary dislocations, typically outnumbering the primary dislocations by two to one even before double glide sets in. These unpredicted dislocations were dubbed "forest dislocations" because they appeared to be pre-existent, or at the least immobile so that they had to be cut by the glide dislocations. In fact the role of those dislocations is quite different as may be best clarified by discussing the transition from stage I to II in fcc single crystals, as follows (18,21,22).

At the end of stage I there exists a poorly formed Taylor lattice. It exhibits the already mentioned alternating compressive and tensile stresses due to the extra and missing lattice half planes of the edge dislocation sequences of opposite sign on parallel glide planes (18,21,22). When with increasing dislocation density these have built up to the level of the flow stress of the material in the slabs, they trigger "unpredicted glide" on intersecting glide planes. This is carried by the dislocations which are commonly mistaken for "forest dislocations" but whose function is to relieve the said stresses and in the process to transform the sequences of mutually repulsive similar edge dislocations into tilt walls, in accordance with the LEDS principle. Jackson et al. were among the first to make a detailed study of those stresses and the resultant complex dislocation motions in pure fcc metal (23-25). A subsequent analysis of these motions in terms of Frank's formula established the underlying mechanism of cell formation through strain energy reduction without a doubt (22,26). As it turns out, the rotation axis of the tilt walls replacing the initial sequences of like edge dislocations lies in the glide plane, normal to the primary Burgers vector. They are responsible for the so-called "Yamaguchi-Taylor roller orientation" that had been discovered through Laue X-ray asterism and correctly interpreted by Taylor (27) and Yamaguchi (28) many years before.

Besides those studies on the mechanism of dislocation cell formation in early stage II, a very detailed investigation of dislocation wall and cell formation in stage I of tensile specimens, again of fcc single crystals, has been presented by Takamura and coworkers (29). Another analysis was performed on peculiar dislocation patterns in rolled iron single crystals (30), and recently there have been searching studies on the evolution of cell and subgrain boundaries in rolled polycrystals (9, 10). Together, these studies establish details of the dislocation motions which produce observed dislocation cell structures, and the stresses triggering them, for a large enough number of cases to remove any further doubt that the principles are well understood. From those studies, too, it is indisputable that "forest dislocations" are formed in response to unscreened stresses of accumulating glide dislocations. Thus they are not pre-existing, are not stationary, and are not intersected by the glide dislocations. Correspondingly, the term "forest dislocations" ought to be dropped. In summary, then, dislocation cell formation is impossible with only one Burgers vector but it requires the involvement of at least two Burgers vector directions. In cases of small strains in single glide, the non-primary dislocations necessarily involved in dislocation cell formation were named "forest dislocations". Since at the nodes of two sets of networking dislocations a third set with a different Burgers vector is formed (in fcc metals happening to be Lomer-Cottrell locks (22)), the non-primary traditional "forest dislocations", outnumber the primary ones by about two to one, even while macroscopic single glide prevails.

Glide Polygonization, Dynamical Recovery and Point Defects

In an unpublished Ph.D. thesis, H. Shen (31) studied the geometry of polygonization walls in bent aluminum single crystals and the effect of annealing treatments thereon. Rather surprisingly, and in opposition to some earlier work by Gilman (32) and Hibbard and Dunn (33), neither the locations of the polygonization walls nor their rotation angles were affected by long anneals up to a few degrees of the melting temperature. The only change observed was a clearing of the background intensity between the walls and establishment of some additional polygonization walls.

This result is ever more remarkable because the walls are composed of glide dislocations and can move readily. In fact, already the very first in-situ observations on specimens strained in the electron microscope (34,35) showed all dislocation cell walls to be highly mobile during straining. From moment to moment they remained individually distinguishable, but with fluid dislocation densities and shapes. Moreover, elements of beginning tilt walls could be seen forming already while the dislocations were still in motion (36) in the process dubbed "glide polygonization". By itself, Shen's result thus implies that already directly after deformation the structure is close to thermal equilibrium, in excellent accord with the LEDS principle, albeit metastable since the removal of all dislocations would of course reduce the free energy. Beyond this, the in-situ observations demonstrate that the mutual trapping of glide dislocations into the cell structure configuration may already begin while they are still moving through the cell interiors, but at any rate is essentially completed by the time they reach the cell walls and are incorporated into them.

Quite at odds with the demonstrated tendency for minimizing the stored energy per unit length of dislocation line in accord with the LEDS principle is the kinkiness that characterizes cell wall dislocations after low deformations and which

gave rise to the nomen "cottonwool structure". According to early work, it results from dislocation-point defect interactions in a process dubbed "mushrooming". (37-39). While this interpretation has never been questioned in the literature, it still needs independent verification. Facts are that large numbers of point defects are inevitably generated through glide and that these cannot be retained in the lattice and must somehow be removed through absorption at dislocations, thereby causing local climb.

Mushrooming is envisaged to occur at low homologous temperatures, when local plating out of supersaturated point defects at dislocation cores gives rise to kinking, as seen especially clearly in radiation damaged metal (40). The jogs so formed must be dragged in glide and therefore give rise to further distortions of the dislocations when stress is applied. However, in the proximity of nodes, point defects may be adsorbed through simple readjustments of the dislocations at these, and they can escape through free surfaces. Therefore, the cottonwool structure can appear only at combinations of temperature and dislocation density such that pipe diffusion is too slow to transport the defects to nearby nodes or free surfaces. Correspondingly the cottonwool structure is not formed at elevated temperatures nor in very thin foils, and also not when dislocation densities are high; and it is easily removed through mild annealing. It seems almost certain, therefore, that the recovery mechanism indirectly observed by Shen (31) was the smoothing out of the cottonwool structure and the attendant sharpening of the tilt wall structure.

While as indicated, LEDS structures are stable relative to glide, and thermal activation even at temperatures up to the melting point cannot significantly assist glide motions, they are not stable relative to climb. Recovery annealings at temperatures permitting significant climb rates can thus reorganize LEDS structures, - always subject to the law of the conservation of Burgers vectors, of course. Through climb, dislocation walls can thus coalesce but only such that the net Burgers vector content in them is conserved. The frequent increases in the rotation angles of polygonization walls through recovery as first observed by Gilman (32) and Hibbard and Dunn (33) are doubtlessly due to such climb-induced coalescences. In general, recovery annealings can similarly coarsen any cell structures and thereby decrease the total strain energy, partly through decreasing the overall dislocation density and partly through decreasing the average screening distance among the dislocations.

In light of the discussions in this section, the widely used although ill-defined word "dynamic recovery", if meant to explain the presence of seemingly "recovered" LEDS structures directly after plastic deformation, does not appear to serve a useful purpose, since it evokes the image of effects of dislocation dynamics and of thermal activation. Quite likely it is a lingering memory of Becker's early theory of plastic flow (41,42) which assumed that plastic deformation was a fundamentally dynamic process due to thermally activated but otherwise unspecified elementary glide steps but without an equilibrium state (compare the discussion in 8). Becker's ideas remain relevant when deformation temperatures are high enough to permit climb, i.e. in the creep range, but at low homologous temperatures, at which the cumulative effect of thermally activated flow steps during plastic strain amounts to only a fraction of the elastic strain (43), facts are in much better accord with G.I. Taylor's 1933 workhardening theory (3) based on force equilibrium among glide dislocations in the Taylor lattice.

The Dependence of Dislocation Cell Size on Flow Stress

The flow stress in Taylor's theory was the stress required for further edge dislocation generation and motion via the passage of dislocation rows in the Taylor net past each other. The restriction of Taylor's considerations to edge dislocations is natural because screw and mixed dislocations would be introduced into materials science only seven years later (44). Implicit in Taylor's theory is the establishment of a dislocation density (ρ) proportional to the square of the flow stress (τ) as

$$\tau = \text{const } Gb\sqrt{\rho} \quad (2)$$

with G the shear modulus. This is a well-known very widely observed empirical relationship (45-47), but the proportionality constant for Taylor lattices is different from that for cell walls (7,21). Similarly widely observed is the empirical relationship between average dislocation cell diameter, D , and flow stress

$$D = KGb/\tau \quad (3)$$

with $K \approx 10$.

Based on the LEDS principle, eq.3 must minimize the free energy per unit length of dislocations line. The mechanism appears to be as follows (18,48): If a dislocation population of fixed density ρ is assembled into a dislocation cell structure of variable cell size D , the average dislocation spacing, $l = 1/\sqrt{\rho}$, decreases with increasing D . Thus the strain energy stored in the unscreened dislocation stresses, extending to $\approx l$ from the dislocation axes on average, decreases with D . However, finite dislocation walls have end stresses which increase with their extent, i.e. the energy stored in the cell end stresses rises with D . According to semi-quantitative argument (48) which, however, urgently needs refinement, eq.3 in conjunction with eq.2 and $l = 1/\sqrt{\rho}$ is indeed the condition minimizing the sum of the two components of the stored energy. Eq.2, in turn, describes the stress for super-critical bowing of dislocations through dislocation cell walls (7,49), in agreement with the mesh-length theory of workhardening (7,8,14,21).

Geometrically Necessary Versus Incidental Dislocation Rotation Boundaries and Their Hardening Effect

According to the preceding exposition, the dislocation cell boundaries discussed so far are dislocation rotation boundaries resulting from the statistical mutual trapping of glide dislocations into energy wells too deep as if the applied stress could release them. As pointed out already, this concept is in the tradition of Burgers (3) and is supported by a great wealth of experimental evidence. In fundamental contrast thereto, and in the tradition of Becker's theory (41,42), is the proposal of Staker and Holt (47) that moving dislocations establish statistical density fluctuations which will either be seen as dislocation cell walls or be the origin of them. Similarly, Aifantis (50) has proposed a complex theory of dynamical dislocation cell formation. Perhaps these theories will eventually be found useful for understanding dynamical recrystallization or rapid creep, but they cannot be significant for cell structure formation. The only dynamical aspects of low-temperature plastic deformation appear to be the already discussed dislocation point defect interactions plus effects which arise when at high strain rates several glide dislocations traverse any one cell interior at the same time. Those effects have been explained without conflict and without invoking thermal activation (51).

Besides the dislocation cell walls, other dislocation rotation boundaries are formed in the course of plastic deformation, and increasingly so at high strains. They are variously called dense dislocation walls (DDW's) and microbands (MB's) of different types. In order to distinguish simple dislocation cell walls from these, they have been dubbed "incidental boundaries" (52). The second type by contrast belongs to the class of "geometrically necessary boundaries" of which ordinary grain boundaries are the most obvious example. As recent research has documented (10), they come about because, especially in polycrystals, neighboring volume elements (named cell blocks* or CB's for short) deform with selections of different active slip systems whose number falls short of the Taylor criterion. This is for the reason that the simultaneous action of several intersecting glide systems requires profuse jogging and thus an extra stress increment that rises with number of simultaneously acting systems. Therefore neighboring CB's undergo different lattice rotations in the course of straining. The DDW's and MB's delineate the boundaries between CB's and because the rotation angles across them are determined by the lattice orientation differences between the CB's, they are indeed "geometrically necessary". Correspondingly, too, the correlated rotation angles are typically considerably larger than those across cell boundaries.

Much interesting detail is accumulating regarding the mechanisms by which the DDW's and MB's form. On account of the law of the conservation of Burgers vectors, in particular, they cannot form in isolation. As a result they typically form pairwise, either by the splitting of a pre-existing DDW or MB, or by the spontaneous activation of a previously dormant slip system in a narrow zone parallel to an easy glide plane (9,10). That is the origin of the frequently seen dislocation wall pairs which have excited much attention in the literature (53-57).

With increasing strain, the CB's shrink in size faster than the individual dislocation cells in them (9,10). The final condition appears to be that each CB contains but one dislocation cell. In other words, through continued straining "incidental boundaries", meaning ordinary dislocation cell walls, are eliminated in favor of "geometrically necessary dislocation boundaries", i.e. CB boundaries. Across these, the angular misorientation is typically much larger than across cell walls, together with a discontinuity in active slip system combinations not present for cell walls. At that stage, individual dislocations are no longer obvious in the walls and they are called "sub grain boundaries".

As seen, eq.2 is theoretically derivable from the presence of "incidental" cell boundaries across which there is no change of active slip systems (7,21), and is widely confirmed for that case (47). However, theoretically (21,52) as well as experimentally (58,59), the hardening through "geometrically necessary" boundaries, as in particular grain boundaries so also DDW's, MB's and, ultimately, subgrain boundaries (58,59), obeys the Hall-Petch relationship, i.e. $\tau = K_p/\sqrt{D}$.

Acknowledgment

The financial support of this research through the Materials Division (P. Schmidt and M. B. Peterson, Tribology) of the Office of Naval Research, Arlington, VA, is gratefully acknowledged.

REFERENCES

- 1) C.G. Darwin, *Philos. Mag.*, **27**, 315, 675 (1914).
- 2) P. Ewald, in H. Geiger (ed.), *"Röntgenstrahlung"*, Springer, Berlin 1933, p.331.
- 3) G.I. Taylor, *Proc. R. Soc. London, Ser. A* **145**, 362, 388 (1934).
- 4) E. Orowan, *Z. Phys.*, **89**, 605, 614, 634 (1934).
- 5) W.G. Burgers, "Plastizität der Kristalle" in R. Houwink, *"Elastizität, Plastizität und Struktur der Materie"*, Akad. Verl. Ges., Leipzig, 1938.
- 6) A. Kochendorfer, *"Plastische Eigenschaften von Kristallen und metallischen Werkstoffen"*, Springer, Berlin, 1941.
- 7) D. Kuhlmann-Wilsdorf, in J.P. Hirth and J. Weertman (eds.), *"Workhardening"*, Gordon and Breach, N.Y., 1968, p.97.

- 8) D. Kuhlmann-Wilsdorf, *Met. Trans.* **16A**, 2091 (1985).
- 9) B. Bay, N. Hansen and D. Kuhlmann-Wilsdorf, in M.N. Bassim, W.A. Jesser, D. Kuhlmann-Wilsdorf and G.J. Shiflet, (eds.), *"Low-Energy Dislocation Structures II"*, Elsevier Sequoia, Lausanne, 1989, p.385; see also *Mater. Sci. Engg.*, **A113**, 385 (1989).
- 10) B. Bay, N. Hansen, D. A. Hughes and D. Kuhlmann-Wilsdorf, *Acta Met. et Mater.*, **40**, 205 (1992).
- 11) F.C. Frank, in *Pittsburgh Symp. on the Plastic Deformation of Crystalline Solids* (in Rept. NAVEXOS-P-834, 1950, Off. of Naval Res., Washington, DC), p.150.
- 12) W.T. Read, *"Dislocations in Crystals"*, McGraw-Hill, Inc., New York, 1953, pp.181-186.
- 13) R.W. Cahn, *J. Inst. Met.*, **76**, 121 (1949); **79**, 129 (1951).
- 14) D. Kuhlmann-Wilsdorf, in *Proc. Int. Symp. Solid State Physics, Calcutta, 1977*, (Indian Ass. f. the Cultivation of Science, Calcutta) p. 10; see also *Indian Jour. of Physics, Special Issue*, 1980.
- 15) M.N. Bassim, W.A. Jesser, D. Kuhlmann-Wilsdorf and H.G.F. Wilsdorf, (eds.), *"Low-Energy Dislocation Structures"*, Elsevier Sequoia, Lausanne, 1986; see also *Mater. Sci. Engg.*, **81** (1986).
- 16) M.N. Bassim, W.A. Jesser, D. Kuhlmann-Wilsdorf and G.J. Shiflet, (eds.), *"Low-Energy Dislocation Structures II"*, Elsevier Sequoia, Lausanne, 1989; see also *Mater. Sci. Engg.*, **A113** (1989).
- 17) D. Kuhlmann-Wilsdorf, *Mater. Sci. Engg.*, **39**, 231 (1979).
- 18) N. Hansen and D. Kuhlmann-Wilsdorf, in ref.15, p.141; see also *Mater. Sci. Engg.*, **81**, 141 (1986).
- 19) M. N. Bassim and D. Kuhlmann-Wilsdorf, *phys. stat. sol.*, (a) **17**, 281 (1973); (a) **19**, 335 (1973).
- 20) D. Kuhlmann-Wilsdorf, *phys. stat. sol.* (a) **104**, 121 (1987).
- 21) D. Kuhlmann-Wilsdorf, in ref.16, p.1; see also *Mater. Sci. Engg.*, **A113**, 1 (1989).
- 22) D. Kuhlmann-Wilsdorf and N. Comins, *Mater. Sci. Engg.*, **60**, 7 (1983).
- 23) P.D.K. Nathanson, P.J. Jackson, and D.R. Spalding, *Acta Metall.*, **18**, 823 (1980).
- 24) O.L. de Lange, P.J. Jackson and P.D.K. Nathanson, *Acta Metall.*, **28**, 833 (1982).
- 25) P.J. Jackson, O.L. de Lange and C.J. Young, *Acta Metall.*, **30**, 483 (1982).
- 26) P.J. Jackson and D. Kuhlmann-Wilsdorf, *Scripta Metall.*, **16**, 105 (1982).
- 27) G.I. Taylor, *Trans. Faraday Soc.*, **24**, 121 (1928).
- 28) K. Yamaguchi, *Sci. Pap. Inst. Phys. Chem. Res. (Jpn.)*, **11**, 151 (1929).
- 29) K. Higashida, J. Takamura and N. Narita, in ref. 15), p.239; see also *Mater. Sci. Engg.*, **81**, 239 (1986).
- 30) D. Kuhlmann-Wilsdorf and E. Aernoudt, *J. Appl. Phys.*, **54**, 184 (1983).
- 31) H.K. Shen, *Polygonization in Bent Aluminum Single Crystals*, Ph.D. Thesis, U. Pennsylvania, Dept. of Metallurgical Engineering, 1963.
- 32) J.J. Gilman, *Acta Met.* **3**, 277 (1955); *Trans. AIME*, **206**, 998 (1956).
- 33) W.R. Hibbard and C.G. Dunn, *Acta Met.* **4**, 306 (1956).
- 34) H.G.F. Wilsdorf, *Rev. Sci. Inst.*, **29**, 323 (1958).
- 35) H.G.F., Wilsdorf, *ASTM Techn. Publ.* #245, 43 (1958).
- 36) A. Berghezan, A. Fourdeux and S. Amelinckx, *Acta Metall.* **9**, 464 (1961).
- 37) H.G.F. Wilsdorf and D. Kuhlmann-Wilsdorf, *Phys. Rev. Letters*, **4**, 170 (1959).
- 38) D. Kuhlmann-Wilsdorf and H. Wilsdorf, *J. Appl. Phys.*, **31**, 51 (1960).
- 39) D. Kuhlmann-Wilsdorf, R. Maddin and H.G.F. Wilsdorf, in J.J. Harwood (ed.), *Strengthening Mechanisms in Solids*, ASM, Metals Park Ohio, 1962, p. 137.
- 40) H.G.F. Wilsdorf and I.G. Greenfield, *J. Appl. Phys.*, **32**, 827 (1962).
- 41) R. Becker, *Phys. Z.*, **26**, 919 (1925); *Z. techn. Physik*, **7**, 547 (1926).
- 42) R. Becker and W. Boas, *Metallwirtschaft*, **8**, 317 (1928).
- 43) D. Kuhlmann and G. Masing, *Zeits. f. Metallkd.*, **39**, 361 (1948).
- 44) J.M. Burgers, *Proc. Acad. Sci. Amsterdam*, **42**, 293, 378 (1941).
- 45) J.E. Bailey and P.B. Hirsch, *Philos. Mag.*, **5**, 485 (1960).
- 46) H.M. Otte and J.J. Hren, *Exp. Mech.*, **6**, 177 (1966).
- 47) M.R. Staker and D.M. Holt, *Acta Metall.*, **20**, 569 (1972).
- 48) D. Kuhlmann-Wilsdorf and J.H. van der Merwe, *Mater. Sci. Engg.*, **55**, 79 (1982).
- 49) Z.S. Basinski, *Philos. Mag.*, **3**, 393 (1959).
- 50) E.C. Aifantis, in ref.15, p.563; see also *Mater. Sci. Engg.*, **81**, 563 (1986).
- 51) D. Kuhlmann-Wilsdorf, *Acta Metall.*, **37**, 3217 (1989).
- 52) D. Kuhlmann-Wilsdorf and N. Hansen, *Scripta Met. et Mater.*, **25**, 1557 (1991).
- 53) A.S. Malin and M. Hatherley, *Met. Sci.*, **13**, 463 (1979).
- 54) A.S. Malin, I. Huber and M. Hatherley, *Z. Metallkd.*, **72**, 310 (1981).
- 55) F.J. Torrealdea and J. Gil Sevillano, in R.C. Gifkins (ed.), *"Proc. 6th. Intl. Conf. on Strength of Metals and Alloys"*, Pergamon, Oxford, 1982, p.547.
- 56) E. Nes, W.B. Hutchinson and A.A. Ridha, in H.J. Mc Queen, J.P. Bilon, J.I. Dickson, J.J. Jonas and M.G. Akben (eds.), *"Proc. 7th. Intl. Conf. on Strength of Metals and Alloys"*, Pergamon, Oxford, 1985, p.57.
- 57) J. Gil Sevillano and E. Aernoudt, *Mater. Sci. Engg.*, **86**, 35 (1987).
- 58) A.W. Thompson, *Metall. Trans.*, **8a**, 833 (1977).
- 59) N. Hansen and D. Juul Jensen, in D.G. Brandon, R. Chaim and A. Rosen (eds.), *"Proc. 9th. Intl. Conf. on Strength of Metals and Alloys"*, Freund Publishing House, London, 1991, p.953.

LEDS THEORY OF WORKSOFTENING AND HALL-PETCH HARDENING IN EXTRUDED MA ALLOYS

by

Heinz G. F. Wilsdorf and Doris Kuhlmann-Wilsdorf
Department of Materials Science and Engineering
University of Virginia, Charlottesville, VA 22901

ABSTRACT

Mechanically alloyed and extruded aluminum alloys developed for service at temperatures up to 500°C in aerospace applications exhibit worksoftening, as is typical for alloys with grain/sub grain sizes at and below $\approx 1\mu\text{m}$. Experimental evidence is presented and compared with a recent theory of worksoftening based on the LEDS concept. It is concluded that the observed worksoftening stems from a reduction in the τ_0 part of the flow stress, i.e. that part which does not depend on the density of trapped dislocations. In the present alloys τ_0 is dominated by Hall-Petch grain boundary strengthening. TEM evidence suggests that the softening arises as plastic strain weakens what appears to be a continuous layer of "grain boundary substance" (perhaps of carbon, Al_4C_3 , or otherwise enriched in carbon) at which the boundaries are strongly anchored. With the boundaries thus immobilized, the relative lattice rotations among neighboring grains caused by the strain are accommodated by "geometrically necessary" dislocation rotation boundaries formed from reaction products of glide dislocations directly at the film surfaces. This is a new form of LEDS never previously reported. It contributes to, although does not necessarily dominate, the high recrystallization and service temperatures of the alloys.

LED'S THEORY OF WORKSOFTENING AND HALL-PETCH HARDENING IN EXTRUDED AA ALLOYS

by

Heinz G. F. Wilsdorf and Hans-Joachim Wilsdorf
Department of Materials Science and Engineering
University of Virginia, Charlottesville, VA 22901

INTRODUCTION

Motivation

In accordance with long-standing experience, the flow stresses of metals can be greatly increased through grain refinement but typically at the cost of embrittlement. In order to fully exploit the strengthening through small grain sizes modern processing methods have extended even to nano-crystalline materials, while alloys with grains in the sub-micrometer range are becoming almost standard. However, a very unwelcome by-product of extreme grain refinement has been a tendency toward work-softening in which already small strains can lead to very significant reductions of flow stress. The present study aims to make a contribution towards the better understanding of, firstly, the origin of worksoftening for metals with such small grain sizes and, secondly, the nature of grain size strengthening in the sub-micrometer range.

Basic Features of the Alloys Investigated

Commercial aluminum alloys lose their strength, and become essentially unusable for structural applications, at temperatures above 200°C to 300°C, depending on composition. Yet in the aerospace industry there exists a potential need for aluminum alloys with substantially higher service temperatures. For this reason a study was undertaken at the University of Virginia in conjunction with several industrial companies to develop high performance aluminum alloys with useful strengths up to temperatures of 500°C [1].

It was decided early on that the only hope for success would be the incorporation of a high density of very fine dispersoids with such low solubilities in the matrix that they would not significantly change their size or shape even under prolonged exposures to temperatures up to at least 500°C. As partly documented in [1] and in this paper, the strategy has been very successful and alloys with remarkably high strength and serviceability to 500°C have been developed.

The incorporation of dispersoids with the desired characteristics can be achieved by mechanical alloying (MA) [2,3], and a number of the best alloys have been prepared by this method. The MA process begins by mixing fine powders of alloys, intermetallics and/or ceramic particles, as the case may be, which then are milled for prolonged periods. In the course of the milling process, the initial particles are broken up and rewelded among each other to form particles with high densities of defects. Incidental or unconventional deliberate additions to the MA powders, derived from process control agents, add to the complexity of the alloys. For example, in the production of aluminum alloys by MA, stearic acid is used frequently, leading to the incorporation of carbon and, upon annealing, carbides. Grain sizes which in general are considerably smaller than one micrometer are obtained, and indeed not at all infrequently metastable alloys or even amorphous material. After milling, MA powders for aluminum alloys are commonly consolidated through extrusion at temperatures between 350°C and 450°C, with reduction ratios from 15:1 to 50:1.

Microstructures in the As-Received Condition

The microstructures of the discussed high-temperature aluminum alloys are complex but they approach thermodynamical equilibrium on account of dynamical recrystallization during the extrusion at elevated temperature. Their

generally fairly uniform, nearly equiaxed grain structure as shown in Fig. 1, and their considerable stability on annealing or in use at the intended high temperatures, bear this out [4]. Even so, occasional considerable inhomogeneities cause obvious irregularities in the structure, e.g. as shown in Fig. 2. Presumably such are a cause of premature failure.

In the as-received condition, the alloys under consideration had maximum dispersoid volume fractions between about 6% and 32% and had grain sizes (d) from about $0.1\mu\text{m}$ to $0.5\mu\text{m}$, as listed in Table I. That this very fine grain size was retained through the processes of degassing, consolidation and dynamical recrystallization during extrusion, indicates that the high concentrations of finest dispersoids strongly impede grain boundary migration, thereby raising the recrystallization temperature and thus increasing the range of service temperatures. Micrographs at higher magnification, e.g. Figs. 3 and 4, visually demonstrate this fact via the finely serrated and obviously locally pinned grain boundaries. Even so, remnant stresses inside the grains are low as evidenced by the uniform diffraction contrast across any one subgrain seen in Figs. 1 to 4 and subsequent micrographs.

All micrographs in this paper are taken from alloy A3 in the as-received condition and after 18hrs annealing at 550°C (code A3₃). The study has concentrated on A3, the alloy with by far the smallest volume fraction of dispersoids among those in Table I, for the reason that the high dispersoid concentrations in the other alloys tend to obscure micrographic dislocation images and therefore make a detailed study of dislocation behavior in them much more difficult. It may be noted that in A3 as received and after annealing (code A3₃) the total of observed Al_4C_3 particles was far below the expected volume fraction of 4%. This implies a significant invisible presence of carbon, at least in this alloy, presumably segregated at the boundaries. This is an

important point to which we shall return later.

Regarding general features of the microstructures, it has already been pointed out that all of the alloys were dynamically recrystallized during the extrusion and that their structures appeared to be near thermal equilibrium, witness the low internal stresses and, one may add, the very low concentration of dislocations within the grains. However, the larger yttriumoxide particles in A3 and B2 are surrounded by regions of very high dislocation densities [1]. Presumably these are due to lattice misfit as well as to thermal strains during cooling from the extrusion temperature.

Again in agreement with approximate thermodynamical equilibrium, not only in A3 but generally in A and B alloys, dispersoids are enriched at grain boundaries and the grains are typically fairly regular, equiaxed in cross sections and only mildly elongated in extrusion direction. Also, as in Figs.1 to 4 of A3, dispersoids of fairly uniform size occur within the grains of all A and B alloys with a statistically uniform distribution.

The aluminum titanium C series alloys, with their very high concentration of dispersoids, are different in that the aluminum grains and the Al_3Ti particles have similar sizes and form a two-phase duplex structure. The C7 alloy of Fig.7 was extruded at $425^\circ C$ with an extrusion ratio of 18 : 1. When tested at that temperature, pure Al_3Ti yields at 130 MPa so that most of the deformation occurred in the aluminum grains. Correspondingly, the boundaries are not straight but show similar complexities as in other MA alloys. Prolonged annealing at $545^\circ C$, i.e. $120^\circ C$ above the extrusion temperature, simplifies the boundary structure and, along with the reduced strength, the work-softening disappears entirely (Fig.7).

STRESS-STRAIN BEHAVIOR IN RELATION TO COMPOSITION, STRUCTURE AND HEAT TREATING

Fig.5 shows the tensile stress-strain behavior of alloy A3 which as already indicated is at the focus of the present study, in comparison with that of A1 and A2. All A alloys were extruded at 370°C with an extrusion ratio of 33 : 1 and had much the same grain sizes, between 0.25 and 0.5 μm . As seen in Fig.5, at room temperature the yield stress of A3 is 29 MPa and its ultimate tensile strength was 346 MPa, both significantly higher than for A1 and A2, while its 9.3% elongation at failure was much higher than for the other A alloys. Note also that contrary to the behavior of most alloys investigated in the study [1], the fracture of A3 was preceded by necking, indicated by a distinct kink in the curve at a strain of 8.5%.

In combination with the data in Table I, Fig.5 clearly demonstrates that neither the level of the flow stress nor the strain to failure is a direct function of total dispersoid concentration. The lower strength and larger elongation of alloy A3 in comparison with alloys A1 and A2 is believed to be mainly due to its significantly lower Al_4C_3 volume fraction, especially since aluminum carbide is known to be an effective strengthening dispersoid [1,5]. At any rate, the slopes and elongations of the workhardening curves somewhat correlate with the Al_4C_3 and total volume fractions in the three alloys. As additional effects that probably contribute to the differences in mechanical behavior, note that besides the similar amounts of carbon and aluminum oxide in A1 and A2, the A2 alloy included an extra 1 wt/o of copper and A3 an extra 1 wt/o of yttrium oxide.

The lack of a direct relationship between dispersoid volume and magnitude of flow stress and final strain is reemphasized and confirmed in Figs.6 and 7 relating to alloys of the B and C series, respectively. Both B1 and B2 of Fig.6 were extruded at 370°C with an extrusion ratio of 53 : 1, both have

similar total dispersoid volume fractions, namely 16.1% and 15.9% respectively, and both have the same grain size distribution between $0.15\mu\text{m}$ and $0.35\mu\text{m}$. Yet they exhibit sharply different slopes of the stress-strain curves. The significant difference here is the extra 1 w/o (amounting to 0.5 v/o) of Y_2O_3 in B2. Other alloying components in both B1 and B2 included nominally 10 w/o Nb, 1.2 w/o C, and 0.8 w/o of oxygen in the form of Al_2O_3 , yielding the theoretical maximum dispersoid volume fractions based on chemical analysis listed in Table I. Micrographically, the corresponding particles show no significant differences between B1 and B2, ranging between 10nm and 25nm in size and being fairly evenly distributed throughout the alloys, except that the Y_2O_3 particles in B2 have sizes up to $0.4\mu\text{m}$, and are located in boundaries mostly at triple points, and the dislocation density in their vicinity is extremely high.

Figs.7 and 8 introduce the additional point that only annealing well above the extrusion temperature will reduce the flow stress, but that anneals at lower temperatures may mildly reduce the strain to failure. Specifically, annealing of A3 for one hour at 490°C did not affect its strength within a 1% error margin but elongation was decreased to 8.3%. Thus the alloy exhibited very high temperature stability. Significantly, as seen in Fig.8, 18hrs annealing at 550°C (code A3₃) reduced the maximum stress of A3 to just below 300MPa but only restored the ultimate strain to its initial value. Similarly Fig.7, pertaining to one of the C series aluminum titanium MA alloys, indicates a monotonic decrease of strength with annealing time above the extrusion temperature but an initial mild decrease of ultimate strain followed by a small increase.

Aluminum titanium alloys with their $\text{Al}_3\text{Ti}/\text{Al}$ duplex structure have great promise for high temperature performance and at the same time have good room

temperature strength. Notably, too, their worksoftening in the as-received condition (Fig.7) is much smaller than in A and B alloys (Figs.5 and 6) and is more readily removed by annealing, as seen by comparing Figs. 7 and 8, even though the C alloys comprise by far the highest volume fraction of dispersoids, as seen in Table I. Specifically the composition of alloy C7 was 9.0 w/o of Ti, 2.5 w/o of C, 0.8 w/o of O and the balance aluminum. The observed dispersoid volume fractions are not far from the calculated values of $Al_3Ti = 21\%$, $Al_4C_3 = 9.2\%$ and $Al_2O_3 = 1.4\%$, for a total of 31.6%.

The small degree of worksoftening in the C alloys is ascribed to their already mentioned distinctive microstructure, in that the Al_3Ti does not appear as small dispersoid particles but as grains of similar size as the aluminum grains, i.e. $0.1\mu m$ to $0.5\mu m$ for the Al_3Ti and $0.1\mu m$ to $0.35\mu m$ for the aluminum, respectively. Hence these MA aluminum titanium alloys have the duplex structures of two-phase aggregate alloys with many of their boundaries being phase boundaries, i.e. not principally anchored by particles.

We therefore provisionally conclude that small grain size is a necessary but not sufficient condition for worksoftening in our MA alloys but that it is also necessary that the boundaries are grain and not interphase boundaries. Further we provisionally conclude that worksoftening does not depend on the presence or absence of large dispersoid particles surrounded by dislocations but that the presence of carbon has a great influence.

MICROSTRUCTURES IN A3 AFTER DEFORMATION

As-Received Material After Deformation

Superficially, there is very little difference between the microstructures of A3 in the as-received condition and after deformation to fracture. This may be seen by comparing Fig.9 with Fig.4: After as well as before the deformation, there are no dislocation assemblies in the grains, the grain

boundaries have not obviously moved, and they are still convoluted and pinned by dispersoids. This pinning is dramatically demonstrated in Fig.10 by the strong curvature at the upper end of the vertical boundary, albeit this grain boundary movement almost certainly did not take place during the tensile testing but in the course of dynamical recrystallization during extrusion.

For the present paper of greatest importance is a non-obvious feature, that may be observed in this micrograph as well as in Figs.9 and 11. These are networks or grids of very finely spaced dislocations overlaid on the boundaries, which however can be seen only where diffraction conditions are suitable. Thus for example, a large number of nearly parallel dislocations is visible at the lower left in Fig.9. A similar group is present in Fig.10 in the middle of the top of the darker area, a still finer cross grid below that, and a very obvious but less extensive set of more widely spaced parallel dislocations below and to the right thereof.

In order to demonstrate the frequent complexity of such dislocation networks overlying the boundaries of deformed specimens, Fig.11 shows a microstructure, again of a boundary in alloy A3 after tensile deformation, taken by TEM with three different diffraction vectors. More than thirty dislocation groups, typically containing between five and ten dislocations and up to $0.5\ \mu\text{m}$ long can be identified in Fig.11a. These appear to be terminated by dislocations of an intersecting set barely visible in Figs.11b and 11c, besides at least one additional dislocation set which can be discerned in those figures. Thus together these dislocations appear to form one large network overlying the boundary analyzed in Fig.11, approximately $3\ \mu\text{m}$ long and in width varying between $1.3\ \mu\text{m}$ and $0.03\ \mu\text{m}$, as projected into the image plane. The spacings between the dense sets of dislocations (s) vary moderately from group to group between 4 and 9nm with an average of about 7nm, while the area covered by the

smallest group is $0.05\mu\text{m} \times 0.1\mu\text{m}$, and for the largest it is $0.3\mu\text{m} \times 0.4\mu\text{m}$, meaning presumably that the intersecting dislocation set in the network has a spacing of about $0.3\mu\text{m}$.

It is difficult to say whether all grain boundaries in the formed A3 alloy specimen exhibit the demonstrated fine dislocation networks overlaid on the otherwise seemingly almost unchanged boundary structure since high resolution and favorable diffraction conditions are required for their observation. Certainly the phenomenon is very widespread. By contrast such dislocations overlaid on the boundaries are almost absent in the as-received material. The only instances of dislocation grids overlying grain boundaries discovered in as-received A3 material are of two distinct types. One is represented by the somewhat irregular but widely spaced network in the boundary at top right in Fig.3, the other by several small patches of parallel dislocations circled in Fig.4.

The network in Fig.3 appears to be of the same type as the networks after deformation except for the already noted greater irregularity and a larger spacing, namely about 60nm as compared to an average of about 7nm after deformation. Therefore this network is ascribed to mild plastic deformation through thermal stresses after extrusion, and in fact the scattered irregular dislocations seen in the boundary of Fig.4 probably are of the same type.

Quite different are the circled groups in Fig.4. They are rectangled, about $0.05\mu\text{m}$ long, and comprise eight to twelve dislocations spaced about 2nm to 4nm apart. Superficially those groups might seem to resemble the already described groups in the boundary of Fig.11 but unlike those the groups of Fig.4 (i) do not terminate at crossing dislocations, (ii) exhibit still smaller spacings (namely between 2nm and 4nm), (iii) are isolated from each other and (iv) close examination suggests that they extend over areas at which

precipitates anchor the boundary, although they are by no means associated with all such precipitates. For these reasons these small patches of closely spaced parallel dislocations are not believed to be caused by macroscopic strain but to be epitaxial in nature.

Annealed Material After Deformation

Annealing above the extrusion temperature straightens the boundaries and somewhat increases the grain size but still leaves the boundaries anchored at dispersoids. This may be observed in Fig.12 taken of specimen A3₃, i.e. A3 annealed for 18hrs at 550°C and then tensile tested in accordance with Fig.8. Fig.12 is to be compared with Fig.4 except that in Fig.12 there are really two nearly coplanar boundaries, parallel to the plane of the film, in center field. The left grain boundary is clearly very similar to the boundary in Fig.4. Much more attention-catching is, of course, the right boundary with its vivid banding due to sets of dislocations in almost vertical direction. Those sets, of about 7nm spacing, appear to be intersected by much more finely spaced sets, one extending from lower left to upper right and another from upper left to lower right, which are not properly resolved by being out of contrast. Additionally there is a very fine (3nm spaced) set of parallel dislocations bounding the vivid set at its left bottom.

As is the case in A3, so also in A3₃ specimens, such dislocation sets or networks at grain boundaries are very frequent after deformation but scarce without plastic straining. Fig.13 shows one other example in which the prevalence of the discussed networks in a deformed sample is very evident. On occasion the networks are exquisitely well developed, as in the third and last example of Fig.14. And to repeat: in the annealed but undeformed state dislocation groupings overlaid on the boundaries are infrequent, whereas

there are more, although still only relatively few, scattered dislocations seen within the grains before than after deformation.

COMPARISON OF STRESS-STRAIN CURVES WITH WORK-SOFTENING THEORY

General Observations on Worksoftening in Ultra-Fine Grained Materials

The effects of ultra-fine grain size (d smaller than $1\mu\text{m}$) on mechanical properties has been reported more than twenty years ago in ferrous alloys [6]. These investigations explored the improvements in tensile strengths, the reduction in tensile ductility, and the lack of workhardening associated with these. Lüders band formation was observed but worksoftening was not reported. A literature search reveals that worksoftening is typical for very fine-grained materials. Examples can be found in many alloys with ultra-fine grain sizes, respectively sub-grain sizes [7-9]. Specifically the influence of grain size on a particular aluminum alloy (Al-0.8Mn-2.0Fe in w/o) is shown in Fig.15 [7]. Starting with the heavily rolled down material, worksoftening is obvious up to grain sizes of $1.02\mu\text{m}$. Computing the Hall-Petch constant from these curves on the assumption that all of the flow stress is due to grain boundary hardening yields (the somewhat overestimated values of) $K_{HP} = \sigma_y\sqrt{d}$ decreasing from $191\text{MPa}\sqrt{\mu\text{m}}$ for curve 2 to $175\text{MPa}\sqrt{\mu\text{m}}$ for curves 2 to 4 and down to $162\text{MPa}\sqrt{\mu\text{m}}$ for curves 6 and 7.

The evidence already discussed in connection with Figs.5 to 8 together with the approximate Hall-Petch constants derived from Fig.15 and the data in Table I demonstrate that ultra-fine grain size is not the only factor influencing worksoftening. Even so it is obvious that Hall-Petch hardening must be the most important contribution producing the high strengths of these materials. That is highly significant since, according to the theory of workhardening and grain boundary hardening [10], in the relationship between flow stress and dislocation density (ρ)

$$\tau \approx \tau_0 + \alpha G b \sqrt{\zeta} \quad (1)$$

the Hall-Petch stress of

$$\tau_{HP} \approx K_{HP}/M\sqrt{d} = \sigma_{HP}/M \quad (2a)$$

is a part of τ_0 . Here G is the shear modulus, b the Burgers vector, α a slowly varying parameter of about $\frac{1}{2}$, σ_{HP} the Hall-Petch contribution to the tensile stress and $M \approx 3$ is the Taylor factor.

Workhardening Through Increasing Dislocation Density

In accordance with the preceding arguments, in the present alloys grain boundary strengthening not only dominates τ_0 but also the flow stress. However, at issue in worksoftening is the value of the workhardening coefficient $(d\tau/d\gamma) = \theta$, not the flow stress per se. Based on [10] and earlier papers, that part of the workhardening coefficient which is due to changes in dislocation density, i.e. $d(\tau - \tau_0)/d\gamma$ relative to which all other contributions to workhardening are generally negligible, can be simply and approximately derived as follows [11]: According to eq.1, workhardening arises as with increasing dislocation density the mean dislocation spacing

$$\bar{l} \approx m/\sqrt{\zeta} \quad (3)$$

with m comparable to unity shrinks, and therewith the Frank-Read stress

$$\tau_{FR} \approx Gb/3\bar{l} \quad (4)$$

for supercritical bowing of links or of dislocations passing through the gaps rises.

Consider, then, the supercritical bowing of dn dislocations per unit volume. In the alloys considered, in which the grains are not subdivided by

dislocation cell walls, on average the dislocations sweep out an area of

$$d^2 \approx (g\bar{l})^2 \quad (5)$$

before impinging on boundaries where they are partly annihilated. If the reduction of sub-boundary or grain size, d , is a result of increasing dislocation density, g will be roughly constant. Next, of the total so impinging length of about $4d$, only the fraction β , the "dislocation retention parameter", is retained and the rest is annihilated. With it, the incremental dislocation density increase caused by the supercritical bowing of the dislocation links is

$$d\varrho = 4d\beta dn = 4g\bar{l}\beta dn \quad (6)$$

while the incremental shear deformation is

$$d\gamma = \bar{l}^2 b dn = g^2 \bar{l}^2 b dn \quad (7)$$

Combining eqs.6 and 7 with eqs.1 and 3 yields

$$d\tau_G \approx (2\alpha BG/mg)d\gamma \quad (8)$$

and the workhardening coefficient due to dislocations

$$d(\tau - \tau_0)/d\gamma \approx d\tau_0/d\gamma + 2\alpha BG/mg \quad (9a)$$

Of the variables α , β and g , only β can significantly depend on strain. In fact, β decreases with increasing strain, thereby explaining the different stages of the stress-strain curve [12]. In the particular case that the sub-grain or grain boundaries are due to the accumulation of trapped dislocations so that $m \approx 1$ and $g \approx 25$ [10,11] eq.9a reduces to

$$d(\tau - \tau_0)/d\gamma \approx d\tau_0/d\gamma + 8G/25 \quad (9b)$$

but in any event, whatever the values of g and m , the workhardening rate through dislocations is mainly determined by B .

Worksoftening Through Reduction of Dislocation Density

The already cited recent theory of worksoftening in high performance alloys [11] separately considers $d(\tau - \tau_0)/d\gamma$ and $d\tau_0/d\gamma$, both of which can be negative as well as positive. Specifically worksoftening can result from negative B values and thus negative $d(\tau - \tau_0)/d\gamma$. The underlying assumption is that ordinarily with continued straining under the same conditions B diminishes [12] until it becomes zero and workhardening ceases, unless fracture occurs. By implication, dislocation densities in excess of those for which B becomes zero are unstable and yield negative B values, meaning that straining will reduce the dislocation density and thus the flow stress, as every new glide dislocation loop will give rise to the annihilation of more than its own length. Thus worksoftening could arise in MA alloys if in the course of mechanical alloying exceptionally high dislocation densities should have been introduced, i.e. higher than could be sustained under the subsequent deformation conditions. This action parallels that of worksoftening through creep deformation of workhardened metals at elevated temperatures.

The result of the described gradual reduction of dislocation density through straining would be a convex worksoftening curve of the type given by the solid line in Fig.16, no matter what the specific assumptions as to the dependence of B on dislocation density may be, provided only that the absolute value of B monotonically increases with increasing deviation of the dislocation density from that for which $B = 0$. Specific analytic solutions for two simple assumptions for $B(\rho)$ are given in [11].

Worksoftening Through Reduction of the Hall-Petch Stress

If the dislocation density remains essentially constant or if τ_0 strongly dominates the flow stress, worksoftening simply mirrors the decline of τ_0 with strain. In that case the most simple assumption is that such decline is proportional to the strain as represented by the dashed curve in Fig.16. That and a second case are analytically treated in [11]. At any rate, if τ_0 is dominated by the Hall-Petch stress, which we already saw to be most likely in the present study, deviations from the most simple, linear behavior in Fig.16 are likely to yield an accelerated decrease, i.e. a convex instead of the concave shape expected from negative B -values. We may expect this on the plausible model that the deformation destabilizes an existing grain boundary structure which is being replaced by another structure, e.g. via the destruction of grain boundary anchoring through precipitates, dispersoids and/or solute atoms.

The rate of decline of τ_0 is determined by the magnitude of the strain, γ_f , which will bring about the new state. This aspect, too, has been treated in [11], albeit in terms of workhardening through dislocation reduction, and not specifically for grain boundaries. In that case the process should be completed at $\gamma_f \approx 10\%$ strain, within limits of perhaps a factor of two or three. At any rate, since the glide dislocations are blocked at the grain boundaries and these are of very small size, they will almost certainly arrive at the boundaries singly and fairly evenly distributed.

Comparison Between Theory and Experimental Curves

Clearly the stress-strain curves in Figs. 5 to 8 strongly suggest that the major cause of worksoftening in these alloys is not reduction of any excess dislocation density, which is not found micrographically in any event,

but a metastable too high value of τ_0 which is not sustained during deformation. The already presented evidence of the strongly anchored grain boundaries then logically leads to the conclusion that indeed the worksoftening behavior is caused by declining Hall-Petch strengthening.

Accordingly, the reduction in flow stress is simply correlated with a decrease of the Hall-Petch constant which will have to be explained through the corresponding reduction in the stress required to propagate glide through the grain boundaries [10]. The remainder of this paper is devoted to a discussion of the micrographic evidence in relation to that conclusion.

INTERPRETATION OF THE MICROGRAPHIC OBSERVATIONS

LEDS Character of the Dislocation Structures

The visual evidence very powerfully speaks for the operation of the LEDS (i.e. Low-Energy Dislocation Structure, 13,14) principle in generating the observed microstructure: Not only in regard to the grids or networks overlying the boundaries after deformation, but in general, dislocations are in well-organized arrays. All of the networks seen appear to form boundaries delineating mutually misoriented volume elements of relative perfection. In regard to the as-received specimens this means that the great majority of the glide dislocations which produced the severe extrusion strain have been annihilated at the grain boundaries which formed and migrated in the dynamical recrystallization, and the remainder found positions in which they mutually screen their respective long-range stresses, i.e. have formed a LEDS. In fact, as seen from the micrographs, the individual grains before subsequent tensile testing are almost free of dislocations and the boundaries are true grain boundaries, it appears, as will be further confirmed in the discussion.

Somewhat surprisingly, after subsequent straining, the dislocation content within the grains is still smaller than before, i.e. straining has

still improved the LEDS character of the structure. Further, the discussed dislocation grids or networks associated with the grain boundaries after tensile testing, again indisputably of LEDS type, must have been formed overwhelmingly from the glide dislocations generated in the course of tensile testing.

Inferred Values of the Hall-Petch Constant

Hall-Petch constants as defined in eq.2 are properly determined from the stress-strain curves of a series of materials which are essentially alike except for different grain sizes. From the present data we may only deduce a maximum value for K_{HP} , namely as

$$K_{HP} \approx \sigma_y \sqrt{d} \quad (2b)$$

assuming that all of the yield stress is due to Hall-Petch hardening. The thusly computed values, in units of $(\text{MN/m}^2)\mu\text{m}^{1/2}$, are given in Table I.

The listed K_{HP} values, ranging from 159 to 306 $(\text{MN/m}^2)\mu\text{m}^{1/2}$ as seen in the table, compare to K_{HP} between 75 and 220 $(\text{MN/m}^2)\mu\text{m}^{1/2}$ determined for PM aluminum alloys by Kim and Griffith [13], to K_{HP} decreasing from 191 to 159 $(\text{MN/m}^2)\mu\text{m}^{1/2}$ according to the worksoftening curve of severely rolled and then lightly annealed aluminum of $d = 0.83\mu\text{m}$ obtained by Westengen [7] shown in Fig.15, again neglecting all other hardening mechanisms, and to $K_{HP} \approx 40$ $(\text{MN/m}^2)\mu\text{m}^{1/2}$ inferred for moderately rolled pure aluminum by Hansen and Juul Jensen [14]. Accordingly, the listed K_{HP} values compare to those of ordinary aluminum at their lower end but are extremely high at the upper end.

Dislocation Spacing in the Boundary Networks and Correlated Rotational Angles

As previously emphasized, to a considerable extent the micrographical structures before and after deformation are closely similar, since the distri-

bution of the dispersoids and the configurations of the grain boundaries are not obviously affected by the straining. The critical difference is the introduction of the surprisingly regular dislocation networks overlying, or perhaps integrated into, the grain boundaries, while the grain interiors to all appearances are free of significant stresses before as well as after deformation. For both the as-received (A3) and the annealed (A3₃) material, the dislocation spacings (s) in the lattices or networks averaged 7nm, ranging as we saw between about 3nm and much larger values, e.g. up to almost 30nm in Fig.13.

It is instructive to compare these dislocation spacings (s) with the densities expected from the strain if β were zero, as well as with the angular misorientations which these networks geometrically represent. To begin with the associated rotation angle Φ , it may be found from the simplified formula

$$b/s = 2 \sin \Phi/2 \quad (10)$$

where in our case $b = 0.3\text{nm}$. The results, corresponding to the limiting values of the dislocation spacings in the rafts or networks visible in the micrographs, are listed in Table II. As will be seen, they are consistent with the angular lattice reorientations expected from the imposed tensile strain, except for, firstly, the very small patches as indicated in Fig.4 and, secondly, the very wide grid seen in Fig.3. We shall return to these in the theoretical discussion.

Dislocation Spacing in the Boundary Networks and Correlated Trapping Parameter

The observed fine dislocation grids superimposed on the boundaries after the deformation must be dislocations which were trapped there. The equivalent average tensile strain represented by them may be derived from the grid spacing as

$$\bar{\epsilon}_e = b/\bar{S}M \quad (1)$$

with M the Taylor factor $M \approx 3$, as before. The values obtained listed in Table II.

Comparing these $\bar{\epsilon}_e$ data with the tensile strain to failure shows that only a fraction of all dislocations was trapped. The associated average dislocation trapping factors are found from the ratio of $\bar{\epsilon}_e$ to actual strain to failure, ϵ , i.e.

$$\beta_e = \bar{\epsilon}_e/\epsilon \quad (12)$$

again as listed in Table II. Those β_e values ranging about 0.1 are not unreasonable for moderately deformed material but certainly would give rise to quite significant workhardening.

Dislocation Spacings in the Boundary Networks and Correlated Flow Stress

The stress required for the supercritical bowing of a dislocation link in a material of shear modulus G , Poisson's ratio μ and Burgers vector b through a dislocation grid of average spacing \bar{l} is given approximately by eq.4 and more accurately is [10,17,18]

$$\sigma_e \approx M(Gbf(\mu)/6\pi\bar{l}) \ln(3\bar{l}/b) \quad (13a)$$

where

$$f(\mu) = (1-\mu/2)/(1-\mu) \quad (13b)$$

Those values are listed in Table II and with the exception of the grid of Fig.3 lie well above the observed yield and maximum stresses shown in Table I.

DISCUSSION AND CONCLUSIONS

The evidence of the flow stress curves and associated considerations show conclusively that the observed worksoftening cannot be due to decreasing dislocation density but must be due to declining grain boundary hardening.

Certainly, the initial dislocation density in the grains is lower than after straining, and the newly created networks at the boundaries have a theoretical flow resistance well above any flow stress recorded. Conversely, the fact that the nature of the boundaries strongly affects worksoftening, to the effect that the C alloys with their profusion of phase boundaries have almost no worksoftening and the A and B alloys with normal grain boundaries worksoften strongly, implicates not only the Hall-Petch stress but also proves that the Hall-Petch constant depends on the nature of the boundaries and thus could readily change. Indeed, one may go one step further and conclude that the normal grain boundaries in the A and B MA alloys offer a glide resistance which greatly exceeds that expected simply from the orientation changes among neighboring grains. If this were not so the Hall-Petch constants in the MA alloys could not be so much larger than in pure aluminum, i.e. between $200(\text{MN/m}^2)\mu\text{m}^{1/2}$ and $300(\text{MN/m}^2)\mu\text{m}^{1/2}$ as compared to $40(\text{MN/m}^2)\mu\text{m}^{1/2}$ in rolled aluminum according to Hansen and Juul Jensen [14].

It follows that the observed worksoftening reflects a declining critical stress for the propagation of glide through the grain boundaries [10] reflected in the corresponding decrease of Hall-Petch hardening. Off-hand the cause for the exceptionally high Hall-Petch constants in the MA alloys would seem to be anchoring at dispersoids, e.g. as so graphically seen in Figs. 2,3 and 10, and worksoftening to result as the boundaries are moved away from the dispersoids. However, this explanation offers some difficulties. Specifically, there is no evidence for significant grain boundary movement through straining, at least not large enough to break them free of dispersoids. Much more importantly yet, it leaves unanswered the question as to the origin and role of the networks overlaid on the boundaries and why these do not cause rapid hardening.

An additional observation which has not previously been mentioned is a remarkably strong strain rate dependence of the stress-strain curves: With decreased strain rate the flow stress decreases, as would be expected, but somewhat unexpectedly the strain to failure also decreases. This behavior parallels the already discussed effect of increased temperature. While the details of these effects require more study, it is clear that they indicate substantial involvement of thermal activation, i.e. a relatively small activation volume, not compatible with grain boundary pinning at relatively large dispersoids.

Contemplating all of the available evidence it was concluded that the grain boundaries must be anchored by a very thin continuous layer; in view of the deficiency of Al_4C_3 dispersoids compared to the carbon content of the alloys quite likely involving a form of carbon. All of the observations then indicate that this hypothetical thin film of "grain boundary substance" is firmly positioned on account of very slow diffusion rates as well as a strong binding energy to the grain boundary. The glide dislocations are therefore unable to dislodge the film or to move the grain boundary away from it. Rather, glide dislocations will have to intersect the film singly, and the overall strain necessarily lengthens the boundaries in tensile direction and shortens them at right angles thereto. The resulting atomistic ledges and breaks must be expected to weaken the films so as to cause the Hall-Petch constant to decrease which in turn will be manifested as worksoftening.

According to this model, the glide dislocations mostly annihilate mutually through corresponding fairly complex reactions, typically involving more than one glide dislocation with different Burgers vectors arriving at the film from either side. The remnants of not annihilated dislocations form the networks seen overlying the boundaries. In accord with the LEDS principle they are thus not simply randomly trapped dislocations but minimize energy per

unit length of dislocation line by accommodating the angular relative rotation of the neighboring grains which resulted from the glide on different selections of slip systems on the two sides, much in the manner of cell block boundaries [10,19-21]. The networks are thus "geometrically necessary" dislocation boundaries [22] in close association with grain boundaries, a not previously reported form of LEDS.

Certainly the associated rotation angles (Φ of Table II) are in accord with this interpretation, and the model also explains why the spacing in the networks can be so much smaller than could be accounted for through glide (see σ_e of Table II), and the dislocation retention factor larger than would normally be expected (B of Table II). Significantly, also, the model explains the lack of concentrated glide or Lüders band formation which would normally be expected to accompany worksoftening.

The small patches of very densely spaced dislocation grids as in Fig.4 are almost certainly epitaxial dislocations accommodating misfit between matrix and dispersoids and hence are of a quite different nature than the boundary networks, albeit also LEDS. By contrast, the widely spaced network of Fig.3 and similar ones in other micrographs of nominally undeformed samples are considered to be of the same kind as those formed during straining and are ascribed to thermal strains during cooling from the extrusion temperature.

The very low mobility of the grain boundary films will evidently contribute to the high service and recrystallization temperatures of the discussed MA alloys. With little doubt the films are disrupted, pushed about and reformed in the course of dynamical recrystallization during extrusion, however. This must evidently happen in order to permit any dynamical recrystallization at all, but is also indicated by occasional micrographic evidence. Thus the jagged line in the middle of the lower grain and parallel to the

other grain boundaries in Fig.3 is interpreted as the remnants of one such film which were left behind by a moving boundary during dynamical recrystallization. In its further movement that boundary will have swept up other parts or ingredients for the formation of a grain boundary substance film until it became anchored thereby and dispersoids in its new position, probably at lower right of Fig.3.

After the above model was derived as explained, a concerted effort was made to find micrographic evidence for the inferred films of grain boundary substance in existing grain boundaries, i.e. for the otherwise missing link in this interpretation. Two examples could be found which appear to document the films directly, one of which in Fig.13, enlarged in Fig.17. It shows a section of a boundary in A3₃ (i.e. after annealing and thus smoothed out compared to grain boundaries in the as-received condition) which is coincidentally almost precisely normal to the plane of the film. The individual spots along the boundary are believed to be network dislocations of the associated "geometrically necessary" boundary. They appear to be very slightly offset on either side from the dark line which is interpreted to be the elusive film of grain boundary substance. Its thickness is at the most 2nm but quite possibly only 0.3nm or even less. - An additional paper shall be devoted to a further investigation of grain boundary films.

ACKNOWLEDGMENTS

Grateful acknowledgment is made to the following: The experimental work on aluminum alloy development was supported by the U.S. Air Force Wright Aeronautical Laboratories, Materials Laboratory (W.M. Griffith, S. Kirchoff and J. Kleek). J.A. Hawk made the mechanical measurements and micrographs Figs.12 to 14. D.K.-W.'s research was supported through the Materials Division (P. Schmidt and M. B. Peterson, Tribology) of the Office of Naval Research, Arlington, VA.

REFERENCES

- 1) For a first review see H.G.F. Wilsdorf, in "Dispersion Strengthened Aluminum Alloys", (Eds. Y.-W. Kim and W. Griffith, TMS, Warrendale, PA, 1988), p.3.
- 2) J.S. Benjamin and M.J. Bomford, Metall. Trans., 1 (1970) 2943.
- 3) J.S. Benjamin and M.J. Bomford, Metall. Trans., 8A (1977) 1301.
- 4) J.A. Hawk, P.K. Mirchandani, R.C. Benn and H.G.F. Wilsdorf, in "Dispersion Strengthened Aluminum Alloys", (Eds. Y.-W. Kim and W. Griffith, TMS, Warrendale, PA, 1988), p.517.
- 5) G. Jangg, F. Kutner and G. Korb, Powder Met. Int., 2 (1977) 24.
- 6) R. L. Miller, Metall. Trans., 3 (1972) 905.
- 7) H. Westengen, Ardal-Sundal Verk, Sundalsøre, Norway, 1982.
- 8) D.J. Lloyd, Met. Sci., 14 (1980) 193.
- 9) A. Lasalmonie and J. L. Strudel, Mater. Sci., 21 (1986) 1837.
- 10) D. Kuhlmann-Wilsdorf, in M.N. Bassim, W.A. Jesser, D.Kuhlmann-Wilsdorf and G.J. Shiflet, Eds., "Low-Energy Dislocation Structures II", Elsevier Sequoia, Lausanne, 1989; see also Mater. Sci. Engg., A113 (1989) 1.
- 11) D. Kuhlmann-Wilsdorf and H.G.F. Wilsdorf, phys. stat. sol., in the press.
- 12) D. Kuhlmann-Wilsdorf and N. Hansen, Metall. Trans., 20A (1989) 2393.
- 13) Y.W. Kim and W.M. Griffith, in "PM Aerospace Materials", Vol.1 (Shrewsbury U.K., MPR, 1984) as quoted by W.E. Frazier and M.J. Koczak in "Symposium on Dispersion Strengthened Aluminum Alloys" (Eds. Y.-W. Kim and W. Griffith, TMS, Warrendale, PA, 1988), p.577.
- 14) N. Hansen and D. Juul Jensen, in "Proc. 9th Intl. Conf. on Strength of Metals and Alloys" (Eds. D.G. Brandon, R. Chaim and A. Rosen, Freund Publ. House, London), p.953.
- 15) M. N. Bassim, W. A. Jesser, D. Kuhlmann-Wilsdorf and H. G. F. Wilsdorf, Eds., "Low-Energy Dislocation Structures I", Elsevier Sequoia, Lausanne, 1986; see also Mater. Sci. Engg., vol.81 (1986).
- 16) M. N. Bassim, W. A. Jesser, D. Kuhlmann-Wilsdorf and G. J. Shiflet, Eds., "Low-Energy Dislocation Structures II", Elsevier Sequoia, Lausanne, 1989; see also Mater. Sci. Engg., vol.A113 (1989).
- 17) D. Kuhlmann-Wilsdorf, in "Workhardening" (Eds. J. P. Hirth and J. Weertman, Gordon and Breach, N.Y., 1968), p.97.

- 18) T. E. Mitchell and R. L. Smialek, in "Workhardening" (Eds. J.P. Hirth and J. Weertman, Gordon and Breach, N.Y., 1968), p.365.
- 19) D. Kuhlmann-Wilsdorf and N. Hansen, Metall. Trans., 20A (1989) pp.2393-2397.
- 20) B. Bay, N. Hansen and D. Kuhlmann-Wilsdorf, Mater. Sci. Eng., in press.
- 21) B. Bay, N. Hansen, D. A. Hughes and D. Kuhlmann-Wilsdorf, Acta Met. et Mater., 40 (1992) pp.205-219.
- 22) D. Kuhlmann-Wilsdorf and N. Hansen, Scripta Met. et Mater., 25 (1991) 1557.

LEGENDS

Fig.1: TEM micrograph of the cross section of a rod of Alloy A3 (see Table I) in the as-received condition. The average grain size is about $0.35\mu\text{m}$. Note the rather regular grain structure and the uniformity of the diffraction contrast across the individual grains, testifying to the good approach toward thermal equilibrium resulting from dynamical recrystallization during the extrusion at 370°C .

Fig.2: As Fig.1 but at lower magnification and showing a severely distorted area, doubtlessly due to incomplete refinement and mixing during the MA process.

Fig.3: As Fig.1 but showing two grains at high magnification. Again note the essential absence of internal stresses indicated by the uniform contrast within any one grain, but also the evident anchoring of the grain boundaries through dispersoids as indicated by their convoluted structure. The string of dislocations in the center is believed to be the remnant of a grain boundary which moved away in the course of dynamical recrystallization.

Fig.4: Plan view of a grain boundary in A3 as-received showing its anchoring by many dispersoids, as indicated by the somewhat diffuse associated diffraction contrast. The broader fringes about the grain and especially the series of fringes seen bottom middle are fringes of equal thickness indicating how the grain volume tapers through the thickness of the foil. A similar set of fringes is also visible in Fig.3, top left. At the centers of the drawn circles may be seen groups of about ten each, short, parallel, finely spaced dislocations.

Fig.5: Room-temperature tensile stress-strain curves parallel to the extrusion axis of alloys A1, A2 and A3 as-received, at a strain rate of 2×10^{-4} /s. Note in comparison with Table I that neither the flow stress nor the ultimate tensile strain are simple functions of the volume fraction of dispersoids.

Fig.6: As Fig.5 but for the B alloys of Table I.

Fig.7: Room-temperature tensile stress-strain curves parallel to the extrusion axis of Alloy C7 of Table I in the as-received condition and after annealing for 100 and 400hrs at 525°C , i.e. well above the 425°C extrusion temperature, again at a strain rate of 2×10^{-4} /s. Note that with increasing annealing time the flow stress decreases monotonically, as expected, but that the ultimate tensile strain initially decreases before rising.

Fig.8: The room-temperature tensile stress-strain curves for A3 as-received (as in Fig.5), and after annealing for 18hrs at 550°C (code A3₃).

Fig.9: As Fig.4 but after deformation to failure according to the curves in Figs.5 and 8. At lower left, in the boundary, an extensive array of very densely spaced parallel dislocations with almost vertical axis orientation may be seen which is comparable to the arrays encircled in Fig.4 except for a very much larger extent.

Fig.10: As Fig.9, i.e. plan view of a grain boundary of alloy A3 after tensile test to failure. Note the scalloped shape of the boundary at left caused by evident anchoring at a prominent dispersoid. Also visible are many dislocations in the boundary of which the diagonal group near the center is the most obvious. Much more densely spaced parallel dislocations are seen in the dark area at top center and a fine cross grid below that.

Fig.11: As Fig.10 but taken in three different diffraction conditions, revealing an extensive, complex dislocation network in the boundary involving at least three different Burgers vectors.

Fig.12: TEM micrograph of two grain boundaries parallel to the plane of the film in A3₃, i.e. A3 alloy annealed 18hrs. at 550°C, after pulling to failure in accordance with Fig.8. The left boundary is comparable to that in Fig.4, still showing anchoring by dispersoids although apparently somewhat smoothed out. The right boundary contains sets of dislocations comparable to those seen in Figs.9 to 11 of A3 after tensile deformation.

Fig.13: As Fig.12 showing various grain boundaries some with the discussed dislocation networks visible in them.

Fig.14: As Figs.12 and 13 but in darkfield illumination, exhibiting especially well developed dislocation networks.

Fig.15: Dependence of room-temperature tensile stress-strain curves of an aluminum alloy on grain size according to Westengen [7]. The associated Hall-Petch constant drops from $191\text{MPa}/\sqrt{\mu\text{m}}$ for curve 2 to $175\text{MPa}/\sqrt{\mu\text{m}}$ for curves 3 and 4.

Fig.16: The basic two types of worksoftening curves expected from simple theory [10], namely caused by a reduction of dislocation density (solid curve) and of frictional stress τ_0 including the Hall-Petch stress due to grain boundaries (dashed curve). The observed curves (Figs.5 and 6) suggest softening through a reduction of τ_0 .

Fig.17: Detail of Fig.13, i.e. of a grain boundary in A3₃ (annealed A3 alloy after tensile deformation to failure) which is oriented almost exactly normal to the plane of observation. The dots are believed to be intersections of network dislocations overlying the boundary, in fact apparently lying very closely to it on either side, and the continuous fine, mostly dark, line "grain boundary substance", presumed to be rich in carbon. This and similar networks are believed to accommodate lattice misorientations caused by tensile straining.

TABLE I

| # | T _{ex} °C | σ_y MPa | σ_m MPa | σ_F MPa | ϵ % | Al ₄ C ₃ v/o | Al ₂ O ₃ v/o | Al ₂ Cu v/o | Y ₂ O ₃ v/o | Al ₃ Nb v/o | Al ₃ Ti v/o | Total v/o | Grain Size d in μm | K _{HP} σ_y |
|-----------------|-----------------------|-------------------|-------------------|-------------------|-----------------|---------------------------------------|---------------------------------------|---------------------------|--------------------------------------|---------------------------|---------------------------|--------------|----------------------------------|-------------------------------|
| A1 | 370 | 382 | 393 | 303 | 4.5 | 12.1 | 2.0 | 0 | 0 | 0 | 0 | 14.1 | 0.25-0.50 | ~20 |
| A2 | 370 | 500 | 534 | 460 | 4.2 | 10.7 | 1.0 | 1.1 | 0 | 0 | 0 | 12.8 | 0.25-0.50 | ~30 |
| A3 | 370 | 329 | 346 | 140 | 9.3 | 4.0 | 1.4 | 0 | 0.5 | 0 | 0 | 5.9 | 0.25-0.50 | ~20 |
| A3 ₃ | 550* | 276 | 291 | 218 | 9.5 | 4.0 | 1.4 | 0 | 0.5 | 0 | 0 | 5.9 | 0.40-1.50 | ~26 |
| B1 | 370 | 317 | 387 | 145 | 11.3 | 3.0 | 1.0 | 0 | 0 | 12.1 | 0 | 16.1 | 0.15-0.35 | ~15 |
| B2 | 370 | 445 | 447 | 246 | 6.6 | 3.1 | 0.4 | 0 | 0.5 | 11.9 | 0 | 15.9 | 0.15-0.35 | ~22 |
| C7 | 425 | 530 | 570 | 490 | 6.9 | 9.2 | 1.4 | 0 | 0 | 0 | 21.0 | 31.6 | 0.10-0.35 | ~25 |

Legend: Important data for the MA aluminum alloys [1] listed according to their codes, all as received except for A3₃ which was annealed for 18hrs. at 550°C. T_{ex} is the extrusion temperature except for A3₃ where it is the annealing temperature. σ_y , σ_m and σ_F are the tensile stresses at yielding, maximum and failure, respectively and ϵ is the ultimate tensile strain. The volume fractions of the dispersoids listed are theoretical maxima based on chemical analysis, on the assumption that none of the alloying components were dissolved in the aluminum matrix which is not true, certainly not for carbon. The grain sizes, d, refer to the aluminum matrix and are best estimates. Dispersoids were generally much smaller than these, except for the Al₃Ti phase which in all C series alloys had a 0.1 - 0.5 μm grain size and formed a duplex structure with the aluminum matrix. The Hall-Petch constant, $K_{HP} = \sigma_y \sqrt{d}$ in units of $(\text{MN}/\text{m}^2)^{1/2} \mu\text{m}^{1/2}$, was computed for the average between the limits of d as given assuming that all of the flow stress is due to Hall-Petch hardening.

TABLE II

| Fig.# | Alloy | ϵ | s in nm | \bar{s} in nm | Φ from eq.10 | Φ | $\epsilon_e = b/sM$ | $\bar{\epsilon}_e = b/\bar{s}$ | $B_e = \bar{\epsilon}_e/\epsilon$ | σ_e [MPa] |
|-------|-----------------|------------|-----------------------|-----------------|-------------------|--------|---------------------|--------------------------------|-----------------------------------|------------------|
| 3 | A3 | 0% | 57 [♦] | 57 | 0.3° | 0.3° | 0.18% | | -- | 17 |
| 4 | A3 | 0% | 2.0-4.0 ^{♦♦} | 3.0 | 8.6°-4.3° | 6° | 2.5%-5.0% | 3.1% | -- | 180 |
| 9 | A3 | 9.3% | 4.2-7.0 | 9.0 | 2.4°-4.1° | 1.9° | 1.4%-2.4% | 1.1% | 0.12 | 79 |
| 10 | A3 | 9.3% | 4.5-14 | | 1.2°-3.8° | | 0.7%-2.2% | | | |
| 11 | A3 | 9.3% | 6.9-17 | | 1.0°-2.5° | | 0.6%-1.4% | | | |
| 12 | A3 ₃ | 9.5% | 2.9-7.0 | 10 | 2.5°-5.9° | 1.7° | 1.4%-3.4% | 1.0% | 0.11 | 72 |
| 13 | A3 ₃ | 9.5% | 2.9 | | 0.6°-3.1° | | 1.8%-3.4% | | | |
| 14 | A3 ₃ | 9.5% | 2.3 | | 0.8°-3.1° | | 1.8%-4.3% | | | |

♦ Extensive grid believed to be due to thermal strain on cooling from the extrusion temperature.

♦♦ Grids of very small area believed to be associated with precipitates and thus beir epitaxial in nature.

Legend: Comparison between ranges of average spacings (s) of dislocations in grids in or superimposed on grain boundaries and equivalent rotation angles (Φ). Also listed are the equivalent tensile strains that would have produced the grids assuming all dislocations were retained at the boundaries (ϵ_e), the dislocation retention parameters (B_e) derived therefrom, where $M \approx 3$ is the Taylor factor. Further included is σ_e , the tensile stress needed to supercritical bow links through the average network spacing, according to eq.13.

Codes of Negatives of the Micrographs Used in the Figures

| | | | |
|----------|--|-------|--------------|
| Fig.1: | A3 as received | #1868 | 2.8x13,000X |
| Fig.2: | Irregularity in A3 as received | #1856 | 2.8x 8,000X |
| Fig.3: | Two grains with serrated boundaries and coarse network in A3 as received | #1819 | 2.8x22,000X |
| Fig.4: | Flat-on seen boundary in A3 as received | #1808 | 2.8x80,000X |
| Fig.9: | Flat-on seen boundary in A3 after deformation to failure | #5084 | 2.8x60,000X |
| Fig.10: | As Fig.9 | #5104 | 2.8x46,000X |
| Fig.11a: | As Fig.9 | #5166 | 2.8x36,000X |
| Fig.11b: | As Fig.9 but different orientation | #5163 | 2.8x36,000X |
| Fig.11c: | As Fig.9 but third orientation | #5160 | 2.8x36,000X |
| Fig.12: | Two flat-on seen boundaries in A3 ₃ | #6758 | 2.8x100,000X |
| Fig.13: | Structure of A3 ₃ | #6757 | 2.8x46,000X |
| Fig.14: | Grain boundary networks of A3 ₃ | #6747 | 2.8x46,000X |
| Fig.17: | Detail of Fig.13 | #6757 | 400,000X |

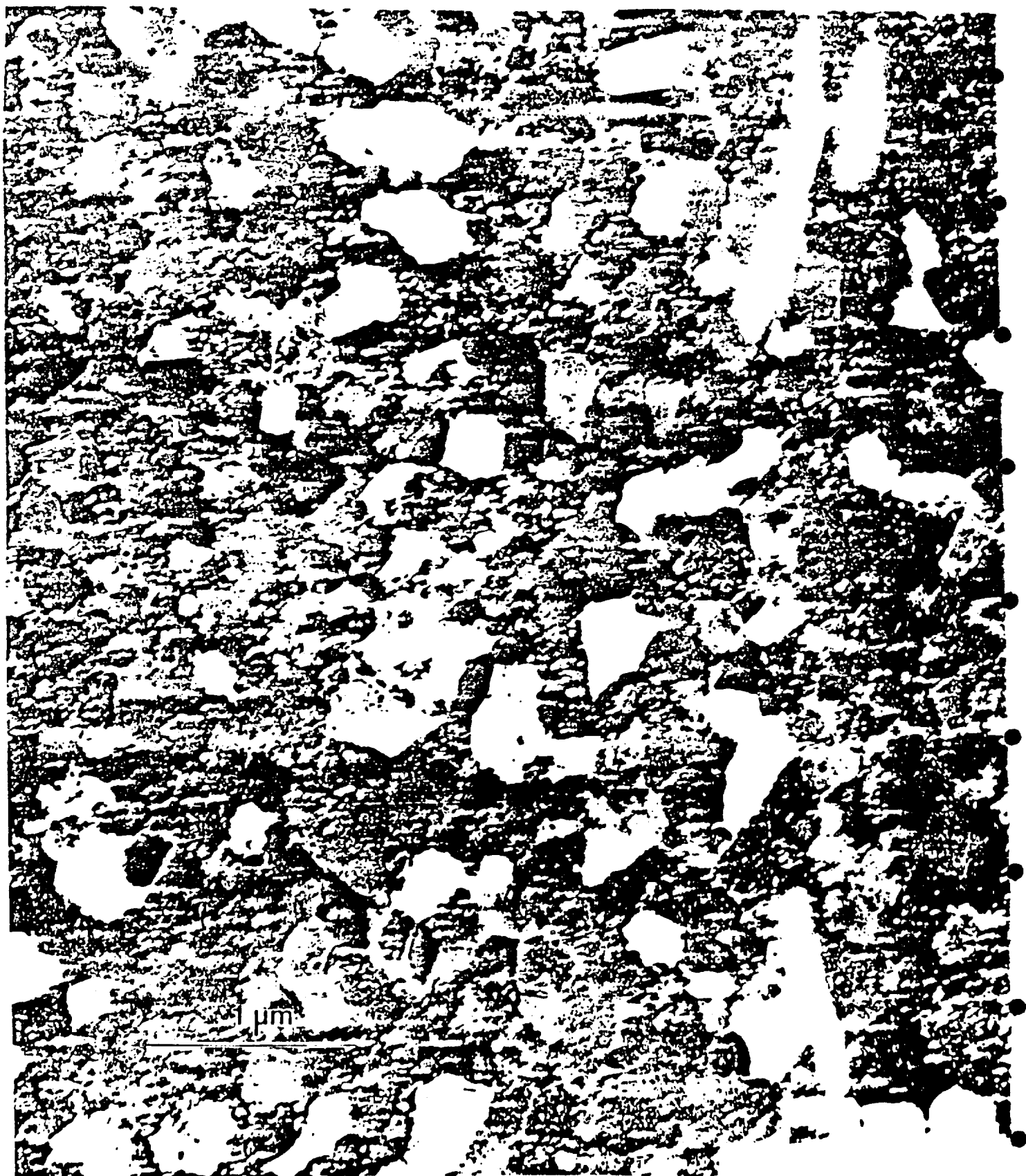


FIG. 1



FIG. 2



FIG. 3

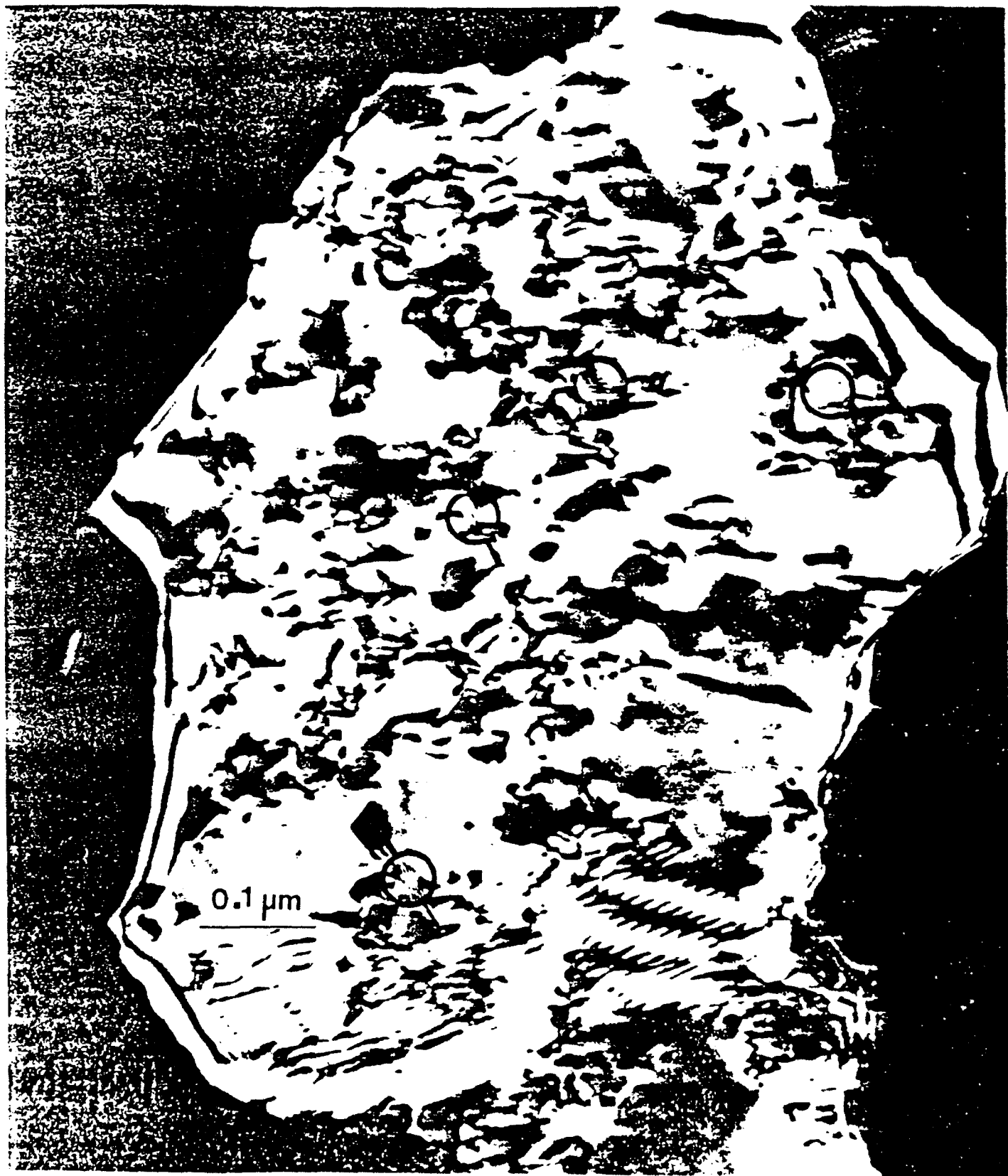
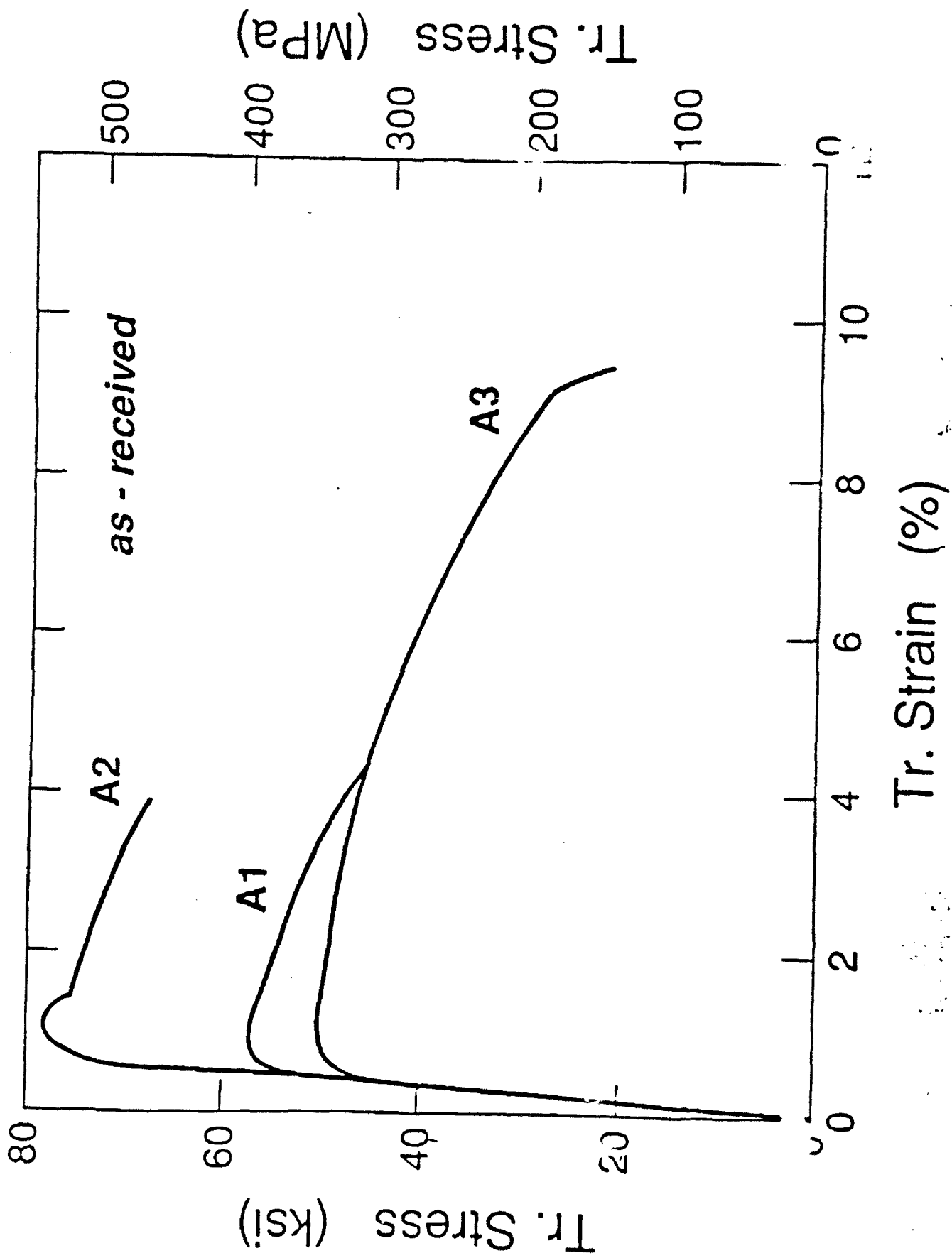
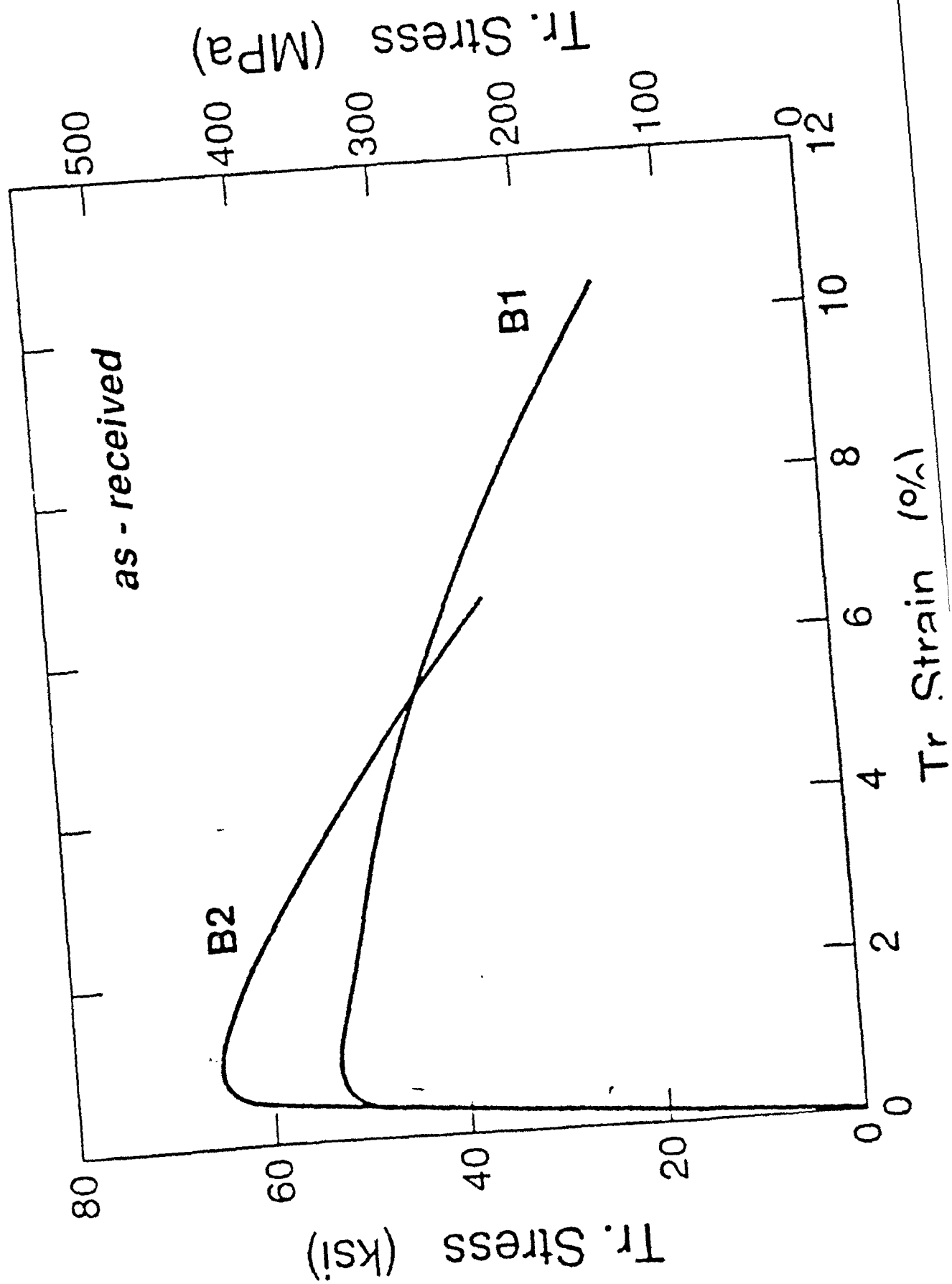
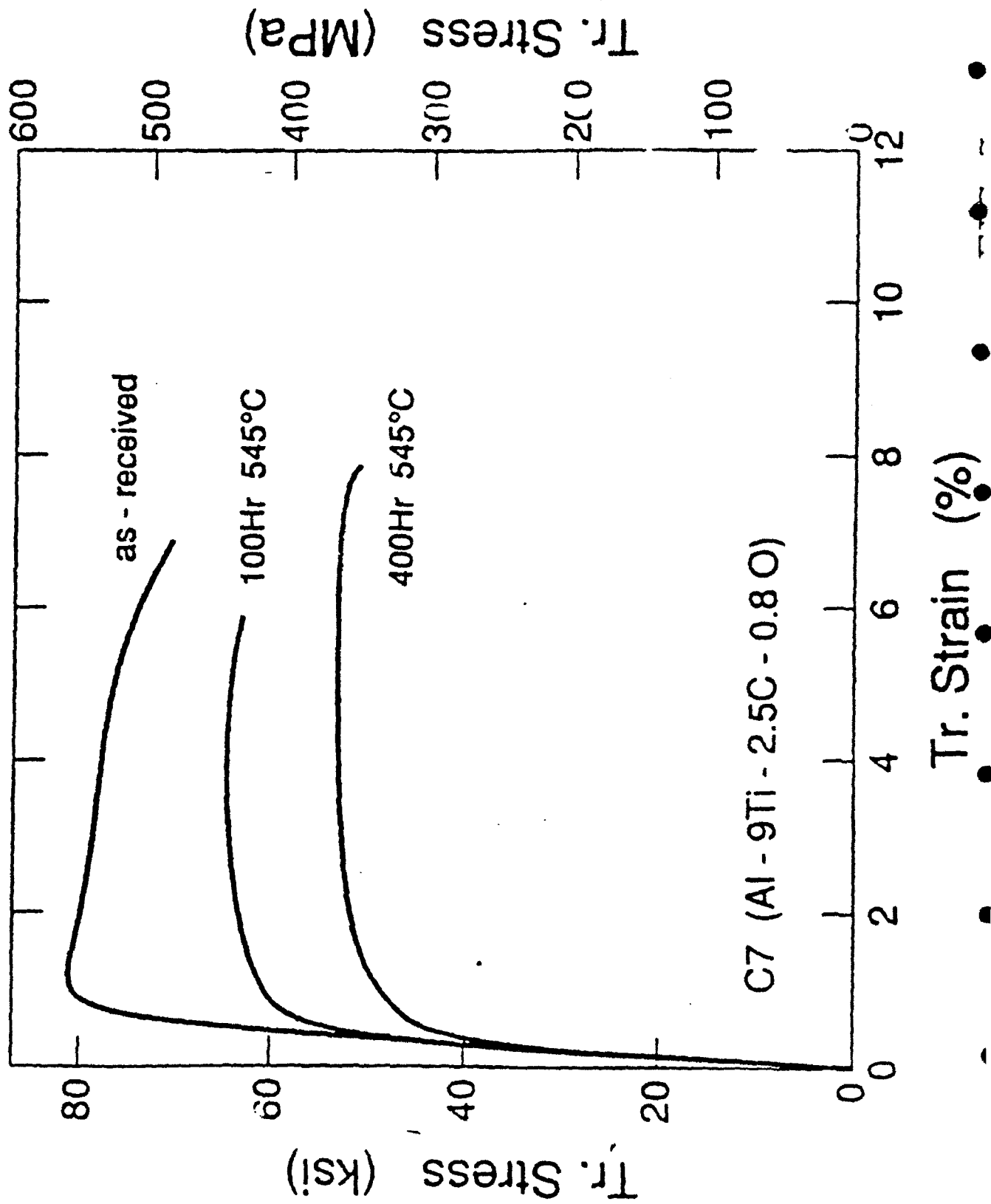


FIG. 4







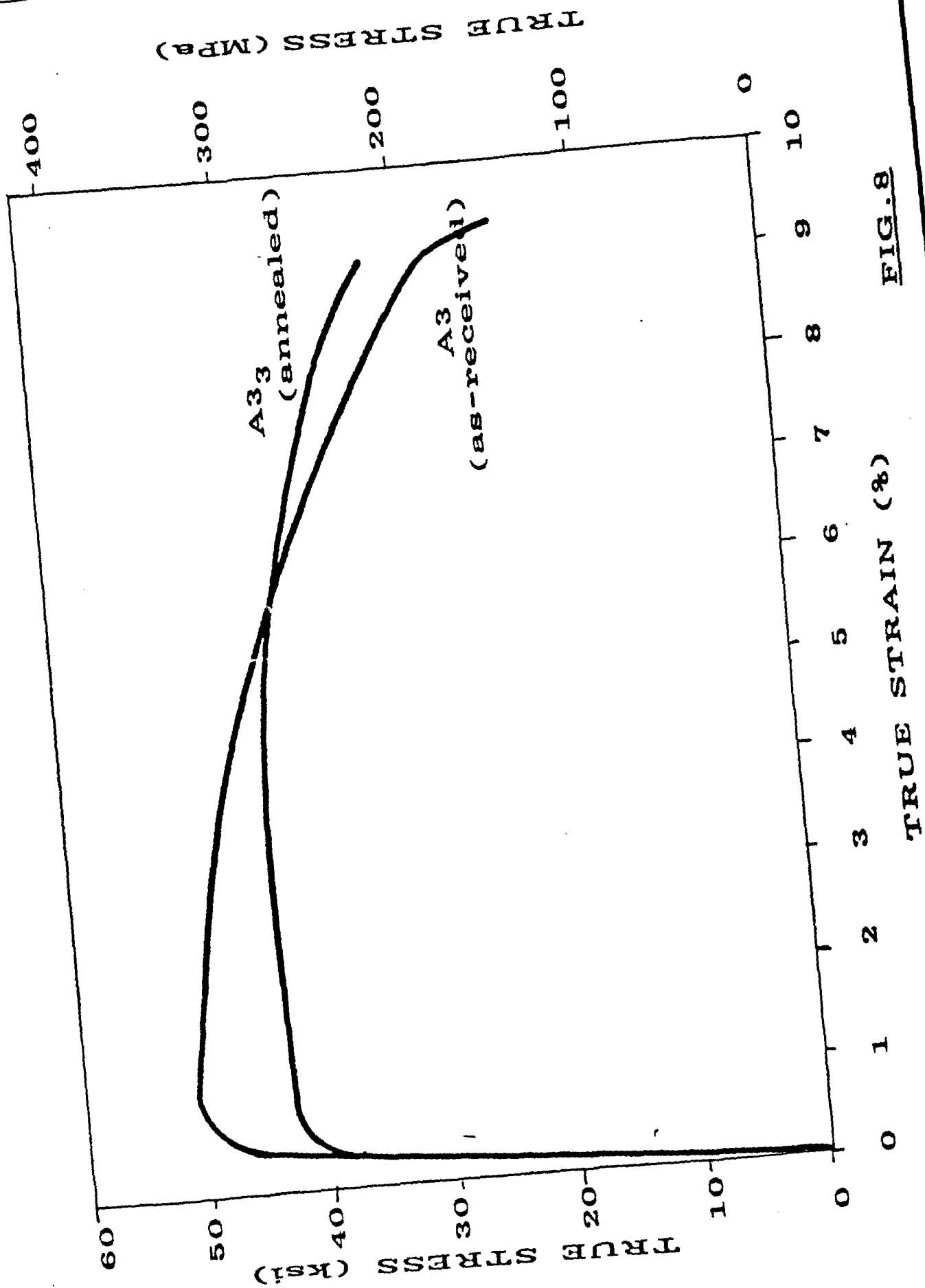


FIG. 8



FIG. 9



FIG. 10



FIG. 11a



FIG. 11b



FIG. 11c



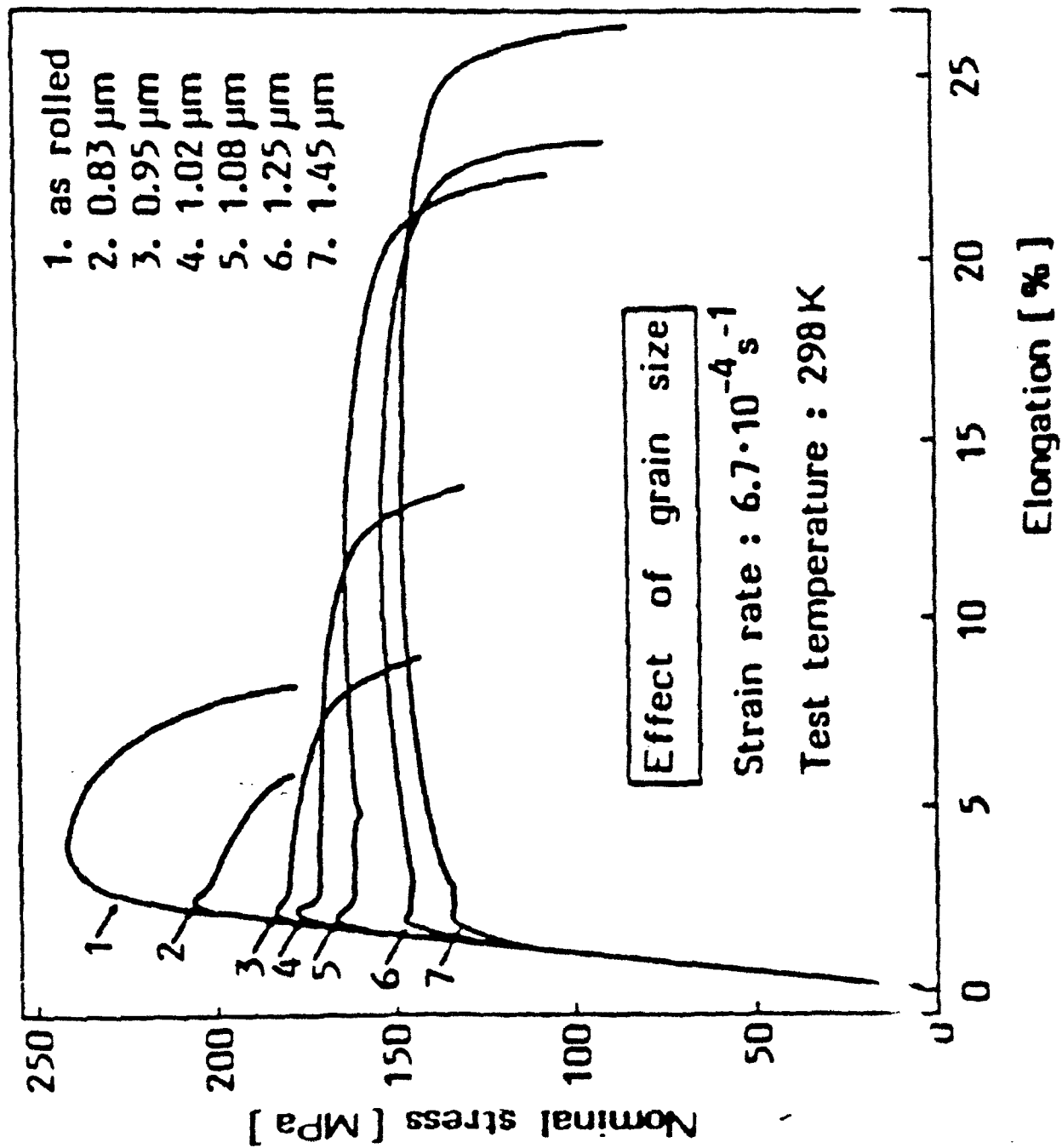
FIG. 12

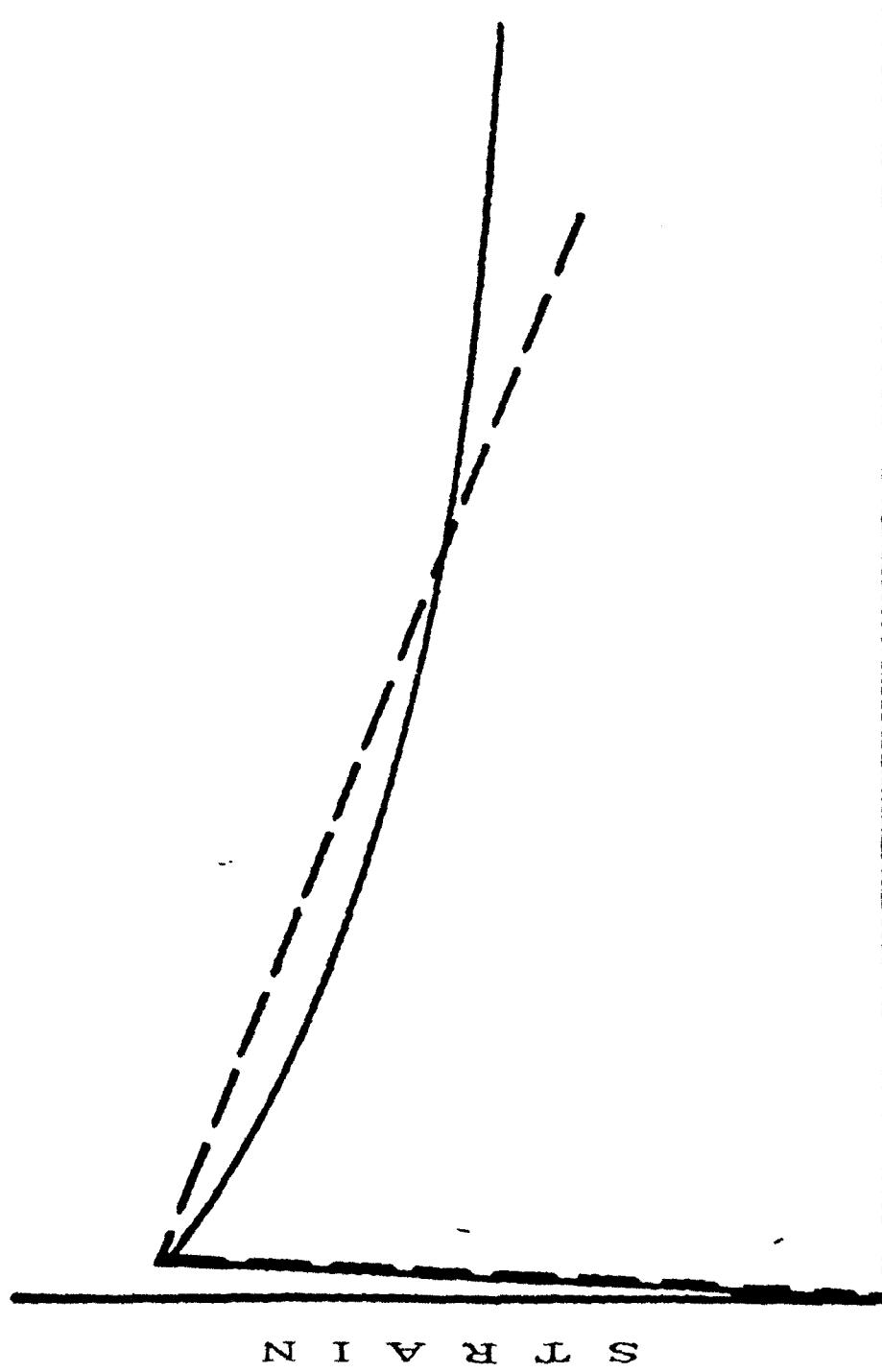


FIG. 13



FIG. 14





S T R E S S

FIG.16

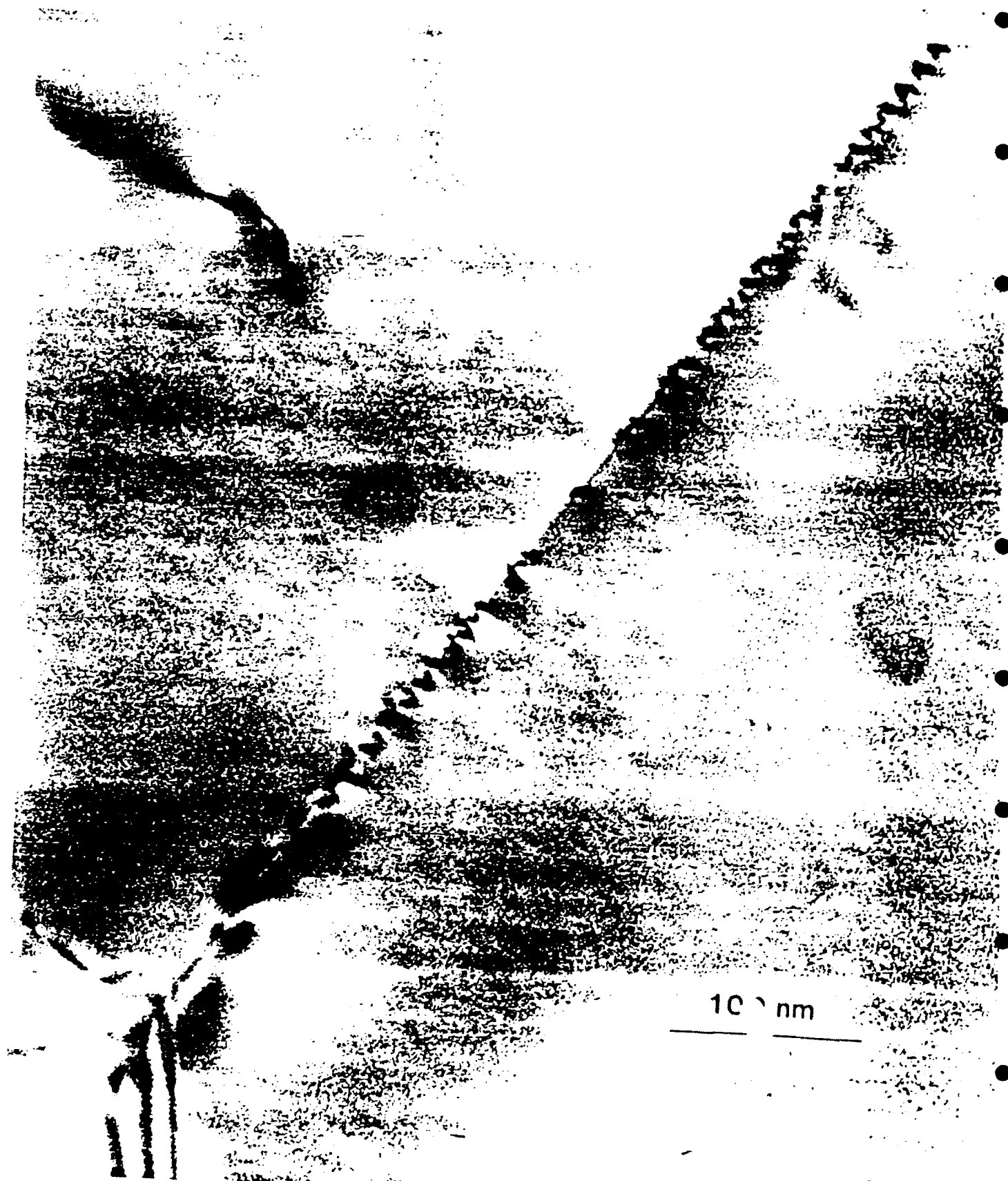


FIG. 17

TAMMANN's GRAIN BOUNDARY SUBSTANCE REVISITED

by

Doris Kuhlmann-Wilsdorf and Heinz G. F. Wilsdorf
Department of Materials Science and Engineering
University of Virginia, Charlottesville, VA 22901

ABSTRACT

Very dense dislocation networks overlying grain boundaries in extruded and cold-deformed MA aluminum alloys, in the as-received or annealed condition, have been identified as dislocation rotation boundaries which accommodate relative misorientations between neighboring grains caused by subsequent deformation. The fact that the dislocations involved are not annihilated at the grain boundaries indicates the presence of a continuous very thin grain boundary film reminiscent of Tammann's grain boundary substance. A search has revealed micrographic evidence for such films whose thickness may be only a few atomic diameters. It is concluded that such films may be fairly prevalent in ultra-fine-grained metals and may contribute both to their hardness and high temperature strength.

TAMMANN's GRAIN BOUNDARY SUBSTANCE REVISITED

by

Doris Kuhlmann-Wilsdorf and Heinz G. F. Wilsdorf
Department of Materials Science and Engineering
University of Virginia, Charlottesville, VA 22901

INTRODUCTION

Those of us old enough to still having been taught by pupils of Gustav Tammann, whom we may now recognize as the founder of materials science if ever a single person may deserve that title, will remember his experiments on "grain boundary substance" or "interstitial substance" (1). These terms embody the very first attempts at understanding the structure of grain boundaries. Through chemical attack, painstakingly avoiding turbulence and bubble formation, Tammann had dissolved metals, specifically cast copper immersed in $\text{NH}_4\text{OH} + \text{H}_2\text{O}_2$ and cast cadmium dissolved in ice-cold 50% NH_4NO_3 , and had observed ghostlike insoluble remnants of the grain boundary structure. He recognized that the substance was formed of insoluble impurities which were pushed ahead of the metal nuclei in the freezing melt until they became entrapped where the nuclei finally met and joined, i.e. at the grain boundaries. Since fractures at low temperatures tended to be transcrystalline but at elevated temperatures intercrystalline, he concluded that the grain boundary substance was composed of complex eutectics and he considered that such grain boundary material was a regular feature of real metals (at that time and for the following two decades invariably fairly impure) as he found it also in rolled and recrystallized cadmium, now with a preferential alignment in rolling direction.

While in his lectures at least until 1945 Georg Masing devoted some time to the above experiments, with the evolution of materials science the concept of the grain boundary substance was quietly dropped and the topic cannot be located in the extensive index of Masing's "Lehrbuch der Allgemeinen Metallkunde" of 1950 (2). That is understandable enough: In course of the steady advances of materials science, micrography revealed many details regarding the structure of grain boundaries. The tendency for enrichment of alloying constituents as well as impurities at grain boundaries and the resulting formation of precipitates became standard

knowledge but there was no sign of the grain boundary substance initially envisaged by Tam-
mann. To be sure, his intuition that low-melting material at the grain boundaries would cause
intercrystalline fracture at elevated temperatures has been fully vindicated, viz "hot shortness"
of metals, in general (3) and of steels in particular, e.g. (4). Also cases of continuous layers
of precipitates along grain boundaries are known e.g. (5), besides, of course, a wealth of
information on precipitates at grain boundaries. Yet, the earlier ideas of necessary major
disturbances at grain boundaries, perhaps including a transition layer of amorphous material
(6,7), have long since given place to the analysis of grain boundaries in terms of dislocation
networks (8-12) in an extension of Frank's analysis of low-angle boundaries (13). For the case
of pure metals, such interpretations have by now attained a high degree of refinement and have
in cases been experimentally verified to exquisite detail (14-16).

For alloys the analysis has similarly been carried to a high level of sophistication,
including the various aspects of preferential precipitation at grain boundaries, the generation and
destruction of point defects there, and the increased resistance against grain boundary migration
in creep (e.g. 5, 17,18) and recrystallization (19). Yet, what about the behavior of essentially
non-diffusing, nominally insoluble impurities? Is there no aggregation of these at grain bound-
aries except in the form of precipitates and/or dispersoids? The very fact that even thoroughly
cleaned metal powders and wires will not stick together spontaneously, and require high
pressures at elevated temperatures (i.e. HIP treatments) before they consolidate, proves the exist-
ence of hard-to-move impurities in exceedingly thin fairly uniform layers, in that case mostly
adsorbed water (20-22) and oxygen, that in the consolidated material may well aggregate at grain
boundaries.

These thoughts are relevant especially in connection with mechanical alloying (MA)
(23,24). In the MA process it is desired that metal powders continue to be mixed, individual
particles be cold-welded and broken up again, but no overall consolidation occur which is brought
about only at the very end, typically through degassing followed by extrusion at elevated tem-
peratures. To accomplish these goals, additives are used which mostly will be insoluble and
surface active, specifically in the case of aluminum alloys frequently stearic acid or carbon black

as in the case of DISPAL (25). One may expect such additives in particular, and doubtlessly numerous incidental and normally unrecognized impurities in general, to aggregate at grain boundaries in the form of exceedingly thin films, without forming either precipitates or dispersoids. It seems that such films do indeed exist in many MA alloys and importantly influence their properties. The case for that assertion is as follows.

DISLOCATION NETWORKS AT GRAIN BOUNDARIES IN EXTRUDED MA ALLOYS

In the course of a careful TEM examination of high-temperature MA aluminum alloys (26,27) developed for service at high temperatures (28), very fine dislocation networks were discovered overlying grain boundaries in deformed samples but not, or almost not, in as-received or as-received and annealed samples. Figs.1 and 2 give examples of the structures in these two types of samples before room temperature deformation and Figs.3 and 4 after room temperature deformation. Annealing appears to affect the grain boundaries *only* at temperatures above 540°C (as seen by comparing Figs.2 and 4) when some grain growth takes place and the boundaries, which are fairly jagged and evidently anchored by dispersoids in the as-received condition, are smoothed. The subsequent room-temperature plastic strain to failure (of about 9% tensile strain) which distinguishes Fig.3 from Fig.1, respectively Fig.4 from Fig.2, has not noticeably changed the smoothness of the grain boundaries, nor the grain size, nor caused any observable indication of grain boundary displacement. Rather, the salient difference of the structure after deformation as compared to the unstrained state is the widespread occurrence of the already mentioned networks overlying the grain boundaries. These may be seen in Figs. 3 and 4 as indicated in the legends but are virtually absent before straining. In fact they are difficult to detect since, on account of the very close dislocation spacing in the order of only a few nm, that requires excellent resolution and just the right illumination conditions. It is therefore not known whether all boundaries or only a significant minority are decorated with those networks.

Comparison with theoretical analysis (26,27) makes it almost certain that the networks are formed from glide dislocations but comprise only a fraction of their total number, i.e. about 10%, and that they are the result of complex reactions among dislocations which arrived from either

sides of the boundaries, and further that the networks constitute dislocation rotation boundaries of LEDS type (28,29) which accommodate the relative misorientation of the two neighboring lattices in response to the imposed plastic deformation, of necessity taking place on different glide systems on the two sides.

IMPLICATIONS OF DISLOCATION NETWORKS AT GRAIN BOUNDARIES

The conventional image of grain boundaries as accommodating differences of lattice orientation in the form of very intricate dislocation networks, perhaps decorated with precipitates and dispersoids, such that the total strain energy is (nearly) minimized (8-16), is incompatible with the presence of the discussed grain boundary networks. This is for the reason that the network dislocations should react with those already present, thereby reorganizing the grain boundary leaving it analyzable in terms of dislocations as before but certainly not including a discrete set of dislocations accommodating the minor, mostly additional, relative misorientation across the boundary which resulted from the preceding strain. Put differently: According to best previous understanding, in the course of straining, glide dislocations and point defects are annihilated at the grain boundaries while these constantly readjust their detailed structure in conformity with the momentary local lattice misorientation across them, without a memory of their preceding structure.

The presence of the boundary networks thus indicates an impediment against the dissolution of glide dislocations at grain boundaries, even while the great majority of the glide dislocations were able to cross them or at the least to largely mutually annihilate with dislocations arriving from the other side. If this were not so the dislocation retention could not amount to only 10% or thereabouts. What, then, could impede dislocation annihilation so very powerfully and not be obvious on TEM micrographs? The answer quite plainly is: only very thin uniform grain boundary films. Even so, the grain boundaries cannot remain totally rigid while the material deforms significantly in tension but are bound to deform more or less homologously therewith. Thus dislocations must cross, or react across, the grain boundaries, and the boundary films must be weakened through the resulting atomistic steps and breaks in them.

INDIRECT EVIDENCE FOR CONTINUOUS GRAIN BOUNDARY FILMS

The initial interest in the grain boundaries of the discussed MA alloys derived from their worksoftening behavior. Together with many ultra-fine grained metals, so also those alloys exhibit substantial worksoftening which is, of course, very detrimental for their practical application. Therefore a general theory of worksoftening was made (29), based on the highly successful LEDS (Low-Energy Dislocation Structures) concept (30,31). This indicated that worksoftening curves whose slope declines with increasing strain are due to dislocation interactions such as to decrease the stored dislocation content of the material, whereas a constant slope or increasing rate of decrease indicates a decline of the τ_0 component of the flow stress (τ) in accordance with the standard equation

$$\tau = \tau_0 + \alpha Gb \sqrt{\rho} \quad (1)$$

where G and b are shear modulus and Burgers vector, respectively, and ρ is the dislocation density (29). In fact, the curves are of the latter type, indicating a decline of τ_0 (26,27). This in turn means that grain boundary softening is taking place since grain size strengthening must be the by far largest part of τ_0 in this case (26,27).

Evidently, the presence and expected behavior of the grain boundary films will account for the exceptionally strong grain boundary hardening as well as for the worksoftening. In addition, these films account for another puzzling observation, namely a surprisingly strong strain rate sensitivity, in the sense that increasing strain rate increases the flow stress more than normal, coupled with a rise of strain to failure. The strong increase of flow stress with strain rate testifies to a significant involvement of thermal activation in the dislocation crossing of boundaries, of course, and implies a quite small activation volume in agreement with the previous conclusion that the films are very thin indeed, as already indicated by their microscopical near-invisibility in TEM. The increase of strain to failure with increasing strain rate, in turn, still awaits a detailed explanation but at any rate indicates that there is no thermally activated healing process at the grain boundary films so as to repair damage caused by crossing dislocations. This

observation is in line with the already noted insensitivity of the grain boundaries to annealing below 540°C, both of these effects proving that the activation energy for diffusion of the grain boundary film material is high.

DIRECT EVIDENCE FOR GRAIN BOUNDARY FILMS

Stimulated by the outlined reasoning, a search was made for the grain boundary films whose presence was so strongly inferred from the discussed evidence. They can indeed be seen in very thin TEM samples in which grain boundaries are fortuitously very nearly normal to the plane of observation and diffraction conditions are favorable. Figs. 5 and 6 show examples. The first of these is from the same alloy to which Figs. 1 to 4 pertain, and Fig. 6 from DISPAL (32).

Reflecting on the evidence and theoretical expectations, it is clear that grain boundary films cannot be a very rare occurrence but are probably present whenever an alloy contains a fair amount of surface active, nearly insoluble impurities. MA alloys are therefore likely to contain Tammann-type grain boundary films, albeit as discussed certainly not eutectic, probably not crystalline (since otherwise one should see epitaxial dislocations), and only in the order of 1nm thick or less. In the case of the A3 alloy of Figs. 1 to 5 carbon is implicated as forming the films, or at the least being strongly represented in them. This is for the reason that substantially less Al_4C_3 is seen in A3 than commensurate with its carbon content (26,27). The use of stearic acid in the mechanical alloying process of A3 is the likely original cause, and normally of carbon black in DISPAL, although the DISPAL type used for Fig. 6 was said not to include additives.

For films of thickness d and grain sizes D , the volume concentration of the grain boundary material is $3d/D$. For the typical values of $D \approx 300\text{nm}$ and an estimated value of $d \approx 1\text{nm}$, this amounts to just about 1% grain boundary material thusly tied up in the form of grain boundary films. That is in the right order of magnitude and is in good accord with actual concentrations of suspected active impurities.

Far from the grain boundary films being a nuisance or worse, we suspect that they are highly beneficial since we may ask ourselves, what else could be responsible for the ultra-fine grain sizes obtained by MA, which indeed make MA alloys exceptionally strong and resistant

against recrystallization, i.e. confer high temperature strength? It is therefore suggested herewith that ultra-fine grain structures and high temperature strength are sometimes, if not quite commonly, associated with, indeed are the result of, ultra-thin Tammann type grain boundary films.

ACKNOWLEDGEMENTS

Grateful acknowledgment is made to the Air Force Wright Aeronautical Laboratories, Materials Laboratory (W. M. Griffith, S. Kirchoff and J. Kleek) under whose auspices the discussed high-temperature MA alloys were developed, to J. A. Hawk who made the micrographs of most of the figures, and to the Materials Division (Tribology, P. Schmidt and M. B. Peterson) of the Office of Naval Research, Arlington, VA, who sponsored D. Kuhlmann-Wilsdorf's theoretical research.

REFERENCES

- 1) G. Tammann, "Lehrbuch der Metallographie" (L. Voss Verlag, Leipzig, translated as "A Textbook of Metallography" by R. S. Dean and L. G. Swenson, The Chemical Catalog Comp., New York, 1925) pp. 16-18.
- 2) G. Masing, "Lehrbuch der Allgemeinen Metallkunde" (Springer Verlag, Berlin, 1950).
- 3) e.g. Metals Handbook , ASM Intl., Metals Park, OH.
- 4) T. Ko and D. Hansen, J. Iron and Steel Inst., 164 (1950) 51.
- 5) M. Schumacher and G. Sauthoff, in "Deformation of Multiphase and Particle Containing Materials" (Eds. J. B. Bilde-Sorensen, N. Hansen, R. Horsewell, T. Leffers and H. Lilholt, Riso Natl. Lab., Roskilde, Denmark, 1983), p. 525.
- 6) W. Rosenhain and J. C. W. Humphrey, J. Iron and Steel Institute, 87 (1913) 219.
- 7) J. E. Sears, Trans. Cambridge Philos. Soc., 21 (1908-1912) 105.
- 8) H. Gleiter, E. Hornbogen and G. Baro, Acta Metall., 16 (1968) 1053.
- 9) W. Bollmann, "Crystal Defects and Crystalline Interfaces" (Springer Verlag, Berlin, 1970).
- 10) A. H. Clauer, B. A. Wilcox and J. P. Hirth, Acta Metall., 18 (1970) 381.
- 11) H. Gleiter, Phys. Stat. Sol., 45 (1971) 9.
- 12) J. P. Hirth, Met. Trans., 3 (1972) 3047.
- 13) F.C. Frank, in "Pittsburgh Symp. on the Plastic Deformation of Crystalline Solids" (in Rept. NAVEXOS-P-834, 1950, Off. of Naval Res., Washington, DC), p.150; see also in "Conf. on Defects in Crystalline Solids", The Phys. Soc. (London) 1955, p.150.
- 14) L. E. Murr, "Interfacial Phenomena in Metals and Alloys", (Addison Wesley, Reading, MA, 1975).
- 15) C. Solenthaler and W. Bollmann, in "Low-Energy Dislocation Structures" (Proc. Intl. Conf. on Low-Energy Dislocation Structures, Eds. M.N. Bassim, W.A. Jesser, D. Kuhlmann-Wilsdorf and H.G.F. Wilsdorf, Elsevier Sequoia, Lausanne, 1986), p.35; see also Mater. Sci. Engg., 81 (1986) 35.

- 16) C. Solenthaler, in "Low-Energy Dislocation Structures II" (Proc. Intl. Conf. on Low-Energy Dislocation Structures, Eds. M. N. Bassim, W. A. Jesser, D. Kuhlmann-Wilsdorf and G. J. Shiflet, Elsevier Sequoia, Lausanne, 1989), p.95; see also Mater. Sci. Engg., A113 (1989) 95.
- 17) A. J. Kennedy, Proc. of "Creep and Fatigue in Metals" (J. Wiley and Sons, NY, 1963).
- 18) F. Garofalo, "Fundamentals in Creep and Creep Rupture in Metals" (The Macmillan Co., NY, 1965).
- 19) B. Liebmann and K. Lucke, J. Metals 8 (1956) 1413.
- 20) C. Gao and D. Kuhlmann-Wilsdorf, (1990 Holm Conf. on Electrical Contacts, IEEE, Piscataway, NJ 1990), p.292; see also IEEE Trans. Comp. Hybrids and Manuf. Techn., 14 (1991) 37.
- 21) Chao Gao, D. Kuhlmann-Wilsdorf and Matthew S. Bednar, "Wear of Materials - 1991" (Ed. K. C. Ludema, Am. Soc. Mech. Eng., New York, 1991), p.433; see also Wear, 149 (1991) 297.
- 22) Chao Gao, Doris Kuhlmann-Wilsdorf and David D. Makel, ASME J. of Trib., 114 (1992) 174.
- 23) J. S. Benjamin and M. J. Bomford, Met. Trans., 1 (1970) 2943.
- 24) J. S. Benjamin and M. J. Bomford, Met. Trans., 8A (1977) 1301.
- 25) G. Jangg, F. Kutner and G. Korb, Aluminium, 51 (1975) 641.
- 26) H. G. F. Wilsdorf and D. Kuhlmann-Wilsdorf, in "Modelling of Plastic Deformation and Its Engineering Applications", (13th Risø Intl. Symp. on Materials Science, Sept. 7-11, 1992), in the press.
- 27) H. G. F. Wilsdorf and D. Kuhlmann-Wilsdorf, Mater. Sci. Engg., submitted for publication.
- 28) For a first review see H. G. F. Wilsdorf, in "Dispersion Strengthened Aluminum Alloys", (Eds. Y.-W. Kim and W. Griffith, TMS Warrendale, PA 1988), p.3
- 29) D. Kuhlmann-Wilsdorf and H.G.F. Wilsdorf, phys. stat. sol., (P. Haasen 65th birthday celebration issue), 1992, in the press.

- 30) "Low-Energy Dislocation Structures" (Proc. Intl. Conf. on Low-Energy Dislocation Structures, Eds. M.N. Bassim, W.A. Jesser, D. Kuhlmann-Wilsdorf and H.G.F. Wilsdorf, Elsevier Sequoia, Lausanne, 1986); see also Mater. Sci. Engg., 81 (1986).
- 31) "Low-Energy Dislocation Structures II" (Proc. Intl. Conf. on Low-Energy Dislocation Structures, Eds. M. N. Bassim, W. A. Jesser, D. Kuhlmann-Wilsdorf and G. J. Shiflet, Elsevier Sequoia, Lausanne, 1989), p.95; see also Mater. Sci. Engg., A113 (1989).
- 32) J. A. Hawk, W. Ruch and H. G. F. Wilsdorf, in "Dispersion Strengthened Aluminum Alloys", (Eds. Y.-W. Kim and W. Griffith, TMS Warrendale, PA 1988), p603.

LEGENDS

Fig.1: Plan view of a grain boundary in the undeformed A3 MA alloy as received (including an expected 4.0 v/o of Al_4C_3 , 1.4 v/o of Al_2O_3 and 0.5 v/o of Y_2O_3) with an average grain size of about $0.35\mu\text{m}$. Note pinning of the boundary by numerous dispersoids.

Fig.2: As Fig.1 but after 10 hrs. annealing at 540°C . As seen, this degree of annealing has not significantly affected the appearance of the grain boundaries, and it did not noticeably change the grain size.

Fig.3: As Fig. 1 but after 9.3% tensile strain to failure. Note the substantially unchanged character of the grain boundary as pinned by dispersoids, except for the fine dislocation grid over-laid on the boundary visible at its upper right. Such dislocation grids are frequent after deformation but not in the undeformed condition whether before or after annealing.

Fig.4: Dislocation grids overlying grain boundaries in highly annealed A3 alloy seen in darkfield illumination. The specimen was tensile strained 9.5% to failure after an 18hrs. anneal at 550°C which greatly straightened the grain boundaries and enlarged the grain size by about a factor of two.

Fig.5: Highly enlarged view of a grain boundary in as-received A3 after tensile straining to failure which coincidentally is almost exactly normal to the plane of observation. The dots are images of dislocations in a grain boundary dislocation grid. An evidently extremely thin grain boundary film may be seen here and there between these dislocation images.

Fig.6: Example of what appears to be grain boundary substance in undeformed DISPAL 0, an MA mixture of aluminum and 4 v/o aluminum oxide. The boundary in this case is not decorated with dislocations but anchored at dispersoids and the grain boundary film is markedly thicker than in Fig.5.



FIG. 1

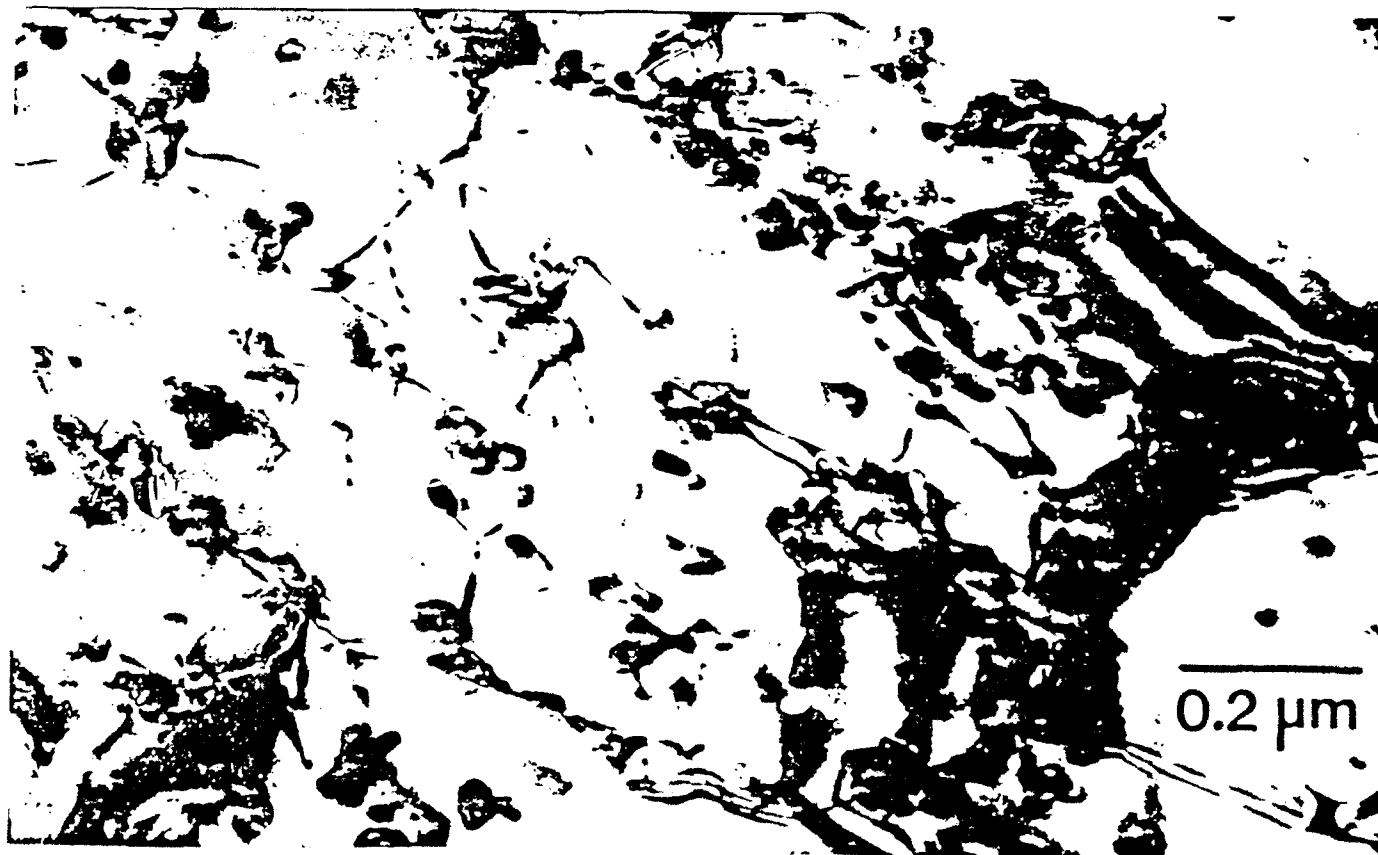


FIG. 2

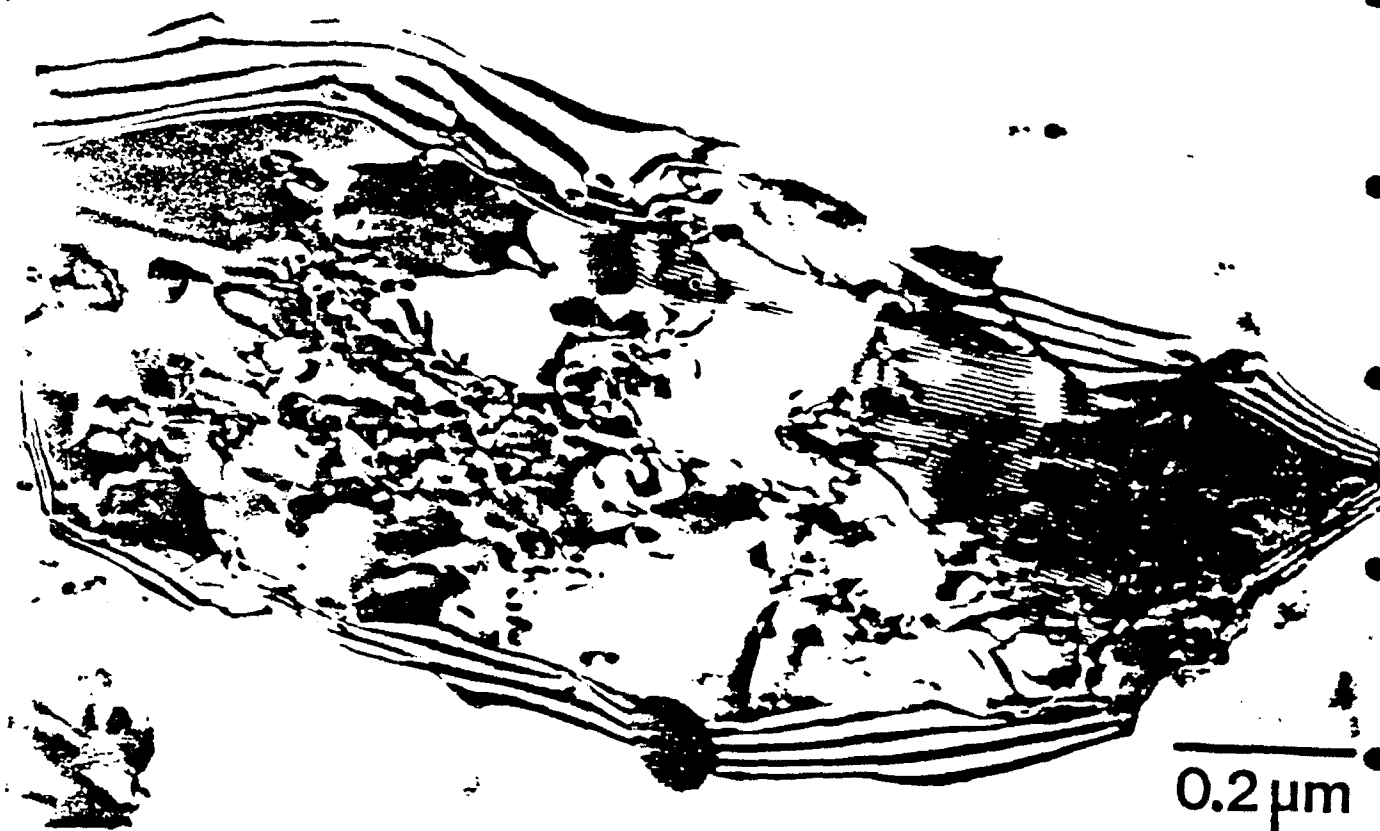


FIG. 3

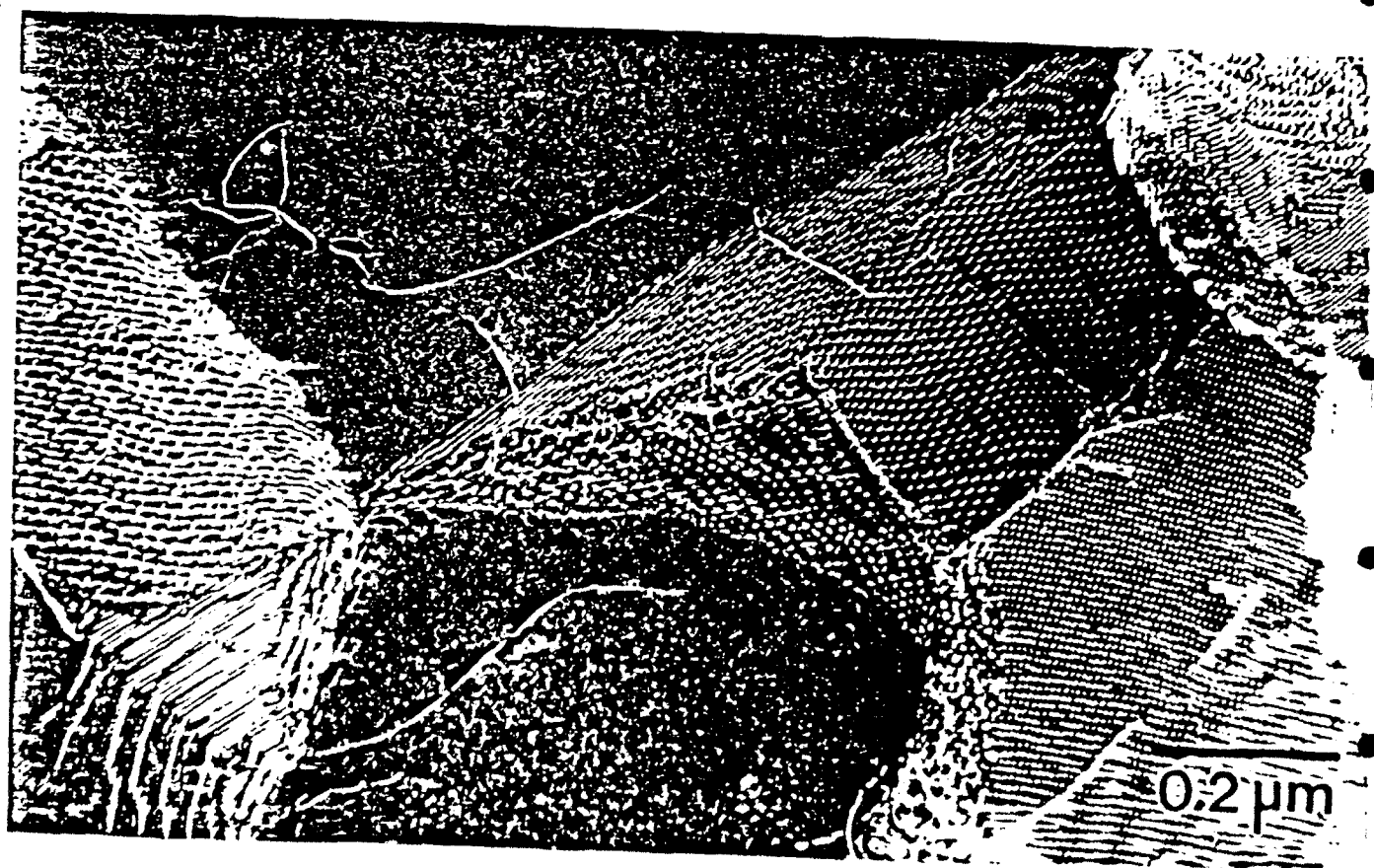


FIG. 4

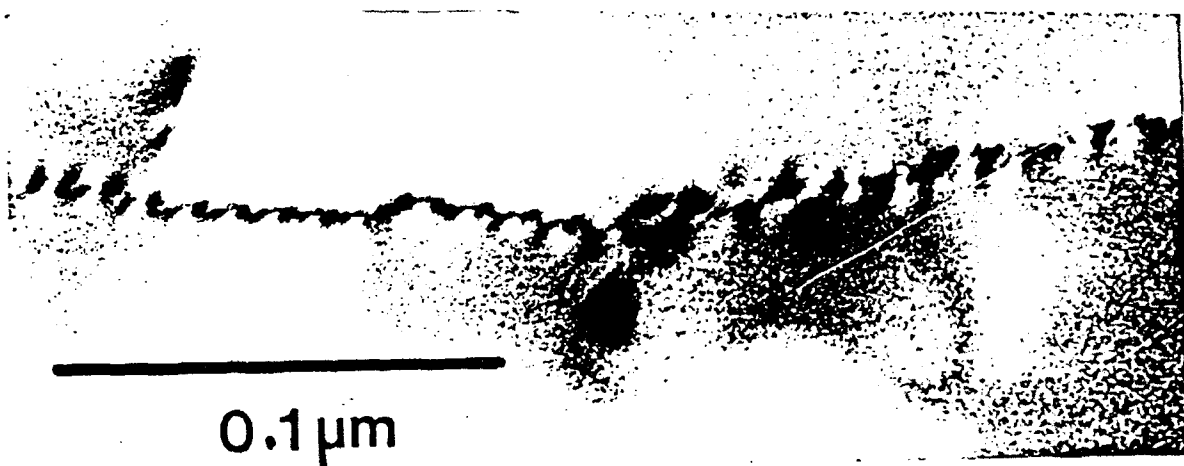


FIG. 5

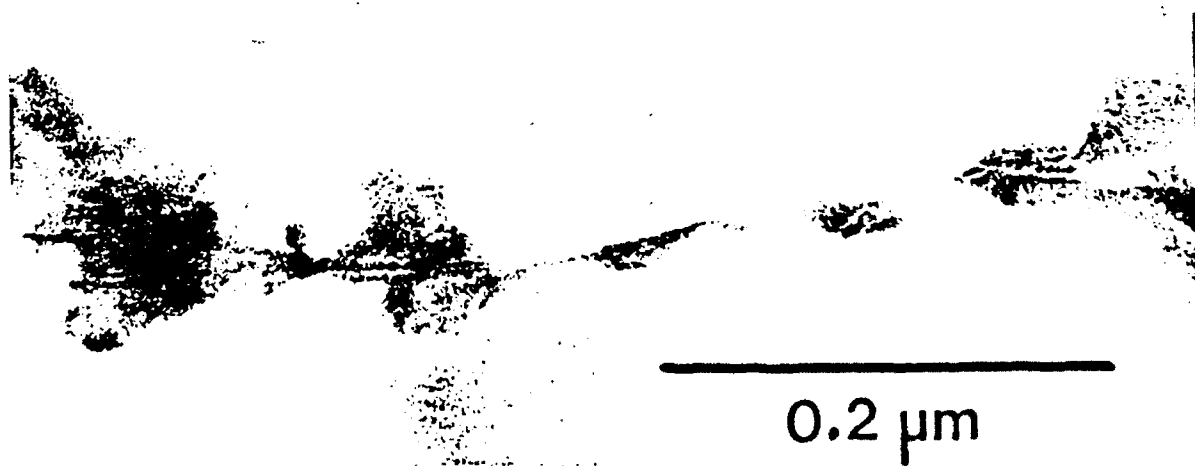


FIG. 6

Reprint from: Proceedings of the 13th.
Risø International Symposium on Materials Science:
*Modelling of Plastic Deformation and
Its Engineering Applications.*
Editors: S.I. Andersen, J.B. Bilde-Sørensen,
N. Hansen, D. Juul Jensen, T. Leffers, H. Lilholt,
T. Lorentzen, O.B. Pedersen and B. Ralph.
Risø National Laboratory, Roskilde, Denmark, 1992

GRAIN BOUNDARY HARDENING, WORKSOFTENING AND LEDS IN MA ALLOYS

H.G.F. Wilsdorf and D. Kuhlmann-Wilsdorf

Department of Materials Science and Engineering
University of Virginia, Charlottesville, VA 22901

ABSTRACT

According to a recent theory of worksoftening based on LEDS (low-energy dislocation structure) considerations, worksoftening in high-performance alloys is due to either reduction of an excess dislocation density or reduction of the τ_0 component of the flow stress, at least a part of which is the Hall-Petch stress. The stress-strain curves of mechanically alloyed (MA) and extruded aluminum alloys for very high temperature applications show distinct worksoftening of the type expected from τ_0 reduction. Also the roughly linear decrease of the flow stress with temperature suggests that it is dominated by τ_0 , and the very small grain size of $\approx 0.4\mu\text{m}$ implicates grain boundary hardening. Since the grain size does not change with straining, the worksoftening must thus be due to a decreasing Hall-Petch constant. Surprisingly regular dislocation networks overlaid on the boundaries in deformed specimens, representing rotation angles of a few degrees, suggest that this occurs through the gradual destruction of a continuous coverage of the grain boundaries by an extremely thin layer of nominally insoluble atoms, probably carbon, while the networks accommodate the mutual rotations of grains during straining.

1. WORKSOFTENING THEORY

The simplified general formula for the flow stress, τ , as a function of dislocation density, ρ , is

$$\tau = \tau_0 + \tau_G = \tau_0 + \alpha Gb\sqrt{\rho} \quad (1)$$

with G and b the shear modulus and Burgers vector, respectively, and α a numerical constant between about 0.2 and 0.6. The "frictional" stress τ_0 includes all parts of the flow stress which are independent of dislocation density, and more often than not is small compared to τ . Parts of τ_0 may be based on thermally activated processes while the $\alpha Gb\sqrt{\rho}$ part is virtually independent of thermal activation even under extreme conditions.

The LEDS theory of workhardening explains eq.1 in accord with all known experimental evidence. According to it, grain boundary hardening is a part of τ_0 as is precipitation hardening (Kuhlmann-Wilsdorf 1989) and the theory accounts for the so often observed Hall-Petch relationship, i.e.

Wilsdorf and Kuhlmann-Wilsdorf

$$\tau_{HP} = K_{HP}/\sqrt{d} \quad (2)$$

with d the grain size and K_{HP} the "Hall-Petch constant". To the extent that grain boundary hardening is simply due to the discontinuous orientation change across the boundaries, τ_{HP} is also proportional to G , and is not thermally activated. Unlike τ_G , however, τ_{HP} does not depend on dislocation density. Therefore both τ_{HP} and the contribution due to dispersion hardening typically stay nearly constant throughout straining, and only that generally minor part of τ_0 which is due to dislocation intersections rises with strain, being proportional to τ_G in accordance with the Cottrell-Stokes law (Cottrell and Stokes 1955, Kuhlmann-Wilsdorf 1968).

In the LEDS (mesh-length) theory of workhardening (Kuhlmann-Wilsdorf 1968, 1989) the workhardening coefficient is given by

$$(d\tau/d\gamma) = \Theta = d\tau_0/d\gamma + d\tau_G/d\gamma = d\tau_0/d\gamma + 2\alpha\beta G/mg \quad (3)$$

where m and g are almost constant parameters in the order of $m=1$ and $g=25$, while Θ is the "dislocation retention parameter". It is the fraction of newly generated dislocations which at the end of their glide path are trapped in the LEDS structure.

As discussed above, typically $d\tau_0/d\gamma$ is negligible compared to $d\tau_G/d\gamma = 2\alpha\beta G/mg$. Since, further, not only m and g but also α is nearly independent of strain, as already mentioned, the strain dependence of Θ i.e. the typical gradual flattening slope of stress-strain curves, essentially mirrors the corresponding gradual decrease of β with strain (Kuhlmann-Wilsdorf and Hansma 1989), i.e. eq.3 often reduces to

$$\Theta = (d\tau_G/d\gamma) = 2\alpha\beta G/mg = 0.02\beta G \quad (4)$$

β may assume negative values, leading to negative Θ values i.e. worksoftening, when straining depletes rather than increases the dislocation content. That will happen when an existing LEDS has a higher dislocation content than the LEDS that would be established under otherwise same conditions if the material had started out with a low dislocation density. An example of this is creep deformation at elevated temperatures of a workhardened metal. Such artificially high workhardened state, i.e. compared to subsequent deformations, could well obtain in mechanically alloyed materials, and a very high dislocation density introduced through the MA process could decrease in subsequent deformation with attendant worksoftening.

The simplest and most reasonable dependence of β on flow stress would be linear, i.e.

$$\beta^* = \beta_0(1 - \tau_G/\tau_m)$$

where τ_m is the flow stress that would have been reached by the otherwise same material had it initially been at a lower dislocation density, and β_0 is the correlated β value at τ_m . If one obtains a workhardening coefficient Θ^* decreasing with strain of (Kuhlmann-Wilsdorf and Wilsdorf 1992)

$$\Theta^* = \Theta_0(1 - \tau_G/\tau_m) \quad (6)$$

and

$$\tau = \tau_m + \delta\tau_m \cdot (-\Theta_0/\tau_m) \quad (7)$$

with $\delta\tau_m$ the initial excess of flow stress above τ_m , as shown in Fig.1.

Hardening, Softening and LEDS in MA Alloys

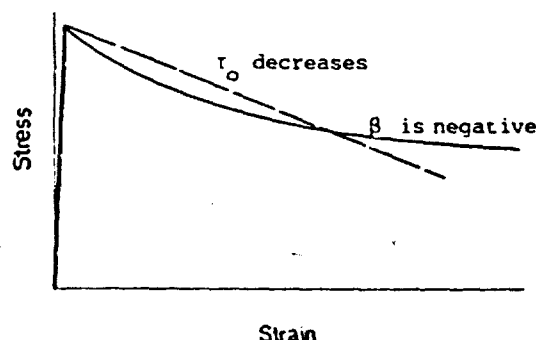


Fig.1. The stress-strain curves resulting from worksoftening due to negative β values (eq.7) and due to reduction of r_0 with strain, (eq. 8) as indicated.

Alternatively, it is possible, also, that r_0 decreases with strain. The most probable case here is a linear decrease of the excess of δr_0 from its initial value r_{0i} with strain, i.e.

$$\delta r_0 = \delta r_{0i} [1 - \delta/\delta_f] \quad (8)$$

This yields the curve in Fig.1 provided that r_0 meanwhile remains constant where, again, r_m is the equilibrium value of the flow stress under the given deformation conditions. The value of the critical strain δ_f may be estimated from considering that transformation from the old to the new LEDS will be completed, and thereby δr_0 will have been eliminated, when the newly generated loop length equals some moderate fraction, C , of the dislocation density $\bar{\rho}_m$ at the stress of r_m . The result is (Kuhlmann-Wilsdorf and Wilsdorf 1992)

$$\delta_f = C g m b \sqrt{\bar{\rho}_m} / 4 \quad (9)$$

Clearly, C must lie well below unity but cannot be a very small number since the new dislocations are not only replacing an equal length of pre-existing dislocation length that had been subject to the excess frictional stress, but in addition will have triggered additional spontaneous reorganization among the pre-existing dislocations. Thus $0.1 < C < 0.5$ may be a reasonable range. With those values and with $b = 3 \times 10^{-10} \text{ m}$, $\zeta = 4 \times 10^{15} / \text{m}^2$, $m = 1$ and $g = 25$ one finds δ_f to range between about 1% and 10%.

2. EXPERIMENTAL WORKSOFTENING CURVES

Fig.2 shows three rather typical worksoftening curves obtained from recently developed high-temperature MA aluminum alloys (see Wilsdorf 1988). As seen in comparison with Fig.1, these clearly are of the type expected from changes in r_0 , not from reduction of dislocation density through negative β values. Indeed, a decreasing slope of the workhardening curve results from negative β values no matter what the specific assumptions as to dependence on stress may be since with decreasing dislocation density the driving force for further dislocation density reduction necessarily declines. By contrast, diminishing r_0 values, though they most likely start out linearly with the length of newly formed dislocations and thus with a linear decrease of the stress-strain curve in accordance with Fig.1, can well continue at an accelerated rate in accordance with the behavior in Fig.2, as the pre-existing LEDS is destabilized.

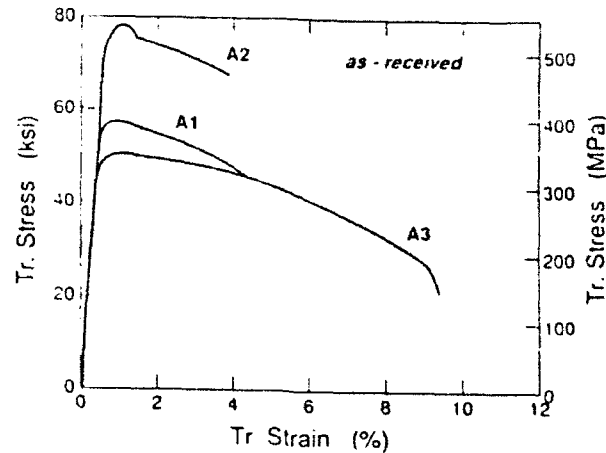


Fig.2: Room-temperature tensile stress-strain curves parallel to the extrusion axis of the high-temperature MA aluminum alloys A1, A2 and A3 in the as-received condition (Wilsdorf 1988).

3. CORRELATED MICROGRAPHY

Micrographs of the A2 alloy, (to which Fig.2 pertains and which is believed to be representative), before and after straining show equiaxed grains of about 0.25 to 0.5 μm diameter. Also, straining did not noticeably change the appearance of the grains except in one crucial aspect: After deformation, many if not most of the grain boundaries were covered with exquisitely fine dislocation network of $\sim 6\text{nm}$ spacing that are rare, and if present at all either of very small extent or composed of much more coarsely spaced dislocations, in the as-received condition. Figs. 3 and 4 show examples.

In both micrographs note the evident anchoring of the boundaries by many dispersoids. The broader fringes about the grain in Fig.3 are fringes of equal thickness indicating how the grain volume tapers through the thickness of the foil. In the drawn circles may be seen groups of about ten each, short, parallel, finely spaced dislocations. In Fig.4 such small groups may also be present although unresolved. More importantly, however, note the set of parallel dislocations in Fig.4 of about 6nm spacing. Such grids or networks are very frequent in deformed specimens but were not seen in the as-received condition except for occasional networks of much larger spacing.



Fig.3: Plan view of grain boundary in A3 as-received. Small encircled patches of very fine grids of parallel dislocations appear to be associated with precipitates and thus being of epitaxial nature.

0.5 μm

Hardening, Softening and LEDS in MA Alloys

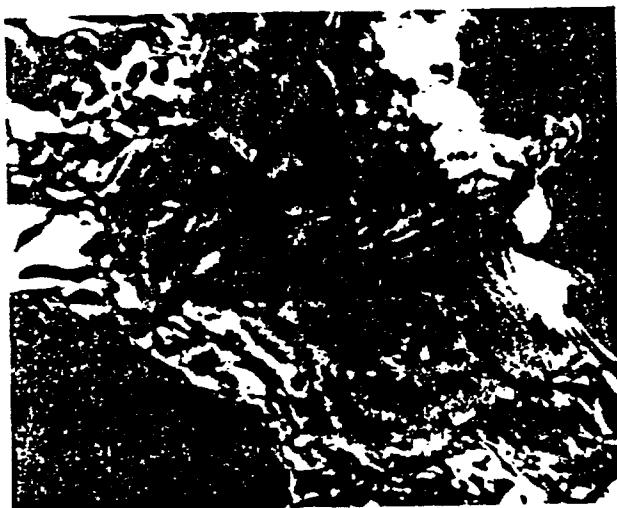


Fig.4: As Fig.3 but after straining to failure. Instead of the small patches of dislocation grids in Fig.3 note extensive similar grids covering a large part of the grain boundary. Such grids are believed to accommodate lattice misorientations due to straining.

4. INTERPRETATION

The indication of the stress-strain curves of Fig.2 in comparison to Fig.1 that the observed work-softening is due to the corresponding decline of τ_0 of eq.1 is confirmed by the micrographs, as these document that the dislocation density did not decrease but increased. Further, the similar appearance of the anchoring of the grain boundaries at dispersoids before and after straining eliminates the possible involvement of precipitate or dispersoid strengthening in the decline of τ_0 . The only remaining candidate for causing the worksoftening is therefore the Hall-Petch strengthening due to boundaries, and here we may additionally rule out the possibility of increasing grain size since the micrographic evidence does not indicate any significant grain size change and such could hardly be expected in any event.

Table I: Important data for the alloys of Fig.2. T_{ex} is the extrusion temperature. σ_y , σ_m and σ_F are the tensile stresses at yielding, maximum and failure, respectively and ϵ the ultimate tensile strain. The volume fractions of the dispersoids are based on the chemical analysis assuming that none of the alloying components were dissolved in the aluminum matrix. The grain sizes, d , are best estimates for the majority of the grains and the K_{HP} values are overestimates since they neglect all other hardening mechanisms..

| # | T_{ex} °C | σ_y MPa | σ_m MPa | σ_F MPa | ϵ % | Al_4C_3 v/o | Al_2O_3 v/o | Al_2Cu v/o | Y_2O_3 v/o | Total Grain Size v/o | d in μm | $K_{HP} = \sigma_{ext} \sqrt{d}$ |
|----|----------------|-------------------|-------------------|-------------------|-----------------|------------------|------------------|-----------------|-----------------|-------------------------|--------------|----------------------------------|
| A1 | 370 | 382 | 393 | 303 | 4.5 | 12.1 | 2.0 | 0 | 0 | 14.1 | 0.25-0.50 | 249-192 |
| A2 | 370 | 500 | 534 | 460 | 4.2 | 10.7 | 1.0 | 1.1 | 0 | 12.8 | 0.25-0.50 | 338-291 |
| A3 | 370 | 329 | 346 | 140 | 9.3 | 4.0 | 1.4 | 0 | 0.5 | 5.9 | 0.25-0.50 | 219- 89 |

Wilsdorf and Kuhlmann-Wilsdorf

Table I summarizes the most important characteristics of the alloys of Fig. 2, including the volume fractions of dispersoids and the starting and final values of the computed Hall-Petch constant, K_{HP} of $\sqrt{2}$ in units of $(\text{MN}/\text{m}^2)\mu\text{m}^{1/2}$, if all of the worksoftening is ascribed to grain decline and all other hardening mechanisms are neglected. This yields an overestimate of K_{HP} which will be modest for the high values of A1 and A2 but significant for A3, especially after deformation. The listed K_{HP} values, ranging from 338 to 89 $(\text{MN}/\text{m}^2)\mu\text{m}^{1/2}$ as seen in the table, compare to K_{HP} between 220 and 75 $(\text{MN}/\text{m}^2)\mu\text{m}^{1/2}$ determined for PM aluminum alloys by Kim and Griffith (1984), to K_{HP} decreasing from 191 to 159 $(\text{MN}/\text{m}^2)\mu\text{m}^{1/2}$ according to a worksoftening curve of severely rolled and then lightly annealed aluminum of $d = 0.83\mu\text{m}$ obtained by Westengen (1982) when again neglecting all other hardening mechanisms, and to $K_{HP} = 40 (\text{MN}/\text{m}^2)\mu\text{m}^{1/2}$ inferred for moderately rolled pure aluminum by Hansen and Juul Jensen (1991). Accordingly, the listed K_{HP} values compare to those of ordinary aluminum at their lower end but are extremely high at the upper end.

These results are compatible with the hypothesis that in the as-received state, the grain boundaries of our alloys, and probably similarly of the PM alloys of Kim and Griffith, contained an extra strengthening agent beyond mere crystallographic misorientation. The peculiar networks seen overlaying the boundaries after deformation are considered to give independent evidence of such extra strengthening. Namely, they are interpreted as LEDS networks accommodating the angular misorientation due to the several percent tensile strain while the initial boundaries remained unchanged because of some strong anchoring. In fact, the misorientations defined by these networks correspond to only a few degrees of angular misorientation and thus are entirely of the expected magnitude, whereas the correlated stress for supercritical bowing through these networks would be in excess of 1000 MPa. The small patches of networks such as circled in Fig. 3, by contrast, are apparently associated with precipitates, i.e. are epitaxial.

It is therefore proposed that the worksoftening arises as grain boundaries are gradually forced from a strong anchoring agent which is destroyed in the process while τ_0 decreases correspondingly. Searching for microscopic evidence of the anchoring agent, some faint traces were seen which are tentatively identified as films of no more than 1 nm width which may be carbon or Al_4C_3 , especially since micrographically there is much less of this dispersoid in the alloys than listed in Table I.

ACKNOWLEDGEMENTS

H.G.F. W. acknowledges support from the Air Force Wright Aeronautical Laboratory, Wright Patterson AFB, Ohio, for research on "Very High Temperature Aluminum Materials Concepts"; and D. K.-W. from the Materials Division (M. B. Peterson, Tribology) of the Office of Naval Research, Arlington, VA, as well as through the Defense Advanced Research Projects Agency (Kemmer, TTO Arlington, VA, monitored by T. Gora, Picatinny Arsenal). Dr. Jeffrey Hawk contributed to the mechanical measurements and micrography.

Hardening, Softening and LEDS in MA Alloys

REFERENCES

- Cottrell, A.H. and Stokes, R.J. (1955), Effects of Temperature on the plastic properties of aluminum single crystals. *Proc. Roy. Soc.*, **A233**, 17-34.
- Hansen, N. and Juul Jensen, D. (1991). Influence of texture and microstructure on flow stress. In: *Proc. 9th Intl. Conf. on Strength of Metals and Alloys*, edited by D. G. Brandon, R. Chaim and A. Rosen (Freund Publ. House, London) 953-960.
- Kim, Y.W. and Griffith, W.M. (1984). In: *PM Aerospace Materials*, Vol.1 (Shrewsbury U.K., MPR) as quoted by Frazier, W.E. and Koczak, M.J. (1988) in: *Symposium on Dispersion Strengthened Aluminum Alloys*, edited by Y.-W. Kim and W. Griffith (TMS, Warrendale, PA, 1988), p.577.
- Kuhlmann-Wilsdorf, D. (1968). Unified theory of stages II and III of workhardening in pure fcc metal crystals. In: *Workhardening*, edited by J.P. Hirth and J. Weertman (Gordon and Breach, N.Y.) 97-132.
- Kuhlmann-Wilsdorf, D. and Hansen, N. (1989). Theory of workhardening applied to stages III and IV., *Metall. Trans.*, **20A**, 2393-2397.
- Kuhlmann-Wilsdorf, D. (1989). Theory of plastic deformation. *Mater. Sci. and Engr. A111*, 1-41.
- Kuhlmann-Wilsdorf, D. and Wilsdorf, H.G.F. (1992). Theory of worksoftening in high-performance alloys. *Phys. Stat. Sol.* in the press.
- Westengen, H. (1982). Ardal-Sundal Verk, Sundalsøre, Norway.
- Wilsdorf, H.G.F., In: *Symposium on Dispersion Strengthened Aluminum Alloys*, edited by Y.-W. Kim and W. Griffith (TMS, Warrendale, PA, 1988), 3-29.

PRESSURE AND STRUCTURE DEPENDENCE OF SOLID LUBRICATION

M. S. Bednar, B. C. Cai* and D. Kuhlmann-Wilsdorf
Department of Materials Science and Engineering
University of Virginia, Charlottesville, VA 22901

ABSTRACT

The major parameters expected to influence the usefulness of non-layer type polycrystals for solid lubrication were investigated using ten pure metals. The high-pressure, large-shear-strain conditions at contact spots of sliding interfaces were simulated through shearing of sample disks between rotating Bridgman anvils, and the effective friction coefficients were determined as a function of pressure. The observations are consistent with the theoretical expectations that, under otherwise same circumstances, the apparent coefficient of friction is roughly proportional to the magnitude of the shear modulus, decreases with decreasing crystal symmetry and hence decreasing number of equivalent crystallographic slip systems, and decreases with increasing homologous temperature, T/T_0 . Additionally the evidence suggests that stacking fault energy and twinning properties play a not previously predicted but theoretically understandable significant role. Since not only the apparent coefficient of friction but also the retention of the lubricant at the interface decreases with pressure, solid lubricants must be selected in accordance with service temperature as well as the hardness of the lubricated materials. The results and theoretical interpretation presented in this paper can assist in such a selection.

*Now at Information Storage Research Centre, Jiao Tong University, Shanghai, P.R. of China

PRESSURE AND STRUCTURE DEPENDENCE OF SOLID LUBRICATION

M.S. Bednar, B.C. Cai* and D. Kuhlmann-Wilsdorf
Department of Materials Science and Engineering
University of Virginia, Charlottesville, VA 22901

THEORETICAL BACKGROUND

Introduction

Especially at high temperatures and in vacuum but also in a wide range of other applications, solid lubricants can be superior to greases or liquid lubricants in protecting sliding interfaces and reducing coefficients of friction. Besides the very widely used layer-type crystalline solids such as graphite and molybdenum disulfide there is a wide selection of other less widely known choices of solid lubricants, among them solid metals. The lubricating ability of lead is one example, and for some demanding applications a plating of gold or silver has served excellently (1-3). In fact, with little doubt solid lubricants will play an increasing role in future technological developments, such as for structural uses of ceramics at elevated temperatures.

In an earlier study (4) some theoretical connections were pointed out between basic materials properties and expected favorable performance of solid lubricants. Mainly, these depended on the need for almost unlimited shearability of the solid lubricant. For crystalline materials this, in turn, depends on dislocation behavior, crystallographic twinning and dynamical recrystallization, all of which are functions of crystal structure and melting temperature. At the time (4) the most serious gap in

*Now at Information Storage Research Centre, Jiao Tong University, Shanghai, P.R. of China

pertinent basic knowledge was the effect of the high local pressure at contact spots on "workhardening", classifying under this name all mechanisms whereby plastic deformation raises the flow stress for further plastic strain.

Workhardening at Ambient and High Pressures

Clearly the degree of workhardening is central since extensive shearing, amounting to tens of thousands of percent strain at contact spots (5), will have to be accommodated and this requires essential cessation of workhardening after some moderate strain. Further, for low coefficients of friction it is critical that the increase of flow stress from the undeformed to the severely sheared state, i.e. that total "workhardening", be as low as possible. Quotation marks are used here because the "workhardening" at issue includes the effect of pressure, and while workhardening at ambient pressures and to true shear strains of several hundred percent is by now quite well understood (e.g. 6-9), the dislocation and workhardening behavior at extreme strains and the effect of pressure thereon still require much more research.

Some of the requisite basic experiments have lately been performed through shearing disk-shaped samples under high pressure, and for the first time ever semi-quantitative shear-stress / shear-strain curves were obtained (10-13) in a Bridgman anvil type apparatus (14). The data accumulated so far are compatible with the earlier conclusion that most of the extra flow stress due to high pressures is enhancement of the Peierls-Nabarro stress (15).

the anvils (13). This paper, then, is devoted to measurements of the apparent coefficient of friction of ten different metals, namely Ag, Al, Au, Cu, Fe, In, Mg, Nb, Sn and Zn.

Fig. 1 shows stress versus rotation curves from which the data were extracted. It is seen that work hardening has almost ceased after less than one half anvil rotation. Therefore, the averaged flow stress between 1/4 and 3/4 anvil rotations was taken to be the saturation flow stress (τ_{SAT}). The effective friction coefficient was obtained by dividing by the applied pressure (14), i.e. $\mu_{EFF} = \tau_{SAT}/P$. As was discussed in detail previously (13), earlier measurements of μ_{EFF} by other authors, including Bridgman, must be discounted because either the samples slipped between the anvils or, unnoticed by the operators, the samples perforated and the anvils ground against each other instead of enforcing internal distributed shearing within the samples. In order to avoid this latter pitfall, the "saturation stress" was chosen to be such modest shear strains.

Crystallographic Texturing of Solid Lubricants

Earlier measurements showing that strong texturing appears to occur routinely in solid lubricants, to the effect that the "easiest" crystallographic glide plane becomes oriented parallel to the plane of shearing. This is well known for layer-type crystals in which the basal plane aligns parallel to the shearing plane, but was also observed for gold (16), silver, and copper in spite of their large number of equivalent glide planes. Because the fcc structure and the layer-type materials, represent the extremes of

the spectrum of crystallographic symmetry, it was inferred that such texturing is the general rule.

Texturing reverses the conventional "rule", that the ductility of polycrystals decreases and work hardening increases with decreasing crystal symmetry. The texturing transforms polycrystals into pseudo single crystals so that for decreasing symmetry, ductility increases and work hardening decreases. Layer-type crystals are a good example: for these the basal plane is strongly preferred, and is the only operating glide plane. Therefore, in the textured state almost no strain hardening occurs because work hardening requires dislocation interactions with three or more Burgers vector directions (6). Moreover, due to a lack of intersecting glide planes, layer-type crystals resist squeezing out from the interface.

Effect of Minor Impurities

Minor impurities in metals make a small additive contribution to the flow stress, typically in the order of 10 MPa or so, which is practically independent of strain (6,17) and also apparently independent of pressure (13). The flow stresses encountered in our tests, are tens to hundreds of times larger, and so the purity of the metals used in this study is not critical. The sample material was selected from nominally pure, (better than 99%) sheet stock with a view to low cost and convenience of procurement.

Proportionality of the Flow Stress with the Shear Modulus, G

Ever since Seeger's pioneering work on the theory of work hardening (17), it has been customary to independently consider two

contributions to the flow stress, generally named τ_c and τ_o . Work hardening raises the former, which is now understood to be that part which is due to dislocation interactions, while τ_o is due to all other causes and is typically little, if at all, dependent on strain (17). Further, τ_c is proportional to the shear modulus (G), as well as a function of a variety of other parameters. The other part, τ_o , includes grain boundary hardening, i.e. the Hall-Petch stress, as well as the Peierls-Nabarro stress, i.e. the frictional stress on dislocations due to periodic dislocation core energy variations as they move through the lattice (6). Both of these are also proportional to G , and in pure metals under high pressure the remaining contributions to τ_o tend to be negligible in comparison. Therefore, to a good first approximation the flow stress of pure metals, especially under pressure at high strains, is proportional to the shear modulus and is to a smaller extent a function of a host of other variables.

Twinning

A complicating factor is twinning. As already mentioned, the theory of work hardening by dislocation motions is fairly well understood. Twinning cannot be as easily predicted. It raises the flow stress by interfering with dislocation motion, and so the effect must depend on the size and number of the twins, but how this may depend on pressure, especially at high strains, is still largely unknown. More will be said about this topic below.

The Effect of Homologous Temperature

The work hardening coefficient, i.e. the slope of the shear

stress-shear strain curve, is proportional to the "dislocation retention factor", β , (6). Work hardening ceases when $\beta=0$, i.e. when none of the newly generated dislocations which accommodate the shear deformation become trapped. At ambient pressure, β decreases continuously with strain (7) from about unity in well-annealed, large-grained materials to less than 0.03 at the highest strains previously investigated in detail. With little doubt β becomes zero at or before the "saturation strain" at 1/4 to 1/2 anvil revolution is reached, as indicated by the flattening of the stress-strain curves (Fig. 1).

Simultaneously with β , the scale of the initial dislocation cell structure shrinks, and the cell walls become more distinct until the structure has been transformed into a sub-grain structure (18). The effect of pressure on this process is still unknown, although the apparently larger Peierls-Nabarro stress seems to slow these processes and delay dislocation cell and subgrain formation (15), as would be expected from theory.

Less problematical is the effect of temperature (in fact one may say with confidence, homologous temperature) since recovery and recrystallization temperatures are all roughly proportional to the melting temperature, T_m (19). Thus it is undisputable that for same strain and otherwise same circumstances β decreases with temperature. Correspondingly, total work hardening decreases with increasing homologous temperature, and in fact dynamical recrystallization sets in at $T/T_m > 1/2$ (19). This is the continual formation of new grains in tandem with the ongoing

deformation, to the effect that the average grain is maintained in a little deformed condition and the shapes of the grains do not reflect the preceding deformation. Moreover, depending on temperature and strain rate the grain size may be larger or smaller than in the initial undeformed state.

The Effect of Strain Rate

For testing between Bridgman anvils, as in Fig. 1, the slope of the stress versus rotation curves does not accurately correlate with the changes of β , even in the absence of dynamical recrystallization. This is because the sample thins and the strain rate increases at constant rotation rate, which leads to a mild increase of the flow stress (6), while perfection of the texturing decreases the shear stress (16). A decrease of the flow stress can therefore result from both dynamical recrystallization or perfection of texturing, while sample thinning increases strain rate, and thus stress.

EXPERIMENTAL PROCEDURE

Shearing was performed in an apparatus based on the Bridgman "opposed anvil" design (14), but modified to permit the determination of shear stress/shear strain curves (11-13). The disk-shaped samples of 3 mm diameter and 125 μm initial thickness were sheared between one 2.9 mm and one 5.4 mm diameter tungsten carbide anvil, compressed between hydraulic cylinders. The shear stress-shear strain curves were determined as previously described (13). From these measurements the effective coefficient of

friction was derived as the ratio of the "saturation" shear stress (τ_{SAT}) divided by the imposed pressure (p), i.e. $\mu_{EFF} = \tau_{SAT}/p$, as mentioned earlier

DEPENDENCE OF τ_{SAT} ON PRESSURE AND SHEAR MODULUS

Fig. 2 presents τ_{SAT} as a function of pressure for the face-centered cubic (fcc) metals copper, silver, gold, and aluminum, the body-centered cubic (bcc) metals, iron and niobium, the hexagonal closed packed (hcp) metals magnesium and zinc, the body-centered tetragonal (bct) indium, and the face-centered tetragonal (fct) tin (see Table 1).

The interpolation curves are best-fit curves assuming a linear rise of flow stress with pressure i.e.

$$\tau_{SAT} = {}_0\tau_{SAT} + \alpha p \quad (1)$$

with $\alpha = d\tau_{SAT}/dp$ (14). The values of ${}_0\tau_{SAT}$ and α are listed in Table 2 together with those previously determined by Bridgman (14) and Towle et. al (20-22). Discrepancies are due to sample perforation (14) and slippage (20-22) in the earlier work (13).

In agreement with Fig. 1, τ_{SAT} increases with pressure. Disregarding twinning for the moment, plastic deformation originates from dislocation movements, and following theory, the flow stresses and thus also τ_{SAT} are proportional to the shear modulus, G. Therefore the average pressure between the anvils, p, as well as the flow stress should logically be measured in units of G, meaning that in Fig. 2 both axis should be scaled in units of

the shear modulus as shown in Fig. 3, based on eq. 1, i.e.

$$\tau_{\text{SAT}}/G = {}_0\tau_{\text{SAT}}/G + \alpha p/G \quad (2)$$

The choice of the specific G values requires some thought due to elastic anisotropy. In view of the strain-induced texturing, the values of G in Tables and figures are taken parallel to the preferred glide plane in the preferred glide direction (closest packed direction) (23). Moreover, the pressure dependence of G was included as follows: In order to verify that the most densely packed crystallographic plane (23), is indeed parallel to the sliding interface, the intensities of x-rays in back-reflection normal to the sample were determined for the examples of gold and tin as a function of shear strain. The data obtained find that the texturing is parallel to the densest planes, namely (111) for gold (16) and (110) for tin. Correspondingly, the shear moduli for all ten metals were calculated parallel to the most densely packed crystallographic plane and direction.

In the correction of the shear modulus for pressure, the known pressure coefficients (24) were linearly extrapolated to span the test pressure range (Δp) listed in Table 1. The degree of this correction may be gauged from the change in shear modulus over the test pressure range listed in Table 1 as $\Delta G/G$.

The curves normalized according to shear modulus as in Fig. 3 show a smaller relative spread than the raw data in Fig. 2; in both Figs. 2 and 3 the curves tend to be grouped according to crystal structure, thereby somewhat vindicating the theoretical premises.

However, that other influences besides elastic constants are important since the curves in Fig. 3 clearly do not fall together, indeed not even among metals of same crystal structure. On account of the much greater practical interest of μ_{EFF} instead of τ_{SAT} , the discussion will concentrate on the influences of these on μ_{EFF} , i.e.

$$\mu_{\text{EFF}} = \tau_{\text{SAT}}/p + \alpha \quad (3)$$

DEPENDENCE OF μ_{eff} ON PRESSURE AND SHEAR MODULUS

Fig. 4 shows the data of Figs. 2 and 3 in terms of μ_{EFF} as a function of pressure. Note here the decrease of μ_{EFF} with increase in pressure, in accordance with eq. 3 as seen in Figs. 2 and 3 and previously recognized by Bridgman (14).

In Fig. 5 the pressure axis of Fig. 4 is normalized in terms of the shear modulus as a function of texture orientation and pressure using the values in Table 1. The usefulness of such normalisation is questionable and its theoretical justification needs further examination. While comparison between Figs. 4 and 5 shows that this normalization causes the μ_{EFF} curves for the fcc metals to move more closely together and the spread of the μ_{EFF} curves overall to mildly diminish, it also shows disordering among the metals of different crystallographic structures. Indeed, contemplating Figs. 4 and 5 with their evident general decrease of μ_{EFF} with decreasing crystal symmetry it becomes apparent that next to the dependence on shear modulus the greatest effect on the μ_{EFF} curves is from crystal structure. This will therefore be considered next.

DEPENDENCE OF μ_{eff} ON THE NUMBER OF CRYSTALLOGRAPHIC GLIDE SYSTEMS
The BCC Metals Iron and Niobium

According to the explanation given in the Introduction, the general decrease of μ_{eff} with decreasing crystal symmetry results from the decrease in the number of slip systems, and hence dislocation intersections: the higher the number of non-parallel crystallographic glide planes, the higher the work hardening, and therefore the larger is the high-strain flow stress and μ_{eff} .

In Fig. 4 the highest μ_{eff} are bcc metals which typically slip on all combinations of $\{110\}$ $1/2\langle 111 \rangle$, $\{112\}$ $1/2\langle 111 \rangle$ and $\{123\}$ $1/2\langle 111 \rangle$ as slip systems (25). Therefore, several of the most highly stressed slip systems are bound to be activated simultaneously. The resulting profuse dislocation intersections should cause the correspondingly strong work hardening.

Niobium has a still higher number of glide systems and thus has a higher μ_{eff} than iron. In niobium, $1/2\langle 111 \rangle$ also $\langle 100 \rangle$ acts as Burgers vector because $2C_{44}/C_{11}-C_{12}$ is substantially smaller than unity (26). As a result, even though the dislocation line energy is proportional to b^2 and favors $1/2\langle 111 \rangle$ over $\langle 100 \rangle$ in the ratio of 3 to 4, this is overcompensated by the strain energy reduction through elastic anisotropy.

Thus the probability of dislocation intersections is further increased in niobium (26). It is herewith suggested that this is the cause of the exceptionally high μ_{eff} values of niobium compared to all other metals tested.

The FCC Metals and Iron.

The fcc metals have fewer slip systems than bcc metals, namely the twelve equivalent $\{111\} \frac{1}{2}\langle 110 \rangle$ slip systems (23,25). Therefore the previous argument about interfering slip systems predicts a lower, but still high, μ_{EFF} value for the fcc metals, which is seen in Fig. 4. Placement of Fe among the fcc metals in Fig. 5 may be a sign that the normalization of p/G is inappropriate, or else the cause may be the proclivity of iron for pencil glide, as contrasted to planar glide. In the textured state after pencil glide, most likely only one Burgers vector will be activated, while probably two participate in fcc glide even in extreme planar glide texturing. A detailed study of the crystallographic texturing direction parallel to the sliding direction should be undertaken to decide this issue.

As seen in Table 1, the melting points of Cu, Ag and Au are similar and that of Al is much lower. Therefore on account of the already discussed decrease of the dislocation trapping factor β with rising homologous temperature, and thus of the work hardening coefficient and with it μ_{EFF} , the close grouping of the Cu, Ag and Au curves and the considerably lower level of the Al curve is explained.

The HCP Metals Magnesium and Zinc

Hexagonal-close packed metals ordinarily glide on the (0001) basal plane along the three equivalent closed-packed $\frac{1}{2}\langle 1120 \rangle$ slip directions (25). Only when basal slip is impeded on account of unfavorable orientation can slip be supplemented in magnesium by $\{1010\} \frac{1}{2}\langle 1120 \rangle$ glide (26) and in zinc by $\{1122\} \frac{1}{3}\langle 1123 \rangle$ glide

(27). Thus the hcp metals have fewer independent slip systems and much fewer easily activated intersecting glide planes than the fcc metals. This is in general accord with the lower μ_{EFF} curves of the hcp metals in Figs. 4 and 5 compared to fcc metals.

The Tetragonal Metals Indium and Tin

The two metals of lowest symmetry, indium and tin, have indeed the lowest μ_{EFF} values. Even so, the relative position of their μ_{EFF} curves does not agree with the number of their glide systems, as follows: Indium with its body centered tetragonal structure has a c:a ratio of $4.951:4.594 = 1.077$. Indium is therefore expected to glide with $1/2\langle 111 \rangle$ glide directions on $\{110\}$ planes for a total of twelve glide systems. Tin with a c:a ratio of $3.1815:5.83148 = 0.546$ and a fct structure will slip along one $1/2\langle 110 \rangle$ direction on each $\{111\}$ slip plane, for a total of only four $\{110\}\langle 110 \rangle$ slip systems. Based on the number of slip systems, indium should therefore have a higher μ_{EFF} curve than the HCP metals, contrary to observation. This, then, brings up yet the last facet of the introduction, namely dynamical recrystallization, to be discussed in the next section.

EFFECT OF DYNAMICAL RECRYSTALLIZATION ON μ_{EFF}

Dynamic recrystallization, expected in all metals at $T > T_M/2$ (19), leads to the drastic lowering of work hardening regardless of crystal symmetry. The relative positions of the μ_{EFF} curves in Figs. 4 and 5 must hence be exceptionally low for metals whose absolute melting temperature is less than twice room temperature, i.e. $T_M \leq 600^\circ\text{K} \approx 300^\circ\text{C}$. As seen in Table 1, among the metals tested only the

melting temperatures of indium and tin are low enough to place them into this category. Hence these two, and only these two metals, are expected to dynamically recrystallize. The driving force for the recrystallization derives from dislocation strain energy, which builds in the grains until in critically deformed grains new crystallites are nucleated and grow. By growing, these replace heavily deformed grains with a generation of new grains until these in turn are replaced.

The action of dynamical recrystallization is documented in Figs. 6 to 9 for the already pinpointed cases of tin and indium. Of these, Fig. 6 is a micrograph of as-received tin foil, showing twinned grains with irregular grain boundaries. By comparison, Fig. 7 is a micrograph of the same foil but after compression at 3000 Mpa for 15 seconds. Evidently, through the imposed compressional strain, recrystallization was triggered, causing smoothing out of grain boundaries and removal of twins.

Figs. 8 and 9 correspond to Figs. 6 and 7 but for indium. Fig. 9, compares to Fig. 7 in showing a changed grain structure derived from the as-received indium foil, Fig. 8, after hammering between steel plates. In both cases dynamical recrystallization led to grain size reduction. However the deformation was much less and was induced in a different manner for indium than for tin, and the resulting microstructure is different, too. At any rate the differences between initial and final microstructures, for both tin and indium, are explainable only through dynamic recrystallization. As dynamical recrystallization takes place at room temperature in

both indium and tin but not in any other of the metals studied, it causes their μ_{EFF} values to be the lowest among the ten metals.

DEPENDENCE OF μ_{EFF} ON STACKING FAULT ENERGY

While the especially low position of indium and tin curves in Figs. 2-5 is explained through dynamical recrystallization, and the offset of the Al curve from those of Cu, Ag and Au through its much lower homologous temperature, remaining differences in the relative μ_{EFF} values for the fcc metals may be explained through their stacking fault energies (SFE's). It may be observed that the μ_{EFF} curves for the fcc metals in Fig. 5 increase in the order of decreasing stacking fault energy, as seen from Table 3 which lists stacking fault energies (SFE) according to several sources. Specifically, Bolling et al. (29) calculated SFE's based on Seeger's theory of work hardening (17) that has since been abandoned. The other sources, Refs. 30-33, are based on experimental techniques with a precision which have increased with time.

A reason for a dependence of μ_{EFF} on SFE in fcc metals is this: $1/2\langle 100 \rangle \{111\}$ glide dislocations extend into ribbons bounded by two partial $1/6\langle 112 \rangle \{111\}$ dislocations with a stacking fault between them. The width of the stacking fault ribbon decreases with increasing SFE. Therefore the stresses required for dislocation intersections increase with decreasing SFE of the metal (17,29). Moreover, widely extended stacking faults between partial dislocations decrease cross-slip out of the glide plane, another factor which tends to harden the metal (6,17) and to increase μ_{EFF} .

THE DEPENDENCE OF μ_{EFF} ON TWINNING

The discussed apparent effect of SFE's on the FCC metals Al, Ag, Au, Cu in increasing order of μ_{EFF} values might be thought to apply also to the {0001} plane of hcp metals. In this connection note that the SFE of Zn is $1.4 \times 10^{-5} \text{ J-cm}^{-2}$ and Mg $1.25 \times 10^{-5} \text{ J-cm}^{-2}$. In fact, the differences in SFE although in the right sense regarding the relative position of the μ_{EFF} curves, is too small as if it could be the dominant factor.

Instead, the difference between the μ_{EFF} curves for these two hcp metals is almost certainly affected by their different twinning behavior which in turn is due to their different c/a ratios. Namely, c/a is 1.623 and 1.856 for magnesium and zinc, respectively, placing them on either side of the ideal c/a=1.632 ratio for the hcp crystal structure. As a result, magnesium twins in uniaxial compression, and zinc in uniaxial tension (23,34). Consequently, in our test conditions of strong compression as well as in tribological situations, twinning is expected in magnesium but not in zinc. The relative positions of the zinc and magnesium μ_{EFF} curves are explained thereby, since twinning is an additional source of work hardening (6,23), supplementing that due to differences in SFE.

CLOSING REMARKS

For otherwise identical conditions, the effective coefficient of friction of solid crystalline lubricants rises with increasing plastic flow stress of the lubricant. Based on simple theory, this

means that μ_{EFF} rises with increasing shear modulus (G) and, hence, melting temperature (T_M) of the lubricant, since G and T_M tend to rise and fall together.

A good solid lubricant requires the ability to accommodate very extensive shear deformations and as low a rise of flow stress through work hardening as possible. Work hardening ceasing at a modest flow stress level is therefore a prime requisite of successful crystalline lubricants.

Among others, the usefulness of otherwise pure metals as solid lubricants depends strongly on their crystal structure, in favor of low symmetry. The reason is texturing of the lubricant through shearing, with the most active crystallographic glide plane orienting parallel to the sliding interface and thereby generating a pseudo single crystal in optimal shear orientation. The shear strength of such crystals is known to decrease with decreasing symmetry.

The above dependence is caused by work hardening, which is principally due to dislocation interactions on intersecting crystallographic glide planes. Therefore decreasing numbers of activated non-parallel slip planes, which in turn means decreasing crystal symmetry, leads to lowered shear strength and thus lower μ_{EFF} values.

Another contribution to the flow stress and thus increased μ_{EFF} , is twinning. Therefore hcp metals with c/a ratios larger than the ideal c/a=1.632, which are not likely to twin in compression (23,34), are favored.

The flow stress is also limited by through dynamical recrystallization which continuously replaces workhardened and/or twinned grains with pristine material. This effect favors solid lubricants whose absolute melting temperature is less than twice the operating temperature, since dynamic recrystallization occurs at temperatures $T \geq T_m/2$. It is for this reason that tin and indium are superior solid lubricants at room temperature.

Relatively high homologous temperatures lower μ_{EFF} values and thus are beneficial in solid lubrication also below $T_m/2$, i.e. without dynamical recrystallization. This is because the dislocation retention coefficient, β , and thereby work hardening, decreases with increasing temperature.

A more subtle effect occurs through stacking fault energy (SFE) in the fcc metals, for the reason that dislocation intersections become increasingly difficult, and thus lead to increased flow stress and hence μ_{EFF} , as the SFE decreases. Fcc metals with high SFE are therefore favored above those with low SFE.

Experimental data on the metals aluminum, copper, gold, indium, iron, magnesium, niobium, silver, tin and zinc obtained with a Bridgman opposed anvil apparatus are consistent with the above principles. The various indicated effects could have, but not all of them actually were, predicted theoretically. Additional materials should be tested to further verify the present findings and to investigate still other expected effects on μ_{EFF} . Foremost among these is the anticipated deleterious effect of pressure-induced phase transformations. Another important effect will be

high reactivity, leading to beneficial or harmful surface film formation as the case may be.

ACKNOWLEDGMENTS

The financial support of this research through the Materials Division (P.P. Schmidt and M. B. Peterson, Tribology) of the Office of Naval Research, Arlington, VA, is gratefully acknowledged.

REFERENCES

- (1) Jahanmir, S.I., Abrahamson II, E.P., Suh, N.P., "Sliding Wear Resistance of Metallic Coated Surfaces", Wear, 40, pp. 75-84, (1976).
- (2) Erdemir, A., Busch, D.E., Erck, R. A., Fenske, G.R. and Lee, R., "Ion-Beam-Assisted Deposition of Silver on Zirconia Ceramics for Improved Tribological Behavior", Lubr. Eng., 47, (1991).
- (3) Erdemir, A., Fenske, G.R., Erck, R.A. and Cheng, C.C., "Ion-Assisted Deposition of Silver Films on Ceramics for Friction and Wear Control", Lubr. Eng., 46 pp. 23-30, (1990).
- (4) Kuhlmann-Wilsdorf, D., "Fundamentals of High Temperature Friction and Wear with Emphasis on Solid Lubrication for Heat Engines", Proceedings of Workshop, Eng. Sciences Div., Ed. Ling, F.F., pp. 65-80, (1985).
- (5) Kuhlmann-Wilsdorf, D., "Dislocation Concepts in Friction and Wear", Fundamentals of Friction and Wear of Materials, ASM Materials Science Seminar, Ed. D.A. Rigney, Am. Soc. for Metals, Metals Park, OH, pp. 119-186, (1980).
- (6) Kuhlmann-Wilsdorf, D., "Theory of Plastic Deformation", Mater. Sci. Eng., A113, pp. 1-41, (1989).
- (7) Kuhlmann-Wilsdorf, D., and Hansen N., "Theory of Work hardening Applied to Stages III and IV", Metall. Trans., 20A pp. 2393-2397, (1989).
- (8) Kuhlmann-Wilsdorf, D., "Correlation Between Dislocation Microstructure and Static/Dynamic Strength of Metals", Modeling the Deformation of Crystalline Solids, Eds. T.C. Lowe, T. Rollett, R.S. Follansbee and G.S. Daehn, TMS, Warrendale, PA, pp. 105-124, (1991).
- (9) Bay B., Hansen N., Hughes, A. and Kuhlmann-Wilsdorf, D., "Evolution of FCC Deformation Structures in Polyslip", Acta Met. et Mater., 40, pp. 205-219 (1992).
- (10) Cai, B.C., Kuhlmann-Wilsdorf, D. and Nelson, R.B., "Simulating Contact Spot Behavior of an AlSiC Fiber Composite in a High-Pressure Apparatus", Tribology of Composite Materials, eds. Rohatgi P., Balu J., and Yust C.S., ASM Intl., Materials Park, OH, pp. 81-91, (1990).
- (11) Cai, B.C., and Kuhlmann-Wilsdorf, D., "A Study of Shear Deformation and Work hardening of Metals Under Pressures to 2100 MPa", Mater. Sci. Eng., A138, pp. 33-47, (1991).

- (12) Cai, B.C., Kuhlmann-Wilsdorf, D. and Nelson, R.B., "Simulation of Solid Lubricants and Contact Spots Between Bridgman Anvils -Part I: A New High-Pressure Apparatus; Part II: Experimental Results on FCC Metals and New Insights Gained", Wear of Materials-1991 eds. Ludema, C., and Bayer, R.G., Am. Soc. Mech. Eng., N.Y., N.Y., pp. 457-473, (1991).
- (13) Kuhlmann-Wilsdorf, D., Cai, B.C. and Nelson, R.B., "Plastic Flow Between Bridgman Anvils Under High Pressures", J. of Mat. Res., 6, pp. 2547-2564, (1991).
- (14) Bridgman, P.W., "Effects of High Shearing Stress Combined with High Hydrostatic Pressure", Phys. Review, 48, pp. 825-847, (1935).
- (15) Jesser, W.A., Kuhlmann-Wilsdorf, D., "The Flow Stress and Dislocation Structure of Nickel Deformed at Very High Pressure", Mater. Sci. and Eng., 9, pp. 111-117, (1972).
- (16) Cai, B.C., Kuhlmann-Wilsdorf, D., and Nelson, R.B., "Studying the Mechanical Properties of Thin Films Under High Pressure" MRS Symp. Proc., (Eds. Koerner M.F., Oliver W.C., Pharr G.M. and Brotzen F.R.), Mater. Res. Soc., Pittsburgh, PA, 188, pp. 183-188, (1991).
- (17) Seeger, A., Handbuch der Physik, Ed. Flügge, S., Springer, Berlin, Vol. VII/2, (1958).
- (18) Kuhlmann-Wilsdorf, D. and Hansen, N., "Geometrically Necessary, Incidental and Subgrain Boundaries", Scripta Met. et Mater., 25, pp. 1557-1562, (1991).
- (19) Courtney, T.H., Mechanical Behavior of Materials, McGraw-Hill, N.Y., (1990).
- (20) Riecker, R. E., and Towle, L. C., "Shear Strength of Grossly Deformed Cu, Ag, and Au at High Pressures and Temperatures", J. Appl. Phy., 38, No. 13, pp. 5189-5194 (1967).
- (21) Riecker, R. E., Towle, L. C., Rooney, T. P., "Shear Strength of Twelve Grossly Deformed Metals at High Pressures and Temperatures", Environmental Research Papers, No. 273, Air Force Cambridge Research Laboratories, pp. 1-22, (1967).
- (22) Towle, L. C., and Riecker, R. E., "Shear Strength of Grossly Deformed Solids", Science, 163, pp. 41-47, (1969).
- (23) Schmid, E., and Boas, W., Plasticity of Crystals, Hughes, London, (1950), Translation of Kristallplastizität, Springer, Berlin (1936).
- (24) Landolt-Börnstein, Numerical Data and Functional Relationships in Science and Technology-Supplement to Vol. III/11, Eds. K.-H.

Hellwege, and A.M. Hellwege, Springer-Verlag, Berlin, Vol. 18, pp. 50-100, (1984).

(25) Tegart, W.J.M., Elements of Mechanical Metallurgy, Eds. Fine, M.E., Weertman, J., Weertman, J.R., The Macmillan Company, N.Y. pp. 100-102, (1966).

(26) Reid, C.N., Gilbert, A. and Hahn, G.T., "Twinning, Slip and Catastrophic Flow in Niobium", Acta. Met., pp. 975-983, (1966).

(27) Reed-Hill, R.E., and Robertson, W.D., "Deformation of Mg Single Crystals by Non-Basal Slip", Trans. AIME, 209, p.496, (1957).

(28) Bell, R.L., and Cahn, R.W., "The Dynamics of Twinning and the Interrelation of Slip and Twinning in Zinc Crystals", Proc. Roy. Soc., A239, pp. 494-521, (1957).

(29) Bolling, G. F., Hays, L.E. and Wiedersich H.W., "The Plasticity of Lead Single Crystals and the Determination of Stacking Fault Energy", Acta Met., 10, pp. 185-194, (1962).

(30) Murr, L.E., Interfacial Phenomena in Metals and Alloys, Addison-Wesley, Reading MA, pp. 146-147, (1975).

(31) Thornton, R. R., and Hirsch, P.B., "The Effect of Stacking Fault Energy on Low Temperature Creep in Pure Metals", Phil. Mag., 3, pp. 738-761, (1958).

(32) Dillamore, I.L., and Smallman, R.E., "The Stacking Fault Energy of F.C.C. metals", Phil Mag., 12, pp. 191-193, (1965).

(33) Hirth, J.P., and Lothe, J., Theory of Dislocations, McGraw-Hill Book Company, N.Y., p. 764, (1968)

(34) Hertzberg R.W., Deformation and Fracture Mechanics of Engineering Materials, John Wiley and Sons, N.Y., p. 69, (1989).

Table 1

| Metal | Tm(°C) | Struct. | μ_{EFF} | Plane | dG/dp | ΔP [MPa] | G [MPa] | G [MPa] Directional at p=0 | $\Delta G/G(\%)$ |
|-------|--------|---------|-------------|--------|-------|------------------|---------|----------------------------------|------------------|
| Nb | 2468 | BCC | 0.268 | (110) | 0.167 | 2000 | 37300 | 29200 | 0.9 |
| Fe | 1536 | BCC | 0.246 | (110) | 1.176 | 3000 | 84000 | 106500 | 4.2 |
| Cu | 1083 | FCC | 0.160 | (111) | 0.675 | 3000 | 46000 | 49000 | 4.4 |
| Ag | 960 | FCC | 0.144 | (111) | 0.877 | 3000 | 28000 | 30000 | 9.4 |
| Au | 1063 | FCC | 0.123 | (111) | 0.513 | 3000 | 27000 | 28700 | 5.7 |
| Zn | 420 | HCP | 0.087 | (0001) | 1.840 | 1500 | 40000 | 46000 | 6.9 |
| Al | 660 | FCC | 0.082 | (111) | 1.300 | 900 | 26000 | 27100 | 4.5 |
| Mg | 650 | HCP | 0.076 | (0001) | 1.756 | 1500 | 17000 | 17000 | 15.5 |
| Sn | 232 | FCT | 0.024 | (110) | - | 975 | 20000 | - | - |
| In | 156 | BCT | 0.011 | (110) | - | 675 | 4000 | - | - |

Table 1: Data on metals tested, listed in decreasing order of their μ_{EFF} curves in Fig. 3. Note that the listed values of μ_{EFF} at 1 MPa follow this same order and that the crystal symmetry decreases also towards the bottom of the list. Also listed are (i) the favored crystallographic glide plane (one of) which orient parallel to the interface after extensive shearing, (ii) the pressure coefficient of the shear modulus (dG/dp) at room temperature, (iii) the range of pressure used (Δp), (iv) the average shear modulus (G) on the preferred glide plane shear modulus at atmospheric pressure, and (vi) the percentage increase of G in the experimental pressure range. ($\Delta G/G$).

Table 2

| Metal | α | σT_{SAT} [MPa] | α/G [MPa ⁻¹] ($\times 10^{-6}$) | $\sigma T_{SAT}/G$ ($\times 10^{-3}$) | α_B | $\sigma T_{SAT} B$ | α_T | $\sigma T_{SAT} T$ |
|-------|----------|------------------------|---|--|------------|--------------------|------------|--------------------|
| Nb | 0.072 | 233.29 | 1.93 | 15.7 | - | - | - | - |
| Fe | 0.075 | 173.82 | 0.89 | 3.8 | 0.295 | -130.0 | - | - |
| Cu | 0.049 | 107.61 | 1.07 | 4.9 | 0.101 | 29.0 | 0.018 | 320.0 |
| Ag | 0.036 | 109.04 | 1.29 | 8.0 | 0.092 | 20.0 | 0.017 | 230.0 |
| Au | 0.029 | 91.82 | 1.07 | 7.6 | 0.099 | -19.0 | 0.020 | 130.0 |
| Zn | 0.032 | 52.64 | 0.80 | 1.1 | 0.027 | 45.1 | - | - |
| Al | 0.035 | 47.56 | 1.35 | 3.6 | 0.052 | 52.0 | 0.025 | 40.0 |
| Mg | 0.022 | 53.36 | 1.29 | 3.0 | 0.069 | 533.0 | 0.012 | 130.0 |
| Sn | 0.012 | 12.30 | 0.60 | 0.6 | 0.013 | 17.0 | 0.013 | 10.0 |
| In | 0.006 | 5.65 | 1.50 | 1.4 | 0.015 | -4.9 | - | - |

Table 2: The flow strength parameters α and σT_{SAT} of eq. 1 according to the interpolation curves in Figs. 2 and 3. Also listed are the corresponding values determined by Bridgman (subscript B, ref. 10) and Towle et al at high pressure (subscript T refs. 20-22). The data in the two right most columns was derived from but not published by Towle et al.

Table 3

| Metal | Stacking Fault Energy ($\times 10^{-7}$ J-cm ⁻²) | | | | |
|-------|---|-------|-----|---------|-----|
| | (acc. to refs: 29 | 30 | 31 | 32 | 33) |
| Ag | 20 | 26-58 | 22 | 14- 28 | 17 |
| Au | 10 | 24-47 | 45 | 37- 67 | 55 |
| Cu | 163 | 40 | 78 | 55-115 | 73 |
| Al | 238 | 200 | 166 | 230-330 | 200 |

Stacking fault energies (SFE) for the fcc metals Cu, Ag, Au and Al according to refs. 29-33 as indicated.

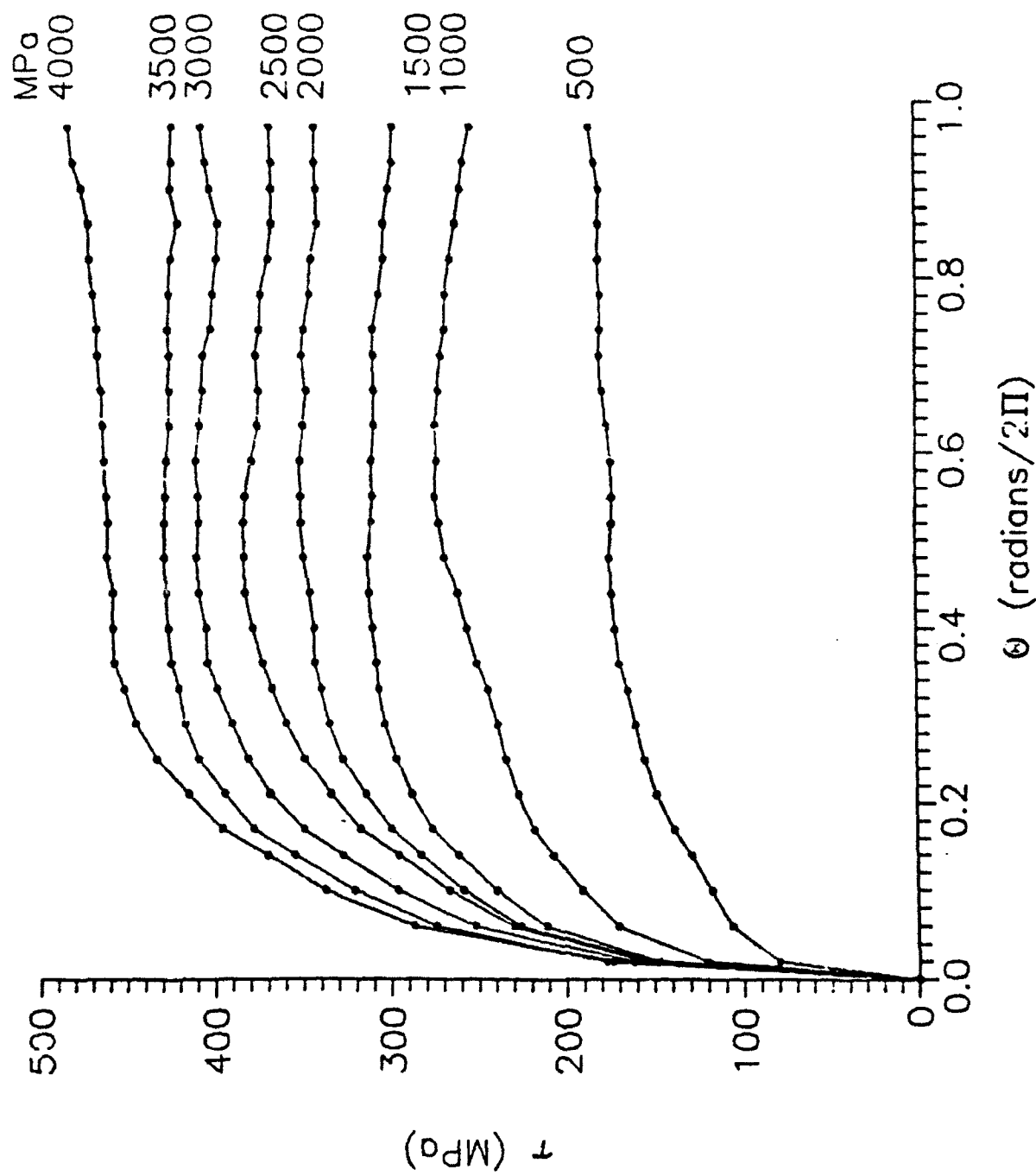


Fig. 1— Shear Stress, τ , as a function of shearing angle for Fe. Note the saturation of τ between $1/4$ and $2/5$ of one rotation.

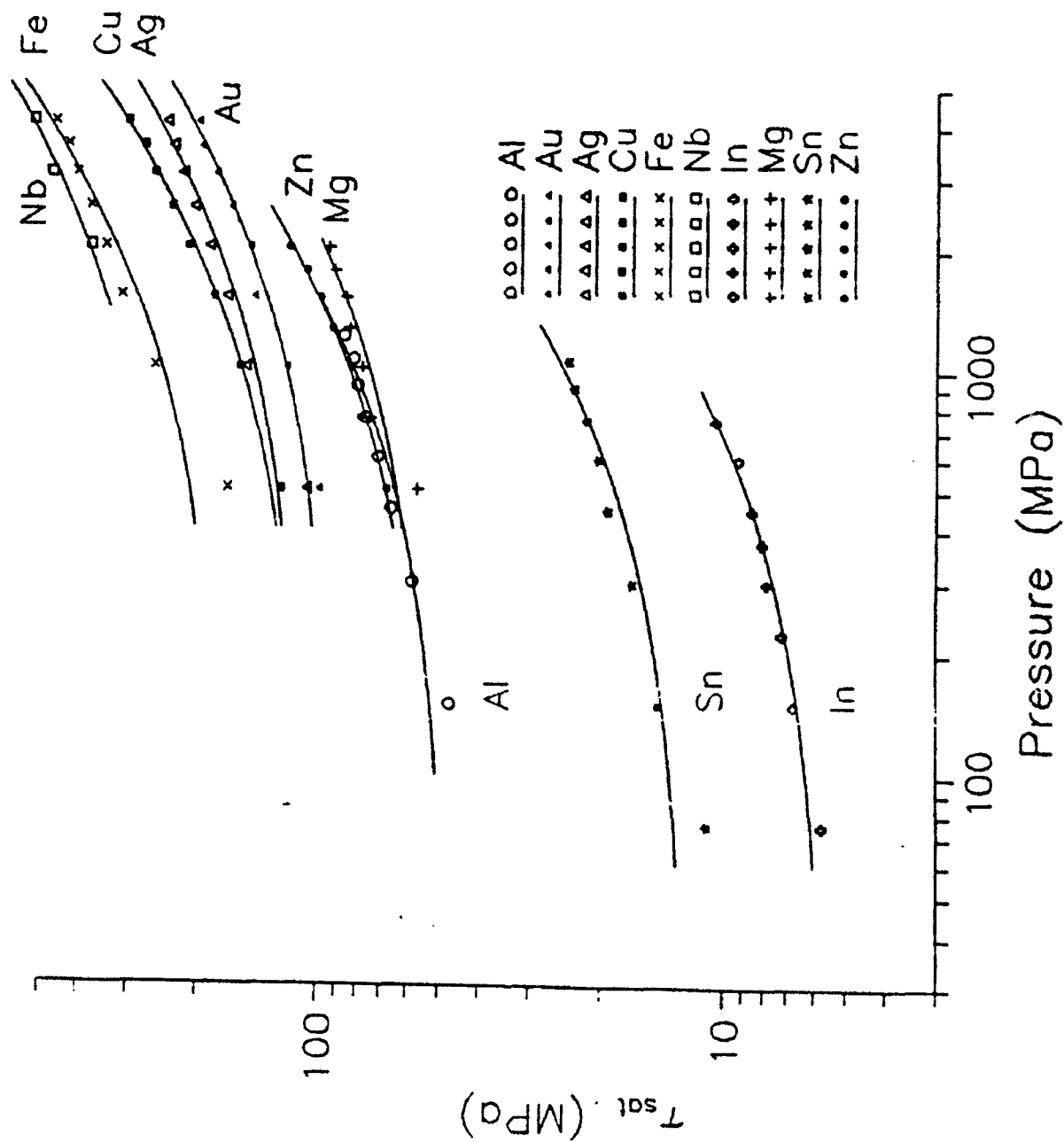


Fig. 2- Saturation shear stress of ten metals as a function of pressure. The interpolation curves are of the type

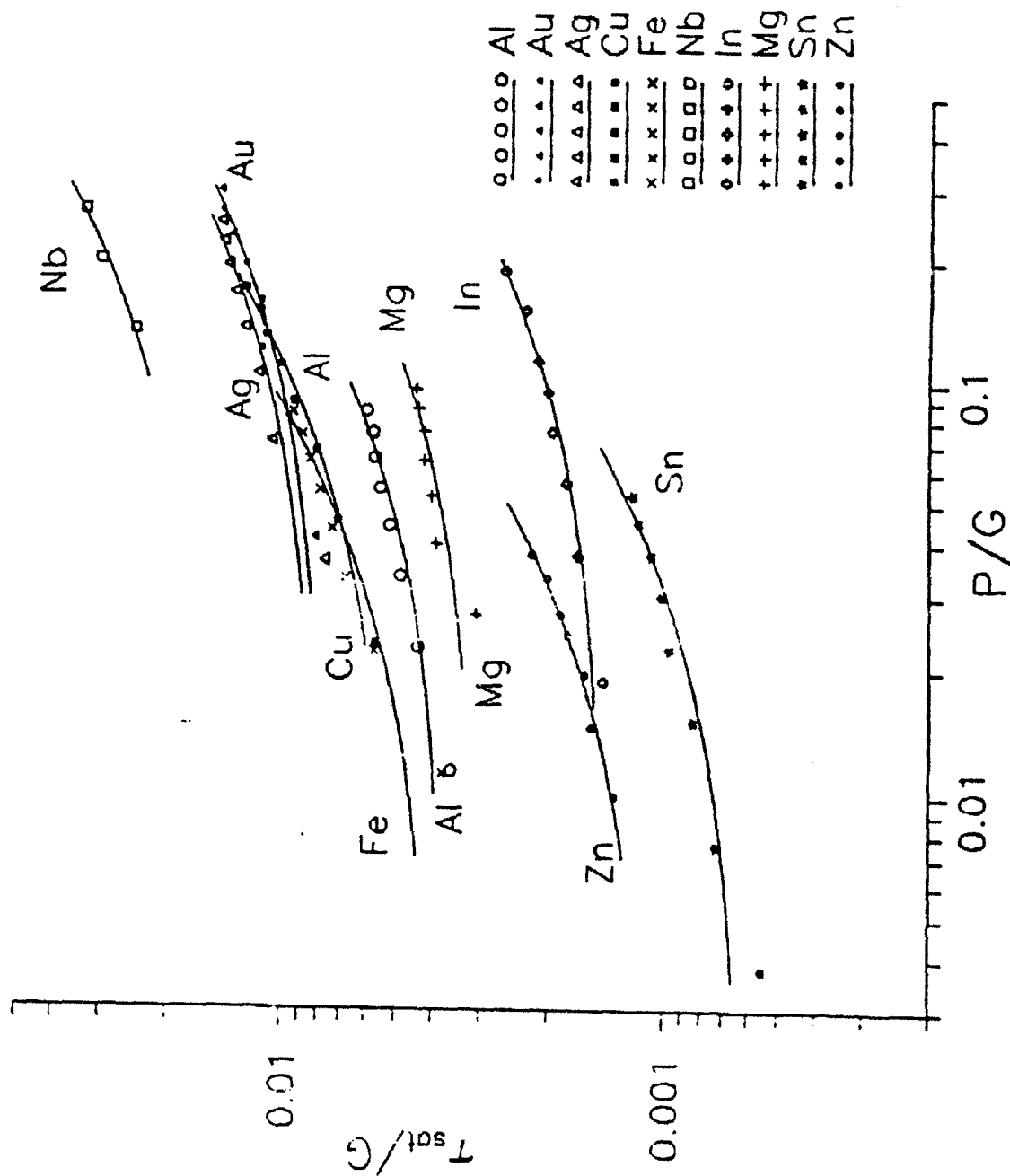


Fig. 3 - As Fig. 2 but in units of shear modulus (G) including its pressure and shear direction dependence.

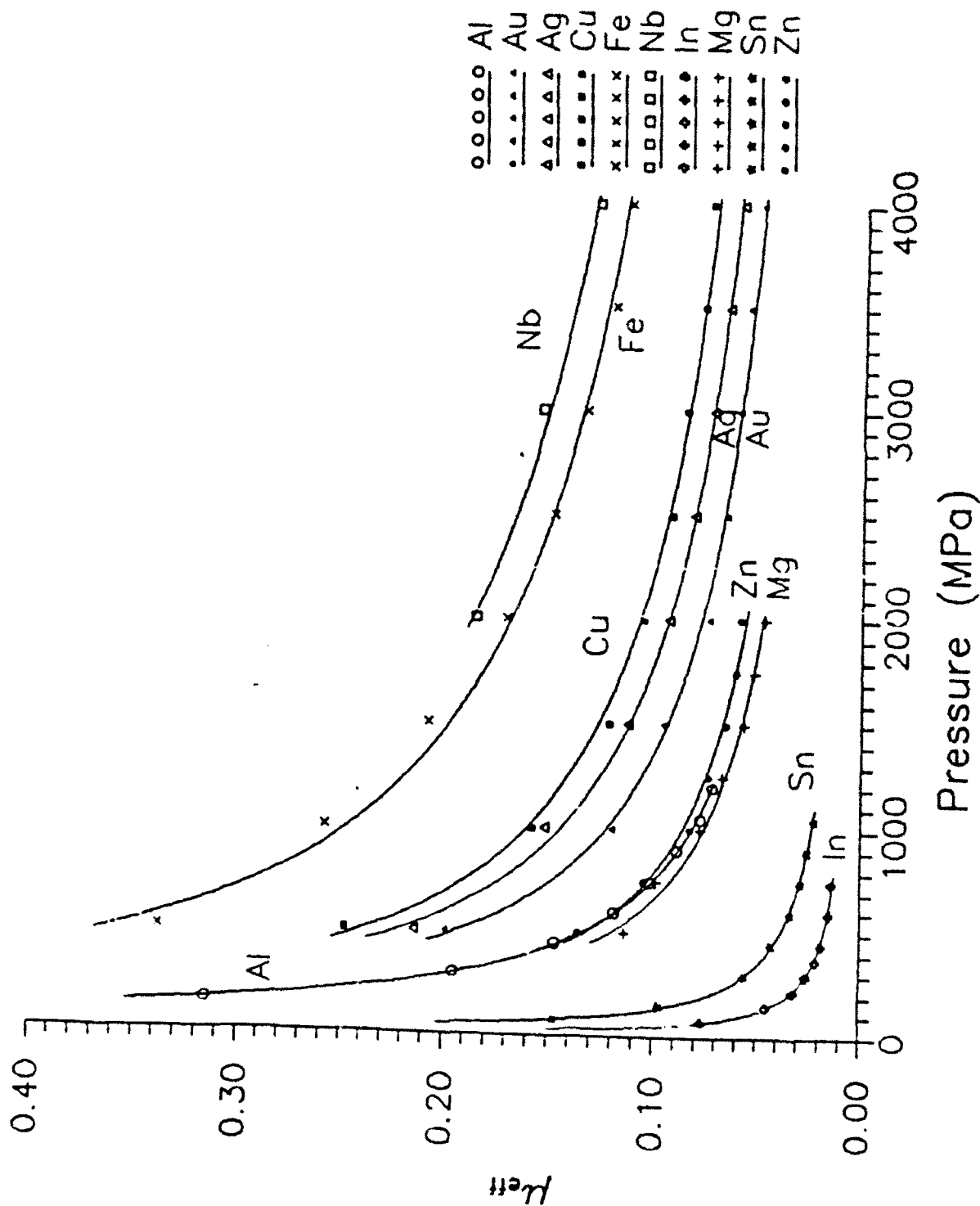


Fig. 4 - The dependence of the effective coefficient of friction on pressure for a variety of metals. Power series curve fitting was applied to the

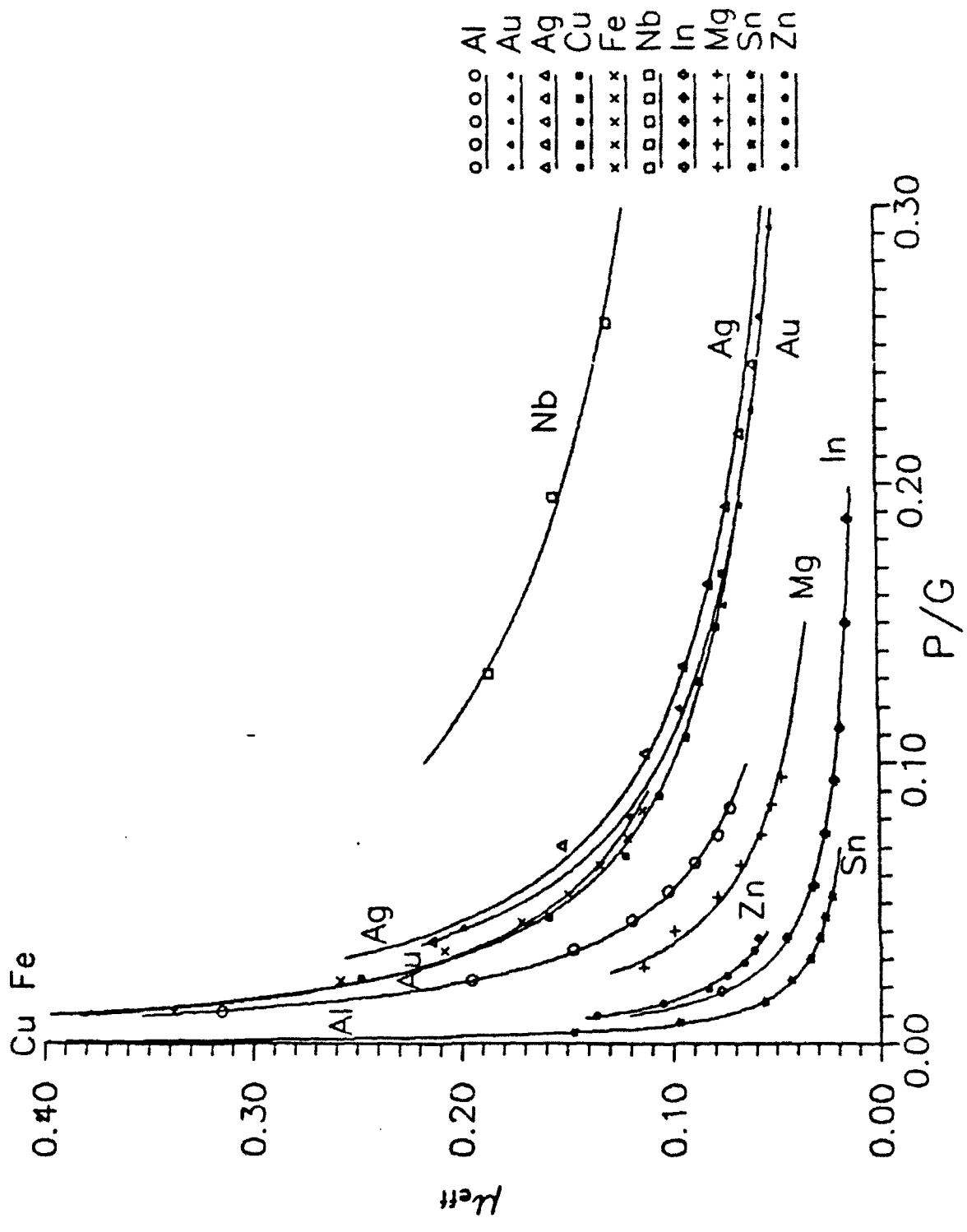


Fig. 5 - The same μ_{eff} values as in Fig. 4 but as a function of p/G with G the average shear modulus as a function of pressure and shear direction.



Fig. 6. As-received 99.9% pure tin, polished and etched.



Fig. 7. Tin sample after compression at 3000 MPa for 15 seconds.



Fig. 8. As-received In foil with 99.9% purity polished



Fig. 9. The same indium foil of Fig. 8 and etched after deformation through hammering between steel plates.

Micromechanics of MoS₂ lubrication

Chao Gao, Louis Bredell, Doris Kuhlmann-Wilsdorf and David D. Makel

Department of Materials Science, University of Virginia, Charlottesville, VA 22901 (USA)

Abstract

The micromechanical behavior of MoS₂ acting as a solid lubricant and the effects of humidity thereon have been studied in moist nitrogen through simultaneous measurements of momentary friction and electrical contact resistance in the so-called hoop apparatus. The sliding couple consisted of a gold-plated copper substrate (the circumferential track inside the hoop) lubricated with a burnished MoS₂ film, and a slider in the form of three bundles of 50 μm thick gold-plated copper fibers. This geometry permits indirect detailed studies of the film conditions at the contact spots, since both the friction and the contact resistance are exclusively determined by the film. All measurements were found to be reversible, with the friction coefficient and contact resistance depending in a somewhat complex manner on average sliding speed between 0.05 and 3.0 cm s^{-1} , load between 0.5 N and 8 N, and relative humidity between 20% and 90%. The data indicate that adsorbed moisture causes the MoS₂ film to mechanically soften, and that the film is partly pushed ahead and to the sides of moving contact spots. As a result, the film thickness between the contact spots, presumably with the basal plane preferentially parallel to the interface, decreases with humidity but increases slightly with sliding speed and contact spot size, i.e. load. Accordingly, the major part of the coefficient of friction, namely $\mu_0 \approx 0.1$ through distributed shearing of the MoS₂ film parallel to the basal plane, is little affected by any of the variables, but the contribution due to film plowing rises with increasing humidity from zero up to $\mu_p \approx 0.1$. The contact resistance, by contrast, varies through almost two orders of magnitude. It increases much faster than proportional with the film thickness at the a-spots, due to a strong increase of the MoS₂ resistivity with film thickness, on account of a semiconductor effect.

1. Introduction

Molybdenum disulfide (MoS₂), a hexagonal layered n-type semiconductor material, is extensively used as a solid lubricant in aeronautical and space applications because of its low coefficient of friction ($0.01 < \mu < 0.1$) and high environmental stability in dry and vacuum conditions [1-9]. However, it is well known that the friction and wear properties of both burnished and sputtered MoS₂ can degrade rapidly when exposed to high humidity [3, 4, 10-14]. In spite of its technological importance, the small-scale "micromechanical" behavior of MoS₂ when acting as a solid lubricant is still largely unknown, and the effect of humidity is even less well understood. It is widely accepted that during sliding MoS₂, along with all layer-type crystalline solid lubricants, becomes textured such that the close-packed planes are preferentially oriented parallel to the interface. Similarly accepted is that the relative motion between the tribo surfaces is preferentially accommodated by sliding on the basal plane [7-9]. Many of the details of MoS₂ action, however, are unclear. Of specific interest is whether the MoS₂ film is squeezed

out from between the two sides of contact spots, in the extreme limit down to a bi-molecular layer, similar to the recently unraveled behavior of adsorbed moisture and other liquid lubricants [15-22]. If squeezing out does occur, it is a result of extensive plastic deformation by distributed shearing within the film. If extensive squeezing leaves only a bi-molecular layer, sliding would most likely occur between those two layers, as appears to be the case with liquids. However, if only minimal film thinning occurs between the contact spots, sliding might take place only between the MoS₂ planes immediately adsorbed at the lubricated material and the otherwise substantially rigid MoS₂ film [1-3].

Questions regarding the action of MoS₂ lubrication raise the possibility of similarities between MoS₂ and graphite, a solid layer-type lubricant whose lubrication mechanism has long been empirically known and is now more fully understood [23, 24]. With graphite, moisture is required for lubrication because it strongly adsorbs onto exposed basal planes, reducing the critical shear stress of the graphite parallel to the basal plane below the shear strength of the lubricated metal and causing lubrication. Additionally the adsorbed moisture binds graphite basal planes to the metal, and thereby

acts to retain the lubricant, as well as incidentally causing "wedge" formation.

In fact, a close similarity between graphite and MoS₂ in this respect is unlikely since increases in moisture level above that required for lubrication have little effect on graphite, while it is clear from the somewhat disjointed literature that water is detrimental to MoS₂ lubrication films. Macroscopically, when exposed to high humidity during sliding, burnished MoS₂ films deteriorate in either of two modes. They soften to a dull gray MoS₂ putty which is wiped or scraped off, or the films scale off after blisters have formed at the substrate-film interface [13]. Either form of attack can be decreased by mixing water-repellent additives with the MoS₂ [14].

Using an X-ray fluorescence technique, Johnston and Moore [11] observed that the density of burnished MoS₂ increases with increasing humidity, and also that the fraction of basal planes oriented parallel to the interface increases with humidity. They concluded that dry burnished MoS₂ films are highly porous and misaligned, and the effect of moisture is to form strongly adsorbed moisture films on the exposed basal planes, causing the planes to align by capillary forces. In that it includes adhesion by adsorbed moisture, this proposed mechanism resembles that of water on graphite.

A related though different conclusion was reached by Holinski and Gansheimer [7] that, especially during run-in, adsorbed water bonds simultaneously to two polarized s-atoms, thereby increasing the coefficient of friction across the basal planes. Roberts [3] attributed the increase of friction with humidity to the absorption of water molecules at two different types of site: edge sites, and intercalation sites from which the water molecules could penetrate between the MoS₂ layers. Finally, it has been suggested by Panitz *et al.* [12] that the water and oxygen chemically react with MoS₂



and that the resulting MoO₃ particles precipitate in, and increase the friction of, the MoS₂ layers.

2. Experiments with the hoop apparatus

2.1. Motivation and the hoop apparatus

Experiments with the previously described hoop apparatus [15–17, 25, 26] can be most helpful in shedding light on details of behavior at the contact spots in a wide range of tribo systems. In this apparatus, a sample slides inside a rotating metal hoop contained in a controllable atmosphere, and the momentary friction and electrical contact resistance are simultaneously monitored and stored for subsequent evaluation and analysis.

The value of this technique derives from the fact that in dry or solid lubricated sliding, both friction and electrical contact resistance are totally controlled by the process occurring at the contact spots. Especially helpful in this regard is the use of samples in the form of bundles of fine metal fibers run end-on. By increasing the number of contact spots this configuration eliminates the constriction resistance and complications due to statistical changes of the number and shape of contact spots. As a result, the contact resistance is directly proportional to the resistivity of the interfacial film, whether of a solid lubricant as in the present case, or of other intentional or incidental surface films without which the two sides would cold-weld.

Thus the hoop apparatus is particularly well suited to gathering detailed information at slow sliding speeds, and it was decided to investigate short-term MoS₂ film behavior as a function of load, average speed and, most importantly, humidity. The tests were, therefore, conducted on burnished MoS₂ films applied to the gold-plated track in a copper hoop, with a gold-plated copper fiber slider, in a humidified nitrogen atmosphere. Gold plating of the copper surfaces was used to help eliminate problems of chemical attack.

2.2. Variables: sliding velocity, contact spot size, local pressure and humidity

In a manner by now well established [15–17], a systematic study of the effect of applied normal force on friction and contact resistance was used to examine the influence of contact spot size, while the dependence on average speed was used to examine effects of viscosity. The measurements were made at different relative humidities to assess the role of moisture.

Additionally, by lowering the normal force to the point that the contact spots deformed elastically rather than plastically [27, 28] the effects of variations of the local pressure were also studied. By way of explanation: at higher loads (P), the softest material at the contact spots is compressed plastically and the local normal pressure (p) at the contact spots approximately equals H_s , the impression (Meyer) hardness of the softest of the materials involved. However, at quite low loads the contact spots become elastic as p falls below H_s , and at lower loads p decreases with decreasing P . In the present system, provided that the film is significantly textured with the basal plane parallel to the interface, H_s is that of the gold plating, since MoS₂ is much stronger in compression normal to the basal plane than either gold or copper. A computer program developed in this laboratory was used to calculate the average size and pressure of both elastic and plastic contact spots given knowledge of H_s , the coefficient of friction, the relevant elastic constants, the normal force and the number of contact spots [29, 30].

Incidentally, mechanical anisotropy is the great virtue of layer-type solid lubricants; they are highly resistant to squeezing out from between the tribo surfaces owing to their great strength normal to the basal plane, but they are easily sheared parallel to the basal planes. This behavior may be compared to that of a pack of playing cards on which one may easily slip without crushing the individual cards.

2.3. Experimental procedure

In the hoop apparatus the same kind of metal hoop, metal fiber sample and other instrumental set-up were used as in previous investigations [15–17, 25, 26]. The sample, consisting of three fiber bundles of 3 mm macroscopic diameter each containing 2700 gold-plated 50 μm diameter copper fibers, slid on a gold-plated track inside a 15 cm i.d. copper hoop to which a burnished MoS₂ film had been applied. A nitrogen atmosphere was used which was humidified to 20% < H < 90% by passing the nitrogen through a water bath or through drying agents, as needed [15–17].

Momentary slider position and contact resistance were recorded during sliding runs of about 2 min. Loads (P) used were 0.5 N (i.e. the sample and slider assembly without extra weights), 2.5 N and 8.0 N, at hoop speeds (v) of 0.5, 0.3, 0.8, 1.3, 2.0 and 3.0 cm s^{-1} , and at relative humidities (H) of 20%, 35%, 55%, 75% and 90%, for a total of 90 runs and 3 h cumulative run time. From these data the average contact resistance and average coefficient of friction were determined for each run.

The runs were performed in random order with regard to selection of load and humidity, and for any one combination of humidity and load, speeds were also varied in random order. This was done in order to check for slow variations with time; however, none were found and the measurements were reversible within the resolution limits of the measurements. This indicated that the total sliding distance and duration of the experiment were too small to be affected by the gradual MoS₂ film deterioration discussed in the introduction. The data are thus uncontaminated by complications of possible chemical reactions between MoS₂ and water, and presumably also by possible intercalation of water into the MoS₂. Accordingly, the effects of humidity observed in the present experiments were attributed to adsorbed moisture only.

The inner track of the hoop was prepared by burnishing (by hand with tissue paper for several minutes) fine (0.4 μm) MoS₂ powder until an even appearance was achieved. Before actual tests the track was run-in for several hours and excess MoS₂ powder was brushed off intermittently, leaving visually uniform and transparent tracks. The thickness of the films therefore was clearly well below 0.5 μm , because films thicker than

0.5 μm have a dark gray appearance, while a specially prepared 0.1 μm thick film on a separate sample (as further explained in the next section) looked similar to that of the burnished track.

2.4. Experimental results

Figure 1 shows the time-averaged friction coefficient as a function of humidity and sliding speed in a nitrogen atmosphere at loads of (a) 0.5 N, (b) 2.5 N and (c) 8.0 N. In all cases the coefficient of friction (μ) rises with speed at low humidities, as would be characteristic of boundary lubrication, albeit the speed dependence is rather weak. For relative humidities of less than 50% μ is equal to 0.14 ± 0.02 , above which it rises with rising humidity to about 0.22. As to load dependence, comparison of Figs. 1(a)–1(c) shows that the moisture level has less effect on μ at the highest load tested (8.0 N) than at the lower loads (0.5 N and 2.5 N).

Figure 2 shows the time-averaged electrical resistance for the burnished film as a function of humidity at loads of (a) 0.5 N, (b) 2.5 N and (c) 8.0 N, at a sliding speed of 1.3 cm s^{-1} . Like μ the average electrical resistance shows only a weak speed dependence, and it was decided to take more data points as a function of humidity. As shown in Table 1, the resistance asymptotically drops with rising humidity to 1.32 $\text{m}\Omega$ for a load of 0.5 N, 0.49 $\text{m}\Omega$ for a load of 2.5 N, and 0.30 $\text{m}\Omega$ for a load of 8 N. By comparison, without a burnished MoS₂ film the resistance of similar gold-plated copper fibers on a gold-plated copper hoop is about 0.6 $\text{m}\Omega$ at a load of 0.5 N, 0.3 $\text{m}\Omega$ at a load of 2.5 N, and 0.1 $\text{m}\Omega$ at a load of 8 N respectively.

The most noteworthy features regarding the measurements summarized in Figs. 1 and 2 are as follows:

(i) Unlike μ , which is nearly constant for relative humidities up to about 50%, resistance drops with increasing humidity starting from the lowest relative humidity.

(ii) At about the same humidity level that μ starts to rise, the electrical resistance decreases at an accelerated rate.

Additionally, and not shown in these figures, the resistance does not change with changing humidity if the slider and the hoop are in stationary contact, and, importantly, the humidity dependence of resistance is reversible with changes in relative humidity.

3. Supplementary information obtained outside the hoop apparatus

3.1. Determination of the number and size of contact spots

By measuring the electric contact resistance, the experiment yielded data on the thickness (d) of the

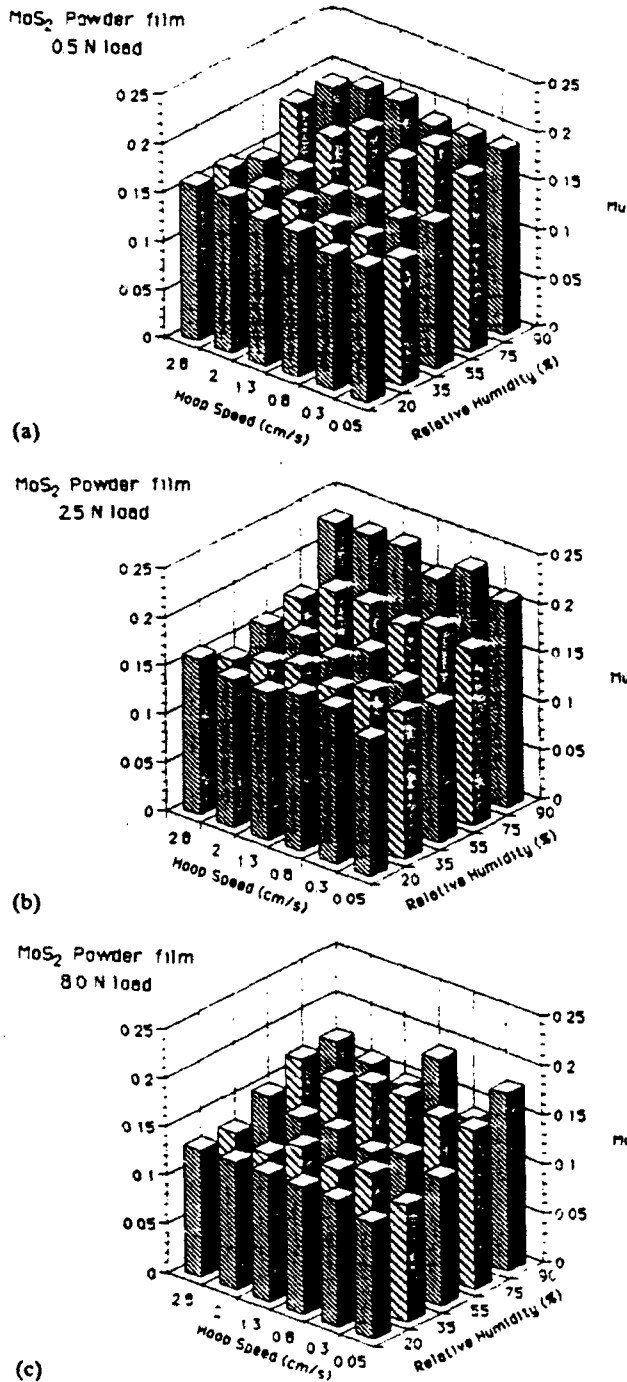


Fig. 1. Friction coefficient (μ) of the burnished MoS₂ film in a nitrogen environment as a function of sliding speed and humidity at loads of $P=0.5$ N, $P=2.5$ N, and $P=8.0$ N.

MoS₂ films at the contact spots as a function of contact spot size, average pressure on the film at the contact spots, and sliding speed (shear rate) of the film material, all as a function of humidity. Past experience has shown that typically such data are so rich in information and so complex that they permit the construction of surprisingly detailed models of the material's behavior at

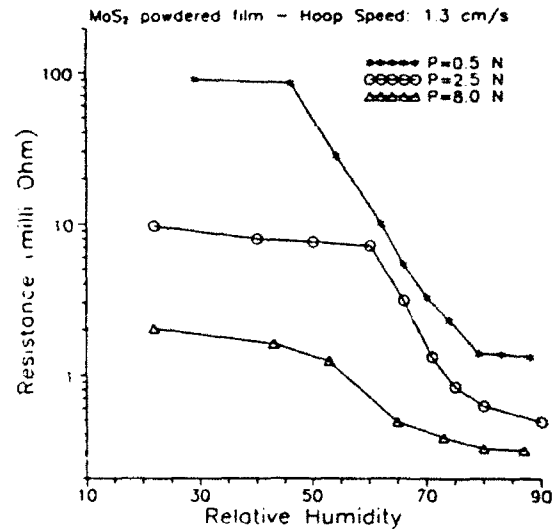


Fig. 2. Electrical resistance (R) of the burnished MoS₂ film in a nitrogen environment as a function of humidity at the sliding speed of 1.3 cm s^{-1} : (a) $P=0.5$ N; (b) $P=2.5$ N; (c) $P=8$ N.

the contact spots, exactly the location of tribological interest.

In general, the electrical resistance of an annulus of constant thickness between an assumed hertzian contact spot is proportional to its thickness and inversely proportional to its area if the thickness is much smaller than the diameter of the annulus, and also if the constriction resistance is negligible, as in the present case [9, 15, 31–33]. With n contact spots, the total electrical resistance (R) is the result of n parallel resistors, and considering that the resistivity (ρ) of MoS₂ can be a function of the thickness, we have

$$\rho(d)d = RA \quad (1)$$

where A represents the area summation of the n individual contact spots. It has been implicitly assumed in eqn. (1) that the average contact spot radius (a) is much larger than the film thickness so that the edge effects around the peripheral regions for the resistance measurements are insignificant. However, the film thickness should be large enough, say larger than 5 nm, so that the tunneling does not have to be considered [9, 15, 34].

To derive the momentary film thickness at the spots from R and the product ρd requires knowledge of the total area of the contact spots (A). In the plastic case, when the local pressure at contact spots approaches the Meyer hardness (H_s), this poses no problem since then:

$$A = \sum_{i=1}^n \pi a_i^2 \approx \frac{P}{H_s} \quad (2)$$

However in the elastic case, when the contact pressure is below the Meyer hardness, A depends on the number

TABLE 1. Contact spot radius (a) calculated from eqns. (2) and (3) [28, 29] (n estimated to be 1500), contact pressure (p), electrical resistance (R), thickness (d) of burnished MoS₂ film in between the contact spots as calculated from eqn. (1), at different loads (P) for the lowest humidity ($H=20\%$) and the highest humidity ($H=90\%$)

| Load P (N) | Humidity H (%) | Cont. rad. a (nm) | Cont. Pre. (10^8 N m^{-2}) | Resist. R (m Ω) | Film thick. d (nm) |
|-----------------|---------------------|------------------------|---|------------------------------|----------------------------|
| 0.5 | 20 | 650 | 2.5 | 90 | 275 |
| 0.5 | 90 | 650 | 2.5 | 1.3 | 47 |
| 2.5 | 20 | 1100 | 4.4 | 10 | 127 |
| 2.5 | 90 | 1100 | 4.4 | 0.5 | 51 |
| 8.0 | 20 | 1950 | 4.5 | 2.0 | 95 |
| 8.0 | 90 | 1950 | 4.5 | 0.3 | 53 |

of spots (n) as [9]

$$A = \sum_{i=1}^n \pi a_i^2 \approx 1.2n^{1/3} \pi \left[\frac{P}{E} r \right]^{2/3} \quad (3)$$

where E is Young's modulus and r is the curvature of the contacting surfaces. Therefore knowing n is critical for distinguishing between plastic and elastic contact spots and for finding p and hence ρd , but n can only be estimated. Finally, the average contact spot radius (a) is of importance for the relative ease or difficulty of the squeezing out of MoS₂ from between contact spots or pushing it ahead of them. Again this requires knowledge of n since, independent of p , for essentially round contact spots:

$$a = \left(\frac{A}{\pi n} \right)^{1/2} \quad (4)$$

For bundles of very fine and not too densely spaced fibers, virtually all fibers touch the substrate and n varies between one and three per fiber [27, 28] but the samples used herein were relatively stiff and the applied loads too low as to cause all fibers to touch at the same time. The number of contact spots, n , was therefore estimated at about 1500 based on scanning electron microscopy examinations because only about 20% of fiber ends appeared to be polished after testing.

As already discussed, the total contact area is determined by eqn. (2) for plastic contact spots and by eqn. (3) for elastic contact spots. The change-over from elastic to plastic spots occurs when the local pressure (P/A) increases to H_c as load increases. Since the interfacial MoS₂ films are thin (less than 1 μm thick), the mechanical properties of the soft substrate (the 5 μm thick gold platings with $H_c \approx 4.5 \times 10^8 \text{ N m}^{-2}$ and $E \approx 80 \text{ GPa}$) control the deformation type and the contact spot radius [35].

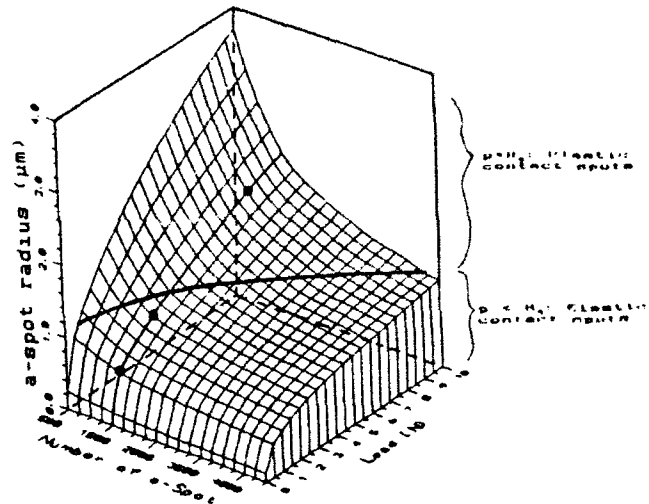


Fig. 3. Calculated contact spot radius [28, 29] as a function of load and number of contact spots. The three heavy dark points designate the experimental loads. The heavy dark line divides the figure into the region of elastically deformed contact spots (below) and the region of plastically deformed contact spots (above).

The availability of our specialized computer program is of great value here as it permits the setting of valuable limits for the values of interest [29, 30]. Altogether, therefore, the desired values of film thickness d as a function of v , p , a , and humidity can be derived from measurements of the contact resistance R . By correlating those data with the coefficients of friction a detailed model of the film behavior at the contact spots can be constructed.

As shown in Fig. 3, the average contact spot radius (a) was obtained via the computer program already discussed [29, 30] as a function of number of contact spots and load. Here the heavy horizontal line indicates the transition between elastic and plastic contact spots. Above the line the local pressure (p) is essentially constant at H_c , but below it, p decreases with decreasing load (P). As the dark line shows, the elastic to plastic transition load increases with increasing number of contact spots as expected, and for the assumed 1500 contact spots the critical load is about 3.5 N. Accordingly, for $n \approx 1500$ the contact spots are elastic for the 0.5 N load with $a = 650 \text{ nm}$, are also elastic for the 2.5 N load with $a = 1100 \text{ nm}$, but are plastic for the 8.0 N load with $a = 1950 \text{ nm}$. Thus, given the applied load and number of contact spots, the contact area can be found from Fig. 3 using $A = n\pi a^2$.

3.2. Determination of the MoS₂ bulk resistivity

As eqn. (1) shows, apart from the contact area (A), the resistivity (ρ) of the MoS₂ is also required in order to calculate the film thickness at the contact spots. Since the MoS₂ used is in the form of a fine powder,

it is expected that the resistivity will depend on its density. This dependence is inferred by measurements outside the hoop apparatus as follows. A pellet of 0.5 g MoS₂ powder was compressed in a die with a 1 cm² cross-section area (A), and both the thickness (d) and the electrical resistance (R) of the pellet were measured. The same experiment was repeated using a wet MoS₂ pellet (stirred into paste with distilled water) so as to investigate the effect of water on the resistivity. The final thicknesses of the pellets were about 0.11 cm in both cases, giving a density close to the theoretical density of 4.7 g cm⁻³. The resistivities of the pellets were then calculated according to eqn. (1), and are presented in Fig. 4.

As Fig. 4 shows, for the dry MoS₂ pellet the resistivity decreases with density, but for the wet pellet it increases with density. Evidently, then, the increase of the resistivity for the wet pellet is due to the decrease of ionic conduction as the water in the MoS₂ pellet was gradually squeezed out. In any event, the measured bulk resistivities differ very little at the highest density and approach the not unreasonable value of 25 Ω m [8]. Indeed, as shown in Fig. 4, at high densities the resistivities vary little. Most significantly, this value of the MoS₂ bulk resistivity would suggest an unbelievably small film thickness of 1×10^{-3} Å (about a ten thousandth of a MoS₂ monolayer) at contact spots when eqn. (1) is applied to the hoop data as shown in Fig. 2. It is proposed that this may be due to two factors which were overlooked in applying eqn. (1).

The first factor is the contact area (A). The contact area used in the estimate of the film thickness was obtained via Fig. 4 and hence it is the load-bearing area. Therefore one may argue that the electrical contact

area rather than the load-bearing area should be used. However, even if the whole fiber cross-sectional area (50 μ m in diameter) is assumed to make electrical contact with the MoS₂ film, the computed film thickness is still less than one monolayer. Moreover, if the argument of a much larger electrical contact area rather than the load-bearing area were correct, the electrical resistance as shown in Fig. 2 would be independent of the applied loads. This is so because the change of the load-bearing area due to the change of the applied load is about 200 times smaller when compared to the fibers' cross-section area, i.e. the change due to the load is too small to be distinguished. Thus, any doubts regarding the contact area can be confidently ruled out.

The second possible factor involves the resistivity measurements. From the appearance of the sliding tracks on the hoop surface, which are more or less transparent films, we know that the thickness of the MoS₂ film is less than 1 μ m. It is well known that the sub-micron thick space charge (or depletion) layer of metal-semiconductor contacts [9, 32, 33] plays an important role in electrical properties, and that the resistivity of thin MoS₂ (n-type semiconductor) films can be very different from their bulk resistivity. Therefore, it is essential to employ the resistivity of thin MoS₂ films rather than that of the bulk MoS₂, as shown in Fig. 4, when applying eqn. (1) to the hoop data. The thickness dependence of the resistivity of thin MoS₂ films was accordingly determined as described in the next section.

3.3. Determination of MoS₂ film resistivity

Burnished films of different thickness were applied to gold-plated copper coupons which were weighed before and after the film application. The average thicknesses of the films were then deduced using the measured MoS₂ mass and areas and by assuming the MoS₂ theoretical density of 4.7×10^3 kg m⁻³, in the light of previous experiments on compressed powders.

Then the electrical resistances of the different films were determined by measuring the voltage drop across the films against the fiber bundle sample without sliding at low loads. Such a set-up constitutes a metal-semiconductor-metal contact. The I - V characteristics were both ohmic and symmetrical with respect to current reversal for thickness less than 500 nm, but for $d > 1000$ nm the behavior was non-ohmic and there was too much data scatter to give meaningful results. From the I - V curves, R was derived on the assumption that in this pseudo-static configuration no MoS₂ was displaced from between the contact spots, especially at low ambient humidities and low load, although micro sliding could not be prevented as the fiber bundle approached and retreated from the films. Nevertheless, this assumption

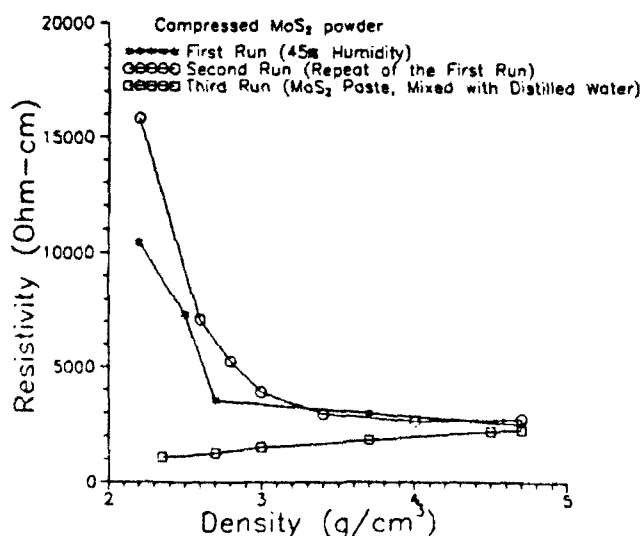


Fig. 4. The bulk resistivity of the dry and wet MoS₂ pellets compressed in a die as a function of density. Note the contribution from the ionic conduction to the wet pellet.

was considered to be valid based on the following considerations:

(i) The electrical contact resistance as measured in the hoop apparatus (Fig. 2) changes very slowly at low humidities.

(ii) The contact resistance did not change with humidity when the hoop was at rest, in which micro sliding equally could not be controlled due to vibrations.

Both cases imply that small vibrations displace very little MoS₂ from between the contact spots.

With these measurements of film thickness (d) and resistance (R) of the burnished MoS₂ film, the product of resistivity and film thickness as a function of film thickness was derived based on eqn. (1). The results, which are shown in Fig. 5(a), are evidently orders of magnitude smaller than found for the compressed pellets in Fig. 4, while the uncertainty for the film thickness is about 40 nm when considering the resolution of the balance used to weigh the burnished substrate.

According to eqn. (1), the product of the MoS₂ film thickness and resistivity (ρd) equals the product of the resistance (R) measured in the hoop apparatus and the load-bearing area (A) (as obtained from Fig. 3), as indicated on the ordinate of Fig. 5(a). Thus d , the film thickness at contact spots under the sliding, can now be derived from measured R values using Fig. 5(a) and computed A values, as in Fig. 3.

Figure 5(b) is a replot of the data in Fig. 5(a) in terms of $\rho(d)$ on a linear scale. It shows that for the first few hundred nanometers the resistivity of the MoS₂ film increases steeply with increasing film thickness up to about 300 nm and then more or less increases linearly at a much lower rate. Note that for MoS₂ films thicker than 1000 nm the I - V curves are non-ohmic and there is much scatter, thus it is probably a coincidence that a linear extrapolation of Fig. 5(b) would roughly intersect the end point of Fig. 4. The initial steep increase in resistivity may be due to grain boundary effects but is more likely due to the space charge distribution about the metal-semiconductor-metal contact interfaces (the depletion regions). It has been reported that the space charge layer is typically 200–300 nm thick [9], and this is very close to the thickness above which the slope of the resistivity about levels off (as seen in Fig. 5(b)) and ohmic behavior ceases. Other related studies have shown that the resistivity of thin films (comparable to those of the present study in thickness) measured parallel to the substrate decrease with film thickness [36–38]. This has been explained by a two-layer model in which the outer layers of the film have a higher resistivity because of surface defects.

3.4. Further considerations of the MoS₂ film resistivity

As was demonstrated in Fig. 2, under sliding conditions the electrical resistance decreases with humidity

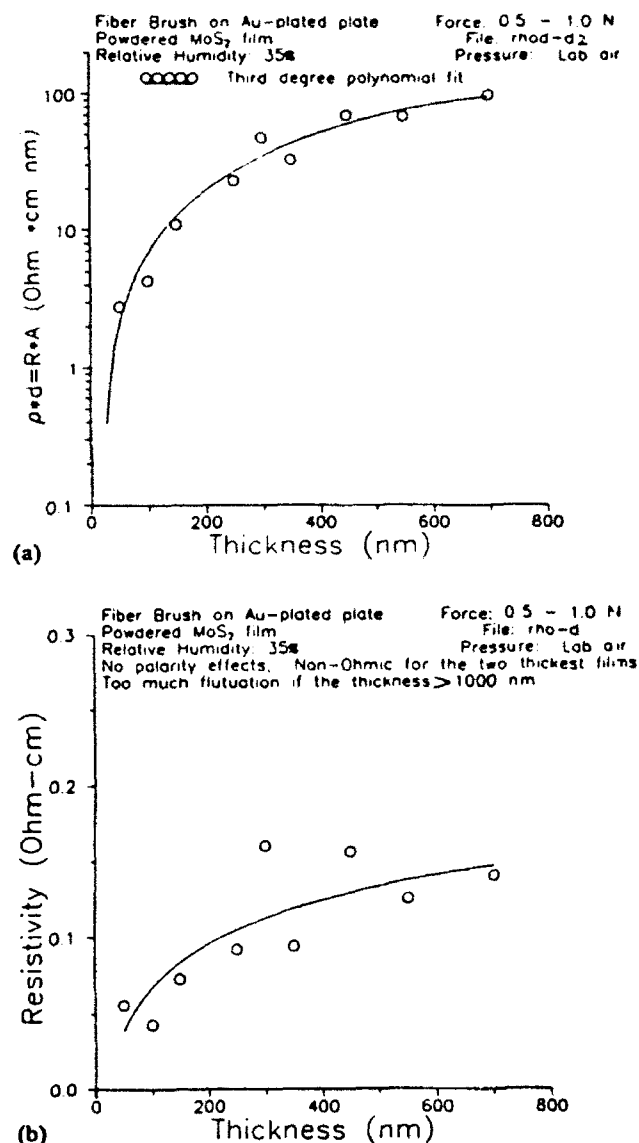


Fig. 5. (a) The product of the resistivity and thickness versus film thickness, to be compared with Fig. 6(a). (b) Resistivity of the burnished MoS₂ film as a function of film thickness.

for all loads. This decrease can be attributed to a decrease in film thickness, reinforced by the discussed decrease of resistivity of MoS₂ with decreasing thickness. However, it is important to test whether indeed the film resistivity is only slightly dependent on humidity as it is with the bulk resistivity, as shown in Fig. 4. Note that although this figure shows that water content in the wet MoS₂ pellet has a large effect on the bulk resistivity at low MoS₂ bulk densities, even with that effect the bulk resistivity is still very much higher than the film resistivity of Fig. 5.

One possible cause of an effect of humidity on MoS₂ film resistivity is ionic conduction through water. To test for this effect a cylindrical compressed slug of MoS₂ (25 mm diameter \times 5 mm high) was submerged

in a 250 ml beaker of distilled water for 14 h. During this time the resistivity of the water was found to decrease by a factor of 1000, from approximately $2.5 \times 10^5 \Omega \text{ cm}$ to $2.5 \times 10^2 \Omega \text{ cm}$ where it leveled out. Even with this significant decrease the ionic resistivity of the water is still over a thousand times larger than that of the burnished films as seen in Fig. 5, making it insignificant. This is quite in line with the data for the wet pellet in Fig. 4. Attempts at further confirmation through measuring the conductivity of MoS₂ powder suspended in water were abandoned because a partial coverage of electrodes with MoS₂ gave inconsistent results.

In addition to the possible effect of water on the resistance of bulk or powdered MoS₂, the effect of humidity on the resistivity of the thin MoS₂ film was investigated by setting the hoop speed to zero and measuring the contact resistance at different humidities. Within our experimental uncertainty, the resistance was found unchanged, even when a drop of water was introduced at the brush/substrate interface. This indeed also indicates a negligible effect of ionic conduction besides absence of any special effect on film properties.

Since, as demonstrated above, neither the resistivity of the MoS₂ film (ρ) nor the contact area (A) changed with humidity, we may thus conclude that the reduction of contact resistance with rising humidity under sliding is due to a reduction in the film thickness (d) between the contact spots. The questions left then are: how thin are the films at the spots, and by what mechanism does the adsorbed moisture affect film thinning during sliding?

4. Discussion

4.1. Estimate of the MoS₂ film thickness at contact spots

Since a functional form of the resistivity on the film thickness is not known, the experimental data in Fig. 2 were plotted in Fig. 6(a) so that the film thickness can be derived by comparing Fig. 6(a) with Fig. 5(a). The resulting film thickness is plotted in Fig. 6(b) as a function of humidity for the three loads. Evidently, the film thickness decreases with increasing load more rapidly at low than at high humidity. Interestingly, at high humidities (more than 70%), the film thickness rises slightly rather than decreases with load. Altogether, then, the discussed results clearly show that the film thickness at the contact spots during sliding generally decreases with humidity and contact pressure, but tends to increase with contact spot size.

Table 1 summarizes the results in terms of average contact spot size, the resistance and the calculated film thickness, all at lowest and highest humidities and at

different loads. Note here that at $P=0.5 \text{ N}$, the contact spot diameter is about five times larger than the film thickness at low humidities which is the lowest diameter to thickness ratio found so that the assumptions made for eqn. (1) are valid. The contact pressures at high loads approach or equal the hardness of the substrate ($4.5 \times 10^8 \text{ N m}^{-2}$).

4.2. Comparing the hoop data with existing models

The present experimental results do not impinge upon the earlier models [7, 12] of MoS₂ degradation mentioned in the introduction since these concern a chemical breakdown of the lubrication film. By contrast, our results apply to short-term tests on fresh MoS₂ films and are reversible with humidity.

Our results evidently rule out any models [11] based solely on enhancement of basal plane texturing parallel to the interface by adsorbed water since that would imply a decrease in friction with increasing moisture, and an increase in resistance due to the higher resistance of $M S_2$ perpendicular to the basal plane. Both deductions are in clear conflict with our data.

Also the possible intercalation of water between basal planes of MoS₂ [3] can be ruled out as this should cause an increase in the resistance with humidity, namely due to film thickening and lowered conductivity through water intercalation at high humidities.

Finally, the model in which water is filling gaps between MoS₂ powder [11] correctly predicts a decrease of resistance with humidity. Even so it cannot explain our results since at 90% relative humidity the adsorbed water content is on the order of 1 wt.% [11] and this is too small for effects so large. Indeed, Fig. 4 demonstrates that the resistivity of bulk MoS₂, lowered through the increase of both density and water content, is still far too high to account for the humidity effect on the data of Fig. 2.

Thus, the inadequacy of these existing models leaves us in need of a new model for moisture-induced MoS₂ film degradation.

4.3. Proposed film thinning model

In crystalline solids, film thinning occurs by the movement of dislocations when the resolved shear stress exceeds the flow stress, and in the case of MoS₂ lubrication we may confidently assume that the dominant shearing mechanism is basal plane slip. Burnished MoS₂ films consist of highly oriented layers with the basal planes nearly parallel to the surface and, subsequently, at rest the applied normal forces result in very low resolved shear stresses parallel to the basal planes. This results in no significant plastic deformation or film thinning.

Application of superimposed shear deformation, however, can cause considerable plastic deformation and

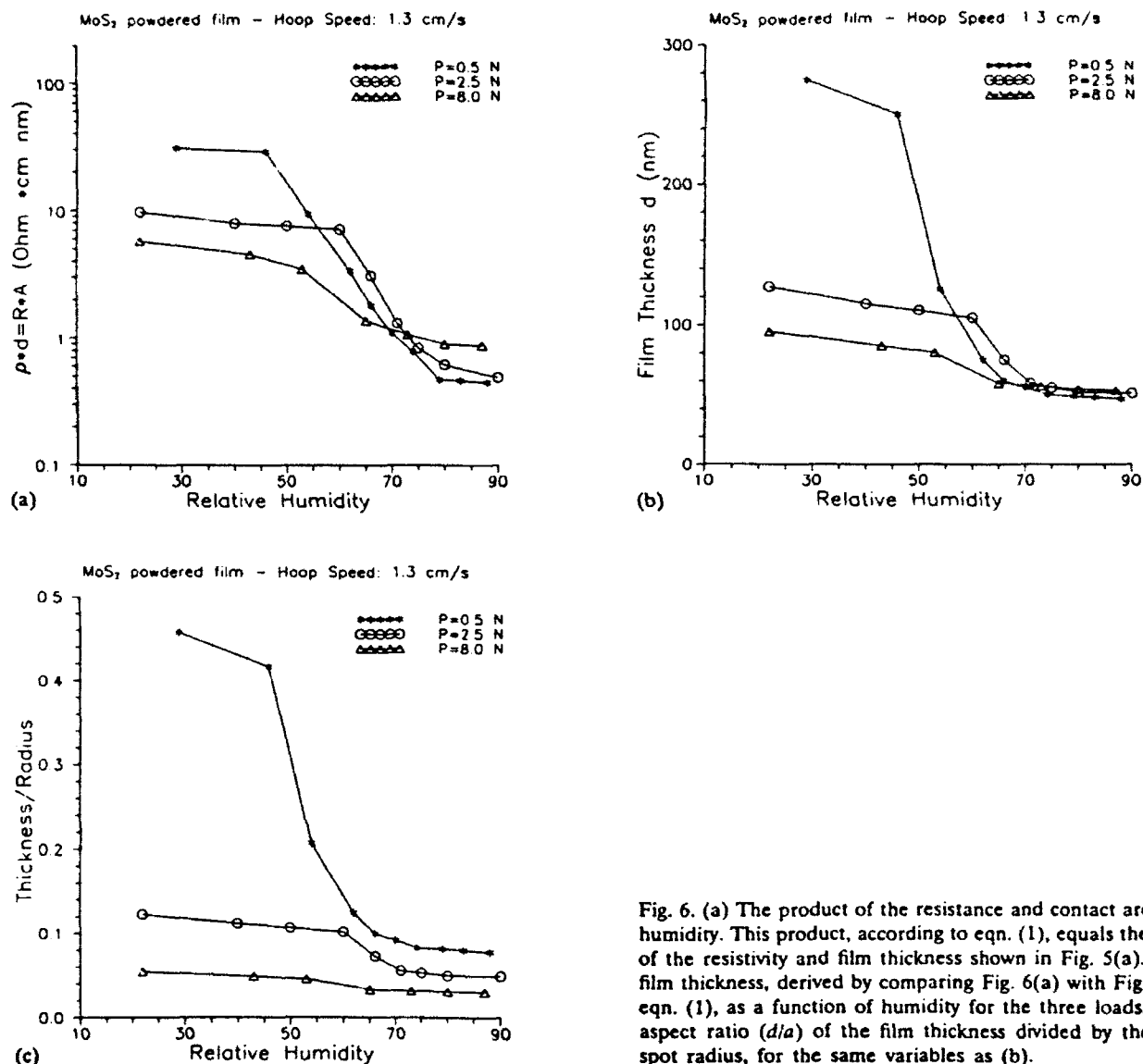


Fig. 6. (a) The product of the resistance and contact area versus humidity. This product, according to eqn. (1), equals the product of the resistivity and film thickness shown in Fig. 5(a). (b) The film thickness, derived by comparing Fig. 6(a) with Fig. 5(a) via eqn. (1), as a function of humidity for the three loads. (c) The aspect ratio (d/a) of the film thickness divided by the contact spot radius, for the same variables as (b).

lead to local thinning, as demonstrated by numerous observations on simulated contact spots between Bridgman anvils [39–43]. In these contact spot simulation experiments the degree of thinning depends primarily upon:

- (i) the shear strength of the film relative to the contact spot pressure;
- (ii) the degree of tangential shear strain at the contact spots;
- (iii) the aspect ratio of film thickness to contact spot diameter.

Thinning is enhanced by a lower film shear strength (or a larger resolved shear stress), a larger degree of strain, and a larger aspect ratio.

4.4. Interpretation of the hoop data

Inspection of the figures reveals qualitative agreement of the above three points with the data if the reasonable

assumption is made that moisture adsorbed on the surfaces of the powder particles increases the ease with which they slide parallel to each other. According to this model, increasing humidity causes the local film thickness (d) and subsequently the contact resistance (R) to decrease under all circumstances, as is indeed observed. For humidities of less than 70% thickness (d) distinctly decreases with increasing applied force (P) due to increases in the local pressure (p). At the highest humidities, however, the softened films are pushed out from between the contact spots even at the lower pressures.

In order to understand the data in greater detail it is necessary to consider the dependence of local contact spot pressure and of aspect ratios (d/a) on force P . This was done by utilizing the already mentioned computer program for the evaluation of local flash tem-

peratures at contact spots [29, 30]. The results are shown in Fig. 3. Specifically, at low loads the contact spots are purely elastic as designated by the region below the dark line. From some critical load per spot upwards the spots deform plastically, as indicated by the area above the dark line. In the plastic condition, the local pressure is effectively independent of load (P), namely about equal to the Meyer hardness of the softer component, which in our present case is the gold plating. Correspondingly, for a fixed number of contact spots, estimated to be 1500 in the present tests, beginning with the smallest loads, local pressure (p) will rise with load (P) until the elastic/plastic transition, above which it will remain close to the Meyer hardness of the gold plating. Consequently, the thickness to contact spot radius ratio (d/a) decreases with increasing load (P) due to increasing radius (a).

Figure 6(b) shows the data converted into the experimentally deduced dependence of film thickness on humidity for the three applied forces. Similarly Fig. 6(c) shows the aspect ratios for the same variables. Plotted in this fashion the self consistency of the data with the model is apparent.

The above analysis is limited by not knowing the exact number of contact spots and the Meyer hardness of the gold plate, thus there remains some ambiguity regarding the absolute values of the pressure. Regardless of these uncertainties, however, the cross-over at which point resistance (R) decreases with load (P) at low humidities but increases somewhat with load at high humidities (Figs. 6(a) and (b)) is now seen to be the result of different aspect ratios (d/a) at different conditions, because d decreases with increasing humidity while a increases with increasing load.

The dependence of friction on humidity and pressure (load), as seen in Fig. 1, is also in agreement with the model: with increasing humidity the more mobile MoS₂ particles cause locally deeper grooves to be plowed through the film, and this plowing causes an increase in friction (μ). Accordingly, low local pressures (as with the lowest applied load, $P=0.5$ N) and smaller aspect ratios (as with the highest load tested, $P=8$ N) result in less grooving and relatively less material displacement, and thus smaller friction μ than observed for the intermediate load of $P=2.5$ N.

Plowing of contact spots through the film would also tend to disorient MoS₂ particles away from basal plane texturing more at higher humidities, since the MoS₂ particles are more mobile. This shearing induced disorientation would cause a decrease in the Schmidt factor [44] of the particles, resulting in a smaller resolved shear stress thus causing μ to rise with increasing humidity.

Another mechanism, so called stiction [16, 17], may also contribute to increased μ values at high humidity

levels. The stiction force has recently been of great interest and concern in the fields of scanning probe microscopy and magnetic recording. Stiction is proposed to occur when the lubricant film reaches a critical thickness at which concave menisci form around contact spots. The resulting negative (Laplace) pressure [11, 16, 45–47] owing to the curvature of the menisci effectively adds an additional normal force, thereby increasing the effective μ .

5. Summary and conclusion

The humidity effects on both shear stress and film thickness of burnished MoS₂ lubrication films have been investigated through a study of the friction coefficient and the electric contact resistance. The friction coefficient was found to equal about 0.14 from 20% to 50% relative humidity, above which it starts to rise with rising humidity to about 0.22 at 90%. By contrast, the electric contact resistance drops only slowly from its level at the lowest humidity of 20% and then drops much faster above about 50% humidity, the same range in which friction starts to increase.

Neither the resistivity of the burnished MoS₂ film nor the contact area (as controlled by the mechanical properties of the gold plating) change with humidity. Therefore, it is the film thickness between the contact spots that is responsible for the decrease of the electric contact resistance. Indeed, the film thickness of the burnished MoS₂ film, which is on the order of 100 nm under the sliding contact spots, also depends strongly on local contact pressure and contact spot size. The film thickness between the contact spots can be calculated by eqn. (1), provided the contact area and the resistivity of the MoS₂ film are known.

Determination of the real contact area for elastic deformation (low loads) requires knowledge of the number of contact spots. For the fiber slider used in the present tests this was estimated at about 1500, assumed independent of load, by SEM examination. Average contact spots radius was then calculated using a specialized computer program, and was found to be on the order of 1 μ m, depending on the load.

The resistivity of the burnished MoS₂ film as a function of film thickness was determined outside the hoop apparatus using a four-probe technique, with the film thickness determined by weighing. The MoS₂ film resistivity obtained in this manner is four orders of magnitude lower than that of bulk MoS₂ (compressed powder) and is three orders of magnitude lower than the ionic resistivity of MoS₂ in water.

Based on the discussed experimental observations, and in line with observations of simulated contact spots between Bridgeman anvils, a thinning model for the

MoS₂ film is proposed. This model is based on three principal points:

(i) Adsorbed moisture enhances MoS₂ thinning by increasing the ease with which MoS₂ particles slide over each other.

(ii) Thinning is enhanced by increasing load (and pressure) until the local pressure reaches the hardness of the softer material, in this case gold, above which the pressure remains constant at the Meyer hardness of gold.

(iii) Film thinning is also enhanced by an increased aspect ratio of film thickness to contact spot radius (d/a).

The interplay of these three factors causes the film thickness in the present experiments to generally decrease with increasing local pressure, except at relative humidity levels over about 70%. At these higher humidities the aspect ratio (d/a) begins to dominate, resulting in a reduced dependence of the film thickness on load.

An increase in friction is found at higher humidity levels, and this is proposed to be a result of: (i) deeper plowing of the contact spots through the MoS₂ film; (ii) capillary forces resulting from thicker adsorbed water layers; (iii) decreases in the Schmidt factor of the MoS₂ basal planes owing to disorientation during plowing.

In conclusion, the primary short-term effect of water on MoS₂ films is, by adsorption onto the MoS₂ particles, to soften the film. This promotes large scale plastic deformation so that the contact spots push the film ahead and to the sides, leaving a thin film between the spots which is sheared during sliding.

Acknowledgment

The financial support of this research through the Materials Division (P. Schmidt and M. B. Peterson, Tribology) of the Office of Naval Research, Arlington, VA is gratefully acknowledged.

References

- 1 I. L. Singer, Solid lubrication films for extreme environments, *Mat. Res. Soc. Proc.*, **140** (1989) 215–225.
- 2 P. D. Ehni and I. L. Singer, Composition of sputter deposited MoS₂ films during run-in in vacuum, *Mat. Res. Soc. Proc.*, **140** (1989) 245–249.
- 3 E. W. Roberts, Towards an optimised sputtered MoS₂ lubrication film, in *20th AMS NASA Conference* Pub. 2423, May 7–9, 1986, pp. 103–119.
- 4 C. Pritchard and J. W. Midgley, The effect of humidity on the friction and life of unbonded molybdenum disulphide films, *Wear*, **13** (1969) 39–51.
- 5 T. Spalvins, Morphological and frictional behavior of sputtered MoS₂ films, *Thin Solid Films*, **96** (1982) 17–24.
- 6 T. Spalvins, A review of recent advances in solid film lubrication, *J. Vac. Sci. Technol.*, **A5** (2) (1987) 212–219.
- 7 R. Holinski and J. Gansheimer, A study of the lubricating mechanism of molybdenum disulfide, *Wear*, **19** (1972) 329–342.
- 8 W. O. Winer, Molybdenum disulfide as a lubricant: a review of the fundamental knowledge, *Wear*, **10** (1967) 422–453.
- 9 R. Holm, *Electrical Contacts*, Springer, Berlin, 4th edn., 1967.
- 10 V. Buck, A neglected parameter (water contamination) in sputtering of MoS₂ films, *Thin Solid Films*, **139** (1986) 157–168.
- 11 R. R. M. Johnston and A. J. W. Moore, The burnishing of molybdenum disulphide onto metal surfaces, *Wear*, **7** (1964) 499–512.
- 12 J. K. G. Panitz, L. E. Pope, J. E. Lyons and D. J. Staley, The tribological properties of MoS₂ coatings in vacuum, low relative humidity and high relative humidity environments, *J. Vac. Sci. Technol.*, **A6** (3) (1988) 1166–1170.
- 13 A. W. J. DeGee, Y. Solomon and J. H. Zaat, On the mechanisms of MoS₂-film failure in sliding friction, *ASLE Trans.*, **8** (1965) 156–163.
- 14 P. Niederhauser, H. E. Hintermann and M. Maillot, Moisture-resistant MoS₂-based composite lubricant films, *Thin Solid Films*, **108** (1983) 209–218.
- 15 C. Gao and D. Kuhlmann-Wilsdorf, Adsorption films, humidity, stick-slip, and resistance of sliding contacts, *IEEE Trans. Components Hybrids Manuf. Tech.*, **14** (1991) 37–44.
- 16 C. Gao, D. Kuhlmann-Wilsdorf and M. S. Bednar, On the tribological behavior of adsorbed layers, especially moisture, *Wear*, **149** (1991) 297–312.
- 17 C. Gao, D. Kuhlmann-Wilsdorf and D. D. Makel, Moisture effects including stiction resulting from adsorbed water films, *J. Tribol.*, **114** (1992) 174–180.
- 18 S. J. Needs, Boundary film investigations, *Trans. ASME*, **62** (1940) 331.
- 19 K. Tanimoto and E. Rabinowicz, *A Fluorescence Technique for Measuring Lubricant Thickness on Hard Magnetic Disks*, STLE Reprint No. 91-TC-3A-1, 1991, pp. 1–7.
- 20 J. V. Alsten and S. Granick, Molecular tribometry of ultrathin liquid films, *Phys. Rev. Lett.*, **61** (1988) 2570–2573.
- 21 A. M. Homola, J. N. Israelachvili, M. L. Gee and P. M. McGuiggon, Measurements of and relation between the adhesion and friction of two surfaces separated by molecularly thin liquid films, *ASME J. Tribol.*, **111** (1989) 675–682.
- 22 D. Y. C. Chan and R. G. Horn, The drainage of thin liquid films between solid surfaces, *Chem. Phys.*, **83** (1985) 5311–5324.
- 23 D. Kuhlmann-Wilsdorf, D. D. Makel, N. A. Sondergaard and D. W. Maribo, On the two modes of operation of monolithic Ag-C brushes, in *Proc. 34th Holm Conference on Electric Contacts*, San Francisco, CA, IEEE, Piscataway, NJ, 1988, pp. 213–222.
- 24 D. Kuhlmann-Wilsdorf and D. D. Makel, Microstructural instability in metal-graphite lubrication films, in *Proc. US-India Workshop on Metastable Microstructures*, Goa, India, March 30–April 2, 1989 in press.
- 25 L. J. Bredell, L. B. Johnson and D. Kuhlmann-Wilsdorf, Teaming measurements of the coefficient of friction and of contact resistance as a tool for the investigation of sliding interfaces, *Wear*, **120** (1987) 161–173.
- 26 D. Kuhlmann-Wilsdorf, Y. J. Chang and L. B. Johnson, Friction, wear and interfacial electrical resistance. Part I. The hoop apparatus, *ASME J. Tribol.*, **109** (1987) 604–608.
- 27 C. M. Adkins III and D. Kuhlmann-Wilsdorf, Development of high-performance metal fiber brushes II – testing and properties, in *Proc. 25th Holm Conference on Electric Contacts*, Illinois Institute of Technology, Chicago, IL, 1979, pp. 171–184.

- 28 C. M. Adkins III and D. Kuhlmann-Wilsdorf, Development of high-performance metal fiber brushes III – further testing and theoretical evaluation, in *Proc. 26th Holm Conference on Electric Contacts*, Illinois Institute of Technology, Chicago, IL, 1980, pp.67–72.
- 29 D. Kuhlmann-Wilsdorf, Temperature at interfacial contact spots: dependence on velocity and on role reversal of two materials in sliding contact, *ASME J. Tribol.*, 109 (1987) 321–329.
- 30 D. Kuhlmann-Wilsdorf, D. D. Makel and N. A. Sondergaard, Refinement of flash temperature calculations, in F. A. Smidt and P. J. Blau (eds.), *Engineered Materials for Advanced Friction and Wear Applications*, ASM, Metals Park, OH, 1988, pp. 23–32.
- 31 M. Visscher and A. F. C. Kanters, Literature review and discussion on measurements of leakage, lubricant film thickness and friction of reciprocating elastometric seals, *J. Soc., Tribol. Lubr. Eng.*, 46 (1991) 785–791.
- 32 R. H. Cox and H. Strack, Ohmic contacts for GaAs devices, *Solid-State Electron.*, 10 (1967) 1213–1218.
- 33 E. H. Rhoderick, *Metal-Semiconductor Contacts*, Clarendon, Oxford, 2nd edn., 1988.
- 34 J. G. Simmons, Generalized formula for the electric effect between similar electrodes separated by a thin insulating film, *J. Appl. Phys.*, 34 (1963) 1793–1803.
- 35 I. L. Singer, R. N. Bolster, J. Wegand and S. Fayeulle, Hertzian stress contribution to low friction behavior of thin MoS₂ coatings, *Appl. Phys. Lett.*, 57 (1990) 995–997.
- 36 V. Danodara Das and B. Seetharama Bhat, A two-layer model to explain the thickness dependence of conductivity and thermoelectric power of semiconductor thin films and application of the model to PbTe thin films, *J. Appl. Phys.*, 67 (1990) 3724–3727.
- 37 R. M. Valletta, G. Guthmiller and G. Gorman, Relation of thickness and some physical properties of NiFe thin films, *J. Vac. Sci. Technol.*, A9 (1991) 2093–2098.
- 38 U. N. Chaudhuri, K. Ramkumar and M. Satyam, Variation of resistivity with thickness of tin oxide films grown by spray pyrolysis, *J. Phys. D*, 23 (1990) 994–995.
- 39 D. J. Dunstan, Theory of the gasket in diamond anvil high-pressure cells, *Rev. Sci. Instrum.*, 60 (1989) 3789–3795.
- 40 J. F. Prins, Cessation of flow between Bridgman anvils, *High Temp.-High Pressures*, 15 (1983) 21–26.
- 41 J. F. Prins, A semiempirical description of pressure generation between Bridgman anvils, *High Temp.-High Pressures*, 16 (1984) 657–664.
- 42 D. Kuhlmann-Wilsdorf, B. C. Cai and R. B. Nelson, Plastic flow between Bridgman anvils under high pressures, *J. Mater. Res.*, 6 (12) (1991) 2547–2564.
- 43 M. Wakatsuki, K. Ichinose and T. Aoki, Notes on compressible gasket and Bridgman-anvil type high pressure apparatus, *Jpn. J. Appl. Phys.*, 11 (1972) 578–590.
- 44 R. W. Hertzberg, in *Deformation and Fracture Mechanics of Engineering Materials*, Wiley, New York, 3rd edn., 1989, pp. 84–85.
- 45 J. Y. Yuan, Z. F. Shao and C. Gao, An alternative method of imaging surface topologies of bulk non-conducting specimens by scanning tunneling microscopy, *Phys. Rev. Lett.*, 67 (1991) 863–866.
- 46 Z. F. Shao, C. Gao and J. Y. Yuan, Scanning tunneling microscopy using ionic conduction for imaging non-conductive specimens, *Mod. Phys. Lett. B*, 6, (1) (1992) 9–13.
- 47 H. K. Christensen, Capillary condensation in systems of immiscible liquids, *J. Colloid Interface Sci.*, 104 (1985) 170–178.

MECHANISM OF METAL AMORPHIZATION THROUGH PLASTIC DEFORMATION

Doris Kuhlmann-Wilsdorf and M. S. Bednar
Department of Materials Science and Engineering
University of Virginia, Charlottesville, VA 22901

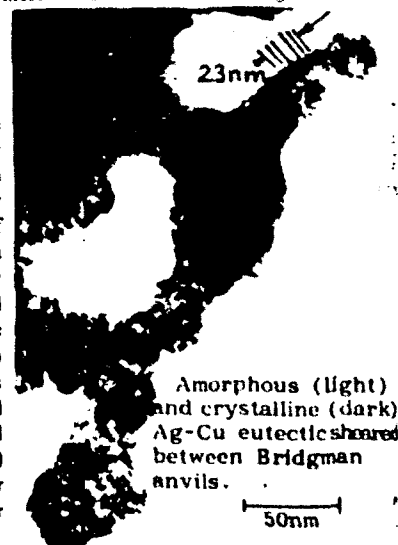
(Received November 12, 1992)
(Revised November 25, 1992)

Introduction

Methods of Amorphization: A fairly wide range of metal alloys can be made amorphous by five different treatments (1): (i) "vapor quenching", i.e. condensation of a metal vapor on a substrate much below melting temperature (2), (ii) quenching of liquid alloys (3-5); (iii) interdiffusion between metals which do not form a solid solution (6,7), (iv) bombardment by fast particles (8,9); and (v) severe cold-deformation, including rolling of stacks of thin foils (10), shearing of such stacks between Bridgman anvils as done by Talyanin et al (11) and in our laboratory, mechanical alloying (12-16), or extrusion (17). In all cases, the pre-requisite for amorphization is that the excess energy due to crystal defects, atomic disorder and/or strain exceeds the heat of melting. Solubility gaps are therefore if not perhaps essential in attempts to amorphize an alloy then at the least very helpful, and so are large negative heats of mixing among the constituent atoms and nearness to a eutectic (10).

Atomistic Mechanisms: For some of the above modes of amorphization the atomistic mechanism seems clear enough. Amorphization through vapor quenching and splat-cooling does not involve changes in composition. Correspondingly, these require nothing but cooling rates fast enough to inhibit crystallization so that the order of statistical atomic deposition or of the melt, respectively, is frozen in. The thermodynamics of the requisite intermixing in the amorphization through interdiffusion as under (iii) is also well understood (1), although the detailed mechanism of the crystalline to amorphous transformation is still unclear. Fairly evident in both respects, i.e. of the intermixing and break-down of crystalline order, is the action of particle bombardment to induce amorphization. Here individual impacts deposit such concentrated energy that profuse atomic displacements result and spikes of localized liquid-like disorder are generated almost instantly. The structure of those spikes is then quenched-in through internal heat conduction even more effectively than quenching through splat cooling. So far obscure, however, in both respects is the manner in which plastic deformation can cause amorphization. The requisite excess energy can be readily accounted for by invoking dislocation and surface energy as stored in sub-, twin, grain and/or phase boundaries inclusive of the energy of the internal stresses generated by them. However, how these translate into intermixing and loss of crystallinity is still an open question for which an answer is proposed herein.

Amorphous Structure: At first glance, an appealing thought is that amorphization through straining occurs gradually, when the ordinary, well-known grain or sub-grain refining which to some degree is caused by every low-temperature plastic deformation is carried to the extreme. This interpretation was apparently initially favored by Y. V. Talyanin and co-workers (11) who pointed out that when the "grains" of coherently scattering volume elements have shrunk to comprise only several atoms, the diffraction contrast has become indistinguishable from that of liquid, i.e. amorphous, metals. However, this hypothesis of amorphization as a consequence of unlimited grain refinement through plastic deformation is certainly incorrect. For one, the computed radial correlation functions for small disordered crystallites of aluminum, lead and mercury (18,19), though strongly resembling those of the corresponding melts, are yet distinctly different from these in implying too much retained order. Another decisive argument is that the amorphous phase makes discontinuous boundaries with the crystalline material. This has been established through micrographic evidence in a number of papers in the literature (e.g. 16,17) and Fig 1 shows an example. Moreover, as discussed by Johnson (section 3.5 of ref. 1) based on (20-23), the nucleation of the amorphous phase may be retarded or inhibited by lack of active nucleation sites. Nucleation has been observed to occur preferentially at twin boundaries (17), and was inferred at grain boundaries (1,22,23).



All this would still leave open the possibility that amorphous metals are indeed ultra-fine grained but without a definite structure, i.e. may be composed of a range of domain sizes which at the upper end have a cut-off at, say, 2.5 nm with the smallest observed grain (or sub-grain) sizes of deformed metals lie somewhat above 10 nm. This possibility may be put out on two different arguments. Firstly, small grain sizes per se do not cause loss of crystalline order. Thus already metal atom clusters in the gas phase tend to be well ordered (24,25), and detailed measurements of crystal orientation and lattice constants can be made on gold crystallites as small as 2 nm on an inert substrate (26-28). Secondly, it appears that for a given alloy the amorphous phase has a well-defined, distinct structure independent of its mode of formation. This is indicated by the fact that, at least in the case of $\text{Cu}_{40}\text{Zr}_{60}$ specifically examined by D. Lee et al. (15), the amorphous phase has the same structure whether formed through melt spinning, proton irradiation or mechanical alloying. Albeit, samples made by the latter two means tend to retain small crystalline inclusions. Such inclusions are indeed very common in metallic glasses produced through plastic deformation. In connection with Fig 1, and with a series of similar samples made from a variety of different alloys to be further discussed below, note that the selected area electron diffraction patterns were unequivocally of the amorphous type when taken of amorphous areas without inclusions and that they were similarly unequivocally crystalline when taken of even the smallest inclusions to which the electron beam could still be focused, e.g. about 40 nm.

The question as to the atomistic mechanism by which amorphous metals form in the course of severe plastic deformation thus is still unanswered. In the following it will be argued that the transformation occurs through a dislocation mechanism which is closely related to melting, of metals in particular and all crystalline materials in general. The theory proposed herein is thus an expansion of the dislocation theory of melting (29,30), and for this reason this will be discussed first.

The Dislocation Theory of Melting

Basic Considerations: Already prior to the theory under discussion here (29,30), several dislocation theories of melting had been proposed as listed by Nabarro (31), but none other has been worked out in greater detail and does as successfully explain so much in regard to melting and liquid structures, as follows: On account of their relative state of disorder as well as of their local volume expansion, dislocation cores have a sizeable entropy. As a result, on heating the free energy of dislocation cores decreases fairly rapidly to vanish at some critical temperature and on to increasingly negative values. However, since mobile dislocations mutually screen at least a major part of their long-range stresses at their distances of separation, and since that screening is particularly effective for parallel dislocations of opposite sign (e.g. positive and negative edge dislocations or left- and right-handed screw dislocations), straight dislocations become unstable once the free energy of their cores assumes negative values. Namely, once the temperature exceeds that critical level, dislocations will spontaneously lengthen into hairpin turns and thereby proliferate dislocation core structure without adding to their long-range stress energy. Indeed, as the whole material transforms into dislocation core structure, all long-range stresses are extinguished. That filling of a crystal with dislocation core structure must necessarily cause the very changes which we associate with melting, and therefore it must be melting since no other comparable transformation is known for crystalline materials. This may be easily seen if one visualizes the results of such dislocation core proliferation: Most obviously, there will be a loss of crystalline order. Further, unless dislocation mobility is low, the material will become fluid, and otherwise it will become glassy. Besides, normally there will be a slight decrease of density in accord with the lower density within dislocation cores where neighboring atomic planes slide over each other.

A simple analysis further showed that two important empirical relationships are effortlessly explained by the above theory (30). One is Richard's law to the effect that the molar heat of fusion (L_u) relates to the melting temperature (T_u) as $L_u/T_u = BR$ with R the gas constant and B a constant not far from unity. The other is Lindemann's formula $T_u = \Theta_D^2 AV^{2/3}/C_L^2$, where Θ_D is the Debye temperature, A the atomic weight, V the molar volume, and C_L a numerical constant of about 140 for fcc metals when expressed in cgs units. All other relevant empirical observations were also found to be in harmony with the theory. Subsequently the theory was employed to compute the interfacial energies between a number of pure crystalline solids and their melts (32), namely as one half of those of the corresponding large-angle grain boundaries. Here, too, good agreement was found between theory and experiment, including for such diverse substances as gold, water, mercury, platinum, bismuth and lithium.

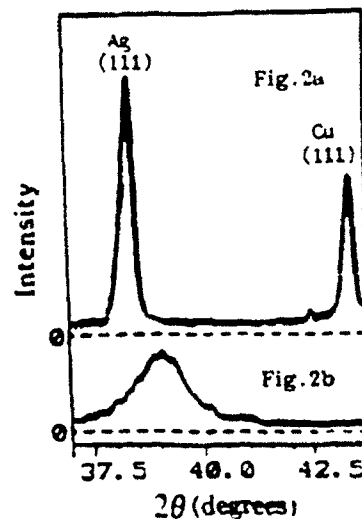
Models of the Atomistic Structures of Amorphous Metals: While the introduction of a profusion of dislocation cores in melting causes the break-down of crystallinity, i.e. causes amorphization, this is not synonymous with complete loss of order. If this were so, the very concept of dislocation cores would lose all meaning. Conceptionally, at a minimum either the order of the glide plane must be locally preserved or the order normal to the Burgers vector (33). Physically, the former will arise from unlimited glide on the most closely-packed crystal plane and is expected for metals which have a strong preference for a particular glide plane, specifically $\{111\}$ in fcc metals. Correspondingly, this model of the melt is dubbed "the planar glide model". The second is dubbed the "pencil glide model" since it would be generated through unlimited pencil glide. This is expected for metals in which slip can take place with a fixed Burgers vector but on a variety of different glide planes, as is the case in particular for iron and other bcc metals. In the planar glide model, ordered domains consisting of stacks of fragments of the most closely packed

plane therefore exist, of the size of the average width of the dislocation cores. The spacing of the planes within the stacks is just a bit larger than the spacing of the corresponding planes in the solid because those plane fragments are randomly shifted parallel their common plane. The pencil glide type of order, by contrast, consists of close-packed atomic "pencils" which form bundles whose arrangement is that of the atomic rows normal to the Burgers vector in the solid.

Radial correlation functions have been calculated for lead, sodium, thallium, mercury, indium and tin, using both models (33). By fitting an obviously physically needed "broadening parameter" function to simulate the diffuseness introduced through thermal oscillations, in all cases at least one of the models was found to closely reproduce the radial correlation functions known from X-ray studies of the respective melts. It may be noted here that the radial correlation functions of different melts vary markedly except that, coincidentally, the correlation function of the $\{111\}$ planar glide model for fcc metals is identical to that of the $\langle 111 \rangle$ pencil glide model for bcc metals although the two structures are, of course, very different (33). In agreement with core widths, the radial correlation functions suggest order to extend from the average atom to about 2nm. If there was a distinct difference in fit, the result correlated with the known glide behavior of the solid. Specifically, fine agreement was found with the planar glide model for fcc lead and fine agreement with the pencil glide model for bcc sodium. Unfortunately a minor mathematical error occurred without which the agreement could have been made better. This, then, strongly supports the theory.

Supporting Evidence for the Dislocation Theory of Melting and Amorphous Metals: A detailed treatment of the thermodynamics of the pencil glide model has been presented by J. A. Barker (34-38) who found it to be in excellent agreement with all relevant thermodynamical data already years before the dislocation model of melting (29,30) was developed. Barker had deduced his model, "the Barker tunnel model", by searching for that atomic arrangement which would best fit the various known thermodynamical parameters. Subsequently, Fessler et al. (19) showed that the Barker tunnel model generates the radial correlation function of fcc metal melts, and thus also for bcc metal melts due to the noted identity between the correlation functions for the bcc pencil glide model (i.e. Barker's tunnel model) and the fcc planar glide model. Together these various investigations thus lend very strong support to the dislocation theory of melting and melts.

A further boost was given to the theory by observations on diffraction patterns of TEM aluminum foils during in-situ melting. In some cases the spots belonging to one of the $\{111\}$ planes remain visible for a fraction of a second after melting (39-40), as would be directly predicted from the planar glide model (41). In all other cases additional spots persist transiently. These patterns could be explained (40) by the generation of Shockley screw dislocation dipoles on $\{111\}$ at the surfaces, which is even more specifically supportive of the theory. These results are further buttressed by the fact that on amorphization of binary eutectic fcc alloys through plastic strain, the $\{111\}$ crystal reflexes of the two components are replaced by a broad "amorphous" diffraction peak where the $\{111\}$ reflex of the homogeneous alloy should be according to Vegard's law. Specifically, Fig. 2a shows the x-ray diffraction diagram for thin copper and silver foils before deformation, and Fig. 2b the comparable diagram from a mixed stack of those foils after they have been severely sheared between one fixed and one rotating Bridgman anvil with superimposed normal pressure (42,43). In much the same manner the peak position of the diffuse diffraction ring of the amorphous phase of TiNi alloy, also gained through straining, coincided with the diffraction ring from the most prominent crystal plane (17), in that case without lattice constant shift as no composition changes appear to be involved (17).



In agreement with the discussed theory, amorphous metals will be describable in terms of the planar glide and the pencil glide dislocation models or similar dislocation models (44,45). Since dislocation images in computer models are often not at all obvious (44), and their features may be described by Bernal polyhedra (46), this may include also models not overtly considering dislocations (47). At any rate, based on the planar and pencil glide models (33) the scale of the domains, i.e. about 2nm, is in good agreement with the scale of the "pepper and salt" mottling which is characteristic of amorphous areas when seen in TEM. However, the mottling cannot be images of the domains throughout the body of the TEM foils as these are much thicker than 2nm and the contrast would average out. This is not so for foil thicknesses of a few to several nm's. For such, Shieh, Stanwood and Howe (48) have recently made diffraction simulation calculations based on a hard-sphere, dense random packing model and also obtained mottling. The simulated contrast was indeed in good agreement with experimental observation in at least one case but is somewhat different from that seen with thicker foils, namely tending to form channels and strings. Altogether, then, it seems almost certain that the mottling observed with TEM foils of tens of nm thickness, such as in Fig. 1, arises at the exit surface. Quite likely, therefore, the mottling mirrors slight strains due to the domains at the exit surface in consonance with (40).

Dislocation Theory of Strain Amorphization

The Model: Just as envisaged in the dislocation theory of melting, the crystalline structure is destroyed through the filling of the material with dislocation cores, which occurs when glide dislocations proliferate through forming hairpin turns. The necessary condition is, of course, that the defected crystalline phase has a higher free energy than the amorphous phase. In multi-phase crystal structures the critical excess energy resides in phase boundaries, and in one-phase crystals may reside in twin boundaries (17) but probably not grain boundaries due to their too wide spacings. In any case, the initial source of the proliferating dislocations are those boundaries, since they are geometrically composed of dislocations and/or can release glide dislocations through minor local atomic rearrangements. If the amorphization requires the intermixing of different phases, e.g. as in the case of binary eutectics, the same dislocation motion by which the crystalline order is destroyed also causes the intermixing.

The Critical Boundary Density: Designating the boundary energy per atom (assuming the boundary to be one atomic diameter, i.e. b thick) by Γ , the average spacing of the boundaries in each of three mutually intersecting sets by D_B , and the difference of the atomistic free energy of the amorphous and the defect-free crystalline phase with ΔE , the critical condition is

$$3 \Gamma (b/D_B) > \Delta E \quad (1)$$

i.e.

$$D_{Bcrit} = 3 \Gamma b / \Delta E \quad (2)$$

Critical Strain: If the critical boundaries are phase boundaries in three dimensions, and deformation occurs through three-dimensional dislocation motion, the shear deformation dy on any arbitrary combination of crystal plane and slip direction will cause ledges on these so as to increase their total area per unit volume by

$$dA_B = (3 dy/D_B) \sin \alpha \approx 3 dy/2D_B \quad (3)$$

where α is the average angle between the slip direction and the trace of the slip plane on the phase boundaries, i.e. $\sin \alpha \approx 1/2$. However, the total boundary area per unit volume is

$$A_B = 3/D_B \quad (4)$$

so that

$$dA_B \approx 1/2 A_B dy \quad (5)$$

and

$$A_B \approx A_0 e^{\gamma/2} \quad (6)$$

for the critical shear strain

$$\gamma_{crit} \approx 2 \ln(D_0/D_{Bcrit}) \approx 2 \ln(D_0 \Delta E / 3 \Gamma b) \quad (7)$$

where D_0 and D_{Bcrit} are the initial and critical spacings of the boundaries.

Intermixing Through Dislocation Motion: If the crystalline two-phase or multi-phase structure falls into a miscibility gap, no spontaneous interdiffusion is to be expected before amorphizing. In this case at least part of the requisite intermixing on amorphizing is automatically effected by the motion of the dislocations, released from the boundaries, while they destroy the crystalline order. This may be the reason why Bordeaux and Yavari (10) found that the results of their annealing treatments for obtaining amorphization of rolled AlPt layers were "not consistent with a single diffusion mechanism". Namely, the intersection of a boundary by the hairpin turns of n coplanar dislocations will on their atomistic slip plane "roughen" the boundary by $\delta \approx \pm nb/2$. As this occurs with dislocations on several mutually intersecting glide planes, complete intermixing will occur for $\delta \approx D_{Bcrit}/2$. With the spacing of the boundaries being D_{Bcrit} the average depth of hairpin turns required for complete mixing is thus

$$L = (D_{Bcrit} b) D_{Bcrit} = D_{Bcrit}^2 / b \quad (8)$$

Comparison with Experiment

The Role of Twin and Phase Boundaries: In our own experiments, thin ($\approx 0.5 \mu m$) foils of Ag, Al, Au and Cu were layered into $\approx 0.1 mm$ stacks. The foils were either all of one kind, or formed any binary combination of alternating layers to generate compositions to approximate 50w% 50w% or the eutectic, where existing. These stacked foil samples were sheared between Bridgman anvils in a wide range of superimposed pressures (42,43). Amorphization, save for occasional crystalline inclusions partly as small as 3nm, could be obtained for all combinations which exhibit eutectics (i.e. Ag/Al, Ag/Cu, Al/Au and

Al/Cu) but not in the others (i.e. pure Ag, Al, Au and Cu and alloys of Ag/Au and Au/Cu). The persistence of remarkably sharp crystal reflexes in unalloyed metal foil stacks up to extreme shears was already documented for the case of gold in (42), as is consistent with the low-energy dislocation structure (LEDS) theory of plastic deformation (49,50). No effect of pressure could be observed but amorphization seemed to be a consequence of plastic strain alone. On the other hand, in the previously mentioned case of amorphization of TiNi alloy (17), deformation occurred mainly through twinning, whereby the width of the twin lamellae decreased with strain to a minimum of $D_{\text{Berrt}} \approx 5\text{nm}$, and no dislocation cell structure was observed. Thus not dislocation sub-boundaries nor foil interfaces per se triggered the discussed amorphizations, but twin boundaries in (17), and phase boundaries between immiscible metals in our experiments.

Numerical Comparison with Experimental Data: A reasonable average estimate for the crystalline-amorphous free energy difference is, say, 6kJ/mole (10) or $\Delta E = 0.063\text{eV/atom}$, and for the phase or twin boundaries 400 ergs/cm^2 or $\Gamma \approx 0.25\text{eV/atom}$, while $b \approx 0.3\text{nm}$. Further, for eutectics one may estimate the initial lamella thickness, i.e. boundary spacing, at $D_0 \approx 10\mu\text{m}$. With these values eqs 2, 7 and 8 yield $D_{\text{Berrt}} \approx 4\text{nm}$; $\gamma_{\text{crit}} \approx 15$ and $L \approx 40\text{nm}$. All of these are reasonable values. Specifically, in the case of amorphization of TiNi alloy (17), the twin lamellae decreased with strain to a minimum width of $D_{\text{Berrt}} \approx 5\text{nm}$; and amorphous regions spread out along the four intersecting sets of twin lamellae observed. In (17) the smallest strain to trigger amorphization was $\gamma = 0.7$, i.e. much smaller than would have been needed to produce interphase boundaries through dislocation shear in accordance with eq 7. In our own experiments shears are not uniform and no reliable values of γ_{crit} have so far been obtained, but the nearest distances between phase boundaries seen in TEM lie between 2 and 4 nm (compare the markers at phase boundaries in Fig. 1), and remnant crystalline inclusions can be as small as 3nm, as already mentioned, all in good agreement with the estimated D_{Berrt} above. Finally, in the experiments by Bordeaux and Yavari (10) cold-rolled Al/Pt multi-layers began to amorphize after 50 rolling passes yielding an average Pt layer size of 60nm, while essentially complete amorphization was achieved only after 130 passes and the TEM micrographs show remnant Pt layer thicknesses of only a few nm.

Nucleation: On account of the interfacial energy between the amorphous and crystalline phase(s), nucleation is required for transformations in both directions. The requisite nuclei for transformation from the crystalline to the solid amorphous state or melt, respectively, are normally preformed and freely available in the form of grain boundaries (32) as also dislocation arrangements, twin and/or phase boundaries. Superficially it would appear that the dislocation cores constituting the melt or amorphous phase, as the case may be, can similarly form crystal nuclei through glide. However, the dislocations which were geometrically well defined in the crystal and by their proliferation destroyed the crystalline order have lost their identity in the melt. Based on (39-41,44) it is herewith suggested that this occurs in two steps, namely that in the short time during which selected crystal reflexes remain visible after melting (39-41), the dislocation cores are already densely packed but still share common glide planes over distances long compared to their loop diameters or hairpin turns. That intermediate state is indeed necessary for intermixing in accordance with eq 8. The fading of the reflexes then indicates a transition in which the orientations of the domains randomize and thereby the dislocations lose their individuality (compare refs 44 to 47). Because that domain randomization cannot be undone by sliding, nucleation of the crystalline phase on heating the amorphous material is typically more difficult than the reverse, especially if atomic segregation is involved as an additional obstacle.

The discussed intrinsic difficulty of nucleating crystals from the amorphous phase will be observable only in materials without retained crystalline inclusions, since those normally provide the nuclei. Without these, there may be an initial crystallization into a metastable phase, especially if the stable phase requires desegregation, e.g. as in (51,52). In another important special case the boundary energy Γ is more than double the amorphous/crystalline phase boundary energy Γ_{CM} (according to (32) in the range $.03 \leq \Gamma_{\text{CM}} \leq 0.25\text{ J/m}^2$, rising with shear modulus and melting temperature), i.e.

$$\Gamma > 2\Gamma_{\text{CM}} \quad (9)$$

Boundaries for which eq 9 is fulfilled should spontaneously dissociate into a narrow zone of amorphous material. This appears to have been the case in (17) and may well be true in numerous spontaneously amorphizing diffusion couples. In those diffusion samples which do not amorphize unless nuclei are provided, the critical condition of eq 9 is presumably not fulfilled.

Acknowledgments

Some of the early measurements on sheared foil stacks on which this work is based, have been made by Prof. B. C. Cai, now at the Information Storage Research Centre, Shanghai Jiao Tong University, P. R. China. The financial support of this research through the Materials Division (P. P. Schmidt and M. B. Peterson, Tribology) of the Office of Naval Research, Arlington, VA, is gratefully acknowledged.

References

- 1) W. L. Johnson, *Progress in Materials Science*, **30**, 81 (1986).
- 2) W. Buckel and R. Hilsch, *Z. Phys.*, **138**, 109 (1954).
- 3) P. Duwez, R. H. Willens and W. Klement, *J. Appl. Phys.*, **31**, 1136 (1960).
- 4) P. Duwez and R. H. Willens, *Trans. Met. Soc. AIME*, **227**, 362 (1963).
- 5) P. Duwez, *Progress in Solid State Chemistry*, Vol. 3, Pergamon Press, Oxford 1966).
- 6) R. B. Schwarz and W. L. Johnson, *Phys. Rev. Lett.*, **51**, 415 (1983).
- 7) R. B. Schwarz, K. L. Wong and W. L. Johnson, *J. Non-Crystalline Solids*, **61/62**, 129 (1984).
- 8) W. A. Grant, A. Ali, L. T. Chadderton, P. J. Grundy and E. Johnson, in *Proc. 3rd Int. Conf. on Rapidly Quenched Metals* (Ed. B. Cantor, The Metals Soc., London, 1978) p. 63.
- 9) G. Thomas, H. Mori, H. Fujita and R. Sinclair, *Scripta Metall.*, **16**, 589 (1982).
- 10) F. Bordeaux and A. R. Yavari, *J. Appl. Phys.*, **67**, 2385 (1990).
- 11) Y. V. Tatyannin, V. G. Kurdyumov and V. B. Fedorov, *Fiz. metal. metalloved.*, **62**, 133 (1986). (*Phys. Met. Metall.* p.118).
- 12) Yermakov, E. E. Yurchikov and V. A. Barinov, *Fiz. metal. metalloved.*, **52**, 1184 (1981).
- 13) C. C. Koch, O. B. Cavin, C. G. McKamey and J. O. Scarborough, *Appl. Phys. Lett.*, **43**, 1017 (1983).
- 14) R. B. Schwarz and C. C. Koch, *Appl. Phys. Lett.*, **49**, 146 (1986).
- 15) D. Lee, J. Cheng, M. Yuan, C. N. J. Wagner and A. J. Ardell, *J. Appl. Phys.*, **64**, 4772 (1988).
- 16) P. Y. Lee, J. Yang and C. C. Koch, *J. of Less-Common Metals*, **140**, 73 (1988).
- 17) Y. V. Tatyannin and V. G. Kurdyumov, *phys. stat. sol.*, **a121**, 455 (1990).
- 18) R. Kaplow, S. L. Strong and B. L. Averbach, *Phys. Rev.*, **138**, A1336 (1965).
- 19) R. R. Fessler, R. Kaplow and B. L. Averbach, *Phys. Rev.*, **150**, 34 (1965).
- 20) J. F. M. Westendorp, Ph.D. thesis University of Utrecht, Netherlands (1986).
- 21) F. W. Saris, J. F. M. Westendorp and A. Vredenberg, *Beam - Solid Interactions and Phase Transf.*, (MRS, Boston, 1986) p.405.
- 22) K. Samwer, H. Schroeder and M. Moske, *Phase Transitions in Condensed Systems - Experiment and Theory* (MRS, Boston, 1987) p.405.
- 23) P. R. Okamoto, H. Hahn and R. Averbach, *Beam - Solid Interactions and Phase Transformations*, (MRS, Boston, 1986).
- 24) J. P. Bucher, D. C. Douglass and L. A. Bloomfield, *Phys. Rev. Lett.*, **66**, 3052 (1991).
- 25) D. C. Douglass, J. P. Bucher and L. A. Bloomfield, *Phys. Rev. Lett.*, **68**, 1774 (1992).
- 26) W. A. Jesser and D. Kuhlmann-Wilsdorf, *J. Appl. Phys.*, **38**, 5128 (1967).
- 27) W. A. Jesser and D. Kuhlmann-Wilsdorf, *Acta Metall.*, **16**, 1325 (1968).
- 28) J. S. Vermaak and D. Kuhlmann-Wilsdorf, *J. Phys. Chem.*, **72**, 4150 (1968).
- 29) D. Kuhlmann-Wilsdorf, *Physics Letters*, **17**, 113 (1965).
- 30) D. Kuhlmann-Wilsdorf, *Phys. Rev.*, **140**, A1599 (1965).
- 31) F. R. N. Nabarro, *Theory of Crystal Dislocations*, Clarendon Press, Oxford 1967, p. 688.
- 32) I. A. Kotzé, and D. Kuhlmann-Wilsdorf, *Applied Physics Letters*, **9**, 96 (1966).
- 33) I. A. Kotzé, and D. Kuhlmann-Wilsdorf, *Phil. Mag.*, **23**, 1133 (1971).
- 34) J. A. Barker, *Australian J. Chem.*, **13**, 187 (1960).
- 35) J. A. Barker, *Proc. Roy. Soc. (London)* **A259**, 442 (1961).
- 36) J. A. Barker, *Australian J. Physics*, **15**, 127 (1962).
- 37) J. A. Barker, *J. Chem.*, **37**, 1061 (1962).
- 38) J. A. Barker, in *Lattice Theories of the Liquid State*, (Pergamon Press, Oxford, 1963), pp. 42, 104.
- 39) H. Fujita, T. Tabata, K. Yoshida, N. Sumida and S. Katagiri, *Japan. J. Appl. Phys.*, **11**, 1522 (1972).
- 40) R. M. J. Cotterill and J. K. Kristensen, *Philos. Mag.*, **36**, 453 (1977).
- 41) I. A. Kotzé, and D. Kuhlmann-Wilsdorf, *Jap. J. Appl. Phys.*, **12**, 605 (1973).
- 42) B. C. Cai, D. Kuhlmann-Wilsdorf, and R. B. Nelson, "Thin Films: Stresses and Mechanical Properties II" (MRS Symp. Proc. **188**, Eds. M. F. Doerner, W. C. Oliver, G. M. Pharr and F. R. Brotzen, Mater. Res. Soc. Pittsburgh, PA, 1990), p. 183.
- 43) D. Kuhlmann-Wilsdorf, B. C. Cai and R. B. Nelson, *J. Mater. Res.*, **6**, 2547 (1991).
- 44) R. M. J. Cotterill, W. Damgard Kristensen and E. J. Jensen, *Philos. Mag.*, **30**, 745 (1974).
- 45) H. Koizumi and T. Ninomiya, *J. Phys. Soc. Japan*, **44**, 898 (1978).
- 46) H. Koizumi and T. Ninomiya, *J. Phys. Soc. Japan*, **49**, 1022 (1980).
- 47) D. Deng, A. S. Argon and S. Yip, *Phil. Trans. Roy. Soc. (London)*, **329**, 549-640 (1989).
- 48) P. C. Shieh, C. O. Stanwood and J. M. Howe, *Ultramicroscopy*, **43**, 99 (1991).
- 49) D. Kuhlmann-Wilsdorf, *Mater. Sci. Engg.*, **A113**, 1 (1988).
- 50) M. S. Bednar, B. C. Cai and D. Kuhlmann-Wilsdorf, *J. Lubrication Engineering*, 1992, in the press.
- 51) S. Mader, A. S. Nowick and H. Widmer, *Acta Metall.*, **15**, 203 (1967).
- 52) S. Mader and A. S. Nowick, *Acta Metall.*, **15**, 215 (1967).

DISTRIBUTION LIST

- 1 - 3 Scientific Officer Code: 1131N
Peter P. Schmidt
Office of Naval Research
800 North Quincy Street
Arlington, VA 22217-5000
- 4 Administrative Grants Officer
Office of Naval Research
Resident Representative N66002
Administrative Contracting Officer
National Academy of Sciences
2135 Wisconsin Avenue, N. W., Suite 102
Washington, DC 20007-3259
- 5 Director, Naval Research Laboratory
Attn: Code 2627
Washington, DC 20375
- 6 - 7 Defense Technical Information Center
Building 5, Cameron Station
Alexandria, VA 22304-6145
- 8 - 9 E. H. Pancake, Clark Hall
- 10 - 11 D. D. Makel
- 12 D. Kuhlmann-Wilsdorf
- 13 W. A. Jesser
- * SEAS Postaward Research Administration
- 14 SEAS Preaward Research Administration

*Cover Letter

JO#5143:ph